Surfzone vorticity dynamics in a directional wave basin

Christine Marie Baker

A dissertation
submitted in partial fulfillment of the
requirements for the degree of

Doctor of Philosophy

University of Washington

2023

Reading Committee:

Melissa Moulton, Chair

C. Chris Chickadel

Jim Thomson

Program Authorized to Offer Degree:
Civil and Environmental Engineering

University of Washington

Abstract

Surfzone vorticity dynamics in a directional wave basin

Christine Marie Baker

Chair of the Supervisory Committee:
Melissa Moulton
Research Scientist/Engineer, Applied Physics Laboratory; Affiliate Faculty, Civil Environmental Engineering

The surf zone is an energetic and evolving region where waves break near the coast. This region, the transition zone from the shoreline to the deeper waters of the shelf, is critical for supporting ecosystems and valuable recreational and economic resources, and at the same time, is increasingly vulnerable to anthropogenic impacts and the effects of climate change. Breaking waves in this region drive complex circulation patterns, including eddies and rip currents, that disperse material such as pathogens, contaminants, larvae, and excess nutrients from terrestrial runoff.

Rip currents, an important material transport mechanism, are fast, narrow, offshore-flowing jets driven by breaking waves in the surf zone. They occur on beaches under a wide range of conditions and are a dominant contributor to cross-shore exchange of material between the surf zone and the shelf. Transient rip currents are ephemeral ejections associated with surfzone eddies that can occur even on alongshore-uniform beaches. These rip currents are less understood in comparison to bathymetric rip currents that persist at fixed locations determined by bathymetry, but are ubiquitous on many beaches. Under directionally spread wave conditions, waves break in finite-length – short-crested – regions, leading to spatial variations in the breaking force and a corresponding input of rotational motion – vorticity – to the water column. Energy associated with injected vorticity is hypothesized to nonlin-

early transfer to larger scale rotational currents – eddies – that enhance dispersion within the surf zone, interact with other eddies, and episodically eject offshore as a transient rip current. This hypothesis is widely discussed, however, we do not have strong observational evidence for, or a good understanding of, the processes connecting directionally spread wave fields to the formation of large-scale eddies. To overcome the challenges of isolating and studying surfzone vorticity dynamics in the field, large-scale wave basin experiments with an alongshore-uniform barred beach were conducted.

In the first chapter of the thesis, I detail the ecosystem and human health implications and scientific knowledge gaps motivating the laboratory study of surfzone eddies. I also review the dynamics of surface gravity waves, breaking-wave driven mean surfzone currents, including longshore currents and bathymetric rip currents, surfzone eddy forcing and evolution, and transient rip current formation.

The second chapter describes my work investigating short-crested wave breaking that results from directionally spread wave conditions. I quantified wave transformation and directional properties with a 3-d scanning lidar, stereo cameras, and in situ pressure and velocity sensors, which yielded similar estimates. Highly resolved spatiotemporal patterns of wave breaking were characterized by developing a remote breaker identification scheme (RBIS) using a combination of thresholded brightness imagery and stereo camera reconstruction of the water surface elevation. The RBIS estimated average along-crest-length of breaking waves decreases while the number of crest ends increases with increasing directional spread. Parameterized relationships between directional spread and crest properties exhibit similar trends to observed breaking crest length and the number of crest ends within the surf zone.

In the third chapter, I investigate how the wave breaking patterns characterized in the previous chapter relate to the forces driving surfzone eddies and the subsequent eddy evolution. This is hypothesized to include nonlinear energy transfers to larger scales through

an inverse cascade, similar to two-dimensional turbulence. Using stereo reconstructions of the laboratory water surface, I applied a bore model to estimate the along-crest profile of wave dissipation. Next, I computed the breaking force and its curl, which drives a time-rate of change in surfzone vorticity. The estimated curl of the breaking force is highly irregular along individual wave crests and varied from crest to crest. Averaging over many crests, the curl of the breaking force is positively and negatively signed near opposite crest ends. The shape of the crest-averaged curl of the breaking force varies by surfzone region, and the shape near crest ends strongly depends on assumptions about the decay of dissipation outside of an identified crest region. The spatial characteristics of low-frequency currents, estimated from in situ sensors and remote particle image velocimetry, varies with wave directional spread and is similar to expected relationships for a two-dimensional turbulence inverse energy cascade. I synthesize the relationships between the short-crested wave field, estimates of the curl of the breaking force, and low-frequency currents, and describe these relationships in the context of a conceptual model of mechanisms leading to transient rip currents.

In the final chapter, I describe the overall findings and implications of this research, including observational evidence for a conceptual model linking directionally spread wave fields to large-scale, low-frequency motions in the surf zone. I also discuss future research directions needed to improve understanding of these links, including field-based studies, by quantifying individual eddy evolution within and beyond the surf-zone, and exploring implications for swimmer hazard and transport of pollutants, larvae, and sediment.

TABLE OF CONTENTS

LIST OF FIGURES

LIST OF TABLES

ACKNOWLEDGMENTS

The research included in this dissertation was performed in the lands of the Coast Salish peoples, including the tribes and bands of the Duwamish, Puyallup, Suquamish, Tulalip and Muckleshoot nations, as well as the traditional homelands of the Marys River or Ampinefu Band of Kalapuya. I honor with gratitude the water and land, as well as the people, past, present, and future.

This work was supported by the National Science Foundation (NSF), a National Defense Graduate Student Fellowship (NDSEG), and the University of Washington's Royalty Research Fund and Burges Presidential Graduate Fellowship. I thank the staff of the O.H. Hinsdale Wave Research Laboratory at Oregon State University for helping to run experimental trials and obtain, collect, and quality-control in situ measurements. Additionally, thank you to the staff and interns at the Naval Research Laboratory at the John C. Stennis Space Center and at the U.S. Army Corps of Engineers Coastal and Hydraulics Laboratory Field Research Facility for many engaging research discussions.

Thank you to Nirnimesh (Nirni) Kumar (1984–2020) for sharing his love for and extensive knowledge of coastal processes and, most of all, for his compassion and generosity as an advisor and mentor. Nirni's ability to provide an optimal balance of constructive feedback and continuous encouragement was immensely valuable. I, and many others, miss the thrill of doing science with him and his gregarious laughter.

I cannot thank my advisor, Melissa Moulton, enough for being an incredibly thoughtful and tactful mentor. Melissa's creative mindset and innovative approach to tackling research questions, combined with her comprehensive understanding of surfzone processes, is inspiring. Melissa's sustained support and positive attitude have helped me navigate the complexities

of research and life with grace and confidence.

I am very appreciative of all the insightful feedback I received from my committee, which has greatly improved this research. Thank you to Chris Chickadel for always bringing a novel outlook and cheerful demeanor to research meetings. Thank you to Jim Thomson for bringing me to field to learn how to study waves that aren't bound by side walls and for sharing fruitful suggestions throughout every step of my PhD. Thank you to Meg Palmsten and Katherine Brodie for sharing their extensive expertise in all things remote sensing and for welcoming me into their community through internships. Thank you to Michelle DiBenedetto for sharing her fresh perspective on fluid mechanics problems.

Thank you to Judy Liu, Harry Yeh, and Christopher Higgins for introducing me to coastal engineering research in the laboratory. Also, thank you to many other mentors whom have shared guidance, scientific and otherwise, including Alex Horner-Devine, Steve Elgar, and Alexis Kaminski.

I would like to express my deep gratitude to the Environmental Fluid Mechanics group. Thank you to the faculty members for actively cultivating a supportive and flat culture that inspires students to take initiative and voice ideas. I am immensely grateful to all the students and postdocs who were integral to my growth and development as a student and brought joy to my daily life within and outside of the university. Thank you as well to the 2017 oceanography cohort and the broader nearshore processes community.

Thank you to my favorite co-worker, Sneaker, even when you sleep through most work days. Thank you to Brian for inspiring me to pursue this endeavor and helping me to retain a smile the whole way through, even when we were across the world for most of the experience. Thank you, Mom, Dad, and Sarah, for supporting me, without hesitation, and for instilling in me the belief that nature is a source of both inspiration and rejuvenation.

DEDICATION

to Nirnimesh Kumar,
your love of science and
generosity towards others
lives on in us

Chapter 1

INTRODUCTION

1.1 Motivation

The nearshore region consists two parts: the surf zone, extending from the shoreline to the seaward limit of depth-induced wave breaking, and the inner shelf, which has overlapping surface and bottom boundary layers on the continental shelf offshore of the surf zone [*Lentz and Fewings*, 2012]. This highly dynamic region, the boundary between land and open ocean, hosts a rapidly increasing human population, progressively vulnerable infrastructure, degrading water quality, and coastal hazards further magnified by a changing climate [*Intergovernmental Panel on Climate Change (IPCC)*, 2022]. Therefore, it is essential to understand how complex nearshore processes spanning surf-shelf environments impact public safety, economic activity, and fragile ecosystems.

Critical to human and ecosystem health, nearshore dispersion and surf-shelf exchange define the fate of materials [*Moulton et al.*, 2023], such as excess nutrients [*Prosch and McLachlan*, 1984], larvae [*Morgan et al.*, 2017], phytoplankton [*Shanks et al.*, 2018], pollution [*Kim et al.*, 2004], and bacteria [*Boehm et al.*, 2017]. Unfortunately, omnipresent contaminated coastal water due to the disposal of anthropogenic waste [*Halpern et al.*, 2008, 2012; *Boehm et al.*, 2017] is dispersed along coastlines via alongshore currents driven by oblique waves or ejected into deeper waters via cross-shore exchange pathways [*Clark et al.*, 2010; *Hally-Rosendahl et al.*, 2014]. These processes determine if excess nutrients from terrestrial runoff lead to harmful algae blooms [*Anderson*, 2009; *Omand et al.*, 2011] or if recreational swimmers encounter pathogens, which increase the risk of pathogen-born gastrointestinal and viral infections [*Stoner and Dorfman*, 2007]. In addition, species inhabiting the nearshore, such as larvae, exploit surf-shelf exchange pathways for recruitment and settlement, necessary to sus-

tain a thriving ecosystems [*Shanks et al.*, 2010; *Morgan et al.*, 2018]. Comprehensive knowledge of transport pathways within the nearshore can improve our ability to predict water quality and ecosystem vulnerabilities to promote more sustainable environmental practices [*Cowen and Sponaugle*, 2009; *Wu et al.*, 2021].

Covered within this introduction, several processes augment material dispersion and exchange within the nearshore region. In particular, the research within this dissertation aims to deepen our knowledge of the dynamics of surfzone vorticity – the chaotic, multi-scaled, temporally evolving rotational flow – with the principal aim of improving our understanding of rip-current formation and surf-shelf exchange. Rip currents – narrow, fast-moving jets of water extending from the surf zone to the inner shelf – have the additional significance of being the leading cause of fatalities and rescues on U.S. beaches [*Brewster et al.*, 2019].

Cross-shore exchange between the surf zone and inner shelf is primarily driven by transient [*Hally-Rosendahl et al.*, 2014, 2015; *Suanda and Feddersen*, 2015; *Hally-Rosendahl and Feddersen*, 2016] or bathymetrically controlled [*Reniers et al.*, 2009; *Brown et al.*, 2015] rip currents. Unlike bathymetric rip currents that persist at fixed channels or depressions over timescales of hours to days [*e.g., MacMahan et al.*, 2006, 2010a; *Reniers et al.*, 2010; *Castelle and Coco*, 2013; *Brown et al.*, 2015], transient rip currents occur on relatively short timescales, $\mathcal{O}(1-10$ min), with no preferred alongshore location [*Hally-Rosendahl et al.*, 2014, 2015]. It is hypothesized that transient rip currents are offshore ejections of large-scale surfzone eddies generated by nonlinear transfers of energy from vorticity injected at crest ends, similar to a forced two-dimensional turbulence system [*Peregrine*, 1998; *Spydell and Feddersen*, 2009; *Clark et al.*, 2012; *Feddersen*, 2014; *Elgar and Raubenheimer*, 2020]. However, much of this process remains elusive and unobserved. For example, the breaking properties of a short-crested wave field and the resulting vorticity injection are not well characterized, and the consistency of surfzone vorticity dynamics with two-dimensional turbulence is not well established. This body of research elucidates dynamics linking incident waves to large-scale rotational motions within the surf zone that expel water offshore as transient rip currents.

Although surfzone eddies and transient rip currents are ubiquitous on many beaches,

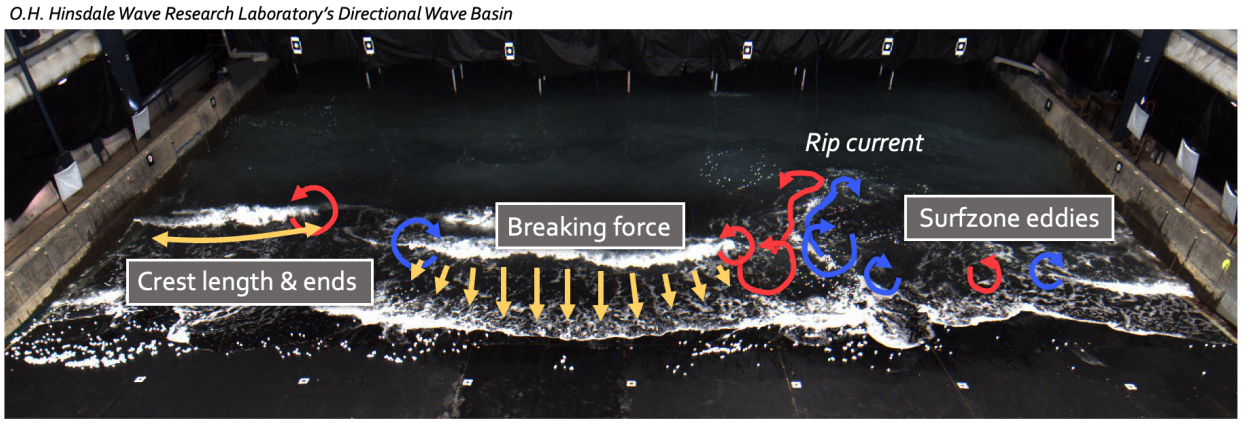

Figure 1.1: Image of the Directional Wave Basin at the O.H. Hinsdale Wave Research Laboratory. Irregular directionally spread waves were generated to study short-crested wave breaking and surfzone vorticity dynamics that led to transient rip current ejections, such as shown by the foam and wiffle balls ejecting offshore. This dissertation investigates the breaking crest length and ends (arrow along bright breaking wave crest), the wave-by-wave breaking force (grey arrows in the direction of wave propagation), and evolution of surfzone eddies (red and blue curled arrows).

their unpredictable nature and narrow alongshore length-scales [*Hally-Rosendahl et al.*, 2014] present challenges when studying them in the field environment. Laboratory experiments allow for measurements of surfzone currents and eddies, without variations in wave breaking due to local or offshore bathymetric non-uniformity or shear instabilities in strong longshore currents that may be present in a field environment. Directional wave basin experiments, equipped with state-of-the-art remote sensing measurements, further our grasp on surfzone vorticity dynamics and transient rip current formation (Figure 1.1, see more details about the laboratory setup in Section 2.2.1).

The remainder of this chapter introduces background on wave breaking and surfzone currents, providing a foundation of the subsequent chapters. This chapter ends with a brief outline of the thesis.

1.2 Surface gravity waves

The surf zone is a narrow, highly dynamic region where waves break, dissipating an abundance of energy that rapidly reshapes the shoreline and disperses material. Understanding wave characteristics as they propagate from deep to shallow water and break within the surf zone is essential to predict potential consequences to our coastal environment. This section provides a brief overview of wave theory, bulk wave statistics, and the kinematics of depth-limited wave breaking. Here, I focus on surface gravity waves; however, waves with longer frequencies from infragravity waves to tides are also have strong effects on our coastlines.

1.2.1 Wave theory basics

Energy in surface gravity waves is divided into potential and kinetic energy. Wave energy (E) is proportional to the wave height squared:

$$E = \frac{1}{8}\rho g H^2 \tag{1.1}$$

where H is the wave height, ρ is the water density, and g is the acceleration due to gravity. The simplest theory to describe the shape, velocity, and associated motions of a single wave train is Airy wave theory (*i.e.,* linear wave theory) based on potential flow. The governing equation for displacement of the water surface ($\eta(x,t)$) from the mean water level is:

$$\eta(x,t) = a\cos k(x - ct + \phi) = a\cos(kx - \sigma t - \phi) \tag{1.2}$$

where x is the distance in the direction of wave propagation, a is the wave amplitude ($H/2$), ϕ is a phase shift, c is wave celerity, and t is time. The wavenumber (k) is related to wavelength (L) by $k = 2\pi/L$, and the angular frequency σ is similarly related to the wave period (T) by $\sigma = 2\pi/T$. Note that if we consider waves propagating at an angle relative to an $xy-$coordinate system, the water surface displacement can be written as $\eta(x,y,t) = a\cos(\boldsymbol{kx} - \sigma t + \phi) = a\cos(k_x x + k_y y - \sigma t + \phi)$. The wave celerity, the speed that the wave travels, is:

$$c = \frac{\sigma}{k} = \frac{L}{T} \tag{1.3}$$

The wave period and length are related by the dispersion relation:

$$\sigma^2 = gk \tanh kh \tag{1.4}$$

where h is the water depth. In deep water when $kh > \pi/2$ ($h/L > 1/2$) and shallow water when $kh < \pi/10$ ($h/L < 1/20$), the dispersion relation and wave celerity simplify to:

$$\begin{aligned} \text{deep water :} \quad & \sigma^2 = gk \qquad & c = \frac{g}{\sigma} \\ \text{shallow water :} \quad & \sigma^2 = k^2 gh \qquad & c = \sqrt{gh} \end{aligned} \tag{1.5}$$

In reality, many wave trains exist simultaneously. Wave groups, the envelope shape of wave amplitudes due to constructive interference, travel at a different speed (c_g) owing to the dispersive nature of waves:

$$c_g = nc \tag{1.6}$$

where:

$$n = \frac{1}{2}\left(1 + \frac{2kh}{\sinh 2kh}\right) \tag{1.7}$$

For example, waves from multiple directions and periods lead to inhomogenous water surface amplitudes that are examined and compared with linear wave theory in Chapter 2. This next section overviews statistical descriptors of wave fields with energy spread in both frequency and direction.

Linear wave theory assumes that the wave steepness is small and wave height is infinitesimally small relative to the water depth. For cases where this is not true (*e.g.,* the surf zone), other approaches such as Stokes, cnoidal, and solitary wave theories may be more appropriate. There are a plethora of books allowing further reading about nonlinear approaches and other aspects of water wave mechanics [*e.g., Dean and Dalrymple*, 1991; *Mei et al.*, 2005, among others].

1.2.2 Bulk wave statistical properties

Ocean waves that arrive at our coastlines are often generated by local or distant storms. As the wind blows along the water surface, turbulent-eddy-induced pressure fluctuations

lead to water surface undulations that develop and grow from wavelets to waves [*Phillips*, 1957]. The continued growth of waves into a developed sea is due to energy transfer from the wind arising shear-flow instabilities [*Miles*, 1957]. Wind-wave fields are heterogeneous with energy distributed broadly over many frequencies and directions. Due to wave dispersion, waves propagating away from a storm travel with different speeds [*Munk et al.*, 1963]. Thus, waves traveling across the ocean arrive at different times as swell with relatively narrow spread in frequency and direction.

Irregular waves with energy distributed over many frequencies are often characterized in spectral space. The energy distribution of these waves can be represented irrespective of wave direction as a frequency spectrum ($S(f)$, where f is frequency) or as a function of both frequency and direction as a directional wave spectrum ($S(f, \theta)$, where θ is direction).

The wave spectrum or the wave variance spectral density function can be estimated from a finite time series record of the water surface elevation with a finite discrete Fourier transform. A full description of frequency domain analysis of a wave record can be found in text books such as *Massel* [1996]; *Thomson and Emery* [2014] and *Kamphuis* [2020]. For practical reasons, representative wave parameters that can be computed from $S(f)$ are used to describe the wave field. One of the common descriptors for wave height is the significant wave height (H_s), the average wave height of the highest 1/3 of waves. Assuming a Rayleigh distribution of wave heights, this is equivalent to four times the standard deviation of the water surface elevation. H_s is thus defined based on $S(f)$ as:

$$H_s = 4\sqrt{\int S(f)df} = 4\sigma_\eta \tag{1.8}$$

where σ_η is the standard deviation of the time series, related to $S(f)$ via Parseval's theorem. Depending on the modality of $S(f)$, different descriptors of wave period may be preferred. Here, we assume that $S(f)$ is uni-modal and well represented by the peak wave period (T_p), simply the frequency of the maximum value of the spectra.

The JONSWAP spectrum, a parametric representation of fully developed wind waves in the ocean, was proposed by *Hasselmann et al.* [1973] based on observations in the North Sea.

An approximate form of the JONSWAP spectrum written in terms of the wave height and period [*Goda*, 1988] is:

$$S(f) = \beta_J H_s^2 T_p^{-4} f^{-5} \exp[-1.25(T_p f)^{-4}] \gamma^{\exp[-(T_p f-1)^2/2\sigma^2]} \tag{1.9}$$

where

$$\beta_J = \frac{0.0624}{0.230 + 0.0336\gamma - 0.185(1.9+\gamma)^{-1}}[1.094 - 0.01915 \ln \gamma] \tag{1.10}$$

$$\sigma = \begin{cases} \sigma_a : f \leq f_p, \\ \sigma_b : f \geq f_p, \end{cases} \tag{1.11}$$

$$\gamma = 1 \sim 7, \sigma \simeq 0.07, \sigma \simeq 0.09 \tag{1.12}$$

The peak enhancement factor (γ) controls the sharpness of the spectral peak. For laboratory experiments described in this dissertation, a JONSWAP spectrum with $\gamma = 3.3$ was used (Section 2.2.1), which is the mean value determined for the North Sea and may not necessarily be transferable to other regions.

Inherent to all wave fields, wave energy is spread over multiple directions due to variability in wind directionality, interaction with surface ocean currents [*Smit and Janssen*, 2019], and refraction and diffraction around bathymetric features in shallow water [*Berkhoff*, 1972; *Svendsen*, 2006]. The directional wave spectrum ($S(f,\theta)$) describes the state of the superimposed directional components and can elude to characteristics such as how short- or long-crested a wave field appears, an essential component of Chapter 2. It is typically expressed as:

$$S(f,\theta) = S(f)D(\theta,f) \tag{1.13}$$

where $D(\theta,f)$ is the directional spreading function. $S(f)$ is the absolute value of the wave energy density, while $D(\theta,f)$ is non-dimensional and normalized, such that:

$$\int_{-\pi}^{\pi} \int_{f_{\min}}^{f_{max}} D(\theta,f) d\theta df = 1 \tag{1.14}$$

Thus, $D(\theta, f)$ provides the relative magnitude of directional spreading (σ_θ). A common functional form for the directional spectrum [*Mitsuyasu et al.*, 1975] is:

$$D(\theta, f) = \frac{1}{\pi} 2^{2s-1} \frac{\Gamma^2(s+1)}{\Gamma(2s+1)} \cos^{2s}\left(\frac{\theta - \theta_0}{2}\right) \tag{1.15}$$

where θ_0 is the principal wave direction and s is the degree of directional energy concentration at the peak of the $S(f)$). s is related to the directional spread (σ_θ) by:

$$\sigma_\theta = \left(\frac{2}{1+s}\right)^{1/2} \tag{1.16}$$

Directional wave proprieties can be inferred with measurements, such as pitch and roll measured by a buoy [*Longuet-Higgins et al.*, 1963], a pressure sensor paired with two-component velocities [*Kuik et al.*, 1988], or an array of sensors measuring the water surface elevation [*Pawka*, 1983]. Estimator methods for the directional spectrum vary in complexity from a direct Fourier transform to the Bayesian directional spectrum estimation [*Hashimoto et al.*, 1988]. For laboratory analysis purposes discussed in Chapter 2, the directional estimator selected for describing laboratory waves was the Extended Maximum Entropy Method (EMEM), a method based on an auto-regressive process of directional waves [*Hashimoto et al.*, 1995], and the directional spread was estimated by both fitting a $\cos^{2s}$ distribution to the spectra and from moments (a_2, b_2) from measurements from colocated pressure gauges and Acoustic Doppler Velocimeters (see Sec 2.3.4). Excellent additional resources on directional spectra are *Goda* [2010] and *Massel* [1996].

1.2.3 Depth-limited wave breaking

Waves transform dramatically as they propagate from deep waters, where their waveform is approximately a sinusoid, to the onset of depth-limited breaking in the surf zone. Offshore of breaking, energy flux is conserved:

$$\nabla \cdot (E c_g) = 0 \tag{1.17}$$

As waves feel the bottom in shallow waters, wave crests become more peaked and their troughs flatten, referred to as wave shoaling. Waves gradually turn toward regions of shallow

water, called wave refraction, causing oblique waves to become closer to shore-normal near the coastline. Snell's law relates the wave direction (θ) and celerity (c) from offshore (subscript 0) to near the shoreline by:

$$\frac{\sin\theta}{c} = \frac{\sin\theta_0}{c_0} = \text{constant} \tag{1.18}$$

This can also result in directional narrowing of a wave field from offshore to the edge of the surf zone, as seen by comparing lab estimates of directional spread offshore and in the surf zone in Section 2.3.4.

Waves continue to steepen until the water particles at the crest exceed the velocity of the wave [*Iversen*, 1952; *Adeyemo*, 1970], causing the crest to become unstable and break. The breakpoint can be described by the Miche criterion [*Micha*, 1951], based on a limiting steepness:

$$\left(\frac{H}{L}\right)_{\max} = 0.142\tanh kh \tag{1.19}$$

Alternatively, the depth at which waves break (h_b) is often described by the breaker index (γ_b):

$$\gamma_b = \frac{H_b}{h_b} \tag{1.20}$$

where H_b and h_b are the wave height and water depth at breaking, respectively. Based on Solitary Wave Theory [*McCowan*, 1894], γ_b is 0.78, but observations suggest that this ratio may vary between $0.2 < \gamma_b < 0.8$ depending on beach slope [*Raubenheimer et al.*, 1996]. Many functional forms have been proposed for the breaking index formula, including some that depend on beach slope, the surf similarity number, wave steepness, and others [*Battjes*, 1974; *Komar and Gaughan*, 1972; *Kaminsky and Kraus*, 1994; *Battjes and Stive*, 1985; *Derakhti et al.*, 2020]. In a saturated inner surf zone, wave heights decay as a function of the water depth and are independent of offshore wave heights [*Thornton and Guza*, 1982; *Raubenheimer et al.*, 1996]. In contrast, wave heights in unsaturated surf zones increase with the offshore wave height [*Baldock et al.*, 1998; *Power et al.*, 2010]. In Section 2.3.5, a breaking gamma index was employed to identify actively breaking regions in water surface elevation maps.

Once waves break, energy flux is no longer conserved and instead is lost due to wave dissipation (*i.e.,* $\nabla \cdot (Ec_g) \approx -D$, where D is dissipation). Accurately describing wave energy dissipation within the surf zone is essential for predicting wave height transformation used for coastal management applications [*e.g.,* predicting sediment transport or runup *Kamphuis*, 2020; *Basco*, 2020]. Wave energy dissipation can be modeled parametrically as a hydraulic jump [*Svendsen*, 1984a] or shear stress exerted by the wave roller along the sloping front face of the underlying wave [*Duncan*, 1981], as described in Section 3.2. Numerical models use several approaches to accurately represent wave dissipation. For example, depth-averaged, wave-resolved models typically represent dissipation by wave breaking with a depth-averaged 'breaking force' term ($\boldsymbol{F_{br}}$) in the momentum equations with horizontal velocities ($\boldsymbol{u} = [u(x,y,t), v(x,y,t)]$), such as:

$$\underbrace{\frac{\partial \boldsymbol{u}}{\partial t}}_{\text{tendency}} + \underbrace{\boldsymbol{u} \cdot \nabla \boldsymbol{u}}_{\text{advection}} + \underbrace{\rho^{-1} \nabla p}_{\text{grav. force}} = \underbrace{\boldsymbol{F_{br}} - \boldsymbol{\tau_b} - \boldsymbol{\tau_w}}_{\text{body forces}} + \underbrace{\nu \nabla^2 \omega}_{\text{viscosity}} \tag{1.21}$$

where ν is the kinematic viscosity and p is the pressure, including the hydrostatic and hydrodynamic contribution to body forces due to gravity (grav.). The right-hand-side terms are viscous forces and additional body force terms that could include the depth-normalized instantaneous bottom stress ($\boldsymbol{\tau_b}$) and surface (wind) stress ($\boldsymbol{\tau_w}$). In Boussinesqu-type modes [*e.g.,* FunwaveC, *Spydell and Feddersen*, 2009; *Feddersen*, 2014], the breaking force term can be approximated with an eddy viscosity-type formulation, parameterized as Newtonian dampening [*Kennedy et al.*, 2000] where:

$$\boldsymbol{F_{br}} = (h+\eta)^{-1} \nabla \cdot [\nu_{\text{br}} (h+\eta) \nabla \boldsymbol{u}] \tag{1.22}$$

The breaking wave eddy viscosity (ν_{br}) is given by:

$$\nu_{\text{br}} = B \delta^2 (h+\eta) \frac{\partial \eta}{\partial t} \tag{1.23}$$

where δ is a constant and B is a function of the surface slope which varies between 0 and 1. The choices of these parameters were tuned based on laboratory observations [*e.g., Chen*

et al., 2003], but have not been tuned with observations of dissipation during short-crested wave breaking. Although this type of model is not used for this dissertation, most of the foundational work on transient rip current processes was completed with phase-resolved Boussinesq models. Realizations of the breaking force estimates in Section 3.4.1 are motivated by a similar framework [*Spydell and Feddersen*, 2009; *Feddersen*, 2014].

The alongshore variability of breaking crests is also consequential for runup, sediment transport, and vorticity generation [*Peregrine and Bokhove*, 1998; *Reniers et al.*, 2004; *Guza and Feddersen*, 2012], but not as well understood. Since depth-limited wave breaking is reliant on changes in water depth (*e.g.,* Eqn. 1.20), alongshore variability in wave breaking is modulated by the bathymetry [*Bowen and Inman*, 1969; *Keeley and Bowen*, 1977; *Putrevu et al.*, 1995; *Slinn et al.*, 2000]. Alongshore variability in wave heights, and therefore, breaking crest length also manifests from wave field directional spreading [*Longuet-Higgins*, 1957]. To date, there are still a limited number of studies examining short-crested wave breaking characteristic, such as their length scales and dissipation properties, most of which are numerical modeling studies [*e.g., Wei et al.*, 2017; *Kirby and Derakhti*, 2019]. Chapter 2 provides an in depth description of the current knowledge about short-crested wave breaking and seeks to better characterize breaker properties based on observations. Consequentially, along-crest variability in wave energy dissipation and the force associated with a breaker (*i.e.,* dissipation over phase speed) are the focus in Sections 3.4.1 and 3.5.1.

1.3 Surfzone currents and eddies

Wave breaking and dissipation within the surf zone drive complex circulation patterns and changes in the water level. The spatial and temporal scales of these processes are highly modified by nearshore bathymetry and incident wave conditions. This section describes theory and relevant literature related to mean currents based on radiation stress, eddy generation and evolution within the surf zone, and transient rip-current-driven exchange.

1.3.1 Mean currents

Mean currents are defined as circulation patterns persisting on timescales of many waves (*e.g.,* hours). Theory for mean water levels and longshore currents in the surf zone originated from the concept of radiation stress [*Longuet-Higgins and Stewart*, 1964], the depth-averaged excess flux of momentum due to surface gravity waves. Radiation stress is a second-order tensor derived from the sum of the transfer of momentum associated with the particle velocity and the wave-induced mean pressure, written as:

$$S = E \begin{bmatrix} n(\cos^2\theta + 1) - \frac{1}{2} & \frac{1}{2} n \cos\theta \sin\theta \\ \frac{1}{2} n \cos\theta \sin\theta & n(\sin^2\theta + 1) - \frac{1}{2} \end{bmatrix} \tag{1.24}$$

where n simplifies to 1 in shallow water. As waves break, energy decreases. This results in cross-shore gradients in the radiation stress that induce forces in the surf zone acting in the wave direction. This is key to theory developed to approximate the breaking force in Section 3.2.

Gradients in the onshore-directed momentum flux (S_{xx}) are balanced by the slope in the mean water level ($\partial\overline{\eta}/\partial x$, known as 'setup'), such that [*Bowen et al.*, 1968]:

$$\frac{\partial \overline{\eta}}{\partial x} = -\frac{1}{\rho g(h + \overline{\eta})} \frac{\partial S_{xx}}{\partial x} \tag{1.25}$$

The wave-induced onshore mass transport is balanced by a return flow [also referred to as 'undertow' *Longuet-Higgins and Stewart*, 1964; *Bowen et al.*, 1968]. This often leads to a vertically sheared cross-shore profile due to the vertical imbalance of these processes [*Svendsen*, 1984b].

Theory for longshore currents was developed by balancing frictional forces with radiation-stress gradients [*Bowen*, 1969; *Longuet-Higgins*, 1970; *Thornton*, 1970]. For long straight beaches, the cross-shore gradient in S_{xy} is approximately equal to the alongshore bottom shear stress (τ_y^b). For example, τ_y^b can be expressed in terms of the alongshore velocity (v) as [*Longuet-Higgins*, 1970; *Feddersen et al.*, 1998]:

$$\frac{\partial S_{xy}}{\partial x} = -\tau_y^b = -\rho c_f \langle |\mathbf{u}| v \rangle \tag{1.26}$$

where c_f is a drag coefficient, $|\mathbf{u}|$ is the magnitude of the total velocity vector above the bottom boundary layer, and $\langle\rangle$ represents a time-average. Thus, oblique waves ($\theta >> 0°$) drive mean longshore currents, often characterized by a logarithmic vertical profile [*Apotsos et al.*, 2008; *Hansen et al.*, 2015]. For further reading about variations in expressions for the longshore momentum balance or derivation of the cross-shore profile of the longshore current, see *Svendsen* [2006].

Bathymetric rip currents are driven by alongshore variation in pressure gradients often resulting from local or offshore bathymetric variations, such as variable patterns in sand bars and troughs [*MacMahan et al.*, 2006; *Dalrymple et al.*, 2011; *Castelle et al.*, 2016]. These rip currents can persist at fixed locations on timescales of hours to days and with speeds that are modulated by wave height and orientation, water level, and channel characteristics [*Moulton et al.*, 2017b]. Due to their persistent location and relative ease of measurements, bathymetric rip currents remain the most well documented and characterized rip current type.

1.3.2 Eddy processes in the surf zone

Low-frequency (frequency, $f < 0.04$ Hz) currents and eddies in the surf zone are hypothesized to be generated by intrinsic instabilities in alongshore currents [*Bowen and Holman*, 1989; *Oltman-Shay et al.*, 1989; *Allen et al.*, 1996] or forced by individual or groups of breaking waves [*Haller et al.*, 1999; *Reniers et al.*, 2004; *Long and Özkan Haller*, 2009; *Peregrine*, 1998; *Johnson and Pattiaratchi*, 2006; *Bonneton et al.*, 2010]. Shear instabilities in alongshore currents due to intrinsic variability of wave-induced currents (*i.e.,* 'shear waves') generate eddies with temporal scales of $\mathcal{O}(0.01$ Hz) [*Bowen and Holman*, 1989; *Dodd et al.*, 1992; *Oltman-Shay et al.*, 1989; *Feddersen*, 1998] and were observed with length scales of 40–250 m [*Özkan Haller and Kirby*, 1999; *Noyes et al.*, 2004].

Wave breaking may generate eddies on multiple scales. Wave-group driven alongshore radiation stress gradients from alongshore wave-breaking variability may contribute to surfzone eddy generation with length scales of [$\mathcal{O}(100$ m) *Haller et al.*, 1999; *Reniers et al.*,

2004; *Long and Özkan Haller*, 2009]. During directionally spread wave conditions, vorticity is injected at the edges of short-crested breaking waves due to the curl in the breaking force [$\nabla \times \mathbf{F}_{\mathrm{br}}$, *Johnson and Pattiaratchi*, 2006; *Bonneton et al.*, 2010; *Feddersen et al.*, 2011; *Clark et al.*, 2012]. The injected vortices with relatively small length scales [*e.g.,* 4–20 m, *Spydell and Feddersen*, 2009; *Feddersen*, 2014; *Kirby and Derakhti*, 2019] may non-linearly transfer energy to larger scales, similar to two-dimensional turbulence [see Section 3.2 for a detailed description of this process, *Kraichnan*, 1967; *Spydell and Feddersen*, 2009; *Boffetta and Ecke*, 2012]. Vorticity injection by individually breaking waves may explain the broad spread of vorticity over frequency and length scales observed in the surf zone, responsible for dispersion and transport on alongshore-uniform beaches [*Feddersen*, 2014].

Low-frequency eddies are often characterized as depth-uniform within the surf zone and weakly vertically dependent in the outer edge of the surf zone [*Henderson et al.*, 2017; *Lippmann and Bowen*, 2016; *Baker et al.*, 2021]. Recent studies suggest that the vertical structure of low-frequency eddies may alter their life-span and the efficiency of an inverse cascade [*Uchiyama et al.*, 2017; *Marchesiello et al.*, 2021a]. The vertical vorticity (ω_z) evolution for three-dimensional, incompressible flow with velocities ($\boldsymbol{u} = [u(x,y,z,t), v(x,y,z,t), w(x,y,z,t)]$) is given as [*Uchiyama et al.*, 2017; *Kirby and Derakhti*, 2019]:

$$\underbrace{\frac{\partial \omega}{\partial t}}_{\text{tendency}} + \underbrace{(\boldsymbol{u}\cdot\nabla)\omega_z}_{\text{advection}} = \underbrace{\omega_x \partial_x w + \omega_y \partial_y w}_{\text{vortex tilting}} - \underbrace{\omega_z(\partial_x u + \partial_y v)}_{\text{vortex stretching}} + \underbrace{\partial_z(K_v \partial_z \omega_z)}_{\text{vertical diffusion}} + \underbrace{\nabla \times [\boldsymbol{F}_{\mathbf{br}} - \boldsymbol{\tau_b} - \boldsymbol{\tau_w}]}_{\text{body forces}} \tag{1.27}$$

where vorticity in three-dimensions is $\boldsymbol{\omega} = \nabla \times \boldsymbol{u} = (\omega_x, \omega_y, \omega_z)$ and K_v is vertical eddy viscosity. If eddies are considered two-dimensional, vortex stretching and tilting as well as vertical diffusion are neglected, resulting in more coherent and long-lived eddies [see theoretical framework in Section 3.2 *Uchiyama et al.*, 2017]. In contrast, depth-dependent eddies may enhance a forward kinetic energy cascade if tilting or stretching is important [*Uchiyama et al.*, 2017; *McWilliams et al.*, 2018]. This may be most relevant near the outer surf zone and as eddies eject offshore.

Many aspects of surfzone vorticity dynamics remain unresolved. Vorticity injection by

short-crested wave breaking and evolution within the surf zone is not well characterized. How does the breaking force vary along a wave crest, and what are the resulting length scales of injected vortices? Is our hypothesis that the surfzone exhibits characteristics similar to two-dimensional turbulence accurate? How do these processes vary with breaking wave characteristics? These are a subset of questions examined within this dissertation.

1.3.3 Transient rip-current-driven cross-shore exchange

Bathymetric and transient rip currents exchange material (*e.g.,* sediment, pollutants, and larvae) up to two to four surfzone widths from the shoreline in observations [*MacMahan et al.*, 2010a; *Hally-Rosendahl et al.*, 2014; *Brown et al.*, 2015; *Hally-Rosendahl et al.*, 2015] and numerical models [*Reniers et al.*, 2009; *Suanda and Feddersen*, 2015]. Bathymetrically controlled rip currents may recirculate water between the surf zone and inner shelf, resulting in little net cross-shore exchange of material in some cases [*Brown et al.*, 2015]. Although net exchange of material by transient rip currents is not yet quantified, transient rip currents, pairs of counter-rotating eddies mutually advecting out of the surf zone, are considered the primary mechanism driving cross-shore exchange on alongshore-uniform beaches [*Clark et al.*, 2011; *Hally-Rosendahl et al.*, 2014, 2015].

Often cross-shore exchange is estimated as the approximate magnitude of the cross-shore component of a wave-averaged and depth-averaged Lagrangian velocity ($u_L^-(x,y,t)$), with the sum of the mean Eulerian velocity and Stokes drift [*MacCready*, 2011; *Suanda and Feddersen*, 2015; *Grimes et al.*, 2020a]:

$$U_{\text{ex}}(x) = \frac{1}{L_y}\left\langle \int_0^{L_y} u_L^-(x,y,t)dy \right\rangle \tag{1.28}$$

where $u_L^-(x,y,t) = u_L(x,y,t)$ when u_L is directed offshore and $u_L^-(x,y,t) = 0$ when u_L is directed onshore. This quantity is integrated over a length of coastline (L_y) and time averaged, $\langle\cdot\rangle$. The rotational component of the cross-shore velocity (U_{ex}^r) depicts the contributions of exchange due to transient rip currents [*Suanda and Feddersen*, 2015; *O'Dea et al.*, 2021b],

following the irrational and rotational velocity decomposition method in *Spydell and Feddersen* [2009]. An ensemble of numerical simulations found a self-similar relationship scaling for transient rip-current-driven cross-shore exchange [*Suanda and Feddersen*, 2015]:

$$\frac{U^r_{\text{ex}}}{\sqrt{gh_b}} = 0.029\sigma_{\theta b}\left(1 + 70S_b\right) \tag{1.29}$$

where h_b is the water depth, $\sigma_{\theta b}$ is the directional spread, and S_b is the wave steepness at the breakpoint (b). The cross-shore exchange via transient rip currents is strongly dependent on wave directional spreading and weakly dependent on the wave steepness at the breakpoint [*Suanda and Feddersen*, 2015]. Not included in the parameterization, wave obliquity may suppress transient rip current activity [*Spydell et al.*, 2007].

Results from dye exchange experiments [*Hally-Rosendahl et al.*, 2014] and exchange parameterizations [*Suanda and Feddersen*, 2015] galvanized further investigation of surfzone-inner-shelf exchange driven by surfzone eddies. It is now well established that transient rip currents elevate mixing within the inner shelf [*Kumar and Feddersen*, 2017c, a; *Grimes et al.*, 2020b; *O'Dea et al.*, 2021a]. Ejected eddies may lead to irreversible vertical mixing of the water column on a stratified shelf [*Kumar and Feddersen*, 2017b; *Grimes et al.*, 2020a]. Transient rip current contributions to exchange and mixing in the nearshore, relative to other physical processes (*e.g.,* internal waves, stokes drive, winds), is a prevailing topic of strong interest with consequential implications for human and ecosystem health [*Moulton et al.*, 2023]. Although transient rip-current-driven exchange is not directly quantified within this dissertation, it elicits a compelling reason to investigate eddy processes.

1.4 Outline

This dissertation describes findings from large scale laboratory experiments in the O.H. Hinsdale Wave Research Laboratory designed to investigate surfzone vorticity dynamics. The overarching goal of this dissertation is to *assess the dynamics linking directionally spread wave fields to large-scale, low-frequency surfzone eddies.* Most of the analyses undertaken are the first observation to address many questions regarding eddy processes within the surf

zone.

Chapter 2 provides an in-depth description of the laboratory experiments, compares two remote sensing techniques with in situ observations, and quantifies breaking crest characteristics. The results show strong potential for lidar and visible-band stereo imagery to investigate wave transformation within the surf zone. Also, results show that the breaking crest length decreases and number of crest ends increases with directional spread. These characteristics are compared with a proposed parameterization of the relationship between directional spread and crest characteristics.

Chapter 3 investigates the wave-by-wave breaking force and resulting vorticity field. The along-crest gradient of the breaking force is highly irregular for individual crests and depends on surfzone region. Evidence of an inverse cascade is found with length scales that vary with directional spread. We progress towards a conceptual model connecting wave-forced vorticity to cross-shore exchange.

Chapter 4 summarizes main conclusions, describes their significance, and discusses relevant future topics requiring more attention. Future topics are broken down into (1) short-crested wave breaking and vorticity injection, (2) eddy evolution and ejection, and (3) field implications for water quality, ecosystems, and human safety. The chapter ends by discussing the role of laboratory experiments in exploring eddy dynamics.

Chapter 2

REMOTELY SENSED SHORT-CRESTED WAVES IN A LABORATORY DIRECTIONAL WAVE BASIN

2.1 Introduction

Waves approaching the shoreline shoal, break, and transform into bores [*Basco*, 1985; *Battjes*, 1988], driving setup and mean currents including undertow [*Longuet-Higgins and Stewart*, 1964; *Bowen et al.*, 1968] and alongshore currents [*Longuet-Higgins*, 1970]. Wave breaking and bore propagation often have complex spatial patterns, including wave amplitude variation along wave crests. Along-crest wave height variation may be the result of alongshore bathymetric variability [*Bowen and Inman*, 1969; *Keeley and Bowen*, 1977; *Putrevu et al.*, 1995; *Slinn et al.*, 2000], wave-current interaction [*Battjes*, 1988], or constructive interference of wave components from a distribution of directions [*Longuet-Higgins*, 1957]. During shore-normal wave conditions on relatively alongshore-uniform beaches, wave directional spread – the directional distribution of wave energy around the mean wave angle – is the primary cause of along-crest variations in depth-limited wave breaking. Sections of wave crests with higher elevation break farther offshore, resulting in breaking along finite lengths, known as short-crested wave breaking. The patterns of wave breaking, ranging from long-crested to short-crested, affect mean currents and sediment transport [*Reniers et al.*, 2004], wave runup [*Guza and Feddersen*, 2012], and the distribution of force on and subsequent damage to engineered structures [*Lin et al.*, 1986; *Song and Tao*, 2007; *Ji et al.*, 2015; *Maciñeira and Burcharth*, 2016; *Warrick et al.*, 2017]. Furthermore, positive- and negative-signed vertical vorticity – counter-clockwise and clockwise horizontal eddies – may be injected at the edges of finite-crested breaking waves [*Peregrine*, 1998, 1999; *Bühler and Jacobson*, 2001; *Johnson and Pattiaratchi*, 2006; *Sullivan et al.*, 2007; *Bruneau et al.*, 2011; *Clark et al.*,

2012; *Wei et al.*, 2017; *Kirby and Derakhti*, 2019]. The wave-generated vortices contribute to mixing within the surf zone [*Spydell and Feddersen*, 2009; *Feddersen*, 2014; *Elgar and Raubenheimer*, 2020; *O'Dea et al.*, 2021b; *Baker et al.*, 2021] and may lead to the generation of transient rip currents via an inverse cascade of energy to larger-scale lower-frequency horizontal motions within the surf zone, similar to behaviors in two-dimensional turbulence [*Johnson and Pattiaratchi*, 2004b; *Suanda and Feddersen*, 2015; *Castelle et al.*, 2016; *Kumar and Feddersen*, 2017a; *Moulton et al.*, 2023]. The local rate of increase in vertical vorticity at breaking crest ends is expected to depend on the along-crest variation in the wave height [*Peregrine*, 1998, 1999; *Bühler and Jacobson*, 2001; *Bonneton et al.*, 2010; *Clark et al.*, 2012; *Kirby and Derakhti*, 2019], but the relationship between the directional properties of irregular wave fields and the along-crest length scales of breaking waves in the surf zone is not well established.

In the open ocean, wave steepness and breaking location are affected by the interference pattern of wave directional components [*Banner et al.*, 2000; *Plant*, 2012]. The distribution of breaking wave crest lengths in deep water has been quantified from airborne camera imagery and lidar observations for directionally spread wind waves [*Kleiss and Melville*, 2010; *Romero and Melville*, 2011; *Sutherland and Melville*, 2013]. Based on observations in deep water, breaker crest lengths are expected to be shorter for incident waves with larger directional spreads, but this relationship has not been tested with observations for irregular wave fields in shallow waters.

Previous work has investigated sea-surface elevation patterns in shallow waters resulting from two obliquely intersecting wave trains with laboratory experiments [*Dalrymple*, 1975; *Hammack et al.*, 1989; *Garnier et al.*, 2006; *Choi and Roh*, 2021] and numerical modeling [*Kirby and Dalrymple*, 1986; *Wei et al.*, 2017; *Postacchini et al.*, 2014]. Based on linear wave theory, the along-crest variation in wave height for two intersecting wave trains with equivalent frequencies is a function of the wavelength and angle between wave trains [*Dalrymple*, 1975]. However, recent numerical modeling experiments suggest that nonlinear wave-wave and wave-current interaction may lead to shorter wave crest within the surf zone [*Wei et al.*,

2017; *Kirby and Derakhti*, 2019]. Although previous physical and numerical modeling experiments have examined breaker characteristics for regular intersecting wave trains, these conditions are not representative of directionally spread irregular wave fields commonly found in the field environment. Theory suggests that crest-length characteristics of non-breaking refracting short-crested directionally spread sea waves may depend on wavelength and directional spread [*Longuet-Higgins*, 1956]. However, a quantitative relationship between breaker length scales and the directional properties for irregular wave fields in the surf zone is not well established.

There is a lack of observations available to investigate the relationship between the directional wave properties and wave-breaking along-crest length scales in the surf zone, partly as a result of the difficulties of measuring breaking crest characteristics using traditional techniques such as subsurface pressure sensors [*King et al.*, 1990; *Lentz and Raubenheimer*, 1999; *Raubenheimer et al.*, 2001] or surface-piercing wire resistance gauges [*Thornton et al.*, 1976; *Thornton and Guza*, 1983; *Battjes and Stive*, 1985]. Remote sensing techniques (*e.g.,* visible imaging, thermal infrared imaging, radar, lidar) can be used to achieve comprehensive spatio-temporal measurements of phase-resolved wave properties during breaking. For example, wave breaking characteristics, such as wave energy dissipation and breaker type, can be quantified from visible-band imagery [*Holman and Haller*, 2013; *Díaz et al.*, 2018; *Carini et al.*, 2021; *Sáez et al.*, 2021]. Alternatively, lidar scanners and photogrammetry techniques from synchronized stereo cameras can provide highly resolved measurements of the water surface elevation. These techniques can directly measure the free surface elevation, whereas pressure gauges require a depth-attenuation correction and commonly underestimate the free surface due to aerated, nonlinear breaking waves [*Martins et al.*, 2020].

Previous studies have used lidar measurements and photogrammetry techniques to map water surfaces to study a wide range of nearshore processes. In the field environment, high-resolution cross-shore transects measured with lidar scanners were used to measure surfzone wave shape, cross-shore transformation, breaker type, and swashzone run-up [*Brodie et al.*, 2015; *Martins et al.*, 2017b; *Almeida et al.*, 2020; *Carini et al.*, 2021; *O'Dea et al.*, 2021a].

In laboratory experiments with unidirectional waves, lidar measurements captured wave-by-wave swashzone excursions and reflections [*Vousdoukas et al.*, 2014; *Martins et al.*, 2017a; *Blenkinsopp et al.*, 2021] and were paired with a subsurface multibeam sonar to quantify splash up and bubbles plumes [*Bryan et al.*, 2019]. Additionally, stereo reconstruction, a photogrammetry technique using synchronized cameras in the visible or infrared band, has been used to estimate highly resolved three-dimensional properties of the sea-surface, such as deep water directional wave spectra, statistics of extreme waves, and surface waves interacting with ice [*Benetazzo*, 2006; *Gallego et al.*, 2011; *Fedele et al.*, 2013; *Sutherland and Melville*, 2013; *Campbell et al.*, 2014; *Benetazzo et al.*, 2015; *Leckler et al.*, 2015; *Schwendeman and Thomson*, 2017; *Peureux et al.*, 2018; *Malila et al.*, 2022b]. Stereo techniques have been used in the laboratory and field to examine nearshore wave characteristics, such as runup, shoaling, and wave-structure interaction [*Dugan et al.*, 2001; *Bechle and Wu*, 2011; *Palmsten and Holman*, 2012; *Molfetta et al.*, 2020; *Vieira et al.*, 2020]. However, few studies have applied stereo reconstruction techniques to measure nearshore breaking waves [*de Vries et al.*, 2011; *Filipot et al.*, 2019; *Kim et al.*, 2022] and no studies have used stereo methods to evaluate wave transformation across and directional characteristics within the surf zone.

Here, laboratory experiments were performed to compare two remote sensing techniques (*i.e.,* lidar, visible-band stereo imagery) with in situ observations and to examine the dependence of breaking crest length and number of ends on directional spread. Laboratory experiments allow for repeatable wave conditions over alongshore-uniform bathymetry, controlled lighting, and a relative ease of sampling in comparison with natural beach environments. Experiments with a multidirectional irregular wave field incident on an alongshore-uniform barred beach were performed in a directional wave basin. In Section 2, the design and analysis methods are described. In Section 3, remotely sensed spectral and bulk wave statistics are compared with in situ measurements and the crest length and orientation of directionally spread waves are quantified. In Section 4, the breaker crest length and ends are compared with a parameterization. Additionally, Section 4 discusses the limitations and biases of different measuring techniques and the applicability of laboratory findings to other environments.

A summary of the findings is presented in Section 5.

2.2 Methods

2.2.1 Laboratory experiment design

Directional wave basin

Laboratory experiments were performed in the Directional Wave Basin at the Oregon State University O.H. Hinsdale Wave Research Laboratory (HWRL, https://wave.oregonstate.edu/). The basin is 48.8 m long, 26.5 m wide, and up to 2.1 m deep. The 29-board piston-type wavemaker can simulate multidirectional irregular wave fields following second-order multidirectional wavemaker theory [*Schäffer and Steenberg*, 2003]. Observations and analyses are presented in the wave basin coordinate system, where the origin is at the center of the bottom of the wavemaker with positive cross-shore (x) coordinates toward the beach, positive alongshore (y) coordinates toward the south (right handed coordinate system), and elevation (z) upward from the base of the basin. For this experiment, the basin bathymetry was flat from $x = 0 - 22$ m and had a constant $1:10$ slope from $x = 22 - 48.8$ m. An alongshore-uniform concrete bar centered at $x = 27.7$ m rested on top of the metal slope (Figure 2.1b). The bar had a triangular cross section (without the bottom vertices where concrete would be too thin and fragile) that was approximately 3.8 m long at the base ($x = 25.4 - 29.2$ m) and 0.30 m tall at the apex (slope of 0.19 and -0.04 on offshore and onshore side of the bar). For the experiments shown here (Table 2.1), the water depth (h) in the flat region was set to $h = 1.07$ m, leading to a depth at the bar crest of $h = 0.19$ m. Alongshore variability of the concrete bar consisting of 28 sections were small (indentations between sections $\mathcal{O}(1)$ cm) and not expected to impact the dynamics of interest. Previous studies examining finite-crested wave breaking [*Garnier et al.*, 2014; *Wei et al.*, 2017] and other surfzone dynamics [*e.g., Fowler and Dalrymple*, 1991] were similarly performed on a 1:10 beach slope, but did not include a bar and therefore had a smaller surfzone width. Although this slope may be steeper than found on natural beaches, the surf similarity number [*Battjes*, 1975] – the ratio

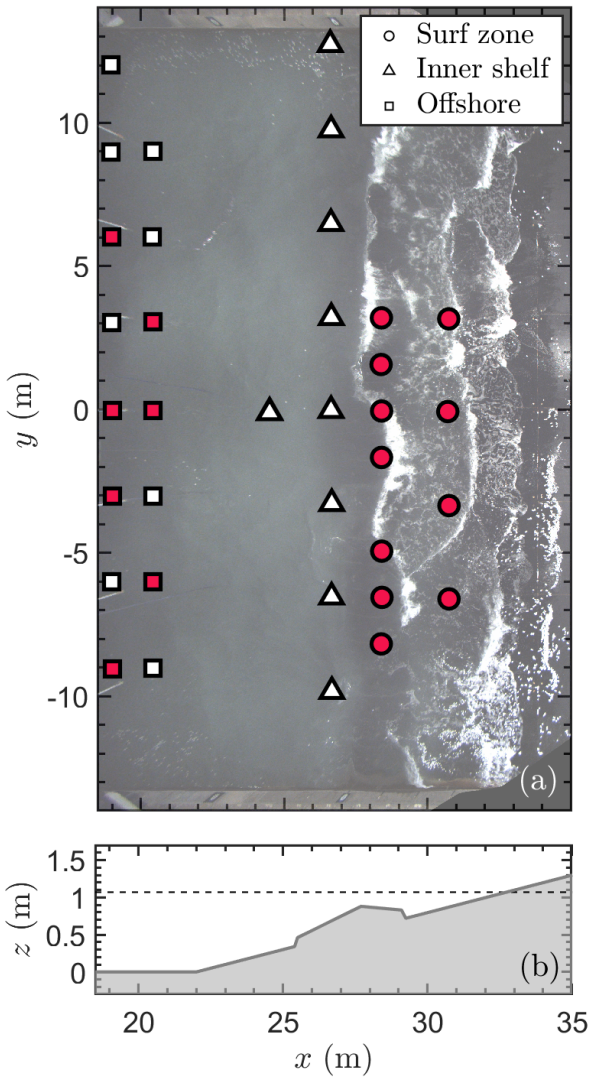

Figure 2.1: (a) Plan view of the cross-shore (x) and alongshore (y) location of the surfzone (circles) and inner-shelf (triangles) arrays of colocated pressure gauges and Acoustic Doppler Velocimeters and the offshore wire resistance gauges (squares). The opaque color image in the background is a rectified image from trial *G1d* ($\sigma_\theta = 26°$) at $t = 16 : 06.3$ from the center ceiling-mounted camera, c2 (oblique image in Figure 2.2). The wire resistance gauge array and the surfzone pressure sensor array were sampled for directional spectra calculations (red squares and circles). (b) The cross-shore profile of the elevations (z) of the seafloor (shaded) and mean water level (dashed, $z = 1.07$ m).

of wave steepness to beach slope – is similar to some field environments (*e.g.,* $H_s = 1$ m, $T = 10$ s, and a beach slope of 2.5–3°).

The irregular wave fields were generated using JONSWAP spectra [*Hasselmann et al.*, 1973] as a function of significant wave height (H_s), peak period (T_p), and a spectral width gamma parameter of 3.3 [*Hasselmann et al.*, 1973]. The directional distribution of the wave fields were generated using a $\cos^{2s}$ directional distribution [*Longuet-Higgins et al.*, 1963] as a function of the mean wave angle (θ) and directional spread (σ_θ). The second-order multidirectional wave theory used for the physical model wave generation by the hydraulic servo-system [*Schäffer and Steenberg*, 2003] may deviate from theory due to the finite basin width, the lack of active absorption for irregular wave fields, reflections from boundaries, wave-wave interaction, resonance of water near the wave board, or recirculating currents within the facility. Thus, the 'offshore' conditions for each trial are characterized by wave statistics observed at the wire resistance gauges ($19.0 - 20.4$ m onshore of the wavemaker, Figure 2.4, squares) for the time range of $15-25$ min (Table 2.1). Each set of wave conditions was repeated for two in situ arrays (Figure 2.4, triangles and circles), with additional repeats for some trials. The offshore significant wave heights varied from $H_s = 0.18$ to 0.30 m, resulting in an approximately 3.5–4.5-m wide surf zone, where initiation of wave breaking typically occurred just offshore or near the bar crest ($x \approx 27.7$ m). The peak period was either $T_p \approx 2$ or 3 sec. Waves had a shore-normal mean direction ($\theta \approx 0°$) with directional spreads ranging from nearly unidirectional to highly directionally spread ($\sigma_\theta = 2 - 30°$). Trials were grouped based on wave height and period, and here after will be referred to by the average wave condition (*e.g., G2a-e* as $H_s \approx 0.23$ m). Within a trial, there were no statistically significant changes in wave height, and directional spread varied by a few degrees when computed in 10-min increments for the time range of $5 - 45$ min.

The laboratory was setup to optimize post-processing of imagery, including stereo reconstruction, which are sensitive to the interior lighting. Specular reflections on the water surface can create false matches in stereo processing [*Jähne et al.*, 1994; *Benetazzo*, 2006] and were mitigated by covering all exterior windows and some reflective surfaces (including a

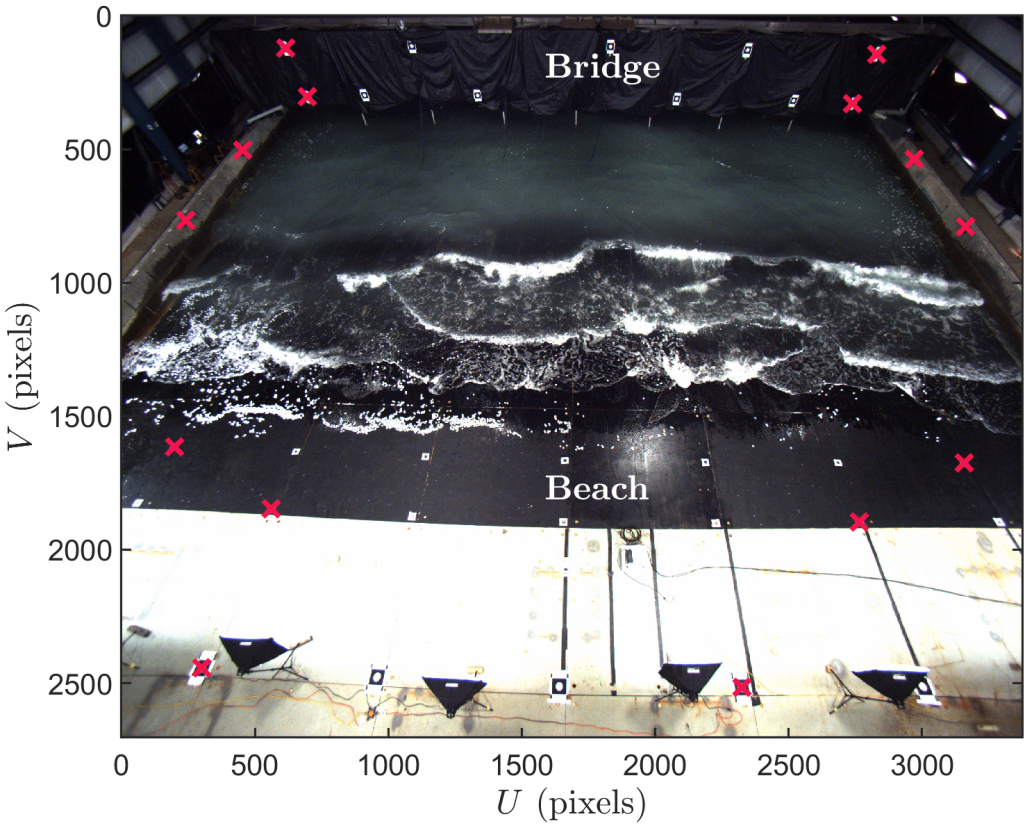

Figure 2.2: Image from trial *G1d* ($\sigma_\theta = 26°$) at $t = 16:06.3$ (rectified image in Figure 2.1a) from the center ceiling-mounted camera (c2, Table 2.2) with a field of view including the bridge, beach, and basin side walls. A subset of the ground control points (red X's) were selected to compute the camera projection matrix during stereo processing. Diffuse lighting on the sides of the basin and on the beach ($V \approx 2500$ pixels) was added to decrease glare for stereo imagery, and the beach ($V < 1800$ pixels) was painted black to reduce visibility of features on the basin floor and increase contrast with the white wave-breaking foam and wiffle balls.

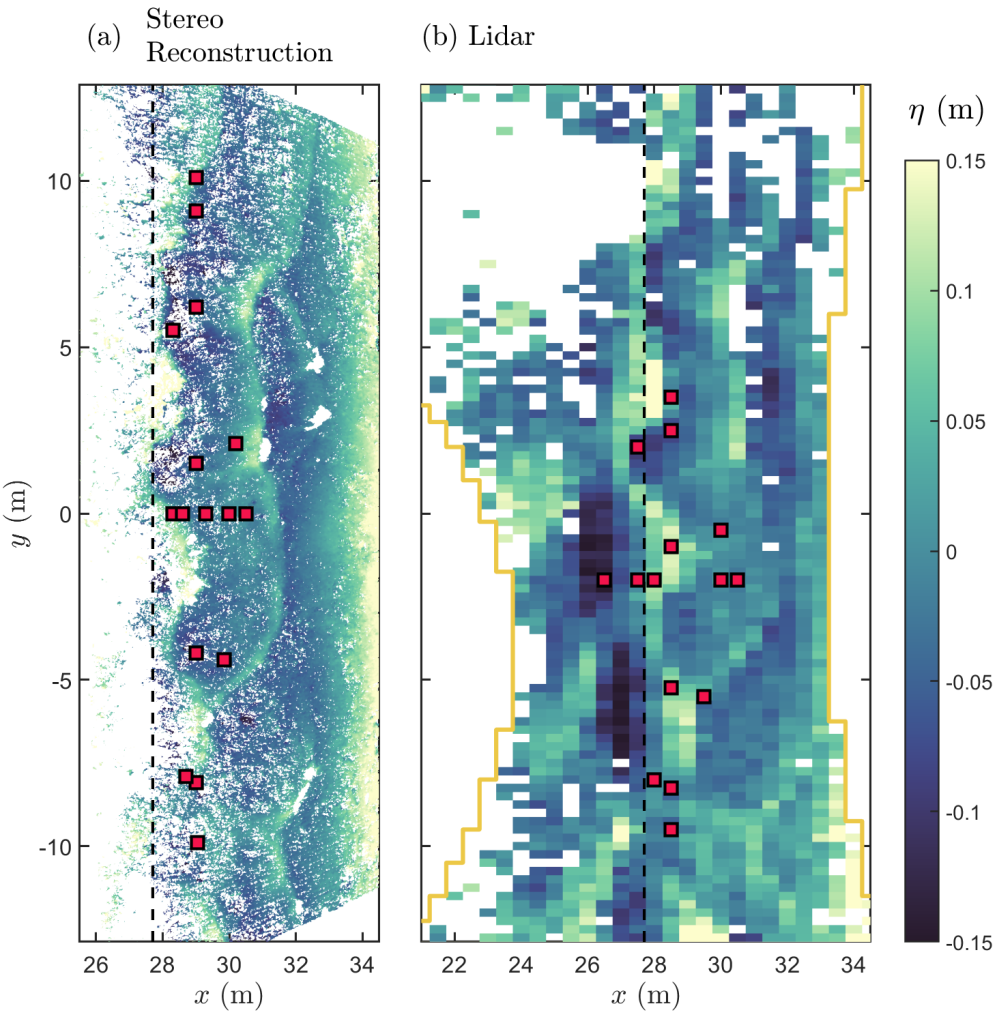

Figure 2.3: Snapshot of the sea-surface elevation (color shading) vs. cross-shore (x) and alongshore (y) position at $t = 16:06.3$ from (a) stereo reconstructions and (b) lidar measurements from trial *G1d* ($H_s = 0.27$ m, $\sigma_\theta = 26°$). The surfzone edge was near the bar crest ($x = 27.6$ m, dashed black line). Stereo reconstructions ($dx, dy = 0.01$ m) were mapped to a higher resolution than lidar measurements ($dx, dy = 0.5, 0.25$ m, parameter of the sampling area in yellow). Directional spectra were computed from sea-surface elevation arrays sampled from remote sensing observations (red squares).

metal bridge) with black plastic tarps. Overhead lights directly above the basin were turned off, while several overhead lights onshore of the basin beach remained on as they added light from an oblique direction without producing strong reflections on the water surface. Eight soft lights positioned around the front of the basin (*e.g.,* $V \approx 2500$ pixels in Figure 2.2) provided diffuse and oblique lighting of the water surface. In addition to lighting, subsurface features visible through the water (*e.g.,* instrument mounts, creases between concrete bar slabs) were undesirable for optical water surface measurements including feature matching in stereo processing. The visibility of subsurface features was reduced by painting the basin beach and floor black ($V < 1800$ pixels in Figure 2.2) and adding additional ADV seeding material (about 100 L, used in fresh water basins to provide sufficient backscatter for ADV measurements) to the basin to increase the water turbidity. The black basin bottom also provided contrast against the bright foam illuminated by the low side lighting.

Surface features, such as foam created during wave breaking, were crucial for stereo matching. As bubbles created in fresh water dissipate more quickly than in seawater [*Monahan and Zietlow*, 1969], TritonX-100 surfactant was added (6 L) to the basin to increase the lifespan of surface foam. The basin also was seeded with white plastic, perforated, hollow golf balls (approximately 4-cm diameter), which were transported by surfzone currents and stood out with high contrast to the black-painted beach. In contrast to more buoyant tracers that were tested (*i.e.,* packing peanuts, synthetic flower petals), the balls sat low in the water and did not appear to 'surf' onto shore when hit by a breaking wave. Variation in the number of balls seeded in the basin (from 3,000 to 8,000) had a small influence on the density of surface features and did not significantly affect the remote sensing measurements.

In situ measurements

Near-bed pressures and velocities were measured with an array of 12 colocated pressure gauges and Acoustic Doppler Velocimeters (ADVs, Vectrino Profiler) sampling at 100 Hz (Figure 2.1a, circles, triangles). The gauges were mounted to the concrete bar or the metal slope approximately 0.05 m above the bed elevation. The colocated gauges first were de-

Table 2.1: Wave conditions theoretically imposed at the wavemaker and measured onshore of the wavemaker for shore-normal waves (θ) with significant wave height (H_s), peak period (T_p), and directional spread (σ_θ). H_s and T_p are reported at two locations in the outer (p6, $x = 28.4$ m, $y = -0.1$ m) and inner (p11, $x = 30.7$ m, $y = -0.1$ m) surf zone for remote sensing and in situ sensors. θ and σ_θ are reported as the surfzone average (sea-surface elevation array, SEE-A, approach with remote sensing and in situ sensors) and surfzone point (PUV with in situ sensors) estimates. The edge of the surfzone (x_{sz}) was estimated from lidar measurements.

Sensors	Location	Statistic	*G1a*	*G1b*	*G1c*	*G1d*	*G2a*	*G2b*	*G2c*	*G2d*	*G2e*	*G3*	*G4a*	*G4b*
		H_s (m)	0.30	0.30	0.30	0.30	0.25	0.25	0.25	0.25	0.25	0.20	0.30	0.30
	Wavemaker	T_p (s)	2	2	2	2	2	2	2	2	2	2	3	3
		θ(°)	0	0	0	0	0	0	0	0	0	0	0	0
		σ_θ (°)	0.0	19.6	28.6	36.2	0.0	10.0	19.6	28.6	36.2	36.2	19.6	36.2
		H_s (m)	0.28	0.27	0.26	0.27	0.25	0.23	0.22	0.24	0.23	0.18	0.29	0.30
Wave	Offshore	T_p (s)	2.1	2.0	2.0	2.0	2.0	2.0	2.0	2.0	2.0	2.0	3.0	3.0
Gauges		θ (°)	-0.1	0.4	-5.9	-3.3	0.2	-1.0	0.8	4.8	2.1	0.4	-3.8	-2.3
		σ_θ (°)	2.4	16.8	25.2	26.1	2.4	9.6	18.3	24.2	25.9	27.6	19.5	30.0
		H_s (m)	0.17	0.16	0.17	0.17	0.15	0.15	0.15	0.15	0.16	0.13	0.20	0.20
In Situ	Outer	T_p (s)	2.0	2.0	2.0	2.0	2.0	2.0	2.0	2.0	2.0	2.0	3.0	3.0
Sensors	Surf Zone	PUV θ (°)	-0.5	-0.1	0.1	-1.4	-0.6	1.2	0.0	-0.5	-0.6	-0.9	-0.4	0.5
		PUV σ_θ (°)	11	14.8	14.7	15.4	10.2	14.6	16.6	17.7	17.4	19.7	12.7	12.1
		H_s (m)	0.13	0.13	0.13	0.13	0.12	0.12	0.12	0.13	0.12	0.12	0.15	0.16
In Situ	Inner	T_p (s)	2.1	1.9	2.0	2.0	2.0	2.0	2.0	2.0	2.0	1.9	3.0	3.0
Sensors	Surf Zone	PUV θ (°)	-0.4	-1.1	-0.5	-0.5	0.1	0.5	0.0	1.2	-0.1	1.0	0.7	-0.6
		PUV σ_θ (°)	11.9	17.4	17.8	18.0	9.6	13.0	15.8	16.3	17.5	17.8	15.2	15.9
In Situ	Across	SSE-A θ (°)	0.0	-0.8	0.0	-1.1	-0.3	-2.1	0.5	-0.5	-0.4	0.3	-3.4	-2.9
Sensors	Surf Zone	SSE-A σ_θ (°)	2.8	13.7	16.6	17.3	2.7	6.6	11.4	16.5	17.8	18.3	12.0	14.0
Stereo	Outer	H_s (m)	0.29	0.25	0.26	0.27	0.29	0.26	0.25	0.24	0.25	0.19	0.31	0.31
Recon.	Surf Zone	T_p (s)	2.1	2.0	2.0	2.0	2.1	2.0	2.0	2.0	2.0	2.0	2.9	2.9
Stereo	Inner	H_s (m)	0.15	0.14	0.15	0.15	0.15	0.15	0.15	0.15	0.16	0.15	0.18	0.18
Recon.	Surf Zone	T_p (s)	2.1	1.9	2.0	1.9	2.0	2.0	2.1	2.0	2.0	1.9	2.9	2.9
Stereo	Across	SSE-A θ (°)	0.5	-2.0	-2.1	-2.2	0.6	-1.0	-1.1	-1.2	0.3	-5.1	0.0	-5.4
Recon.	Surf Zone	SSE-A σ_θ (°)	2.3	11.0	15.9	20.7	2.3	6.3	11.7	16.4	22.5	18.5	12.2	16.1
Lidar	Outer	H_s (m)	0.26	0.20	0.22	0.21	0.25	0.21	0.20	0.24	0.19	0.17	0.26	0.27
	Surf Zone	T_p (s)	2.1	1.9	2.0	2.0	2.0	2.0	2.0	2.0	2.0	2.0	2.9	3.0
Lidar	Inner	H_s (m)	0.14	0.13	0.13	0.14	0.14	0.15	0.14	0.16	0.12	0.14	0.16	0.17
	Surf Zone	T_p (s)	2.2	1.9	2.0	2.0	2.0	2.0	2.0	2.0	2.0	2.0	2.9	3.0
Lidar	Across	SSE-A θ (°)	0.5	-2.2	-3.0	-4.2	0.4	-1.7	-0.3	-3.5	-2.4	3.3	-1.7	-3.3
	Surf Zone	SSE-A σ_θ (°)	2.8	12.6	19.6	20.3	2.8	7.7	12.3	15.5	19.2	20.5	10.2	18.6
Lidar		x_{sz} (m)	27.1	27.3	27.3	27.3	27.2	27.4	27.6	27.6	27.5	28.2	27.3	27.3

ployed onshore of the bar crest in a 'surfzone array' consisting of two rows of sensors ($x = 28.4$ and 30.7 m) spread in the alongshore ($y = -8.2$ to 3.2 m, Figure 2.1a, circles). Then, wave conditions were repeated with the colocated gauges reconfigured offshore of the bar crest in an 'inner-shelf array' ($x = 26.6$ m, $y = -9.8$ to 9.7 m), which also included three vertically stacked sensors at $x, y = 24.5, -0.1$ m (Figure 2.1a, triangles). Velocity and pressure measurements were cleaned, despiked, and rotated into the HWRL coordinate system. One pressure sensor (p4, not shown in Figure 2.1: 'surfzone array': $x, y = 28.4, -3.3$ m, 'inner-shelf array': $x, y = 26.7, -12.4$ m) was removed during post-processing as it was unresponsive to fluctuations in the signal during many trials (*i.e.,* only noise in the pressure signal). The offshore wave conditions were measured with 15 surface-piercing wire resistance gauges (sampling at 100 Hz) mounted on the offshore and onshore sides of the laboratory bridge ($x = 19.0$ m and 20.4 m, $y = -9.0$ to 9.0 m, above the flat bottom of the wave basin, Figure 2.1,a, squares). Resistance gauges were calibrated twice daily and each time the still water level was changed. In situ sensor locations were surveyed with a total station (0.15-cm accuracy).

Camera System

Three cameras (c1, c2, c3) were mounted to a beam on the HWRL building ceiling ($x = 47.0$ m, Table 2.2) with overlapping, oblique fields of view spanning the width of the basin ($y = -13.3$ to 13.3 m) from the bridge to the beach ($x = 20 - 41.5$ m, Figure 2.2). The center camera (c2, $y = 0$ m) was pointed forward directly offshore (toward wavemaker) and the cameras on either side of c2 were angled inward by 6–7° (c1 and c3, $y = -1.8$ and 1.7 m). Camera c2 was positioned $z = 0.8$ m below the side cameras (c1 and c3). The camera system had identical cameras (Point Grey GS3-PGE-91S6C-C Grasshopper3, 9.1 MP, Sony ICX814 Color, Resolution: 3376 x 2704) and wide-angle lenses (Kowa LM6Hc 1" 6 mm lenses). The resolution of the raw images ranged from 0.05–2 cm. A secondary set of three cameras (not shown here) were mounted farther onshore with a more oblique angle and smaller differences between camera angles, but are not reported here as that configuration resulted in fewer matching features during stereo processing. Each camera geometry was computed with

Table 2.2: Extrinsic parameters including sensor location (O.H. Hinsdale Wave Research Laboratory coordinates) and principle axes angles. The standard deviation of camera extrinsic parameters across all trials were less than 0.008 m for the x, y, z-locations and less than 0.07° for the azimuth, tilt, and roll.

Sensor	x (m)	y (m)	z (m)	Azimuth (°)	Tilt (°)	Roll (°)
c1	39.4	-1.7	10.8	272.6	32.3	-1.9
c2	39.3	0.1	11.0	268.7	32.8	-0.2
c3	39.3	1.8	10.8	266.6	33.1	2.0
3D Lidar	22.0	-3.5	7.3	180	47.9	2.6

ground control points (GCPs) – points in the laboratory with a known location – positioned on the bridge, sidewalls, and beach (Figure 2.2, red X's). GCPs (cardboard targets or painted white circles silhouetted with a black square) were surveyed with a total station at the beginning and end of the experiment. Differences between pre- and post-experiment surveys were small and on the order of the total station accuracy.

Lidar System

A three-dimensional (3D) lidar sensor (Velodyne Lidar HDL-32E, 903-nm laser) collected point clouds of the water surface-elevation at 10 Hz (about 695,000 points per second) by computing the distance based on the time for a pulsed laser beam to travel to a target and back. The sensor was mounted 6.3 m above the water surface on a steel beam attached to the bridge ($x, y, z = 22.0, -3.0, 7.3$ m) at an upward angle ($\sim$50°) relative to the horizontal. The lidar's 32 beams had 1.33° angular resolution and swept in the alongshore resulting in a 360° field of view from -30.67° to 10.67° relative to perpendicular from the lidar orientation.

The lidar collected measurements of the water surface spanning the width of the basin (Figure 2.3b) as well as the building side walls and ceiling (removed during post-processing).

The cross-shore width of the bow-tie shaped sampling area varied from 9 m below the instrument to 13 m near the sides of the basin (the entire cross-shore extent of the basin onshore of the bridge, Figure 2.3b, yellow outline). The orientation of the lidar provided high-resolution alongshore measurements (< 0.05 m alongshore resolution near the center of the tank), important for quantifying the along-crest length scales of the breaking waves, and 0.25–0.40 m resolution in the cross-shore as a result of the cross-shore spacing at the water surface of the 32 channels. Measurements were rotated into the HWRL coordinate system using the surveyed position, measured orientation, and known level features in the horizontal and vertical planes (*e.g.,* facility side walls). Measurements were then binned using a nearest neighbor gridding technique to a resolution of 0.50 m in the cross-shore and 0.25 m in the alongshore. Lidar returns off the water surface were strong within and outside of the surf zone, enabling measurements of the wave field offshore of breaking. A thin layer of ADV seeding material at the water surface led to the highest returns at the beginning of the trial run with decreasing returns throughout the trial as the water column was mixed, particularly near the side of the basin ($y > 8$ m) with most oblique angles that potentially lead to more specular reflection away from the lidar.

Uncertainty in lidar observations may be due to the offshore position and oblique grazing angle leading to the obstruction of the front face of the wave and deflection away from the scanner [*Brodie et al.*, 2015]. Additionally multiple reflections off the water surface has been shown to increase laser time of flight, resulting in lower sea-surface elevation measurements from lidar [*Vousdoukas et al.*, 2014; *Brodie et al.*, 2015]. Uncertainty may also be introduced due to errors in lidar extrinsics or movement of the scanner due to vibrations of the bridge associated with the waves.

2.2.2 Post-processing and analysis

Stereo reconstructions

The sea-surface elevation was reconstructed for each trial for 10 minutes with 8-Hz imagery from 3 cameras (4800 images per camera from $t = 15 - 25$ min) with Agisoft Metashape's multiframe camera functionality in HWRL coordinates (*e.g.,* Figure 2.3a). Stereo reconstructions were viable in the surf zone of the basin, where surface features including foam and wiffle balls were present. Limited surface features offshore of the surf zone resulted in few features to match between images resulting in sparse reconstructions at $x < 27.5$ m. Stereo processing workflow steps for each trial were (1) build a sparse point cloud from aligned images, (2) manually select GCPs to solve for camera extrinsics, (3) filter the sparse point cloud, and (4) build a dense point cloud from the filtered aligned points. The certainty in aligned points was optimized by removing points in the sparse point cloud through an iterative process based on reconstruction uncertainty, projection accuracy, and reprojection error, leading to higher quality stereo reconstructions [*Over et al.*, 2021]. Digital elevation maps (DEMs) – representations of a surface model as a regular grid of height values – were computed from the dense point clouds and exported at 1-cm resolution. DEMs output from Metashape were binned using a nearest neighbor gridding technique to 5-cm cross- and alongshore resolution to remove additional noise and filtered with a 3-point temporal median filter. The stereo reconstructions were computed over a time span of 10 minutes per trial due to stereo processing computational constraints (3 days of processing time per 10 min of data) on a RAID-configured Dell 7820 Tower Workstation.

Camera extrinsic parameters (location and orientation in laboratory coordinates) and intrinsic parameters (internal properties for a particular camera setup encompassing focal length, image sensor format, and principal point) were resolved separately for each trial run to compensate for any movement, stretching, or shrinking of the cameras and camera lenses between trials. Camera extrinsic parameters were computed from the manually-selected pixel location of a subset of the GCPs (14 out of the 36, Figure 2.2, red X's) in the first

image from each camera and set as constant for the rest of the trial. The estimated camera extrinsics were not sensitive to the number or arrangement of selected GCPs as long as the selected GCPs reasonably spanned the image. During step 3, camera intrinsics were computed by an iterative process of filtering the sparse point cloud and optimizing for camera intrinsics, which becomes computationally expensive if the optimization was attempted for an entire trial time series. Therefore, camera intrinsics were resolved by performing the stereo workflow with 10 image pairs from the trial run. Those intrinsics were ascribed to the cameras in the stereo workflow and held constant for the full run at the beginning of step 3. The intrinsics including camera affinity and non-orthogonality (skew) coefficients and higher-order tangential distortion (3rd and 4th) and radiation distortion (4th) coefficients were set to zero (values expected to be negligible).

Uncertainty in the stereo processing techniques may be due to reflections, instrument geometry, and other sources during post-processing. Previous studies have suggested that differences at a range of frequencies could result from remote sensing processing procedures, including spatial jitter of the remote sensing pixel location and quantization errors [*Benetazzo*, 2006; *Zavadsky et al.*, 2017]. During stereo processing, specular reflections from the water surface may be detected as texture, causing false matches [*Jähne*, 1993; *Benetazzo*, 2006]. A drawback of the approach implemented in the laboratory to reduce specular reflections (*i.e.,* using diffuse side lighting) is that the bright breaking waves and foam were occasionally overexposed in the images, prohibiting stereo-matching (Figure 2.3a, $x, y = 31, 2$ m). Further, feature matching on subsurface features (*i.e.,* the encasement for instruments, metal slats on and creases between the concrete bars) occasionally occurred when minimal surface foam was present and was reduced by bin averaging and filtering the output. Errors may also have been introduced by uncertainty of the camera intrinsic and extrinsic parameters (internal and external calibration error), in part owing to possible errors during surveying and selection of GCPs.

Wave Statistics

Wave statistics computed from the in situ gauges were compared with remotely sensed estimates for concurrent 10-minutes sections of each 45-minute trial (from $t = 15 - 25$ min). The pressure gauge measurements were corrected for depth attenuation with a tapered cutoff frequency of 1.2 Hz [*Guza and Thornton*, 1980; *Bishop and Donelan*, 1987]. To correct an identified time lag between measurements from the in situ instruments, stereo reconstructions, and lidar, a time-lagged cross-correlation with each data set was computed using the center outer surfzone sensor ($x, y = 28.5, -0.1$ m) as the standard. Adjustments to the timing were typically a few seconds. For stereo reconstructions and lidar measurements, locations with >10% of data missing from the 10-min time series were excluded from the analysis. Typically, this resulted in passing data for all cross-shore locations from $x < 27$ m for the stereo reconstructions and between $x < 24$ m, -13 m$< y < 8$ m for the lidar. The offshore edge of the surf zone (x_{sz}, Table 2.1) was defined as the cross-shore position where the alongshore-average wave energy estimated from lidar measurements decreased to 95% of the energy offshore of breaking at $x = 26$ m, the farthest offshore position with lidar returns >10% of the time for all trials.

To investigate the cross-shore wave transformation, wave characteristics were estimated as the auto-spectra from a sea-surface elevation timeseries at individual locations with the pressure sensors, stereo reconstructions, and lidar observations. For all measurement types, the sea-surface elevation spectral analysis ($S_{\eta\eta}(f)$) was performed using a Hanning window period of 32 s with an overlap period of 16 s over the 10-min time series (DOF = 48), and H_s was computed from $S_{\eta\eta}(f)$ from 0.3 to 1.20 Hz. Additionally, colocated near-bottom pressure and horizontal velocities were used to determine the directional moments (a_2, b_2) in a single-point system [PUV approach, *Kuik et al.*, 1988]. The mean wave angle and direction spread for colocated sensors were computed as the energy-weighted average spread and direction between 0.3 and 0.8 Hz (Table 2.1).

An array of sea-surface elevation measurements was used to estimate directional wave

properties offshore and within the surf zone. Directional wave spectra ($(S_{\eta\eta}(f,\theta))$), as a function of frequency (f) and direction (θ), were estimated using a spatial array of the sea-surface elevation measurements computed with the in situ gauges, lidar measurements, and stereo reconstructions. For all data types, the Extended Maximum Entropy Method (EMEM), a method based on an auto-regressive process of directional waves [*Hashimoto et al.*, 1995], was used to compute $S_{\eta\eta}(f,\theta)$ with directional resolution of 1° and frequency resolution of 0.0156 Hz with a Parzen window of 64 s and overlap of 36 s [*Brodtkorb et al.*, 2000]. The EMEM was selected due to the optimal performance relative to other directional estimators (*e.g.,* Iterative Maximum Likelihood Method) when the array geometries were tested with synthetic wave fields and has previously been used for directional spectra estimates from stereo reconstructions [*Bechle and Wu*, 2011]. The array approach was used for remote sensing estimates, as opposed to a three-dimensional Fourier Transform of the space-time data [*Benetazzo et al.*, 2012; *Leckler et al.*, 2015], due to the relatively small wavelength to surfzone width in the laboratory environment and for consistency with in situ observations.

The sea-surface elevation array design varied due to constraints of each instrument type. For wire resistance gauges, the spectra were computed from a 7-sensor sub-sampled array (Figure 2.1, red squares) designed to optimize the non-redundant spatial lags between sensor locations [*Young*, 1994] and were used to estimate offshore directional properties (*e.g.,* Figure 2.4). Based on the performance of arrays with synthetic wave fields, all 11 sensors were selected for the pressure gauges (Figure 2.1, red circles). Highly resolved maps of the water surface from lidar and stereo reconstructions facilitated optimal array geometries to be selected. Here, 15–16 sampling locations were selected to maximize the number of separate lags while also resolving the range of wavelengths feasible for each remote sensing method [*Chickadel*, 2007]. The sampling array for stereo reconstructions was confined to the outer to mid-surf zone to minimize substantial dissipation in the sampled region (Figure 2.3a, red squares, $x = 28.3 - 30.5$ m). The lidar array encompassed a longer cross-shore region due to the larger cross-shore footprint (Figure 2.3b, red squares, $x = 26.5 - 30.5$ m) and was centered at $y = -2$ m due to intermittent returns off the water surface near the side of the

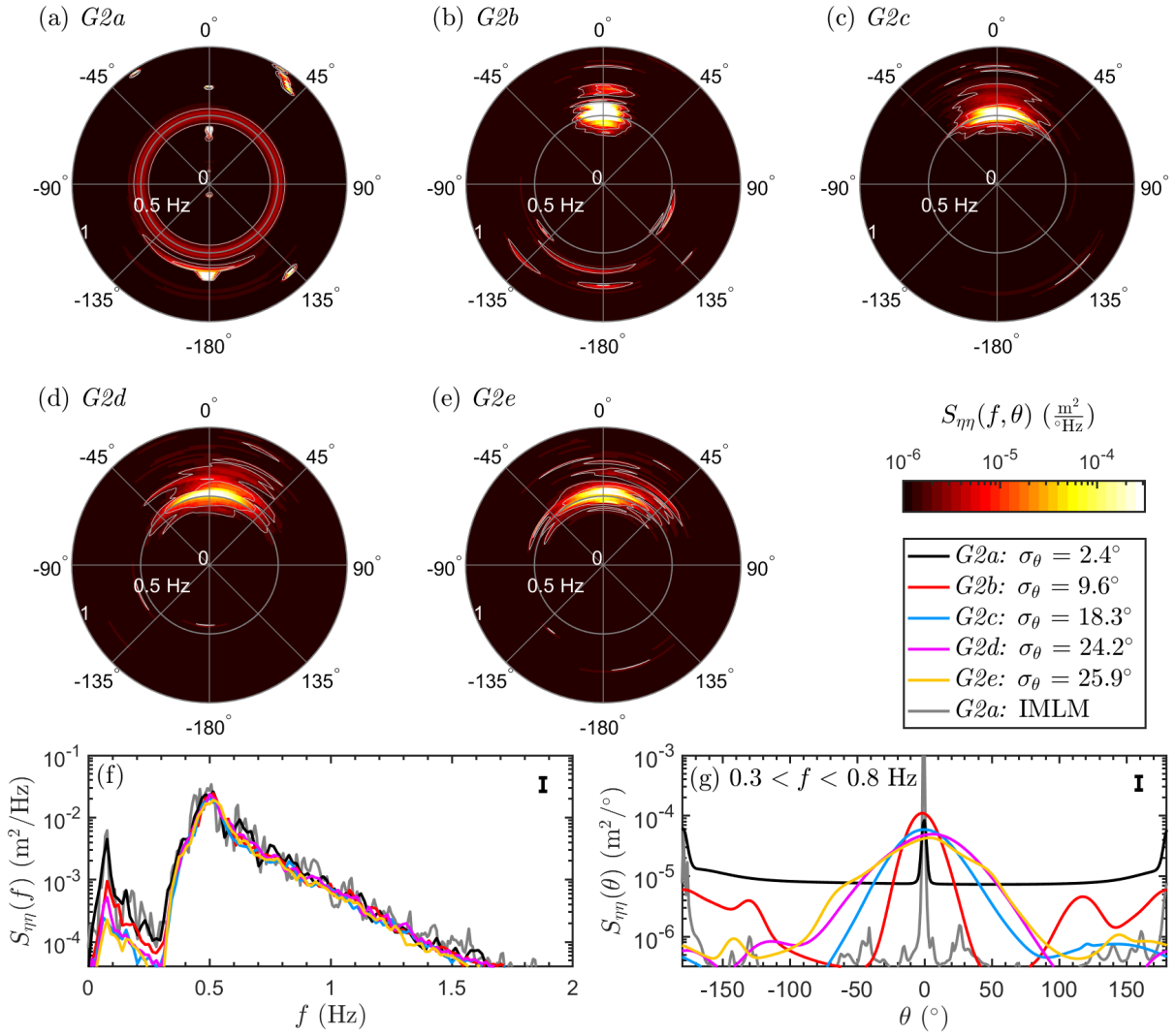

Figure 2.4: (a-e) The directional spectra ($S_{\eta\eta}(f,\theta)$, color contours) as a function of frequency (f, radial distance) and direction (θ, angle) estimated with an Extended Maximum Entropy Method (EMEM) estimator from the sub-sampled array of wire resistance gauges (Figure 2.1, red squares). The directional spectra integrated over all directions (f, $S_{\eta\eta}(\theta)$) and from 0.3< f < 0.8 Hz (g, $S_{\eta\eta}(\theta)$) for *G2a*–*G2e* (colors). Results for *G2a* with an EMEM estimator (g, black) had a higher noise floor than the Interative Maximum Likelihood Method (IMLM) estimator (g, grey) but resulted in similar estimates of directional spread (σ_θ). Waves propagating toward the shoreline have an angle of $\theta = 0°$ and waves propagating towards offshore have an angle of $\theta = 180°$. The vertical bar in (f,g) is the 95% confidence interval.

tank farthest from the lidar ($y > 5$ m).

The array geometries and estimators were tested with a synthetic near-unidirectional and directionally spread wave field with Wave Analysis for Fatigue and Oceanography software [WAFO, *Brodtkorb et al.*, 2000]. The array geometries selected for application to the observations were able to estimate the directional spread (of the peak in onshore wave energy) of the synthetic wave fields within 2.5°. Array geometries used for the remote sensing observations yielded directional spectra that were more consistent with the analytical directional spectra than in situ array geometries, likely due to the more optimized array geometry. Synthetic tests suggested that in situ arrays may erroneously identify energy in the offshore direction that cannot solely be attributed to reflected energy for unidirectional waves, which was less severe for directionally spread waves. Further, analytic testing confirmed that the high noise floor exhibited for unidirectional conditions with the wire resistance gauge array may be partially due to the array geometry (Figure 2.4a). For near-unidirectional wave conditions, the noise floor was lower when an IMLM [*Pawka*, 1983] estimator was tested (Figure 2.4g, compare black and grey). However, for directionally spread wave conditions, directional spectra estimated with the IMLM estimator was less consistent with the analytical directional than estimates with the EMEM estimator, partially due to erroneous peaks in IMLM estimates [*Hashimoto et al.*, 1995]. Because the focus of this paper is on directionally spread wave conditions, the EMEM estimator was selected to resolve the wave field directional properties.

From each directional spectrum, the wave height and peak period were computed by integrating the spectrum over all directions ($\theta = -\pi$ to π) from $f = 0.3-1.2$ Hz. To estimate the mean wave angle and directional spread, the spectrum as a function of only direction ($S_{\eta\eta}(\theta)$) was computed as the energy-weighted sum of $S_{\eta\eta}(f, \theta)$ between $f = 0.3 - 0.8$ Hz, constrained close to the peak frequency due to the frequency-dependent directional spread of the wave field. Rather than computing the mean wave angle and directional spread from directional moments (sensitive to reflected energy), a $\cos^{2s}$ directional distribution was fit to $S_{\eta\eta}(\theta)$ to identify the width of the onshore propagating wave peak [*Longuet-Higgins*

et al., 1963]. Prior to computing the directional properties, a noise floor (typically 1–2 magnitudes lower than the peak) was subtracted and $S_{\eta\eta}(\theta)$ was normalized by the total onshore-propagating energy from $\theta = -\pi/2$ to $\pi/2$ [*Squire and Montiel*, 2016], where waves toward shore are $\theta = 0$:

$$E = \int_{-\pi/2}^{\pi/2} S_{\eta\eta}(\theta) d\theta \tag{2.1}$$

The normalized spectra ($\tilde{S}_{\eta\eta}(\theta) = S_{\eta\eta}(\theta)/E$) were fit with a $\cos^{2s}$ distribution:

$$\tilde{S}_{\eta\eta}(\theta) = a \cos^{2s}\left(\frac{\theta - \theta_0}{2}\right) \tag{2.2}$$

where s is the spreading factor, θ_0 is the mean wave angle, and a is a spread-dependent constant that retains an area of $\int_{-\pi/2}^{\pi/2} \tilde{S}_{\eta\eta}(\theta) d\theta = 1$. The spreading factor and mean angle were computed by varying both values and selecting the spectrum with the lowest root-mean-squared deviation to the observed $\tilde{S}_{\eta\eta}(\theta)$. The directional spread (σ_θ) was computed from the spreading factor as [*Kuik et al.*, 1988]:

$$\sigma_\theta = \sqrt{\frac{2}{s+1}} \tag{2.3}$$

Results were similar (within 1°) when a was computed with a commonly used analytic form for the normalization constant [*Longuet-Higgins et al.*, 1963; *Mitsuyasu et al.*, 1975; *Hasselmann et al.*, 1980]. However, this function behaves poorly when $s > 171$ ($\sigma_\theta < 6.2°$) and thus was not used here. The angles associated with the peaks and centroid of $\tilde{S}_{\eta\eta}(\theta)$ were typically within 2° of θ computed from fitting the spectra. Directional spread estimates vary by less than a degree when cos^{2s} distribution was centered at the peak or centroid angle rather than the fitting method. The mean angles and directional spreads typically varied by less than 3° when two sensors were omitted from in situ arrays or sensors were shifted by 1 m for remote sensing arrays.

The percentage of energy reflected offshore was calculated as:

$$K = \frac{E_r - E_i}{E_i} * 100 \tag{2.4}$$

where the incident (E_i) and reflected energy (E_r) were computed from the directional spectra as:

$$E_i = \int_{f_1}^{f_2} \int_{-\pi/2}^{\pi/2} S_{\eta\eta}(f,\theta) d\theta df \tag{2.5}$$

$$E_r = \int_{f_1}^{f_2} \left[\int_{-\pi}^{-\pi/2} S_{\eta\eta}(f,\theta) d\theta + \int_{\pi/2}^{\pi} S_{\eta\eta}(f,\theta) d\theta \right] d\theta df \tag{2.6}$$

For $f_1 = 0.3$ Hz to $f_2 = 1.2$ Hz, the reflected energy estimated from the wire resistance gauges with the noise floor removed was 4–8% for directional spread trials (*i.e.,* $\sigma_\theta > 10°$). Estimates of reflected energy from wire resistance gauges were higher for $\sigma_\theta \leq 10°$ as the directional estimates were unable to resolve the on- and offshore directed energy well for the repeated lags in the wire resistance gauge array. However, the percent of reflected wave energy was around 10–14% for $\sigma_\theta \leq 10°$ cases in the surf zone when estimated from the stereo reconstruction and lidar arrays with more optimized array geometries. For all trials, 1–4% of the energy was reflected when computed from the on- and offshore directed peak of the directional spectrum offshore and in the surf zone. When infragravity wave frequencies ($f > 0.3$ Hz) were included, reflection estimates at the wire resistance gauges were similar to those computed over surface gravity wave frequencies ($f = 0.3 - 1.2$ Hz), while the proportion of offshore directed energy computed from stereo reconstructions was twice as large as estimates only over surface gravity wave frequencies.

Breaking wave crest length, orientation, and number of ends

The dependence of the breaking crest length, orientation, and number of ends on wave directional spread was addressed by developing and applying a Remote Breaker Identification Scheme (RBIS) using a combination of the water surface amplitude (stereo reconstructions) and brightness (imagery). Crests were identified in a region spanning the surf zone ($x = 27$ to 31.5 m, $y = -13.2$ to -13.2 m) at 8 Hz for 10 min for all trials (*e.g.,* Figure 2.5). The offshore edge of the analysis region was positioned offshore of the surfzone edge (x_{sz}) for all wave conditions, and the inner edge was the located offshore of where waves were

observed to run up and down the beachface. Images were rectified into HWRL coordinates with the solution for intrinsic and extrinsic parameters resolved during stereo processing and maps of the z-elevations from each stereo reconstruction [*Bruder and Brodie*, 2020]. Prior to thresholding, stereo reconstructions and rectified images were interpolated to 0.05-m resolution and spatially smoothed with a 0.3-m running mean in the alongshore. Results were similar when sub-sampling the imagery at lower rates (*e.g.,* 0.5 Hz) or varying the choices of grid size and running mean filter size by a factor of two.

The basis of RBIS identifies breaking crests as regions that exceed an imagery threshold and also an elevation-based breaking-gamma threshold. The following steps are performed to identify breakers with RBIS (Figure 2.5): (1) identify a set of polygons encompassing potential breakers in imagery based on a pixel-intensity criteria, (2) separately identify potential crest features in stereo reconstructions based on an elevation-based criteria, (3) quality control regions that meet both the pixel-intensity and elevation-based criteria and extract crest characteristics (length, orientation, and location of ends).

Using pixel intensity as a proxy for wave breaking, wave crests were identified in each frame of rectified black and white images from c2 when the pixel intensity was 20% brighter than the 10-sec (5-wave) running mean pixel intensity (Figure 2.5a). This threshold was selected as the optimal brightness over all the trials to identify breaking wave crests while minimizing identification of persistent bubble plumes transported by surface currents.

Potential crest features were identified in stereo reconstructions as regions exceeding a threshold ratio, γ, of wave height to mean water depth h. Wave height was calculated as twice the wave amplitude, which was approximated as the sea-surface elevation minus the 10-sec running mean sea-surface elevation. γ was set to 0.2, which was chosen via manual tuning by comparing identified waves in stereo reconstructions with imagery (Figure 2.5b).

To quality control identified crest features that met both pixel-intensity and elevation-based criteria, individual wave crests were only retained if the crest area was greater than 0.375 m^2. This removes regions where small residual bubble plumes in imagery or elevated features (*e.g.,* spray) in stereo reconstructions were selected. Additionally, any identified

crests within 0.3 m of another wave crest were designated as one continuous wave crest. This compensates for intermittency in foam or stereo reconstructions that are not indicative of separate wave crests and reduces any sensitivity to imagery and stereo-reconstruction filtering scales. The crest length results from RBIS vary by 10% and 5% when the pixel intensity and γ thresholds where changed by 20%.

The crest length, number of crest ends, and wave orientation were estimated from the polygon shapes of identified breaking wave crests in each frame. The breaking crest length was estimated from a curve transecting the wave crest between crest ends (Figure 2.5c, yellow curves). Each curve spans between the farthest alongshore extents of each wave crest, specified as the cross-shore position equidistant between the farthest off- and onshore extent of the crest for each alongshore grid point. The crest transects were each smoothed over 0.2 m with a running median filter to reduce the sensitivity to changes in the cross-shore crest width. Estimating crest length as the alongshore extent of each polygon does not account for waves propagating obliquely to the shoreline or with curved crests and resulted in $\sim 2\%$ shorter crest lengths than the along-crest estimates on average. Additionally, the crest orientation was estimated as the angle relative to shore-parallel of the major axis of an ellipse fit to each wave crest (Figure 2.5c, green dashed ellipses).

Crest length and orientation were not included in crest statistics if the identified crest extended on- or offshore of the surfzone region but were included if the crest intersected the side wall (note that if crests intersecting the sidewall were not included, most crests would be omitted from the near-unidirectional cases). Crest ends were counted at the alongshore minimum and maximum position of each crest polygon and were omitted if a crest end was within 0.2 m of the side walls or the cross-shore extent of the analysis region (Figure 2.5c, red/blue circles). For all trials, average breaking crest lengths and number of ends did not differ significantly with differing threshold values, smoothing filters, or sampling rates. Results were similar when computed over a larger cross-shore width (*i.e.,* starting farther offshore), as RBIS method only identifies breaking surfzone waves due to the method's reliance on bright features that were resolved well in stereo reconstructions. As an alternative to

the individual crest identification approaches shown here, alongshore wavenumber spectral analysis applied to the sea-surface elevation and normalized pixel intensity lead to similar results to the mean crest lengths identified with RBIS (*e.g.,* the alongshore wavenumber spectra peaks were approximately twice the identified mean crest lengths). However, alongshore wavenumber results are not presented here due to the limitations of applying spectral estimates in a setting where the length scales of interest were near the length of the signal (*i.e.,* the basin width).

Several aspects of this remote sensing technique may bias the crest characteristics, particularly for unidirectional wave conditions. Although the most commonly identified along-crest-length (mode) for nearly unidirectional waves (*G1a* and *G2a* with $\sigma_\theta = 2°$) was the width of the basin ($y = 26.5$ m), smaller-scale features identified for unidirectional waves lead to smaller mean breaker lengths than the modes and a non-zero number of crest ends. This may be due to reflections off the water surface from overhead lights causing alongshore-varying brightness of wave crests or other small irregularities in breaking crests leading to intermittency in breaker aeration (*e.g.,* Figure 2.6b).

Constraining the crests identified in imagery with the stereo reconstructions typically restricted the identification of residual foam as a breaker. However, occasionally bright residual bubble plumes from an active breaking crest re-emerged at the water surface and were coincident with an elevated water surface immediately proceeding a breaker [*Masnadi et al.*, 2021], leading to an erroneously identified crest (*e.g.,* Figure 2.6f). To alleviate the impact of these erroneous crests on the overall crest statistics, identified features within 0.3 m of another feature are marked as a continuous feature. Joining these features can increase the cross-shore width of the crest (*e.g.,* Figure 2.6d) and therefore, can occasionally alter the length of an individual breaking crest. However, this has little impact on the average crest length as occurrences of this phenomena were infrequent.

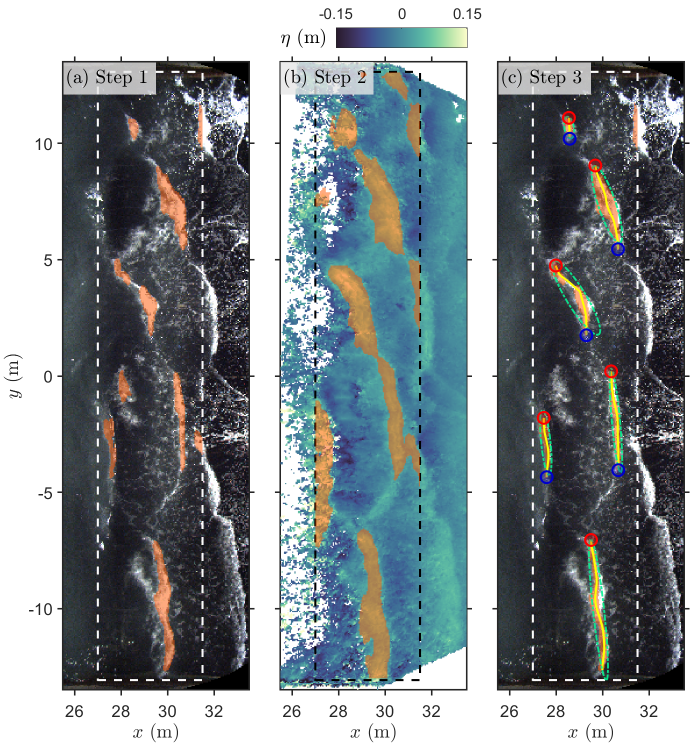

Figure 2.5: Snapshot of the Remote Breaker Identification Scheme (RBIS) workflow. Breaking wave crests (orange regions) were identified with a pixel-intensity based threshold in rectified images (a, *Step 1*) and with an elevation-based threshold in stereo reconstructions (b, *Step. 2*, colored by water-surface elevation, η) at $t = 16 : 14.3$ from *G1d* ($H_s = 0.27$ m, $\sigma_\theta = 26°$). (c, *Step 3*) Crests length, ends, and orientation were characterized from the breaking crests identified with the combined data products (inset region extending 4.5 m in the cross-shore, x, and 26.5 m in the alongshore, y). The crest length was estimated from an along-crest transect (yellow) and the orientation was the angle relative to shore-parallel of the major axis of an ellipse fit to each crest (green dashed). The crest ends, where positive and negative vertical vorticity may be generated, were the farthest alongshore extent of each crest (red and blue circles).

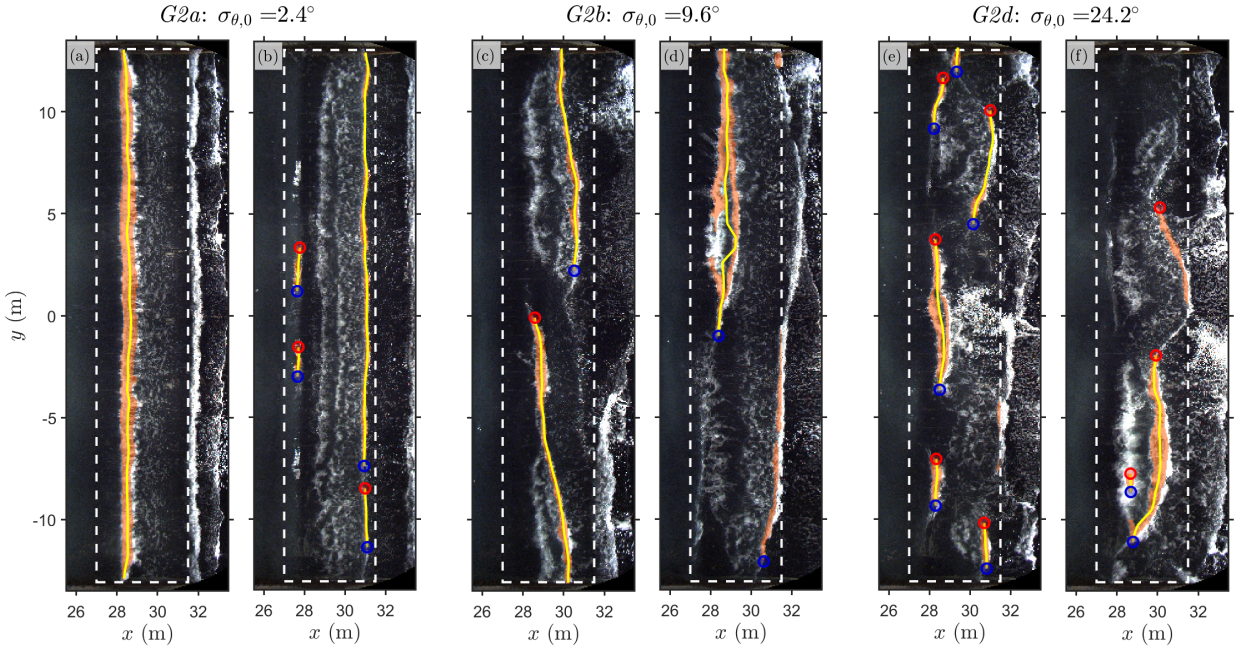

Figure 2.6: Examples of the Remote Breaker Identification Scheme (RBIS) identified wave crests (orange region) for wave conditions with varying directional spreads. The estimated along-crest-length (yellow curve) and crest ends (red/blue circle) in the surf zone (inset darker region) are overlain on rectified imagery as a function of the cross- (x) and alongshore (y) location. Trials presented here are for $H_s \approx 0.24$ m including *G2a* (a,d, $\sigma_\theta = 2°$), *G2b* (b,e, $\sigma_\theta = 10°$), and *G2d* (c,f, $\sigma_\theta = 24°$). Often RBIS identified wave crests are comparable to visual identification of crest features (a,c,e), but occasionally crests may be misidentified due to residual foam despite filtering based on water level elevation exceedance (d,f). Near-unidirectional (*G2a*) waves occasionally had alongshore-varying crest features due to reflections of lights or variation in aerated breakers (b).

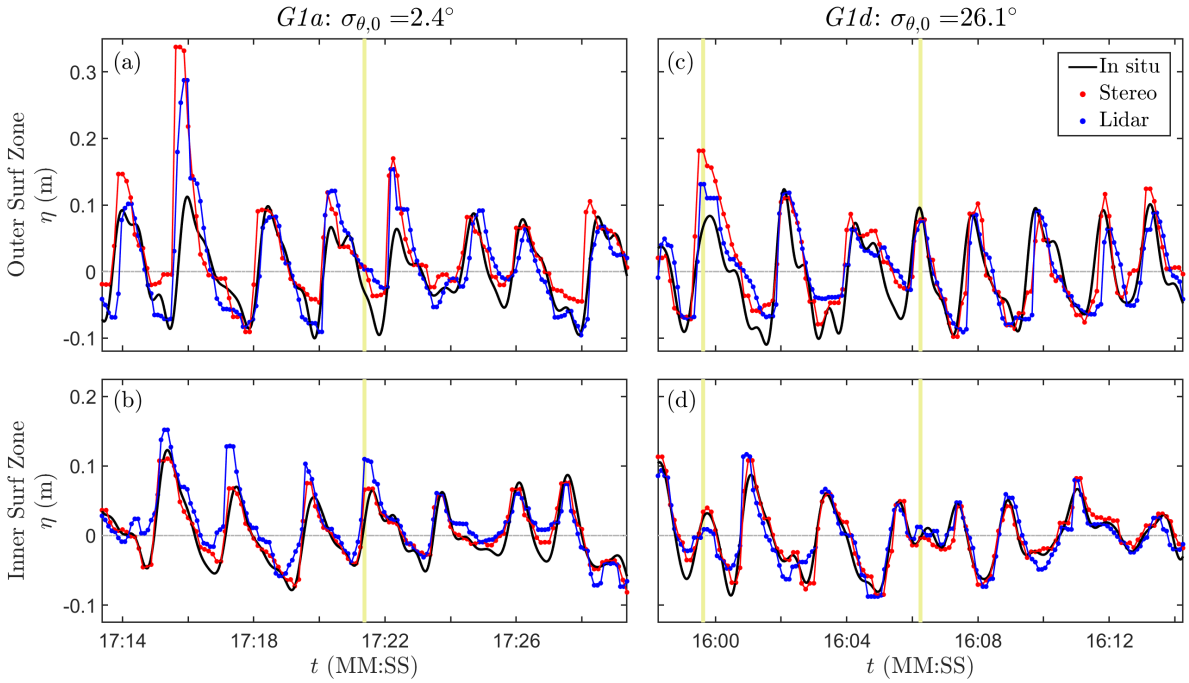

Figure 2.7: Time series of the sea-surface elevation (η) from pressure gauges (black), stereo reconstructions (red), and lidar (blue) in the inner surf zone (a,c, p11: $x, y = 30.7, -0.1$ m) and outer surf zone (b,d, p6: $x, y = 28.4, -0.1$ m) from unidirectional waves (*G1a*, $\sigma_\theta = 2°$) (a,b) and directionally spread waves (*G1d*, $\sigma_\theta = 26°$) (c,d, time series centered at snapshot in Figure 2.3 at $t = 16:06.3$). The sea-surface elevation was reconstructed from pressure gauge measurements using a frequency-dependent depth attenuation correction (black). Three of the times selected for the cross-shore profile snapshots in Figure 2.8a,c,d are shown (yellow vertical lines).

2.3 Results

2.3.1 Surfzone time series and cross-shore profiles

Sea-surface elevation time series measured with the stereo reconstructions and lidar are correlated with pressure gauge estimates of the sea surface for unidirectional (*G1a*) and directionally spread (*G1d*) waves in the inner and outer surf zone (Figure 2.7, correlation coefficients, r^2 in Table 2.3). Three example cross-shore profile snapshots from the stereo reconstructions (gridded to $dx = 0.01$ m) and lidar measurements (gridded to $dx = 0.5$ m) are selected from the time series (Figure 2.7, yellow vertical lines) for unidirectional (Figure 2.8a) and directionally spread (Figure 2.8b,c) waves. As evident in the cross-shore profiles, waves shoal as they propagate onto the beach slope and offshore edge of the bar ($x < 27$ m, beach profile shown with grey shaded region), break near the bar crest ($x \approx 27.5$ m) in either a plunging (Figure 2.8a,b) or spilling (Figure 2.8c) shape, propagate onshore as an aerated bore ($29 < x < 31.5$ m), and run up on the concrete beach ($x > 31.5$ m). The remotely sensed sea-surface elevation from the lidar measurements and stereo reconstructions are mostly consistent in the surf zone (average $r^2 = 0.67$ for *G1a* and *G1d*). The closest lidar grid to the in situ sensor is not directly colocated with the sensor and there are small time offsets between lidar measurements and stereo reconstructions due to the different sampling rates, possibly explaining why lidar measurements can occasionally appear lagged relative to the stereo reconstructions (Figure 2.7a, t=17:25, Figure 2.8a at $x = 30.7$ m). Other possible reasons for the lagged appearance are the lower spatial resolution in lidar measurements smoothing over abrupt changes in the sea-surface elevation or obstruction of the front-face of the wave crest due to the lidar's offshore position.

For the selected cross-shore profiles, the sea-surface elevation estimates reconstructed from pressure gauge measurements are similar to the remotely sensed elevations in the inner surf zone for all wave conditions, with a root-mean-squared deviation (RMSD) of 0.02 m (Figure 2.8). The RMSD between remote sensing and in situ observations is larger in the outer surf zone (average RMSD = 0.06 m). The sea-surface elevation from remote sensing

Table 2.3: The r^2 and root-mean-squared deviation (RMSD) between pressure gauge, stereo reconstructions, and lidar measurements at the center outer (p6, $x, y = 28.4, -0.1$ m) and inner (p11, $x, y = 30.7, -0.1$ m) surfzone sensor for unidirectional (*G1a*) and directionally spread (*G1d*) conditions.

	Outer				Inner			
Trial	*G1a*		*G1d*		*G1a*		*G1d*	
	r^2	RMSD (m)	r^2	RMSD (m)	r^2	RMSD (m)	r^2	RMSD (m)
In Situ vs. Stereo	0.27	0.075	0.50	0.053	0.75	0.022	0.82	0.017
In Situ vs. Lidar	0.30	0.067	0.43	0.046	0.59	0.029	0.77	0.019
Stereo vs. Lidar	0.66	0.051	0.64	0.045	0.66	0.027	0.71	0.023

and pressure gauges are similar for spilling waves in the outer surf zone (Figure 2.8c), whereas the remotely sensed sea-surface elevation is often higher than pressure gauge estimates during plunging breakers (Figure 2.7 a, $t = 17:15.8$ and $17:22.3$ s, Figure 2.8a,c). Occasionally during time periods with small waves causing little to no breaking on the bar (not shown here), surfzone surface foam was insufficient to achieve strong signals and returns in the remote sensing (see Section 2.4.2 for more details).

2.3.2 Sea-surface elevation spectra

The sea-surface elevation spectra computed from the stereo reconstructions and lidar measurements are statistically indistinguishable (within the 95% confidence interval, Figure 2.9) for all surfzone regions and trials, suggesting that the remote sensing techniques measure a similar surface envelope. Relative to the pressure gauge measurements in the outer surf zone, the variance in the remotely sensed sea-surface elevation is 61% larger for the unidirectional waves and 44% larger for directionally spread waves at $0.3 < f < 1.2$ Hz (Figure 2.9a,c).

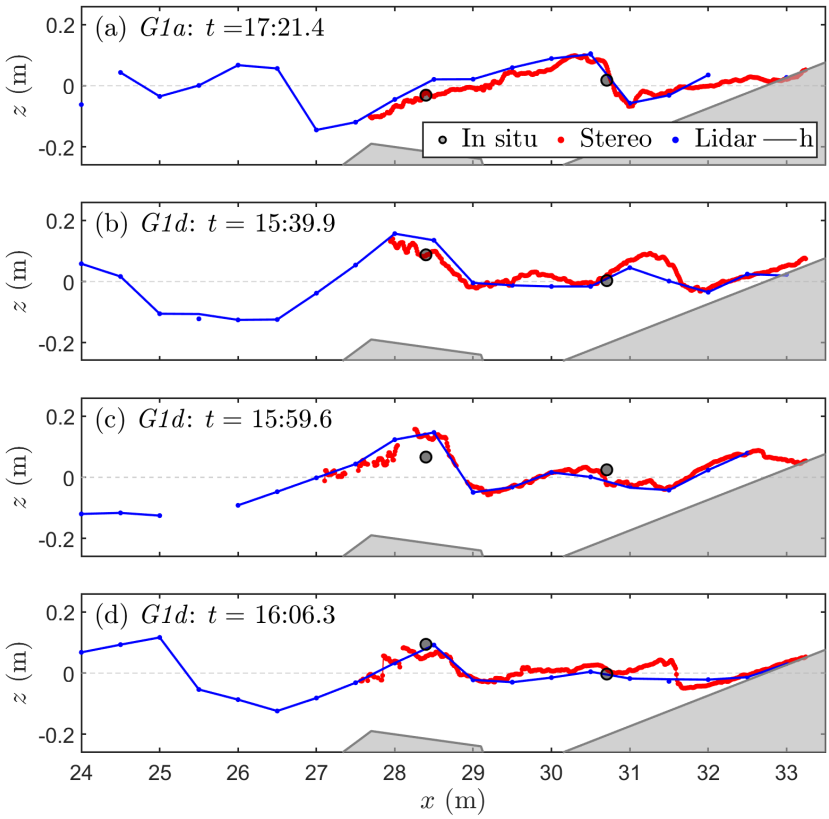

Figure 2.8: Instantaneous cross-shore profiles of the elevation (z) of the sea-surface (η, still water level shown with dashed grey line) at $y = 0$ m from unidirectional waves (*G1a*) at (a) $t = 17:21.4$ and directionally spread waves (*G1d*) at (b) $t = 15:39.9$, (c) $t = 15:59.6$, and (d) $t = 16:06.3$ (see time series in Figure 2.7) as a function of cross-shore position (x) over varying bathymetry (h, solid gray curve and shading). Pressure gauges in the surf zone are black circles (p6 and p11, $x = 28.4, 30.7$ m), stereo-reconstructed elevations are red ($dx = 0.01$ m, 0.03 m spatial moving median filter applied), and lidar measurements are blue ($dx = 0.5$ m). Waves break at the offshore edge of the wave crest ($x \approx 27.5$ m). Snapshots are selected as the closest point in time for the instruments with different sampling rates (*e.g.,* cameras at 8 Hz, lidar at 10 Hz), which may lead to small differences between the lidar and stereo reconstruction.

Both remote sensing estimates have higher variance at low frequencies than the pressure gauge estimates in the outer surf zone ($\mathcal{O}(0.5-1)$ magnitude greater at $f < 0.3$ Hz).

In the inner surf zone, the variance of the remotely sensed data is similar (within the 95% confidence interval) to the variance of the pressure gauges at surface-gravity-wave frequencies ($0.3 < f < 1.2$ Hz) for unidirectional and directionally spread waves (*G1a* and *G1d*, Figure 2.9b,d). The low-frequency variance ($f < 0.3$ Hz) measured by the remote sensing in the inner surf zone is similar to the pressure gauges for directionally spread waves, however, for the unidirectional case, the remotely sensed sea-surface elevation variance is 52% larger than the pressure gauges at low-frequencies. These trends are similar for other trials with unidirectional and directionally spread waves.

The decrease in sea-surface elevation variance as waves propagate toward shore and dissipate within the surf is represented by all measurement methods (Figure 2.9, compare top row with bottom row). The variance measured by pressure gauges in the outer surf zone is lower than measured offshore (Figure 2.9a,c, compare black solid line with grey dot-dashed line), indicating that energy has been dissipated. Consistent with the energy transfer to infragravity frequencies in the swash zone [*Guza and Thornton*, 1982], the pressure gauge measurements have more variance at low frequencies in the inner surf zone than the outer surf zone. Similar to the pressure gauge estimates, the variance measured with remote sensing decreases in the cross-shore at frequencies associated with surface waves near the spectral peak ($0.3 < f < 1.2$ Hz), except in the outer surf zone for unidirectional waves where the variance is similar in magnitude to the offshore conditions (Figure 2.9a, compare red/blue solid line with grey dot-dashed line). Remote sensing techniques may overestimate the low-frequency variance ($f < 0.3$ Hz) in the outer surf zone, leading to a decrease in the remotely sensed low-frequency variance from the outer surf zone to the inner surf zone (see Section 2.4.2).

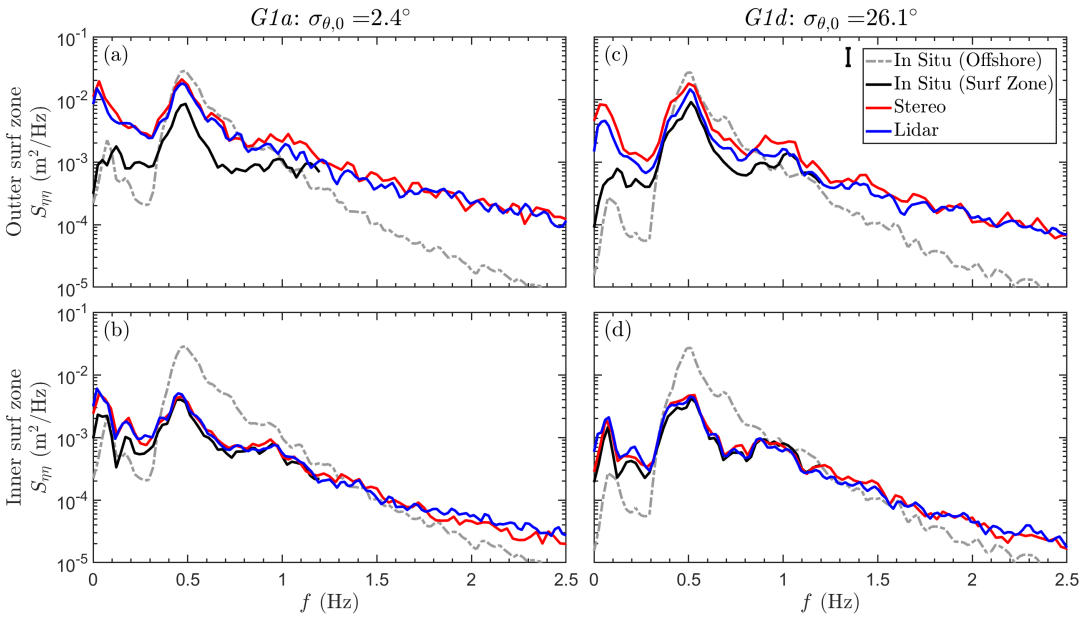

Figure 2.9: Sea-surface elevation spectra ($S_{\eta\eta}$) as a function of frequency (f) were computed from the in situ gauges (black), stereo reconstructions (red), and lidar measurements (blue) in the outer surf zone (a,c, p11: $x, y = 30.7, -0.1$ m) and inner surf zone (b,d, p6: $x, y = 28.4, -0.1$ m) for 10-min time series ($t = 15 - 25$ min) from unidirectional (*G1a*, a,b) and directionally spread (*G1d*, c,d) wave conditions. The offshore spectra were computed from a wire resistance gauge at the bridge (dashed grey, wg4, $x, y = 19.0, -0.04$ m). The vertical bar in (c) is the 95% confidence interval.

2.3.3 Wave height and period

For unidirectional and directionally spread waves, the alongshore-averaged wave height measured by the lidar just offshore of wave breaking is $0.26 - 0.27$ m and is similar to or slightly larger than the pressure gauge wave heights ($H_s = 0.27$ m at $x = 24.5$ m, $H_s = 0.24 - 0.25$ m at $x = 26.6$ m) estimated for a trial with repeated wave conditions and the 'inner-shelf array' of in situ sensors (Figure 2.10a,b, compare blue and black). In the outer surf zone ($x = 28.4$ m), the alongshore-average wave height estimated from stereo reconstructions and lidar are

similar (*G1a*: H_s=0.25 m, *G1d*: H_s=0.23 m) and higher than wave heights estimated from pressure gauges (*G1a*: H_s=0.16 m, *G1d*: H_s=0.17), consistent with comparisons between measurement techniques in the time series and spectra at sensor p6 ($x, y = 28.4, -0.1$ m, Figure 2.7, 2.9). For unidirectional and directionally spread waves, the alongshore-average remotely sensed wave heights are similar to the pressure gauge estimates in the inner surf zone (Figure 2.10, $x = 30.7$ m). Within the surf zone, the alongshore standard deviation of wave height from the stereo reconstructions and lidar measurements are ≤ 1 cm and ≤ 2 cm, respectively, for both wave conditions, indicating there was little variability in the wave height in the along the basin.

Table 2.4: The slope (s), bias, and r^2 for remotely sensed (stereo reconstructions and lidar) wave height (H_s) and peak period (T_p) in the inner (p11: $x = 30.7$ m) and outer (p6: $x = 28.4$ m) surf zone relative to the pressure sensors estimates for all trials in Table 2.1.

		H_s (m)			T_p (s)		
		s	bias (m)	r^2	s	bias (s)	r^2
Outer Surf Zone	Stereo	1.39	0.10	0.65	0.96	0.00	0.98
	Lidar	0.86	0.06	0.34	1.01	-0.01	0.96
Inner Surf Zone	Stereo	0.78	0.03	0.58	0.99	-0.01	0.98
	Lidar	0.71	0.01	0.47	0.99	0.01	0.98

The significant wave height at sensors in the inner and outer surf zone (p6 and p11, $y \approx -0.1$ m) are compared with the remote sensing estimates at the same location for all wave conditions (Figure 2.11). Wave heights computed from the remote sensing are similar to the pressure gauge estimates with a small positive bias in the inner surf zone (Table 2.4, Figure 2.11a, circles) and a larger positive bias relative to the pressure gauge estimates in the outer surf zone (Figure 2.11a, triangles), particularly for the stereo reconstructions. Peak periods (T_p) are correlated with little bias between the remotely sensed and pressure gauge

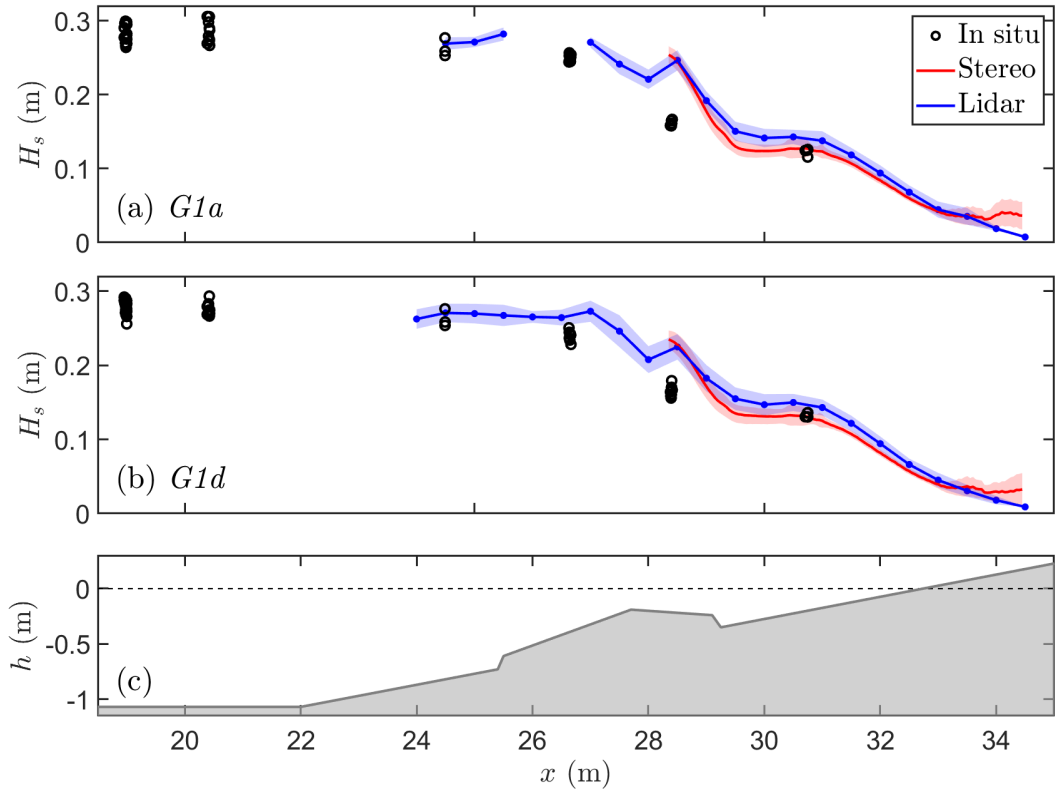

Figure 2.10: The significant wave height (H_s) computed from the in situ gauges (black circles), stereo reconstructions (red), and lidar measurements (blue) for 10-min time series from unidirectional (*G1a*, a) and directionally spread (*G1d*, b) waves. The alongshore average (solid line) and alongshore standard deviation (shaded region) of H_s are shown for the stereo reconstructions and lidar. The in situ sensors include the wire resistance gauges (x = 19.0 m and 20.4 m, $y = -9.0$ to 9.0 m, 3-m alongshore spacing) and pressure gauge arrays in the inner shelf (x = 24.5 and 26.6 m, $y = -12.4$ to 12.7 m) and surf zone (x = 28.4 and 30.7 m, $y = -8.2$ to 3.2 m). (c) The cross-shore profile of the bathymetry (grey) and still water elevation (black dashed).

measurements (Table 2.1 and 2.4). The wave heights computed from the directional spectra (not shown) are between estimates derived from individual sensors in the outer and inner surf zone, as expected for the sea-surface elevation sampled across the surf zone, and T_p is consistent with estimates at individual sensors.

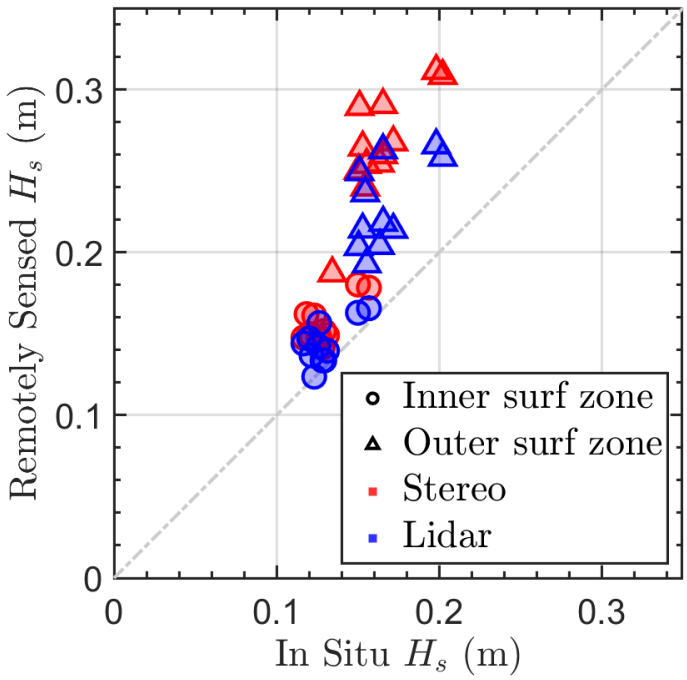

Figure 2.11: The significant wave height (H_s) computed from the pressure gauges in the outer surf zone (p6, triangles) and inner surf zone (p11, circles) are compared with remotely sensed estimates at the same locations from the stereo reconstructions (red) and lidar measurements (blue). A one-to-one line is shown (dashed grey).

2.3.4 Directional spectra and bulk properties

Directional spectra ($S_{\eta\eta}(f,\theta)$) were computed from the sea-surface elevation array approach with pressure gauges, stereo reconstructions, and lidar measurements. For all trials and

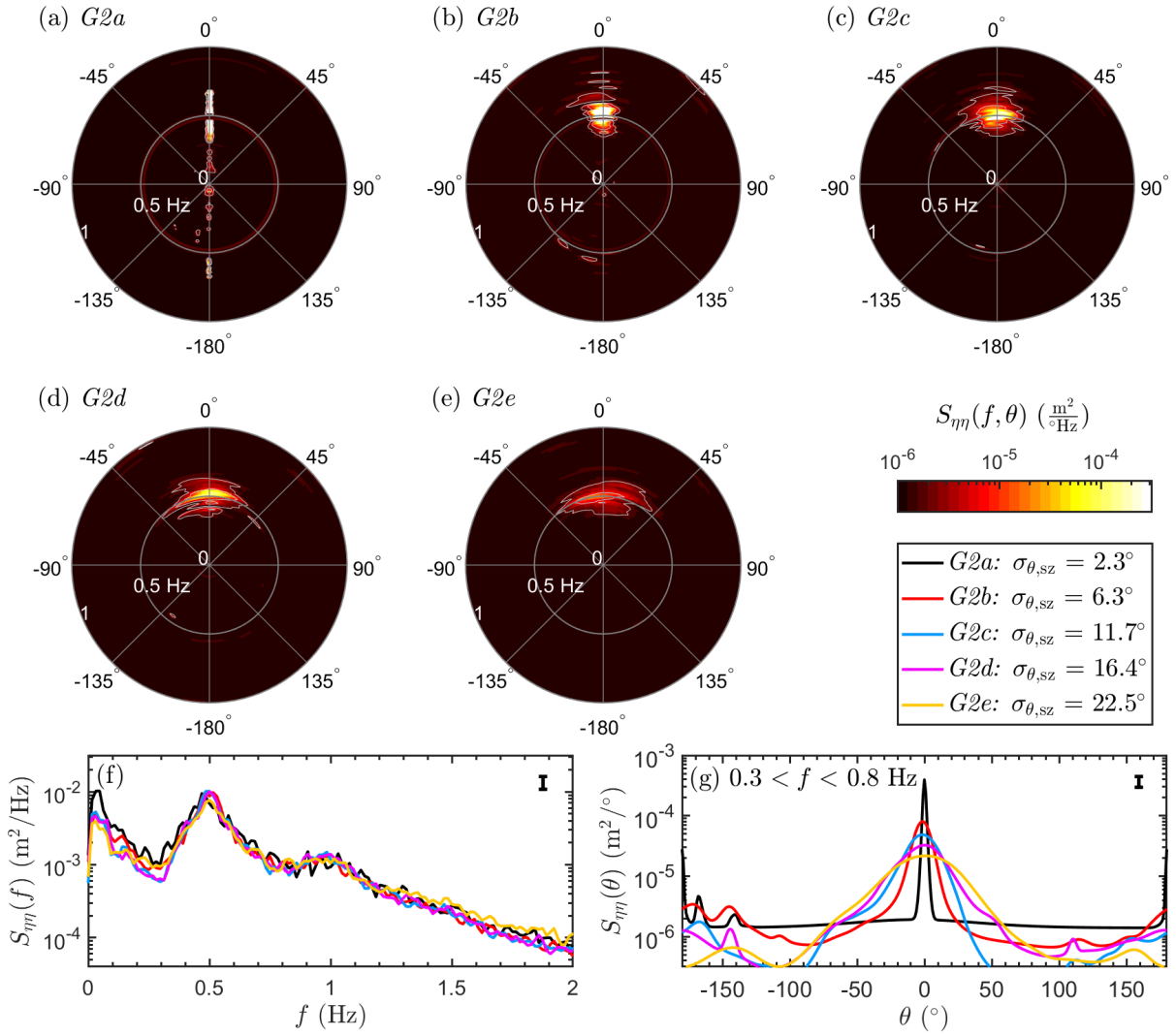

Figure 2.12: (a-e) The surfzone directional spectra ($S_{\eta\eta}(f,\theta)$, color contours) as a function of frequency (f, radial distance) and direction (θ, angle) estimated from the stereo reconstructions in the surf zone (see Figure 2.3a for the array geometry). The directional spectra as a function of only frequency (f, $S_{\eta\eta}(\theta)$, integrated over all directions) or direction (g, $S_{\eta\eta}(\theta)$, integrated from 0.3< f < 0.8 Hz) for *G2a-e* (colors). Waves propagating toward the shoreline have an angle of $\theta = 0°$ and waves propagating towards offshore have an angle of $\theta = 180°$. The estimated surfzone directional spread ($\sigma_{\theta,sz}$) is listed in the legend. The vertical bar in (f,g) is the 95% confidence interval.

measurement types, the peak of $S_{\eta\eta}(f,\theta)$ is near $f = 0.5$ Hz ($T_p = 2$ s) or $f = 0.33$ Hz ($T_p = 3$ s) and 0° (propagating towards shore) with variance more broadly distributed in direction for directionally spread waves than unidirectional waves (example surfzone $S_{\eta\eta}(f,\theta)$ from stereo reconstructions in Figure 2.12). For *G2a-e*, the surfzone directional spectra ($S_{\eta\eta}(\theta)$, summed over $0.3 < f < 0.8$ Hz) from stereo reconstructions is centered at 0° and increases in width and decreases in magnitude at the peak with increasing directional spread (directional spread in the surf zone, $\sigma_{\theta,\mathrm{sz}} = 2 - 23°$, Figure 2.12g). The spread around the peak at 0° for unidirectional waves may be related to small alongshore variation of the wave crest due to interactions with side walls or limitations of the array approach applied to unidirectional waves (Figure 2.12c, black line). At surface gravity wave frequencies ($0.3 < f < 1.2$ Hz), reflected energy at 180° (propagating away from shore) is typically less than 14% of the onshore-directed energy for unidirectional waves and less than 10% for directionally spread waves (see Section 2.2.2).

The mean wave angle (θ) and directional spread (σ_θ) were estimated using the sea-surface elevation array approach by fitting a $\cos^{2s}$ directional distribution and from colocated sensors (at p6, p11) using a PUV approach (see Section 2.2.2). The mean angles estimated from the PUV approach are within 1.5° of 0°, while mean angles estimated with array approaches for all instruments range from θ = -5.9° to 4.8° (see Table 2.5 for bias and RMSD). Tests with a synthetic analytic shore-normal wave field suggest that the non-zero mean direction estimated with the array approaches cannot solely be attributed to the array geometry. Variation of the mean wave direction may be associated with angular resolution of the chosen directional arrays, uncertainties in ADV orientation and remote sensing geometry, and asymmetry in the generated wave field.

PUV estimates of directional spread are similar to the in situ array estimates at $\sigma_\theta \geq 15°$, but yield substantially larger directional spread when $\sigma_\theta < 15°$ (slope = 0.42, Table 2.5). Directional spread may be overestimated with moment-based approaches when there is a high signal to noise ratio [*Herbers and Lentz*, 2010] and may be sensitive to reflections [*Gorman*, 2018], which were more prominent at lower spreads (*e.g.,* Figure 2.12 compare a with b-e).

The directional spreads computed from remote sensing arrays are consistent with estimates from the surfzone in situ array for all directional spreads (r^2=0.93 for stereo, r^2=0.91 for lidar).

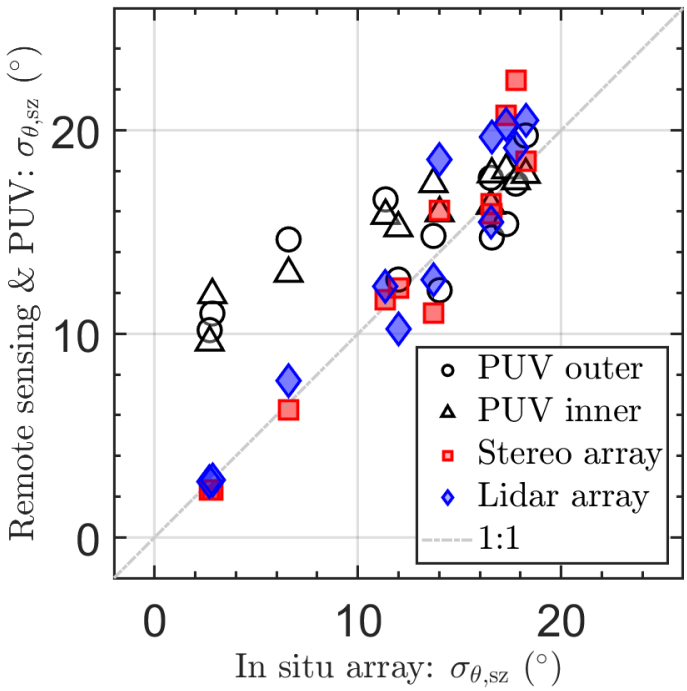

Figure 2.13: The surfzone directional spread ($\sigma_{\theta,sz}$) computed from the surfzone in situ array (values on the x-axis) vs. estimates from the PUV approach at the inner (black circles) and outer surf zone (black triangles) and the sea-surface elevation array approach from the stereo reconstructions (red) and and lidar measurements (blue) (values on the y-axis). A one-to-one line is shown (dashed grey).

2.3.5 Breaking wave crest length, orientation, and number of ends

The dependence of the along-crest length scales of waves in the outer surf zone (x = 29 m) on directional spread (*G2a,b,e*) is evident in the temporal evolution of alongshore transects

Table 2.5: The mean bias and RMSD in mean wave angle (θ) and the slope (s), bias, and r^2 in directional spread (σ_θ) estimated from the sea-surface elevation array approaches (stereo reconstructions and lidar measurements) and PUV directional moment estimates relative to the in situ array estimates for all trials in Table 2.1.

	θ (°)		σ_θ (°)		
	bias (°)	RMSD (°)	s	bias (°)	r^2
Stereo array	-0.33	2.35	1.14	0.52	0.93
Lidar array	-0.62	1.98	1.12	1.04	0.92
PUV	0.79	1.68	0.42	2.66	0.71

(Hovmöller diagrams) of the sea-surface elevation from stereo reconstructions (Figure 2.14) and normalized pixel intensity from rectified camera imagery (c2, Figure 2.15). For unidirectional waves (G2a: $\sigma_\theta = 2°$, Figure 2.14a, 2.15a), wave crests were nearly alongshore uniform and break simultaneously across the width of the basin ($-13.3 < y < 13.3$ m). In contrast, waves fields with larger directional spreads exhibit shorter crest length scales only spanning a portion of the basin width (*e.g., G2b* and *G2d*: $\sigma_\theta = 10,\ 24°$ in Figures 2.14, 2.15b,c).

The lengths, orientation, and number of ends of breaking crests were quantified with RBIS (see Section 2.2.2, Figure 2.5). From the identified wave crests over a 10-min timeseries, the distribution of crest lengths and orientations were determined for each wave condition (Figure 2.16). The average instantaneous number of wave crests (N_{crests}, sum of crests divided by number of frames) per wave crest length (l_{crest}) within the surf zone for *G2a-e* varies with directional spread (Figure 2.16). The number of wave crests at short length scales ($l_{\text{crest}} < 5 - 10$ m) increases with directional spread. In contrast, the number of long wave crests ($l_{\text{crest}} > 10$ m) is greater for waves with less directional spread (*G2b*: $\sigma_\theta = 9°$). The mode crest length for unidirectional waves (*G2a*) is the width of the basin (W_{basin}) and wave crests spanning the full width of the basin were only identified in cases with

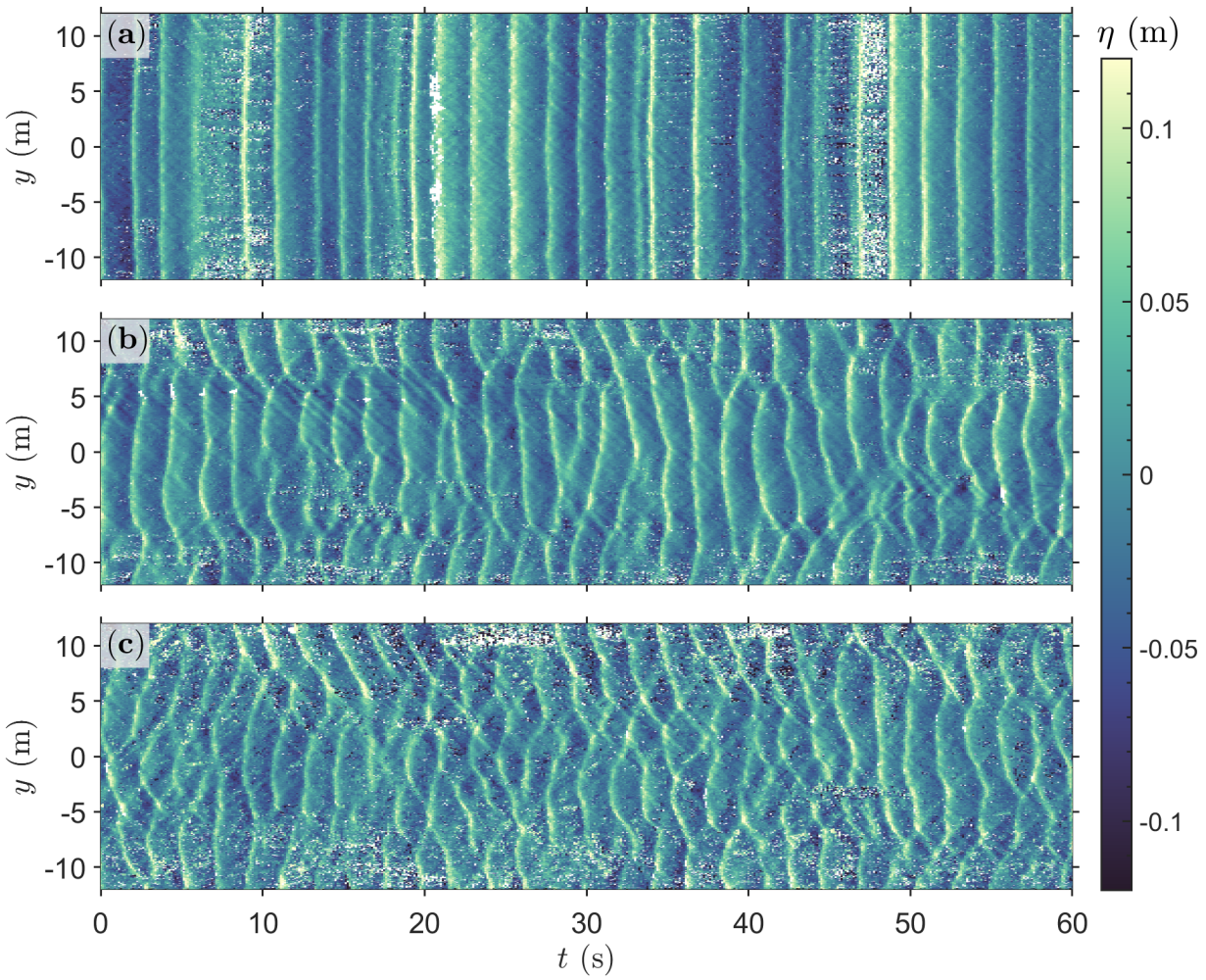

Figure 2.14: Alongshore (y) transects of the sea-elevation (color shading, crests are lighter colors; white are points with no stereo estimate) in the laboratory surf zone ($x = 29$ m) over time (t) from stereo reconstructions. The alongshore structure of the temporally evolving water surface elevation varies as a function of wave directional spread (σ_θ) including 2° (a, *G2a*), 10° (b, *G2b*), and 26° (c, *G2e*).

$\sigma_\theta \leq 10°$ (Figure 2.16, red and black curves). Wave conditions with $\sigma_\theta = 10°$ (*G2b*) had more moderate-length crests (10 m $> l_{\text{crest}} >$ 20 m) than all other directional spreads. The average crest length computed from each distribution decreases with increasing directional

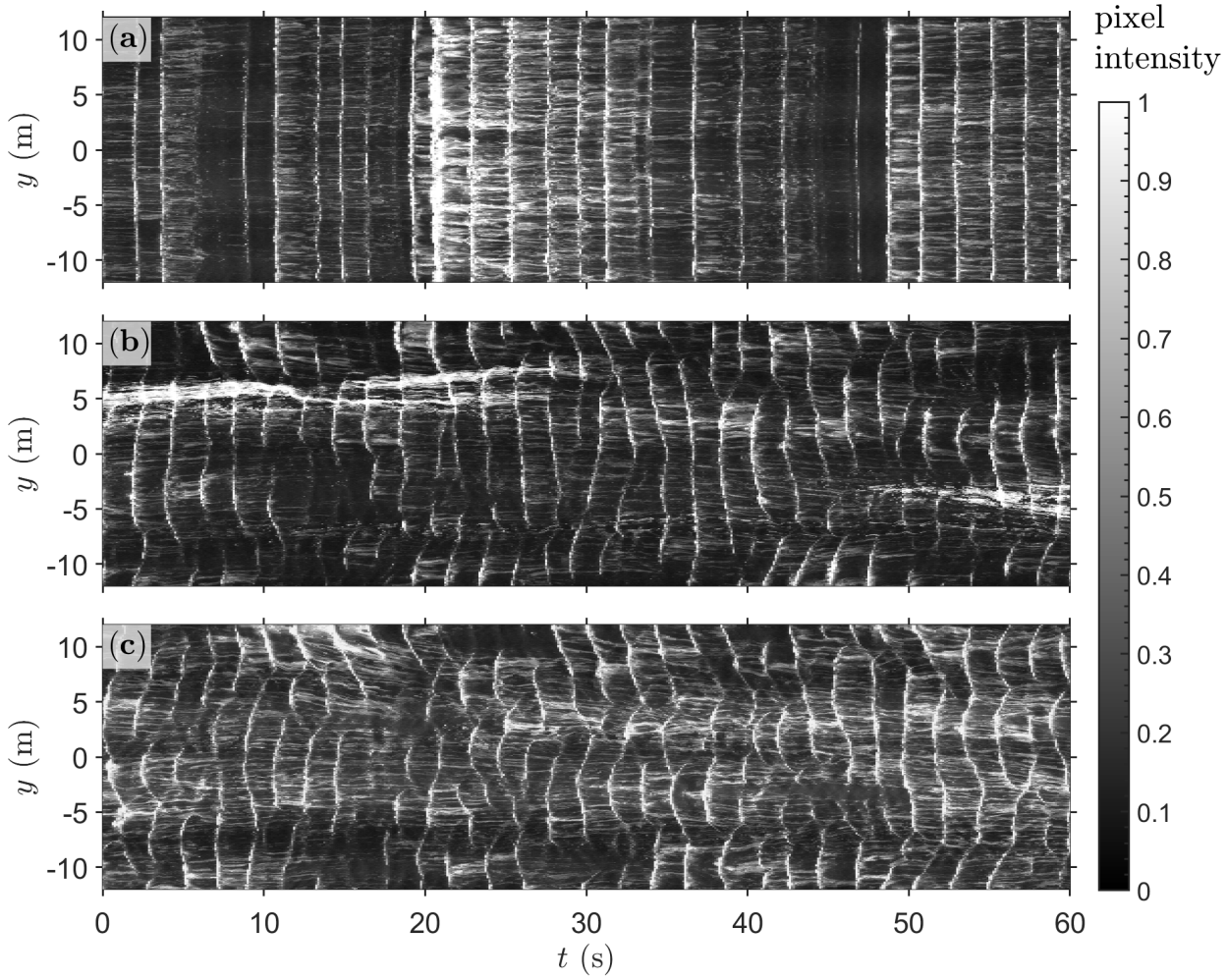

Figure 2.15: Alongshore (y) transects of the normalized pixel intensity (color shading, bright is high intensity indicating bubbles associated with active breaking or residual foam) in the laboratory surf zone (x = 29 m) over time (t) from rectified images (camera c2). The alongshore structure of the temporally evolving brightness signatures of the wave field vary based on wave directional spread (σ_θ) including 2° (a, *G2a*), 10° (b, *G2b*), and 26° (c, *G2e*).

spread from approximately 16.5 m to 4 m (Figure 2.16a, circles).

The distribution of crest orientations (θ_c) estimated with RBIS also varies with the wave field directional spread (Figure 2.16b). Here, $\theta_c = 0°$ are shore-normal waves and $\theta_c > 0°(\theta_c <$

0°) are waves propagating toward the beach counter-clockwise (clockwise) from shore-normal. The number of crests with a shore-normal orientation is greatest for unidirectional waves. For directionally spread waves, the number of shore-normal crests exhibits little dependence on directional spread. The standard deviation of crest orientations ($\sigma_{\text{crest}} = 2-13°$) increases with wave directional spread (Figure 2.16b, horizontal bars). As demonstrated by both the distribution of crest lengths and crest orientations (Figure 2.16a and b), the average number of crests identified per image (area under the curves) increases with directional spread for *G2a-e*. Results are similar for cases with larger wave heights (*G1a-d*, $H_s \approx 0.27$).

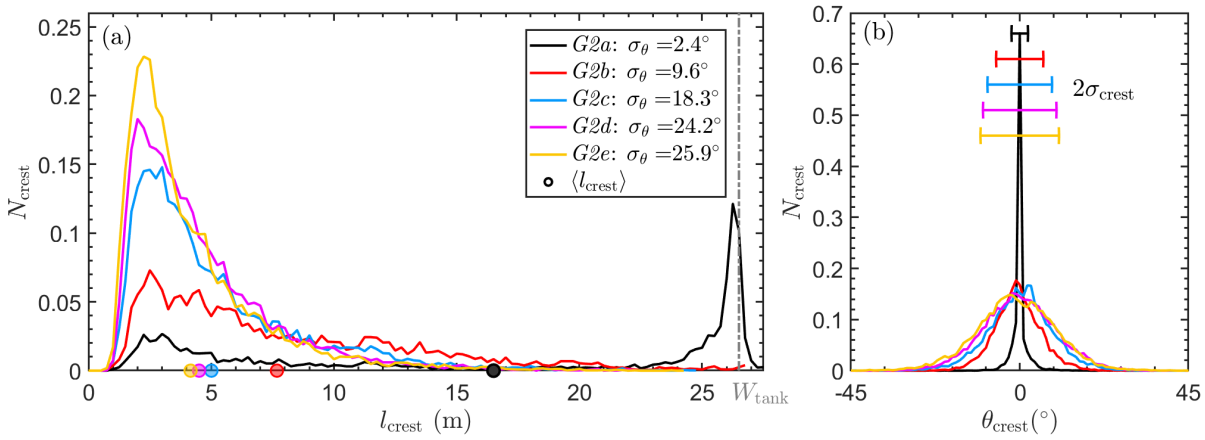

Figure 2.16: Histograms of the crest lengths (l_{crest}, bin width = 0.25 m) and crest orientations (θ_{crest}, bin width = 1°) vs. the average number of wave crests within the surf zone per snapshot (N_{crest}). The average breaker length ($\langle l_{\text{crest}} \rangle$, circles in a) and standard deviation of crest orientation ($2\sigma_{\text{crest}}$, horizontal bars in b) varies with wave directional spread (*G2a-e* with $\sigma_\theta = 2 - 26°$, colors).

2.4 Discussion

2.4.1 Breaking crest length and number of ends

The curl of the force associated with dissipation during wave breaking [*Kennedy et al.*, 2000; *Spydell and Feddersen*, 2009; *Feddersen*, 2014] may be greatest at the crest ends, where the force varies from a non-zero value in the crest to zero outside of the crest, generating vertical vorticity at crest ends [*Peregrine*, 1998; *Johnson and Pattiaratchi*, 2006; *Bonneton et al.*, 2010; *Clark et al.*, 2012; *Wei et al.*, 2017]. Due to spatio-temporal variability of crest lengths, irregular short-crested wave fields drive complex distributions of breaker dissipation and momentum transfer to the water column, enhancing vorticity variance and dispersion in the surf zone [*Spydell and Feddersen*, 2009; *Feddersen*, 2014; *Wei et al.*, 2017; *Elgar and Raubenheimer*, 2020]. Although the precise relationship between the bulk wave properties, breaking crest lengths, and number of crest ends remains unclear, these quantities are expected to play an important role in controlling the spatial and temporal distribution of vertical vorticity injection in the surf zone [*Peregrine*, 1998; *Bühler and Jacobson*, 2001; *Clark et al.*, 2012]. For example, a greater number of crest ends may lead to more eddies with length scales forced by short-crested wave breaking and alter rotational motion at larger and smaller length scales through an inverse cascade of energy or forward cascade of enstrophy [*Spydell and Feddersen*, 2009; *Clark et al.*, 2012; *Elgar and Raubenheimer*, 2020; *Marchesiello et al.*, 2021a]. Here, the dependence of the mean crest length and number of ends on bulk wave properties are investigated with observations and compared with parameterizations based linear wave theory. This subsection includes a proposed nondimensionalization for the parameterizations, a discussion of discrepancies between the observations and parameterizations, and comparisons with previous studies on depth-limited breaker characteristics.

In the laboratory observations with the Remote Breaker Identification Scheme (RBIS, Section 2.2.2), the time- and surfzone area averaged breaking crest length decreases and the number of crest ends increases with directional spread (Figure 2.17a,d, red shapes) for all trials (Table 2.1). The mean crest length has little or no dependence on wave height

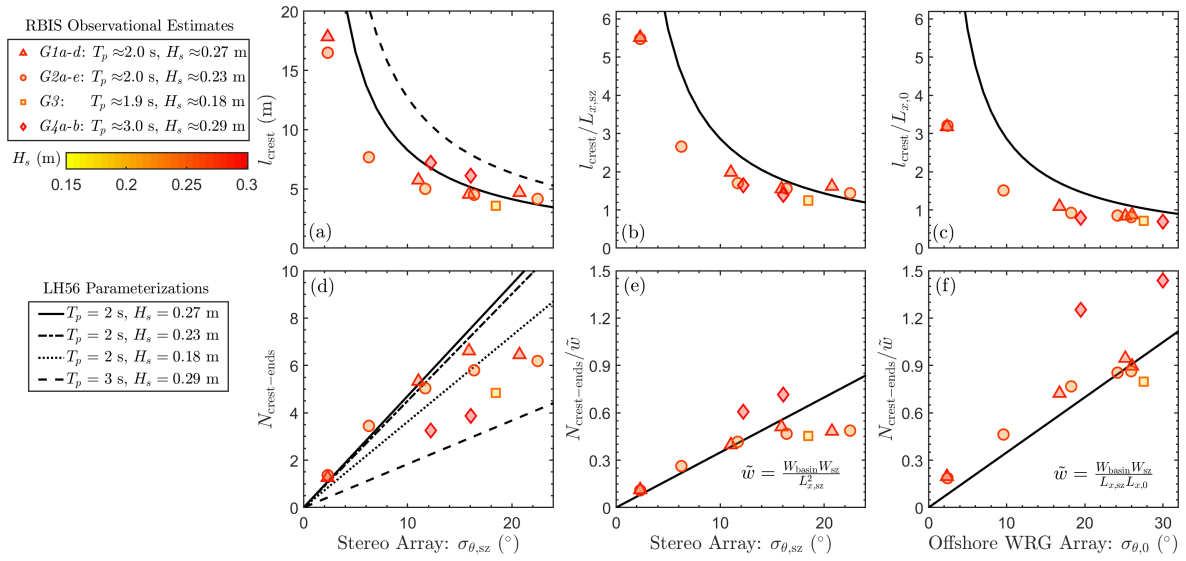

Figure 2.17: The dependence of the (a-c) mean breaking crest length (l_{crest}) and the (d-e) average number of breaking crest ends ($N_{\text{crest-ends}}$) in the surf zone on directional spread for all trials (Table 2.1, legend at left: shapes represent trial groupings with similar peak periods, T_p and offshore wave heights, H_s, colored by H_s). l_{crest} and $N_{\text{crest-ends}}$ are shown as a function of the observed surfzone directional spread from stereo reconstructions ($\sigma_{\theta,\text{sz}}$, a,b,d,e) or the offshore directional spread from wire resistance gauges ($\sigma_{\theta,0}$, c,f). Observations with the Remote Breaker Identification Scheme (RBIS) are compared to *Longuet-Higgins* [1956] (LH56) parameterizations (Eqn. 2.9 in a-c and 2.11 in d-f), where the cross-crest wavelength (L_x) is the surfzone average wavelength given T_p and the surfzone width (W_{sz}). l_{crest} and $N_{\text{crest-ends}}$ are presented as the basin instantaneous estimates (a,d) and nondimensionalized values with the laboratory observed values (b,e, nondimensionalized by the average surfzone wavelength, $L_{x,\text{sz}}$, and a crest-number scale, $\tilde{w} = W_{\text{basin}}W_{\text{sz}}/L_{x,\text{sz}}^2$) or offshore conditions at the wire resistance gauges, WRG (c,f, nondimensionalized by the offshore wavelength, $L_{x,0}$ and a crest-number scale, $\tilde{w} = W_{\text{basin}}W_{\text{sz}}/L_{x,0}L_{x,\text{sz}}$).

(Figure 2.17a, compare red circle, squares, and triangles). The number of crest ends varies

weakly with wave height for the small range of wave heights and surfzone widths tested here ($x_{sz} = 27.1 - 28.2$ m for $H_s = 0.18 - 0.27$ m, Table 2.1), though future work studying a broader range of wave heights and beach slopes may show a more significant relationship (Figure 2.17d). An increase in wave period from $T_p \approx 2$ to 3 s resulted in 20–30% longer mean crest length, and led to about 40% fewer crest ends than conditions with a similar wave height and directional spread (Figure 2.17a,d, compare triangles and diamonds).

To explain the mechanisms for changes in crest length and ends with directional spread and other wave properties, we refer to the characterization of refracting non-breaking, short-crested sea waves in *Longuet-Higgins* [1956] (LH56 hereafter). As short-crested waves propagate into shallower waters, refraction causes changes in the mean wavelength, direction, and along-crests length. A general representation of the root-mean-squared angular deviation of irregular sea waves around their mean direction is defined as:

$$\sigma_{\mathrm{LH56}} = \frac{N_{\min}}{N_{\max}} \tag{2.7}$$

where $N_{\min}$ is the average number of times per unit distance that the water surface crosses a line parallel to the crest and $N_{\max}$ is the corresponding value for a line perpendicular to the crest. For every wave crest, there are two crossings in the cross- and alongshore direction and therefore, σ_{LH56} can be written in terms of the mean wavelength in the wavelength (L_x) and along-crest-length (L_y):

$$N_{\max} = \frac{2}{L_x}, \quad N_{\min} = \frac{2}{L_y}, \quad \sigma_{\mathrm{LH56}} = \frac{L_y}{L_x} \tag{2.8}$$

Given a $\cos^{2s}$ directional distribution, which is nearly Gaussian, σ_{LH56} is analogous to the wave directional spread, σ_θ. Thus, the mean breaker length (l_{crest}) can be estimated as:

$$l_{\mathrm{crest}} = \frac{1}{2} L_y = \frac{1}{2} \frac{L_x}{\sigma_{\mathrm{LH56}}} = \frac{1}{2} \frac{L_x}{\sigma_\theta} \tag{2.9}$$

The factor of 1/2 relating the breaker length (l_{crest}) to along-crest-length (L_y) assumes that, for the surfzone average breaker length, 1/2 of the along-crest-length exceeds the crest-identification threshold, the proxy for an active breaker. For shore-normal regular waves,

the wavelength (L_x) corresponds to the cross-shore wavelength, while along-crest-length (L_y) corresponds to the alongshore wavelength. However, for shore-normal irregular waves, waves propagate onshore with a distribution of angles.

Following linear wave theory, l_{crest} remains constant in the cross-shore as a result of Snell's law assuming a small angle approximation (*i.e.,* $\sin\sigma_\theta \approx \sigma_\theta$), and thus, could be applied for deep water values of the wavelength ($L_{x,0}$ and $\sigma_{\theta,0}$) or values offshore of breaking. However, since Snell's law may not represent the directional spread within the surf zone due to nonlinearities in the wave field and breaking processes [*Herbers et al.*, 1999], applying LH56 with wavelength and directional spread ($L_{x,\text{sz}}$ and $\sigma_{\theta,\text{sz}}$) in the surf zone may be more representative of the breaker characteristics. Note that Eqn. 2.9 is similar to forms derived for a bi-directional wave field [*Dalrymple and Lanan*, 1976; *Kirby and Dalrymple*, 1986; *Dean and Dalrymple*, 1991; *Postacchini et al.*, 2014; *Wei et al.*, 2017; *Choi and Roh*, 2021]. For wave angles θ_1 and θ_2 and applying the assumption that $l_{\text{crest}} = \frac{1}{2}L_y$:

$$l_{\text{crest}} = \frac{1}{2}\frac{L_x}{(\sin\theta_1 - \sin\theta_2)} \tag{2.10}$$

This form is nearly equivalent to LH56 when $\theta_1 = -\theta_2 = \frac{1}{2}\sigma_\theta$ and the small angle approximation is reasonable.

The instantaneous number of crest ends ($N_{\text{crest-ends}}$) are approximated from the surfzone geometry and wave properties as:

$$N_{\text{crest-ends}} = \frac{W_{\text{basin}}}{l_{\text{crest}}}\frac{W_{\text{sz}}}{L_{x,\text{sz}}} = 2\sigma_\theta\frac{W_{\text{basin}}W_{\text{sz}}}{L_x L_{x,\text{sz}}} \tag{2.11}$$

where W_{basin} is the alongshore width of the basin, W_{sz} is the cross-shore length of the surf zone, and $L_{x,\text{sz}}$ is the average wavelength in the surf zone of the basin.

The mean crest length and number of ends were estimated from LH56 (Eqns. 2.9 and 2.11) for trials with $T_p = 2$ and 3 s and $H_s = 0.18 - 0.27$ m (Figure 2.17d, black curves). For consistency with computing LH56 as a function of the surfzone directional spread ($\sigma_{\theta,\text{sz}}$), l_{crest} and $N_{\text{crest-ends}}$ were computed from the surfzone average wavelength ($L_{x,\text{sz}}$) from the dispersion relation given the peak wave period and surfzone water depths (Figure 2.17a,d).

Eqn. 2.9 has no dependence on wave height, and thus, all conditions with the same wave period collapse onto one line. W_{sz} was approximated as the distance between the average observed offshore edge of the surf zone (x_{sz}) for a set of trials with similar wave heights and the offshore extent of the swash zone, set to $x = 31.5$ m for all trials.

LH56 parameterizations trend similarly to RBIS observed crest length and number of crest ends for increasing surfzone directional spread. For directionally spread wave conditions (*i.e.,* $\sigma_\theta > 3°$) with $T_p = 2$ s, crest length from LH56 parameterizations are 34% larger on average (Figure 2.17a, compare red shapes to black curves), except for cases with the largest directional spread ($\sigma_\theta \approx 20°$, underestimated by 13% on average). At small directional spreads, the laboratory basin restricts the maximum observed crest length to the width of the basin, which may reduce the mean observed crest length relative to LH56 parameterizations. For $T_p \approx 2$ s, the number of crest ends observed with RBIS are similar to LH56 parameterizations at small directional spreads ($\sigma_\theta < 15°$), but are over-estimated by LH56 by 37% at larger directional spreads (Figure 2.17d, *e.g.,* compare red triangles to dot-dashed black line). For $T_p = 3$ s, the LH56 parameterizations overestimate the observed mean crest lengths by 38% and underestimate the number of crest ends by 28%.

The mean crest length and number of crest ends are nondimensionalized to evaluate the differences between RBIS observations and LH56 parameterizations as well as to generalize these results to other conditions (Figure 2.17b,c,e,f). The crest length is nondimensionalized by wavelength, L_x at the same location as the directional spread estimates, and the number of crest ends is nondimensionalized by a crest-number scale, $\tilde{w} = W_{\mathrm{basin}} W_{\mathrm{sz}} / L_x L_{\mathrm{sz}}$, effectively a ratio of the surfzone area to a quantity related to the crest-area. The normalized estimates are presented as a function of the surfzone conditions ($L_{x,\mathrm{sz}}$, $\sigma_{\theta,\mathrm{sz}}$) from the stereo reconstructions as well as the offshore conditions ($L_{x,0}$, $\sigma_{\theta,0}$) from the wire resistance gauges, as some applications may require an estimate that is only a function of offshore wave properties. The nondimensionalized LH56 parameterizations of the mean crest length simplify to σ_θ^{-1} and number of crest ends to $2\sigma_\theta$, and therefore, all conditions collapse onto one line for LH56 parameterizations. The average crest length and number of ends estimated with RBIS

generally collapse when normalized by the directional spread and wavelength in the surf zone (Figure 2.17b,e, red shapes) and offshore (Figure 2.17c,f, red shapes), as well as the surfzone width and peak wave period for each individual trial. However, the normalization collapses RBIS results of crest length for varying wave periods better than the number of crest ends, possibly due to the underestimation of crest ends with the LH56 parameterization for longer wave periods or more spurious identification of residual foam as a breaker occurred for longer wave periods (Figure 2.17 compare black curve and red diamonds for b vs. e, c vs. f).

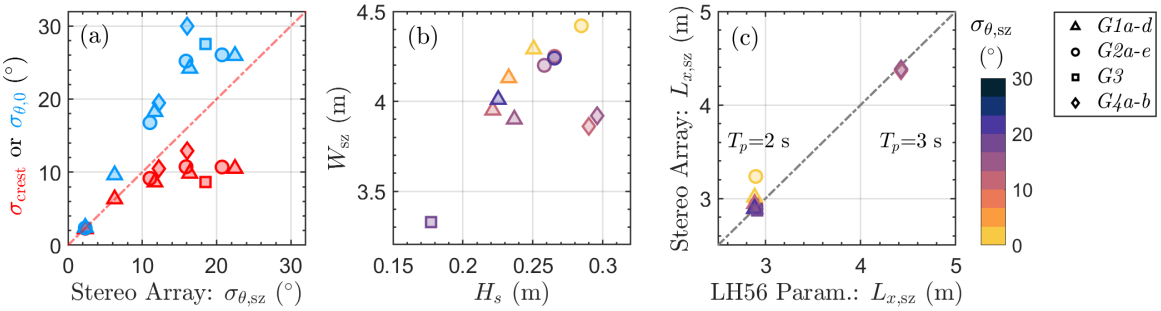

Figure 2.18: Summary of possible sources of uncertainty in the comparisons between the Remote Breaker Identification Scheme (RBIS) observations and *Longuet-Higgins* [1956] (LH56) parameterizations of crest length and ends (Figure 2.17) for various trial groups (shapes, legend at right). (a) The directional spread estimated from stereo reconstructions ($\sigma_{\theta,sz}$) vs. the standard deviation of ellipses fit to wave crests (σ_{crest}, red shapes and red 1:1 line) and offshore directional spread at the wire resistance gauges ($\sigma_{\theta,0}$). (b) The observed offshore wave height (H_s) vs. the surfzone width (W_{sz}) and (c) the surfzone wavelength ($L_{x,sz}$) used for LH56 parameterizations for T_p = 2 and 3 s vs. the surfzone wavelength estimated from T_p in stereo reconstructions with a 1:1 line (grey). (b,c) Trials are colored by the surfzone directional spread ($\sigma_{\theta,sz}$) from stereo reconstructions.

The LH56 parameterizations are presented based on the average conditions observed for different trial groupings (*i.e.,* average T_p and W_{sz}). Therefore, variability intrinsic to

the comparisons between RBIS observations and LH56 parameterizations of crest length and ends may be partially due to variation in wave statistics across trial groups (Figure 2.18b,c) or how the angular deviation of the wave field is represented. The standard deviation of ellipses fit to wave crests (σ_{crest}, possibly more congruent with σ_{LH56} in Eqn. 2.7) are similar to the surfzone directional spread estimated from stereo reconstructions ($\sigma_{\theta,\text{sz}}$) at small directional spreads and plateau at around $\sigma_{\text{crest}} = 10°$ for surfzone directional spreads ($\sigma_{\theta,\text{sz}}$) greater than 10° (Figure 2.18a, compare red shapes with red dashed 1:1 line). This may be a consequence of fitting an ellipse to an irregular breaking crest shapes or could result from differences between deriving directional spread from sea-surface elevations across the surf zone vs. continuous breaking features flagged with RBIS. Due to wave refraction, directional spreads in the surf zone are smaller than those observed offshore, but may be underestimated by shoaling an angle of $\theta = \sigma_\theta$ onshore (Figure 2.18a, blue circles). Therefore, because LH56 applies linear wave theory to retain a constant L_y in the cross-shore, LH56 parameterizations from offshore wave conditions may over-estimate crest length and under-estimate the number of crest ends in the surf zone.

In addition to variations within trial groupings and possible biases in observational methods (Section 2.2.2), differences between LH56 parameterizations and RBIS observed wave characteristics may result from the simplified nature of the LH56 parameterizations, which do not account for breaking or nonlinearities in the wave field. Possibly the largest source of uncertainty arises from the assumption that l_{crest} is half the alongshore wavelength. This assumption may not be representative of the average breaker length across the surf zone, where the largest amplitude section of the wave breaks first and expands as the wave propagates into shallower waters. This assumption may be further complicated due to wave obliquity altering breaking patterns and the steep bar-trough bathymetry that may result in the reformation of bores over the trough. Moreover, in an inhomogenous wave field, the mean crest length may not be representative of the distribution of crests lengths resulting in the total number of crest ends within the surf zone (*e.g.,* Figure 2.16a). For example, the LH56 theory does not reflect how wave properties may vary with the spread in frequency of the wave field (*e.g.,*

the JONSWAP spreading factor for narrow swell conditions vs. broad-banded wind waves). Furthermore, nonlinearities in the wave field may lead to reduced crest lengths relative the linear approximations due to the nonlinear interaction of wave components [*Johannessen and Swan*, 2001], wave-current interaction with complex surfzone currents [*Longuet-Higgins and Stewart*, 1961; *Hasselmann*, 1971], and directional broadening due to the scattering of energy during breaking [*Herbers et al.*, 1999]. Additionally, side walls, reflections, and resonant patterns in the laboratory setting may alter crest length and number of ends and are discussed in Section 2.4.3.

The breaking crest characterizations for an irregular short-crested wave field in the laboratory presented here are the first set of observations of the response of depth-limited breaker along-crest-length characteristics to varying wave directional spreads. These observations can aid our understanding of depth-limited breaking, building on previous numerical modeling and laboratory experiments of crossing wave trains in shallow water [*Dalrymple*, 1975; *Dalrymple and Lanan*, 1976; *Kirby and Dalrymple*, 1986; *Dean and Dalrymple*, 1991; *Postacchini et al.*, 2014; *Garnier et al.*, 2014; *Wei et al.*, 2017; *Choi and Roh*, 2021] and regular short-crested waves [*Kirby and Derakhti*, 2019]. The limited influence of wave height on breaking crest length in RBIS observations and LH56 parameterizations is consistent with previous simulations of crossing-seas with a nonlinear shallow-water equation solver [*Postacchini et al.*, 2014]. Their results suggest that the breaker length only depends on the wave incidence angles and two constants, but does not vary with wave period. However, it is unclear if their framework for bi-directional crossing seas is transferable to directionally spread irregular waves. Highly-resolved nonlinear numerical models that simulated crossing wave trains and regular waves [*Wei et al.*, 2017; *Kirby and Derakhti*, 2019] provide insight into why the breaker length may be overestimated with linear wave theory. In these numerical experiments, nonlinear wave interactions led to the bifurcation of individual short crests – the division of a wave crest into two crests – within the surf zone for barred and planar bathymetry. Even though it is unclear if bifurcation would play a dominant role in wave crest characteristics for irregular wave fields, their results emphasize the contribution

of nonlinearities in the surf zone to altering breaker length characteristics.

Findings presented here suggest that the directional spread of the wave field plays a dominant role in defining the crest length, consistent with linear wave theory [*Longuet-Higgins*, 1956]. Future work could explore how along-crest breaker characteristics vary with wave obliquity and spectral shape (*e.g.,* a narrow frequency spread, common for swell-dominated conditions), as well as the influence of bi-modal wave conditions with both a local-sea and swell. The implications of breaker characteristics during varying sea-states on vorticity generation, surfzone dispersion, and cross-shore exchange are topics for further inquiry.

2.4.2 Remotely sensed sea-surface elevation and array-based wave field characterization

Reconstructing the free surface from the subsurface pressure using linear wave theory does not represent non-hydrostatic effects that typically occur in the aerated region of steep breaking bores [*Van Dorn*, 1978; *Elgar et al.*, 1988], possibly leading to an underestimation of the maximum elevation of wave crests in the surf zone [*Martins et al.*, 2020]. In contrast to subsurface pressure measurements, remote sensing techniques estimate the free surface elevation and can capture the free-surface signature of nonlinear, non-hydrostatic processes (*e.g.,* wave asymmetry, wave-wave interactions) during depth-limited wave breaking. Wave directional spectra, typically computed with a single instrument (i.e., heave-pitch roll or PUV) or a sparse array of in situ sensors, may be augmented with high-resolution sea-surface elevation measurements that can be sub-sampled at locations not defined a priori and are not limited by the number of available sensors. However, when interpreting the remotely sensed free-surface estimates, it must be considered that they may include the surface elevation signature of spray and splash up, the aerated water surface (foam), and the surface above an air cavity (plunging breakers), in contrast to pressure measurements that assume a single vertically connected domain. Due to these differences, remote sensing and pressure gauge measurement techniques may produce different estimates of wave dissipation, particularly for plunging wave conditions, and each may be better suited for distinct science questions.

Remote sensing observations used in this study rely on surface features, such as foam, to

map the water surface elevation. Here, remotely sensed wave heights are similar to in situ observations in the inner surf zone and larger than in situ observations in the outer surf zone (Table 2.1, Figure 2.11). Particularly near the onset of breaking (Figure 2.8a at $x = 28.4$ m), the remote sensing estimates may have more variance near the peak wave frequency due to the presence of aerated bore-fronts and plunging breakers with a void shape and splash up [*e.g.,* Figure 2.19a, *Peregrine*, 1983; *Basco*, 1985; *Cox and Shin*, 2003], and also due to spurious low elevation estimates in wave troughs during periods with less steep waves (*e.g.,* smaller wave sets, Figure 2.19b) resulting in less persistent residual foam [*Callaghan et al.*, 2013] and increased visibility of subsurface features. See stereo reconstructions in the darkest troughs observed in imagery by comparing Figure 2.14 vs. 2.15. These processes resemble a periodic impulse or square wave, with the amplitude varying on timescales of wave groups due to the modulation of breaker type and foam with wave height. Thus, these affects may also contribute to the higher variance observed at frequencies higher or lower than the spectral peak. The modulation of breaker type, foam, and splash up over wave-group timescales was more prolific for unidirectional wave conditions (compare depth-attenuation and hydrostatic corrected pressure gauge measurements with remote sensing in Figure 2.19), leading to greater discrepancies between in situ observations and remote sensing relative to directionally spread wave conditions. Additionally, the lack of harmonics at frequencies higher than the first harmonic in remote sensing may be due to the running median filter applied to these observations or inherent noise and cannot be compared to in situ sensors due to the frequency cutoff in the depth-attenuation correction (Figure 2.9, $f \geq 1.5$ Hz).

Similar differences between lidar and in situ observations have previously been identified. The higher variance measured by a lidar than colocated pressure sensors is consistent with field observations in the outer surf zone during plunging breakers [*Martins et al.*, 2020] and in the inner surf zone with aerated wave rollers [*Brodie et al.*, 2015]. Two laboratory flume experiments that compared in situ observations and stereo reconstructions during spilling breakers found that differences were small [less than 10%, *de Vries et al.*, 2011; *Kim et al.*, 2022], consistent with comparisons presented here in the inner surf zone. Further,

previous studies applying stereo processing techniques in deep or intermediate water have also observed a similar overestimation of variance at low frequencies [*Wanek and Wu*, 2006; *Leckler et al.*, 2015]. However, previous studies have not explored the consistencies between stereo reconstructions and in situ observations during plunging breakers. The comparable spectra and wave height estimates between remote sensing techniques in the outer surf zone suggest that biases observed in previous lidar observations during plungers may be consistent with biases for stereo reconstructions. Additional studies could provide insight into how the differences between remote sensing and in situ sensors vary with differing laboratory setups (*e.g.,* lighting, surface features) and wave fields (*e.g.,* breaker type).

Estimating frequency-directional wave field characteristics via array-based approaches has advantages over single-point approaches, and spatially dense remote sensing sea-surface elevation measurements offer the ability to easily design lagged arrays for such approaches. Surfzone directional spread from array-based approaches are larger than spreads estimated via applying analytical linear wave shoaling to the offshore wire resistance gauges (not shown), possibly due to breaking induced spreading of energy [*Herbers et al.*, 1999] and wave-current interaction [*Battjes*, 1988]. Lagged array approaches might be affected by sub-optimal lags for the pre-defined in situ sensor locations [*Young*, 1994], significant dissipation (breaking) within the array and phase-locked reflections in the laboratory setting [*Huntley and Davidson*, 1998]. Similar to the laboratory findings presented here, previous estimates of the mean direction from lidar observations near breaking found better agreement with in situ observations from array-based approach than with PUV estimates (root-mean-square error of about 8°), but did not test the directional spread [*Irish et al.*, 2006]. Airborne scanning lidars [*Walsh et al.*, 1987; *Hwang et al.*, 2000; *Jahanmard et al.*, 2022] and stereo-photogrammetry techniques from imagery [*Bechle and Wu*, 2011; *Benetazzo et al.*, 2012; *Leckler et al.*, 2015; *Malila et al.*, 2022a] have been applied to estimate directional spectra with an array of single point measurements, similar to estimates herein, and three-dimensional Fourier transforms of space-time sea-surface elevations in intermediate and deep waters. However, a comparison between in situ observations, stereo reconstructions, and lidar measurements has not other-

wise been tested in the surf zone. Further research into the sensitivity of directional spectra results to array geometries and estimator selection in varying settings would be valuable.

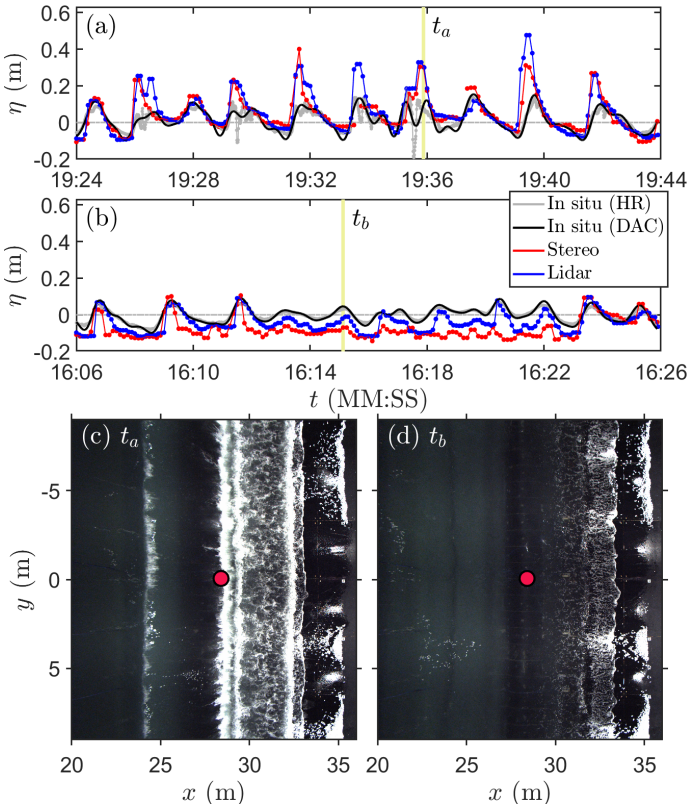

Figure 2.19: Time series (t) of the sea-surface elevation (η) during trial *G1a* with nearly unidirectional ($\sigma_\theta = 2°$) wave conditions for time periods with large plunging breaking waves at the peak of a wave group (a) and small non-breaking waves with little surface foam (b) observed with the in situ gauges (grey: hydrostatic reconstruction, HR, black: depth attenuation correction, DAC), stereo reconstructions (red), and lidar measurements (blue) in the outer surf zone (p11: $x, y = 30.7, -0.1$ m). Rectified images from the center camera (c2) as a function of the cross- (x) and alongshore (y) position during (c) a plunging breaker at time t_a (yellow vertical bar in a) and (d) a small set of waves at time t_b (yellow vertical bar in b). The location of sensor p11 is overlain on the images (c,d, red circle).

2.4.3 Laboratory experimental conditions and applicability

The laboratory directional wave basin experiments presented here were used to study directionally spread wave fields that were normally incident on alongshore-uniform bathymetry, without some of the complexities commonly found in a field environment including local and offshore alongshore bathymetric variations and mean alongshore currents and associated shear instabilities [*Bowen and Holman*, 1989; *Allen et al.*, 1996; *Oltman-Shay et al.*, 1989]. In addition, the repeatable wave conditions generated by the wavemaker, ease of deployment of in situ sensor and camera arrays, and controlled surfactant and lighting were important in achieving the highly resolved dataset and resulting findings.

The closed boundaries and steep beach in the laboratory basin interact with the wave and flow fields, which may limit the ability to use the basin results as a model for extensive alongshore beaches with shallower slopes that are often studied in field environments. For example, particularly for the unidirectional wave cases, strong reflection occurred at surface-gravity and infra-gravity frequencies, leading to interactions with incoming waves and modulation of the breaker type. Directionally spread wave fields reflect off of the hard side walls and back into test area, which may lead to differences in the wave field relative to an open coast; alternatively, the reflected energy may beneficially reduce shadowing effects that would occur for more dissipative sidewalls [*Mansard and Miles*, 1994; *de Reilhac et al.*, 2008; *Dalrymple*, 1989; *Gilbert and Huntington*, 1991].

Another consequence of the reflective sidewalls was the generation of seiching patterns, which led to the exclusion of trials with longer periods from this study (smaller ratio of the alongshore wavelength to basin width) for which pressure gauge records showed strong seiching. Analysis of in situ velocities suggest that seiching modes were small for trial conditions analyzed here and there is no evidence of modes growing throughout the trial run. Some of the wave components in the forced irregular wave fields satisfy the dispersion relation for free edge waves – laterally traveling waves near the shoreline [*Bowen and Inman*, 1971; *Guza and Inman*, 1975; *Holman and Bowen*, 1984] – however, the short wavelengths relative

to the basin width were unlikely to excite lower-mode, higher-energy edge waves [*Guza and Davis*, 1974; *Guza and Inman*, 1975]. Randomness of the irregular wave frequencies may significantly reduce the subharmonic edge wave amplitude [*Vittori et al.*, 2019]. Furthermore, wave breaking leads to broad-banded noise in the fluid motion and may inhibit the excitation of subharmonic edge waves [*Guza and Inman*, 1975; *Guza et al.*, 1976; *Abcha et al.*, 2017].

Given these considerations, further work is needed to determine how the relationships identified here may be adapted for open-coast field environments. Similar to the analyses performed here, field measurements of the water surface elevation on a relatively alongshore-uniform beach using stereo imaging or lidar, paired with observations of nearshore bathymetry and offshore wave conditions, could be used to investigate the dependence of breaking wave crest statistics on offshore wave conditions, with the added complexity of varying bathymetry and other factors. In addition, numerical simulations of the transformation of directionally spread wave fields could assess the behavior of the breaking wave patterns for a range of wave conditions and geometries, including a long beach with periodic boundary conditions or a finite laboratory basin with reflective walls.

2.5 Summary and Conclusions

Short-crested wave breaking leads to the injection of vorticity in the surf zone, influences sediment transport processes, and alters runup and forces on structures. The along-crest-lengths of breaking waves in the surf zone are expected to be shorter when waves are more directionally spread, but this relationship had not been quantified. Additionally, few studies have assessed the feasibility of applying remote sensing, including stereo reconstruction and lidar, to measure wave transformation in the surf zone. Here, laboratory experiments at the O.H. Hinsdale Wave Research Laboratory are used to investigate remotely-sensed breaking wave properties, including the distribution of breaker along-crest-lengths and ends during multidirectional irregular wave conditions.

Stereo reconstructions and lidar measurements of the sea-surface elevation are compared with in situ observations in and just offshore of the surf zone of the basin for 12 trials. The

remotely sensed cross-shore transformation of wave height is similar to in situ observations offshore of wave breaking and in the inner surf zone. Near the onset of wave breaking, larger wave heights are measured by the remote sensing than by the in situ sensors due to differences in measurement techniques. For example, plunging breakers may lead to differing measurements, because remote sensing resolves the top of an aerated water surface whereas the pressure gauges measure the height of the surface below an air pocket. Further, directional spread estimated with sea-surface elevation arrays extracted from remote sensing observations are similar to estimates from in situ sensor arrays for all wave conditions and are smaller than single-point PUV directional estimates for wave conditions with small directional spreads.

The average along-crest length scales of surfzone waves were quantified with the Remote Breaker Identification Scheme to identify individual crests via thresholding of imagery and stereo reconstructions. As wave directional spread increases, the length of breaking crests decreases and the number of crest ends increases. In contrast, as the wave period increases, the along-crest-length increases and number of crest ends decreases. Decreasing the significant wave height led to little or no change in along-crest-length and a decrease in the number of crest ends. The observed crest length and number of crest ends follow a similar relationship with directional spread to parameterizations of crest characteristics based on *Longuet-Higgins* [1956] (LH56). The LH56 parameterizations are larger than the observed crest length for most cases, except for cases with the largest directional spreads. For 2-s waves, the number of crest ends estimated by LH56 parameterizations is consistent with observations at small directional spreads, but larger than observations at larger directional spreads. A nondimensionalization is proposed to generalize expected breaking along-crest-length and number of crest ends for other wave and bathymetry conditions. Further work may refine the relationship between wave field bulk properties and the distribution of crest length scales and assess the translatability of the finite wave basin results to field environments.

Chapter 3

LINKING DIRECTIONALLY SPREAD WAVEFIELDS, SHORT-CRESTED WAVE BREAKING, AND SURFZONE EDDY PROCESSES IN A LABORATORY BASIN

3.1 Introduction

The nearshore region consists of the surf zone, extending from the shoreline to the seaward limit of depth-induced wave breaking, and the inner shelf, which is directly offshore of the surf zone where turbulence extends throughout the water column [*Lentz and Fewings*, 2012]. Essential commercial and recreational resources within this nearshore region are often compromised by degraded water quality due to pathogens, viruses, or excess terrestrial nutrient runoff disrupting coastal ecosystems [*Halpern et al.*, 2008; *Boehm and Soller*, 2013], causing gastrointestinal and viral infections for swimmers [*Prüss*, 1998; *Colford et al.*, 2012], and prompting beach closures [*Boehm et al.*, 2002]. Furthermore, the dispersal of plankton and larval subsidies via surfzone currents affect the growth and reproduction of filter-feeding invertebrates, a foundation of intertidal ecosystems [*Shanks et al.*, 2010; *Morgan et al.*, 2017]. The transport and dispersion of these materials within the surf zone and between the surf zone and inner shelf are in part driven by wave-driven surfzone eddies and rip currents [*Hally-Rosendahl et al.*, 2014, 2015; *Hally-Rosendahl and Feddersen*, 2016]. Accurately characterizing these processes is essential for recreational activities and nearshore ecosystem health.

As waves propagate shoreward and break within the surf zone, they inject turbulence into the water column [*Feddersen*, 2012] and drive complex circulation patterns with varying spatial and temporal scales. Oblique waves drive mean alongshore surfzone currents, transporting material along the coastline [*Longuet-Higgins*, 1970], and bed return flow often promotes

the seaward return of material [*Svendsen*, 1984b]. Bathymetric rip currents, resulting from alongshore variation in pressure gradients, contribute to cross-shore exchange of material on alongshore-varying beaches [*Inman et al.*, 1971; *MacMahan et al.*, 2006; *Dalrymple et al.*, 2011; *Castelle et al.*, 2014]. Additionally, surfzone eddies – horizontal rotational motions with lower frequencies than surface gravity waves – drive rapid dispersion and transport of material within the surf zone [*Spydell and Feddersen*, 2009; *Clark et al.*, 2010; *Feddersen et al.*, 2011; *Clark et al.*, 2011; *Spydell and Feddersen*, 2012; *Hally-Rosendahl et al.*, 2014, 2015]. Ephemeral offshore ejections of surfzone eddies, known as transient rip currents, induce exchange between the surf zone and inner shelf [*Johnson and Pattiaratchi*, 2004b; *Suanda and Feddersen*, 2015; *Kumar and Feddersen*, 2017c, a, b; *Grimes et al.*, 2020a, b]. Despite the importance of surfzone eddies, the generation mechanisms and temporal evolution of surfzone eddies remain elusive.

Wave breaking [*Peregrine*, 1998; *Reniers et al.*, 2004] and shear instabilities in mean alongshore currents [*Bowen and Holman*, 1989; *Dodd et al.*, 1992; *Oltman-Shay et al.*, 1989; *Feddersen*, 1998] generate low-frequency rotational motion and eddies with length scales spanning 10s–100s m and frequencies less than 0.04 Hz [*Spydell et al.*, 2007, 2009]. Wave-breaking-forced eddies may be generated by wave-group driven alongshore radiation stress gradients [*Haller et al.*, 1999; *Reniers et al.*, 2004; *Long and Özkan Haller*, 2009] and individual breaking waves [*Peregrine and Bokhove*, 1998; *Peregrine*, 1999]. Evidence from field observations suggests that horizontal eddies with a broad distribution of length scales are ubiquitous on alongshore-uniform beaches [*Noyes et al.*, 2005; *Spydell and Feddersen*, 2009; *Hally-Rosendahl et al.*, 2015]. In tandem, numerical model results suggest that individual breaking waves with finite crests are responsible for the observed eddy field [*Feddersen*, 2014]. Crucially, eddies generated by individual wave breaking with finite crests are hypothesized to evolve within the surf zone, leading to larger-scale rotational motions that can enhance transient rip-current-driven cross-shore exchange [*Peregrine*, 1998; *Spydell et al.*, 2007; *Spydell and Feddersen*, 2009; *Feddersen*, 2014]. However, the processes connecting the wave field to eddies that can eject material from the surf zone into deeper waters remain poorly

understood.

Directionally spread waves inject vorticity into the surf zone. Wave directional spread – the directional distribution of wave energy around the mean angle – is a significant source of wave-field spatially inhomogenous amplitudes [*Longuet-Higgins*, 1957]. On nearly alongshore-uniform beaches where bathymetric variability contributions are smaller, wave directional spread is the primary source of wave amplitude variability along the coast. As waves propagate into shallow water, the largest amplitude sections of the waves break first, resulting in breaking along finite lengths, known as short-crested wave breaking. Based on theory [*Peregrine*, 1998; *Peregrine and Bokhove*, 1999], numerical modeling [*Bühler and Jacobson*, 2001; *Spydell et al.*, 2009; *Wei et al.*, 2017; *Kirby and Derakhti*, 2019], and limited observations [*Clark et al.*, 2012; *Choi and Roh*, 2021], the gradient in wave dissipation along a wave crest may generate rotational motions at lower frequencies than the momentum from waves. Positive and negative vertical vortices – counter-clockwise and clockwise horizontal eddies, respectively – are hypothesized to be generated near crest ends due to the along-crest gradient in the wave breaking force [scales with dissipation over bore speed, Figure 3.1a, *Bühler*, 2000; *Bonneton et al.*, 2010; *Kirby and Derakhti*, 2019; *Clark et al.*, 2012; *Feddersen*, 2014]. The largest vorticity-injection-forcing may occur in the regions with the most wave dissipation [*e.g.,* bars crests or the shore face, *Feddersen*, 2014]. The length scales of wave-breaking-injected vertical vorticity, termed "vorticity injection" here, are not known, but numerical modeling studies suggest that injection lengths may scale with the width of the breaking region [*Kirby and Derakhti*, 2019] and vary with directional spread [3.1b, *Spydell and Feddersen*, 2009]. In one field experiment, the breaking force was parameterized to estimate vorticity injection based on a single estimate of wave height, water depth, and an assumed alongshore length scale [*Clark et al.*, 2012]. Parameterized injected vorticity was consistent with measured vorticity near crest ends for regions with intense dissipation, but was larger than measured values when the array was positioned at other regions of the surf zone [*e.g.,* a bar trough *Clark et al.*, 2012]. To date, no observations exist of the gradient in the breaking force along an entire wave crest (Figure 3.1a), nor the associated forcing length

scales of short-crested-wave-vorticity for individual breakers (Figure 3.1b), or their dependence on wave field characteristics. Further examination of the wave forcing is necessary to understand the vorticity injection length scales and circulation as well as the implications for vorticity evolution within the surf zone.

Vorticity evolves within the surf zone. Once injected into the water column, vortices may interact with other vortices, waves, mean currents, and bathymetry, resulting in a complex multi-scaled eddy field. Bores propagating shoreward may theoretically continue to inject same-signed vorticity at each crest end, interacting with the trailing vorticity strip [*e.g.,* the rolling up vorticity strip in Figure 3.1b, *Peregrine*, 1999; *Bühler and Jacobson*, 2001]. In an irregular wave field, successive individual waves and wave trains may inject vorticity at different locations along the beach, interacting with the vorticity field generated from previous bores or neighboring bores along the beach [Figure 3.1b, *Johnson and Pattiaratchi*, 2006]. Remarkably, this seemingly random forcing by shore-normal directionally spread waves may lead to more organized, coherent eddies [*Johnson and Pattiaratchi*, 2006].

Energy from wave-breaking-injected vorticity is hypothesized to non-linearly transfer to lower-frequency, larger-scale horizontal motions, similar to a forced two-dimensional turbulence system [*e.g.,* Figure 3.1c *Bühler and Jacobson*, 2001; *Spydell and Feddersen*, 2009; *Feddersen*, 2014; *Elgar and Raubenheimer*, 2020; *Marchesiello et al.*, 2021a]. Energy associated with low-frequency rotational motions have been shown to increase with increasing wave-field directional spread and were larger than offshore of the surf zone [*Spydell et al.*, 2007, 2009; *Spydell and Feddersen*, 2009; *Feddersen*, 2014; *Spydell*, 2016; *Elgar and Raubenheimer*, 2020], consistent with the hypothesis that short-crested wave breaking may lead to greater low-frequency eddy activity. These large scale eddies enhance dispersion within the surf zone [*Spydell and Feddersen*, 2009; *Clark et al.*, 2010, 2011; *Feddersen et al.*, 2011; *Feddersen*, 2014; *Hally-Rosendahl and Feddersen*, 2016] and pairs of adjacent, counterrotating surfzone eddies may mutually-advect offshore with a jet-like ejection as a transient rip current [Figure 3.1c *Johnson and Pattiaratchi*, 2004a, b; *Kumar and Feddersen*, 2017c, a], enhancing exchange between the surf zone and the inner shelf [*Suanda and Feddersen*, 2015]. Despite

the relevance of an inverse energy cascade mechanism within the surf zone, there are a limited number of modeling studies [*Spydell and Feddersen*, 2009; *Feddersen*, 2014; *Marchesiello et al.*, 2021a] and a single observational study [*Elgar and Raubenheimer*, 2020] assessing the dynamical relevance of a two-dimensional turbulence system for surfzone processes.

Here, we seek to characterize the processes connecting the incident waves to low-frequency surfzone eddies by addressing the following questions:

1. How does the breaking force vary along an individual wave crest (Figure 3.1a)?

2. What are the vorticity injection length scales driven by breaking waves (Figure 3.1b)?

3. Is there a nonlinear transfer of energy from breaking-wave-injected vorticity to larger scale, low-frequency eddies within in the surf zone (Figure 3.1c), and if so, over what length scales (Figure 3.1d)?

To address these questions, we performed experiments in a laboratory wave basin with a multi-directional wave field. The relationship between incident waves and breaker properties was assessed previously in *Baker et al.* [in review]. Here, we apply findings about the remotely sensed short-crested wave field to estimate vorticity injection by along-crest variability in breaker dissipation and eddy evolution within the surf zone. In Section 3.2, we describe theory pertaining to two-dimensional turbulence dynamics and vorticity-injection-forcing via individual breaking waves. Section 3.3 describes the experimental setup and observations used to address the posed questions. Results assessing the along-crest variability in the breaking force, vorticity injection length scales, and low-frequency eddy activity in the surfzone are in Section 3.4. Section 3.5 discusses connections between the short-crested breaking wave generated eddies and large-scale rotational motions. A brief summary and conclusions are in Section 3.6. Through this body of work, we provide a better understanding of the dispersion and transport of pollutants, larvae, and other passive material within the nearshore and provide key insights into the mechanisms leading to transient rip current formation.

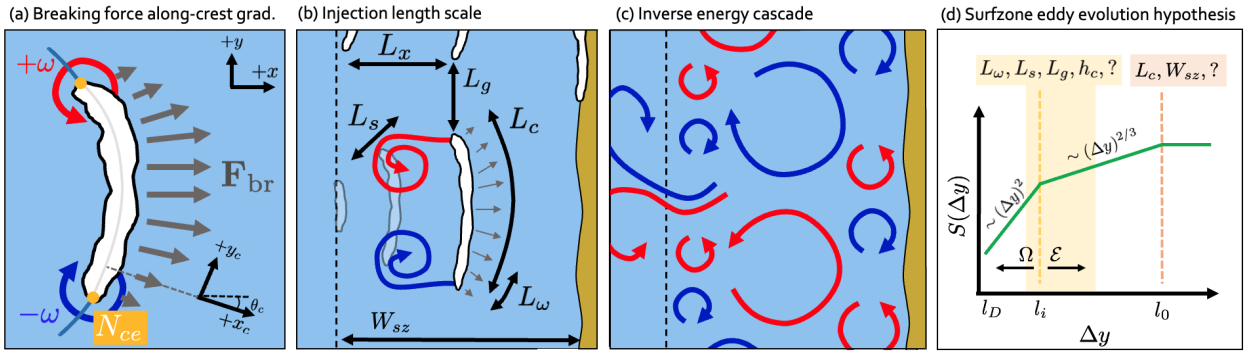

Figure 3.1: Schematic of the hypothesized vorticity injection and evolution within the surf zone. (a) The along-crest (y_c) variability in the breaking force ($\mathbf{F_{br}}$, grey arrows) in the direction of wave propagation (x_c) at an angle θ_c relative to the fixed cross-shore coordinate (x) of a short-crested breaking wave (white feature) generates negative (blue) and positive (red) vertical vorticity (ω) near crest ends, where N_{ce} is the number of crest ends. (b) The length scale over which there is an along-crest gradient in the breaking force (L_ω) may be related to vorticity injection length scales (a), the crest length (L_c), spacing between proximal crests (L_g), wavelength (L_x), vortex length (L_s), and the surfzone width (W_{sz}). (c) Energy associated with wave-breaking-injected vorticity may be non-linearly transferred to larger-scale rotational motions (curled arrows) and counter-rotating eddies may mutually advect offshore, exiting the surf zone as a transient rip current (arrows offshore of black dashed line). (d) In a forced two-dimensional turbulence system, the second-order alongshore velocity structure function ($S(\Delta y)$, green curve) has two inertial ranges separated by the vorticity injection length scale (l_i): the direct enstrophy (Ω) cascade from dissipation length scales (l_D) to l_i with the spectral scaling $\sim (\Delta y)^2$, and the inverse energy (ε) cascade from l_i to the maximum length scales of the system (l_0) with the scaling $\sim (\Delta y)^{2/3}$. The length scales associated with these inertial regions may be altered by the processes in (b) as well as the bore depth (h_c).

3.2 Vorticity dynamics in the surf zone

Surfzone eddies with horizontal length-scales much larger than the water depth are hypothesized to evolve analogously to vorticity in a forced two-dimensional turbulence system in shallow waters [*Peregrine and Bokhove*, 1998; *Spydell and Feddersen*, 2009; *Feddersen*, 2014; *Elgar and Raubenheimer*, 2020]. These eddies may become quasi-two-dimensional in the outer edge of the surf zone, particularly for the highest frequency rotational motions [*Lippmann and Bowen*, 2016; *Henderson et al.*, 2017; *Baker et al.*, 2021]. Although certain aspects of the turbulence are still governed by two-dimensional turbulence dynamics in a quasi-two-dimensional turbulence system, vortex tilting, vortex stretching, and vertical diffusion may lead to more rapid decay of eddies than expected for solely two-dimensional eddies [*Uchiyama et al.*, 2017; *McWilliams et al.*, 2018]. For simplicity, in our study focused on the surf zone we emphasize flow kinematics often used to characterize a forced two-dimensional turbulence system. In particular, we seek to test the hypothesis that surfzone eddy energy is non-linearly transferred from small spatial scales characterized by wave breaking properties to large spatial scales through an inverse cascade. This section begins with a brief review of two-dimensional turbulence dynamics and then provides a theoretical framework for characterizing surfzone vorticity length scales and circulation.

The depth-averaged horizontal momentum equation for an incompressible fluid with horizontal velocities ($\boldsymbol{u} = [u(x, y, t), v(x, y, t)]$) assuming constant atmospheric pressure is:

$$\frac{\partial \boldsymbol{u}}{\partial t} + \boldsymbol{u} \cdot \nabla \boldsymbol{u} + \frac{1}{\rho} \nabla p = \mathbf{F_{br}} + \mathbf{F_s} \tag{3.1}$$

where t is time, ρ is a constant density, and p is the pressure, including hydrostatic and hydrodynamic contributions. The right-hand-side terms are body forces, such as the depth-averaged wave breaking external force ($\mathbf{F_{br}}$) and a sink term ($\mathbf{F_s}$) representing friction (*e.g.,* $\frac{\tau_b}{h}$, the bottom stress normalized by water depth, h) and viscous forces (*e.g.,* $\nu \nabla^2 \boldsymbol{u}$, where ν is the kinematic viscosity). Assuming that the flow is primarily two dimensional (*i.e.,* neglecting vortex stretching and tilting), the momentum equation can be rewritten for the scalar vertical vorticity field, $\omega = \nabla \times \boldsymbol{u}$ [*Salmon*, 1998; *Kellay and Goldburg*, 2002;

Boffetta and Ecke, 2012]:

$$\frac{\partial \omega}{\partial t} + \boldsymbol{u} \cdot \nabla \omega = \nabla \times [\mathbf{F_{br}} + \mathbf{F_s}] \tag{3.2}$$

where $\frac{\partial \omega}{\partial t}$ is the tendency term, representing the time rate of change of vorticity and $\boldsymbol{u} \cdot \nabla \omega$ is the vorticity advection, which is responsible for non-linearly spreading turbulent fluctuations to other length scales. The rotational components of the body forcing terms are retained on the right-hand-side.

For a forced, steady, strictly two-dimensional turbulence system, vorticity is continually injected at an intermediate scale at length (l_i) by external rotational forcing (*e.g.,* $\nabla \times \mathbf{F_{br}}$ in Eqn. 3.2). In three-dimensional turbulence, vortex stretching and strain self-amplification result in a forward energy cascade from l_i to smaller length scales [*Tsinober and Madylam*, 2009], where energy is eventually dissipated by viscous forces. However, in two-dimensional turbulence, there is no axis perpendicular to the flow and thus, vortex stretching is absent [*Kellay and Goldburg*, 2002]. Instead, energy is non-linearly transferred from l_i to larger scales by an inverse energy cascade and eventually constrained by the size of the system at length scale l_0. Vorticity gradients, however, are not bounded in two-dimensions, enabling a direct cascade of enstrophy ($\Omega = \frac{1}{2}\langle \omega^2 \rangle$, spatial average of vorticity squared) from l_i to smaller length scales (l_D), where the enstrophy is dissipated by viscous forces. In the surf zone, it is hypothesized that the wave-breaking-injected vortices with length scales at or near l_i [*Spydell and Feddersen*, 2009] may either dissipate due to bottom friction [*Feddersen*, 2014] and viscous forces at relatively small length scales l_D. Otherwise, energy associated with injected vortices may be non-linearly transferred to longer length scales (l_0) that are constrained by the surf zone geometry (*e.g.,* the surfzone width, W_{sz}) or that eject offshore as a transient rip current (Figure 3.1d).

Over the two inertial ranges with lengths of $l_0 < l < l_i$ and $l_i < l < l_D$, specific spectral scalings are expected. As implemented in previous idealized two-dimensional turbulence experiments [*Smithr and Yakhot*, 1994; *Boffetta et al.*, 2000; *Kellay and Goldburg*, 2002] and studies of the surf zone [*Spydell and Feddersen*, 2009; *Elgar and Raubenheimer*, 2020], structure functions can be used to investigate two-dimensional flow characteristics, including

classifying the direct enstrophy cascade and inverse energy cascade inertial ranges. Here, we write the second-order alongshore structure function ($S(\Delta y)$) in terms of the instantaneous alongshore velocity (v) as a function of the alongshore position (y):

$$S(\Delta y) = \langle [v(y + \Delta y) - v(y)]^2 \rangle \tag{3.3}$$

where Δy is the spatial lag between observations and $\langle \cdot \rangle$ is the temporal average. By dimensional arguments similar to Kolmogorov's derivation for 3D turbulence [*Kraichnan*, 1967], the structure function for both initial ranges are expected to follow [*Kellay and Goldburg*, 2002]:

$$\begin{aligned} \text{inverse energy cascade}: &\quad S(\Delta y) \sim (\epsilon \Delta y)^{2/3}, \quad l_0 > \Delta y > l_i \\ \text{direct enstrophy cascade}: &\quad S(\Delta y) \sim \beta^{2/3} (\Delta y)^2, \quad l_i > \Delta y > l_D \end{aligned} \tag{3.4}$$

where β is the enstrophy injection rate, $\beta = \frac{d\Omega}{dt}$, and ϵ is the energy injection rate, $\epsilon = -\frac{d\mathcal{E}}{dt}$ with kinetic energy per unit mass, $\mathcal{E}$. These structure function scalings are analogous to those derived for energy-wavenumber spectra ($E(k)$), where the inverse energy cascade scales with $E(k) \sim k^{-3}$ and the enstrophy cascade scales with $E(k) \sim k^{-5/3}$. Above the largest length scale of the flow (l_0), velocities are uncorrelated and the structure function asymptotes to a constant that is twice the velocity variance. The transitional regime between the inverse energy cascade and the enstrophy cascade may indirectly provide evidence of the injection length scales [*Spydell and Feddersen*, 2009; *Elgar and Raubenheimer*, 2020]. Alternatively, the rotational component of the external forcing can be directly computed on a wave-by-wave basis to assess vertical vorticity injection length scales.

In a directionally spread wave field, the curl of the spatial inhomogeneity in the wave dissipation drives rotational currents. From Eqn. 3.2, the effect of the short-crested breaking waves on the time-rate of change in vertical vorticity (ω) at vorticity injection scales can be approximated as the gradient of the depth-averaged breaking force ($\mathbf{F_{br}}$):

$$\frac{\partial \omega}{\partial t} \approx \nabla \times \mathbf{F_{br}} \approx -\frac{\partial \mathrm{F}_{\mathrm{br},x_c}}{\partial y_c} \tag{3.5}$$

where advection and sink terms (*e.g.,* bottom stress) are assumed to be small [*Spydell and Feddersen*, 2009; *Clark et al.*, 2012]. As the breaking force is in the direction of wave propagation (x_c), the along-crest (y_c) component of the breaking force ($\mathrm{F}_{\mathrm{br},y_c}$) may be considered negligible (*i.e.,* $\frac{\partial \mathrm{F}_{\mathrm{br},y_c}}{\partial x_c} \approx 0$). Here, the crest coordinate system (x_c, y_c) is related to the cross- and alongshore coordinate system by a local, along-crest varying breaker angle (θ_c, Figure 3.1a). Thus, in the crest-following coordinate system, vorticity is generated due to the along-crest gradient in the cross-crest component of the breaking force (Eqn. 3.5, right).

Theory suggests that the breaking force in the direction of wave propagation ($\mathrm{F}_{\mathrm{br},x_c}$) can be approximated as the dominant component of radiation stress ($S_{x_c x_c}$) divergence in breaking waves [*Dingemans et al.*, 1987; *Bühler and Jacobson*, 2001]:

$$\mathrm{F}_{\mathrm{br},x_c}(y_c) = \frac{1}{h}\frac{dS_{x_c x_c}(y_c)}{dx_c} = \frac{1}{\rho_w h}\frac{d}{dx_c}\frac{3}{2}E(y_c) \tag{3.6}$$

where $E(y_c)$ is the wave-averaged energy at a given along-crest position and ρ_w is the water density. For the small discrete section of crest propagating at angle θ_c, the off-diagonal component of the radiation stress (*e.g.,* $S_{x_c y_c}$) is zero and the flux of momentum occurs in the direction of wave propagation, x_c. Similar to previous studies, the spatial derivative can be transformed to the temporal derivative using the bore velocity (c_b) [*Bonneton et al.*, 2010; *Clark et al.*, 2012]. Thus, for an individual breaker, $\mathrm{F}_{\mathrm{br},x_c}$ can be approximated at a given along-crest position as:

$$\mathrm{F}_{\mathrm{br},x_c}(y_c) = \frac{1}{\rho_w h c_b}\frac{d}{dt}\frac{3}{2}E(y_c) = \frac{3}{2}\frac{D(y_c)}{\rho_w h c_b} \tag{3.7}$$

where the $D(y_c)$ is the wave-averaged dissipation for a given along-crest position (*i.e.,* $E = dD/dt$). Note that this result extends the derivation in *Clark et al.* [2012], which assumed waves were shore-normal and did not consider along-crest variability in the crest orientation.

The along-crest dissipation profile can be estimated with Duncan's wave roller dissipation model [*Duncan*, 1981]. This approach relates the dissipation of wave energy to the shear stress exerted by the wave roller along the sloping front face of the underlying wave. The shear stress (τ_r) in the direction of wave propagation can be expressed as the weight of the

aerated bore with a cross-sectional area (A) and a density (ρ_r):

$$\tau_r = \rho_r g A sin\theta_r \tag{3.8}$$

where θ is the roller angle (Figure 3.2). For a fully developed breaking and steady state wave, the geometry of the breaking region is empirically self-similar as the wave propagates shoreward. Laboratory observations suggest that the ratio of the average breaker thickness (A/L_r) to the roller length (L_r) is approximately 0.11 ± 0.01, such that $A = 0.11 L_r^2$ [*Duncan*, 1981]. Thus, the wave-averaged dissipation (D) due to breaking corresponds to the shear stress (τ_r) over the wave period (T):

$$D = \frac{\tau_r}{T} = \frac{1}{T} 0.11 \rho_r g L_r^2 \sin\theta_r \tag{3.9}$$

where T is the wave period. Duncan's wave roller model has been employed in many studies to approximate roller dissipation due to wave breaking in a steady state bore [*Dally and Brown*, 1995; *Lippmann et al.*, 1996; *Walstra et al.*, 1997; *Ruessink et al.*, 2001; *Carini et al.*, 2015; *Flores et al.*, 2016; *Haller and Catalán*, 2009], including a study extracting crest characteristics from a cross-shore scanning LiDAR [*Martins et al.*, 2018].

Another approach to assess vorticity injection at a specific length scale is with the Kelvin Circulation theorem [*Peregrine*, 1998; *Peregrine and Bokhove*, 1999; *Peregrine*, 1999; *Pizzo and Melville*, 2013], which may be favorable to measure vorticity directly [*Clark et al.*, 2012]. Regardless of the approach to assess vorticity injection, it is anticipated that the along-crest non-uniformity in dissipation rate or the breaking force over an along-crest length scale L_ω may be largest near the ends of breakers [*Peregrine and Bokhove*, 1998; *Peregrine*, 1999], where there may be an abrupt demarcation between the breaking crest and an unbroken water surface. Nevertheless, low-frequency surfzone eddies may be governed by a broader distribution of injection scales than solely described by L_ω (Figure 3.1b,d).

Although examining the length-scales of L_ω is the primary focus here, the following processes may alter vorticity injection and evolution (Figure 3.1a). The crest length (L_c) and spacing between proximal crests (L_g) varies as the bore propagates shoreward, where

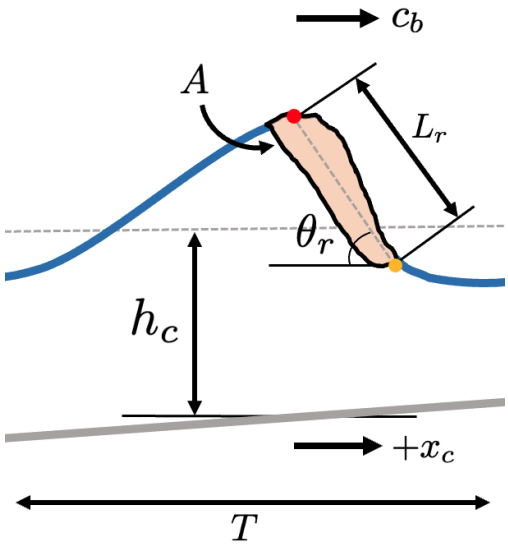

Figure 3.2: Schematic of the cross-crest profile (x_c) of a broken wave. The cross-sectional area of the aerated breaker (A) was approximated from the angle (θ_r) from horizontal at the toe of the breaking wave (yellow dot) to the crest (red dot) and roller length (L_r). The cross-wave extent of the aerated bore was identified with the RBIS method (orange region in Figure 3.4). The average depth (h_c) at the crest is the difference between the mean water elevation (dashed grey) and seafloor (solid grey) below the crest of the breaker. The wave period (T) is the time between the trough preceding and following the breaking wave, and the bore celerity (c_b) is the speed in the cross-wave direction.

they may continue to inject the same-signed vorticity at different locations, resulting in a vortex strip that can roll up with scales (L_s). The number of crest ends (N_{ce}) may limit the number of injection sites. Maximum length scales may be limited by the surfzone width (W_{sz}), while minimum length scales may be limited by the water depth (h_c), because eddies with length scales less than this are not two-dimensional. The wavelength, L_x, also may be an important scale, governed by wave period and water depth. For the same wave height and period, our previous study found that the crest length decreases and number of breaking crest ends increases with directional spread [*Baker et al.*, in review]. Therefore, the directional

spread (σ_θ) alters the number and distribution of locations where vorticity is generated within the surf zone. However, the role of these mechanisms in surfzone vorticity dynamics remains unknown. We advance our understanding of these processes by examining the along-crest variability in the breaking force.

3.3 Laboratory observations

3.3.1 Experimental setup and in situ sensors

Laboratory experiments were performed in the Directional Wave Basin at the O.H. Hinsdale Wave Research Laboratory (HWRL), Oregon State University, USA. The basin dimensions are 48.8 m in the cross-shore direction, 26.5 m in the alongshore direction, and up to 2 m deep. The origin of the basin coordinate system is centered along the width of the basin at the bottom of the wavemaker. The positive coordinate in the cross-shore (x) is to the west toward the beach, alongshore (y) is toward the south (right handed coordinate system), and elevation (z) is upward from the base of the basin. The basin bathymetry was configured with a flat region from $x = 0 - 22$ m ($z = 0$ m) and a planar $1 : 10$ sloping beach from $x = 22 - 48.8$ m. An alongshore-uniform concrete bar with a triangular cross-section rested on the metal slope and extended from $x = 25.4 - 29.2$ m with a 0.30-m tall apex (Figure 3.3). The water depth (h) of the bar crest was $h = 0.19$ m when the basin still water level was set to $h = 1.07$.

The piston-type wavemaker consisting of 29 segments can simulate multidirectional wave fields following second-order multi-directional wavemaker theory [*Schäffer and Steenberg*, 2003]. The wave field was generated using a JONSWAP spectrum given a significant wave height (H_s), peak wave period (T_p), and a spectral width gamma parameter set to 3.3 [*Hasselmann et al.*, 1973] and a $\cos^{2s}$ directional distribution from a mean wave angle (θ) and directional spread (σ_θ). Wave conditions offshore of the toe of the beach slope ($x = 19.0$ m and $x = 20.4$ m) were measured with 15 surface-piercing wire resistance gauges (Figure 3.3, squares). Trials are reported in terms of the offshore wave conditions estimated from

a sub-sampled array of the wire resistance gauges (x = 19.0 m and 20.4 m) from minute 15–25 of each 45-min trial (Table 3.1, grouped by wave heights less than or greater than 0.25 m). The offshore H_s varied from 0.22–0.30 m, where the onset of breaking typically occurred just offshore of or near the bar crest ($x = 27.1 - 28.2$ m), and T_p was 2 s. Wave conditions were near shore-normal ($\theta \approx 0°$) with directional spreads ranging from narrow to large ($\sigma_\theta = 2 - 30°$). More details about the experimental setup and methods to compute offshore wave conditions are described in *Baker et al.* [in review].

On the beach slope, near-bed pressure and velocities were measured with a 12-sensor array of colocated pressure gauges and Acoustic Doppler Velocimeters (ADVs, Vectrino Profilers) mounted about 0.05-m above the bed. Colocated sensors were first deployed in two alongshore transects in the surf zone (x = 28.4 m and 30.7 m, $y = -8.2$ m to 3.2 m, Figure 3.3, blue and pink circles) and then re-deployed for repeated wave conditions in the inner shelf (Figure 3.3, red and black circles). The inner-shelf array consisted of an alongshore transect spanning the width of the tank ($y = -9.8$ m to 9.7 m) just offshore of the surf zone (x = 26.6 m) and the vertically stacked sensors farther offshore ($x, y = 24.5, -0.1$ m). All in situ sensors synchronously sampled at 100 Hz. In situ calibration, quality control, and surveying details are described in *Baker et al.* [in review].

3.3.2 Remotely-sensed water surface elevation and crest features

Three cameras mounted to the building ceiling (x = 47.0 m) captured images at 8 Hz with overlapping fields of view. The center camera ($y, z = 0.0, 10.1$ m) was pointed in the offshore direction with an oblique view of the water surface from the shoreline to the bridge (268.8° azimuth, 22.8° tilt, 0.1° roll). The camera resolution of the basin water surface ranged from 0.05 cm in the surf zone to 2 cm near the bridge. The geometry of each camera was computed from known locations on the beach, bridge, and side walls. Stereo processing techniques were applied to 8-Hz trinocular camera imagery to reconstruct the water surface elevation at 1-cm resolution in the surf zone (x = 27 to 35 m, $y = -13.3$ to 13.3 m), the region where sufficient surface features for stereo processing were persistent [*Baker et al.*, in review].

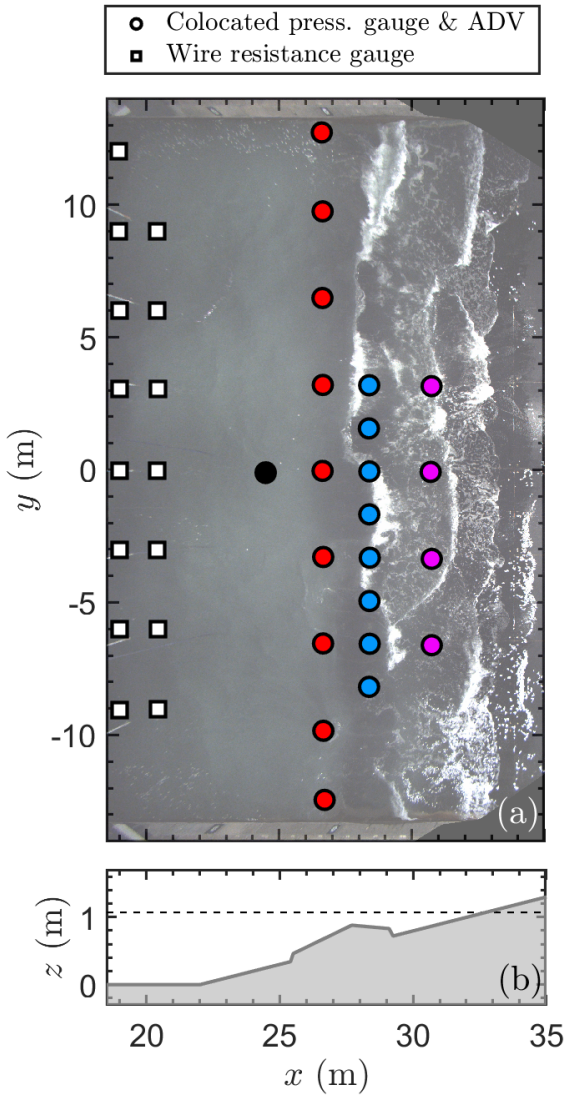

Figure 3.3: (a) Plan view of the cross-shore (x) and alongshore (y) location of the surfzone (pink and blue circles) and inner-shelf (red and black circles) arrays of colocated pressure (press.) gauges and Acoustic Doppler Velocimeters (ADVs) and the offshore wire resistance gauges (white squares). The opaque color image in the background is a rectified image from trial *G1d* ($\sigma_\theta = 26°$) from the center ceiling-mounted camera. (b) The cross-shore profile of the elevations (z) of the seafloor (shaded) and mean water level (dashed, $z = 1.07$ m).

Table 3.1: Wave conditions measured onshore of the wavemaker at the wire resistance gauges (Figure 3.3), including the significant wave height (H_s), peak period (T_p), mean wave angle (θ), and directional spread (σ_θ). The offshore edge of the surf zone (x_{sz}) was estimated from the LiDAR cross-shore profiles.

Trial	H_s (m)	T_p (s)	$\theta(^\circ)$	σ_θ ($^\circ$)	x_{sz} (m)
G1a	0.28	2.1	-0.1	2.4	27.1
G1b	0.27	2.0	0.4	16.8	27.3
G1c	0.26	2.0	-5.9	25.2	27.3
G1d	0.27	2.0	-3.3	26.1	27.3
G2a	0.25	2.0	0.2	2.4	27.2
G2b	0.23	2.0	-1.0	9.6	27.4
G2c	0.22	2.0	0.8	18.3	27.6
G2d	0.24	2.0	4.8	24.2	27.6

For crest identification and Particle Image Velocimetry (PIV) processing, images from the center camera were rectified into HWRL coordinates with the stereo-processing-resolved solution for intrinsic and extrinsic parameters and the z-elevation from reconstructed surface elevation maps in the surf zone and set to the still water elevation offshore. Individual breaking wave crests in each frame were identified with the Remote Breaker Identification Scheme [RBIS, *Baker et al.*, in review], a method designed to detect active breaking and exclude residual foam. RBIS extracts regions encompassing breakers based on regions that exceed an intensity threshold of 0.2 applied to visible-band imagery and also an elevation-based breaking-gamma threshold of 0.2 applied to stereo reconstructions.

3.3.3 Remotely-sensed surface velocities

In the surf zone, foam and bubbles generated by wave breaking result in bright features in visible-band imagery that contrast with darker non-breaking regions. The conspicuous signal of an active breaker has been used to estimate phase-velocity, energy dissipation, and other crest characteristics [*Puleo et al.*, 2003; *Holman and Haller*, 2013; *Díaz et al.*, 2018; *Carini et al.*, 2021; *Sáez et al.*, 2021]. The residual foam following an active breaker advects with surface currents, often imparting a rich signal to track mean alongshore currents [*Chickadel et al.*, 2003; *Perkovic et al.*, 2009; *Almar et al.*, 2016] and mean velocities [*Anderson et al.*, 2021].

Here, highly-resolved horizontal, surface velocities were derived by tracking shifts in coherent surface texture (tracer such as bubbles generated during active breaking, residual foam, and wiffle balls) across a sequence of visible-band images with a feature-based PIV technique developed by *Chickadel et al.* [2011]. PIV was performed on the 8 Hz, 1-cm resolution rectified imagery from the center camera for a field of view spanning the width of the tank ($y = -13.3$ m to 13.3 m) from the shoreline to just offshore of the surf zone ($x = 25$ to 33.5 m). This PIV technique uses a phase correlation between image pairs to better refine feature motion given large-scale background variation [*Adrian*, 2005]. Sub-pixel refinement was achieved by computing the peak of a two-dimensional Gaussian fit to the phase map [*Eckstein et al.*, 2008]. A multi-pass approach with decreasing interrogation windows and 50% overlap started with 256 x 256 pixels, followed by 128 x 128 pixels, 64 x 64 pixels, 32 x 32 pixels, and culminated with 16 x 16 pixels. This resulted in an 8 Hz timeseries of cross- (u) and alongshore (v) velocities with an effective spatial resolution of 8 cm in the cross- and alongshore. Velocity estimates were omitted if the signal to noise ratio fell below 0.68, indicative of insufficient image contrast for optimal PIV performance.

PIV-derived velocity signals were comprised of processes spanning frequency and spatial scales, including breaker celerity and low-frequency horizontal motions. Low-frequency PIV velocities ($f < 0.2$ Hz) were used to analyze surfzone eddy processes. To reduce contamina-

tion of the low-frequency signal by surface-gravity waves, regions encompassing crest features identified with RBIS in the subsequent frames and enlarged by 20-cm on all sides were removed from the PIV instantaneous estimates. The remaining PIV velocities were filtered with a time-space moving median filter over 8 s and 24 cm in the cross- and alongshore direction (9-point spatial median). Grid locations with PIV observations less than 50% of the time were omitted. For comparisons between surface and in situ velocities, in situ observations were also median filtered over 8 s (Appendix 3.7). After filtering, there were few gaps without PIV velocities within the surf zone ($< 5\%$ for the inner surf zone and $<15\%$ in the outer edge of the surf zone). Vorticity was estimated from gridded low-frequency velocity components from PIV using a central-difference approach [*Patankar*, 1980]. For coherence estimates between the PIV and in situ sensors, the auto-spectra and cross-spectra from the cross- and alongshore velocities were computed using a Hanning window period of 64 s with an overlap period of 32 s over the 10-min time series (degrees of freedom, DOF = 25). For spectral analyses, missing measurements in the PIV velocities were filled via linear interpolation.

Median filtered surface PIV velocities were correlated with 8-s median bottom mounted ADV velocities at the nearest PIV-resolved location (Appendix 3.7), with higher correlations (r) in the inner surf zone than outer surf zone due to the more dense, temporally persistent foam in the inner surf zone and higher signal-to-noise ratios (*e.g.,* alongshore velocities for trial *G2d*: outer surf zone $r = 0.41$, inner surf zone $r = 0.82$). Root-mean-squared-deviations (RMSDs) between PIV and in situ sensors were smaller for alongshore velocities than cross-shore velocities, likely due to an onshore bias in cross-shore velocities introduced by bright breaking waves (*e.g.,* trial *G2d* inner surf zone– RMSD: $u = 0.08$ m/s, $v = 0.05$ m/s, bias: $u = 0.02$ m/s, $v = 0$ m/s). Additionally, PIV velocities were more coherent at low-frequencies, especially for the alongshore velocity component (Figure 3.19). Overall, given potential differences due to different sampling locations in the water column, the surface velocity estimates with PIV agree reasonably well with near-bottom in situ estimates at low-frequencies and are viable for analyses of eddy processes. See Appendix 3.7 for de-

tailed comparisons between the PIV and in situ velocities and discussion on PIV-estimate sensitivities to different median filter designs.

3.3.4 Breaking force estimates

The wave-by-wave along-crest profile of the breaking force (F_{br,x_c}, Eqn. 3.7) for each breaking wave crest was estimated with wave geometric and kinematic properties from sea-surface elevation maps and surface velocities. For each RBIS-identified breaking crest, a local crest coordinate system was defined based on the local crest angle (θ_c), estimated as the curvature of the roller toe, the onshore edge of the identified crest regions (dy = 5 cm) with a 45-cm moving along-crest average. The along-crest coordinate, as opposed to the alongshore coordinate, was used to account for breakers with crescent shapes or obliquity. The following procedure to estimate the along-crest profile of the wave energy dissipation and breaking force was completed at locations along each wave crest with an angle θ_c at 5-cm alongshore spacing for each identified wave crest in the surf zone ($27 < x < 31.5$ m) over an approximately 10 min time series (15-25 min).

Along-crest wave-averaged dissipation was estimated with Duncan's roller model (D, Eqn. 3.9) based on remotely-sensed roller properties. The roller density was set to 60% of the density of fresh water [*i.e.,* $\rho_r/\rho_w = 0.6$, *Duncan*, 1981]. Roller geometry was extracted from cross-wave transects (Δx_c = 5 cm) of the sea-surface elevation from 5-cm resolution stereo reconstructions. Each transect extended 2-m offshore and 1-m onshore of the roller toe at an angle θ_c relative to the cross-shore axis (black cross-wave transects in Figure 3.4a,c). The bore crest was the highest elevation measured onshore of the first zero-crossing of the cross-crest sea-surface elevation slope (*i.e.,* the trough offshore of the bore). The roller and crest elevation were smoothed with a 0.35-cm median filter along the wave crest. The height of the bore ($L_{r,y}$) was estimated as the distance between the elevation of the roller and crest, and the plan view length of the bore ($L_{r,x}$) was the distance along the transect between the roller toe and crest. Thus, the roller length and angle were readily computed as $L_r = \sqrt{(L_{r,x})^2 + (L_{r,y})^2}$ and $\theta_r = \arctan(L_{r,y}/L_{r,x})$ (see Figure 3.2). The wave

period for each identified crest was computed as the time between the trough preceding and following the roller. To determine this, 2-s sea-surface elevation timeseries centered at the instantaneous snapshot were extracted at the locations of the roller toe along the wave crest. The troughs preceding and following the roller were the first zero crossings of the along-crest average slope of the sea-surface elevation before and after the roller.

For the breaking force calculation ($\mathrm{F}_{\mathrm{br},x_c}$, Eqn. 3.7), the mean water depth (h) was estimated as the average difference between the tank floor and the mean sea-surface elevation in stereo reconstructions across the roller. To estimate the bore celerity (c_b) along each crest, the 8-cm resolution PIV cross- and alongshore velocities from the preceding and current frame were extracted over a region 50 cm offshore of the crest and 15 cm on either side of the position y_c. The velocities were rotated into the local crest coordinate system with the angle θ_c, and cross-crest velocities below 30 cm/s were omitted. Then, the bore celerity at a given along-crest position was approximated as the average of the largest 5% of cross-crest velocities. See comparisons between PIV-derived bore celerity and solitary wave theory estimates in Appendix 3.7.

Along-crest gradients in the breaking force are sensitive to noise in the breaking force estimates. Therefore, the roller length, angle, mean water depth, and bore celerity were sub-sampled as the median every 15 cm and smoothed via a 45-cm moving average prior to computing the dissipation with Eqn. 3.5 and the breaking force with Eqn. 3.7. Given the assumption that zero dissipation occurred outside of extended crest region, the breaking force was padded by zeros on both ends of the crest. Finally, the along-crest gradient in the breaking forces was computed along each crest ($\partial \mathrm{F}_{\mathrm{br},x_c}/\partial y_c$), which is approximately equal to the time rate of change vorticity ($\partial\omega/\partial t$ from Eqn. 3.5).

The 'total external vorticity forcing per wave' was computed as the sum of the absolute value of the along-crest gradient of the breaking force from the average along-crest profile ($N_c^{-1}\sum|\partial \mathrm{F}_{\mathrm{br}}/\partial y_c|$). The 'total external vorticity forcing per surf zone' ($\sum|\partial \mathrm{F}_{\mathrm{br}}/\partial y_c|$) was the sum of all the total external vorticity forcing per wave crests per snap shot in time, yielding a 10-min timeseries of estimates per trial.

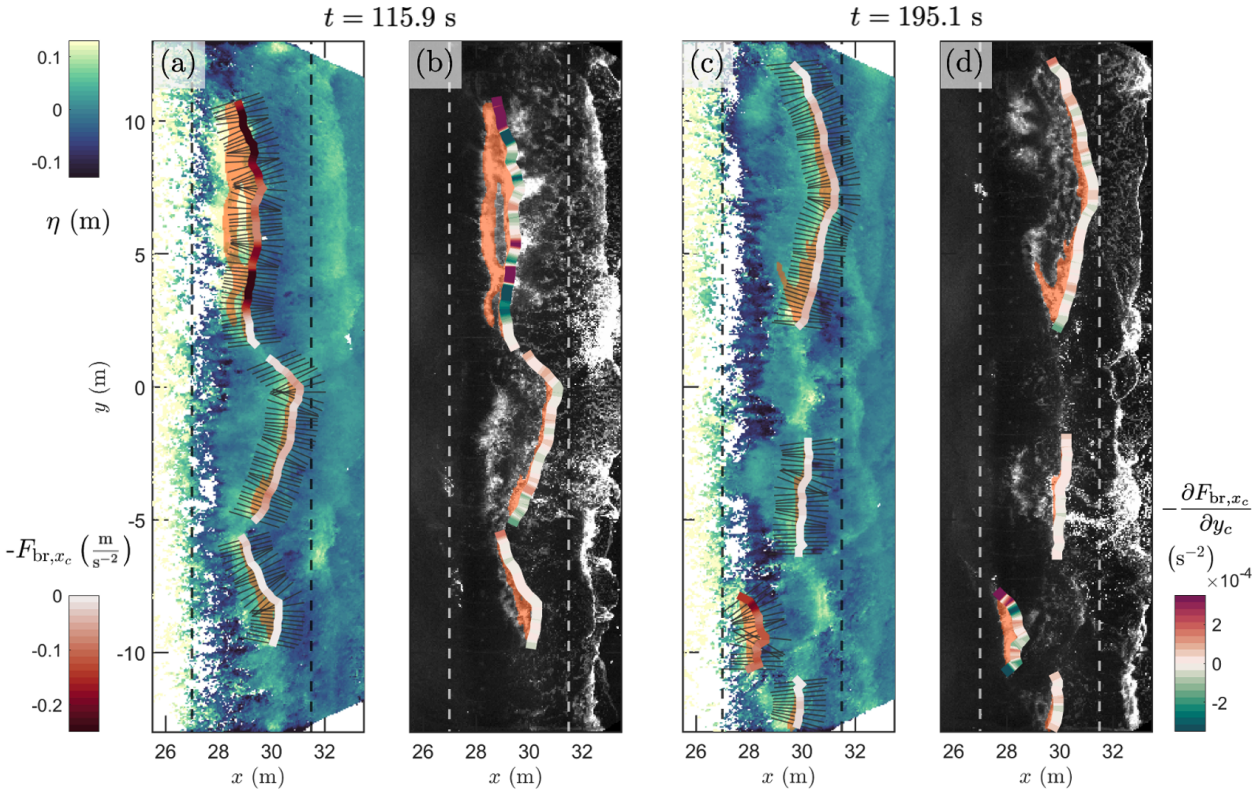

Figure 3.4: Snapshots of the (a,c) cross-crest breaking force ($\mathrm{F}_{\mathrm{br},x_c}$) overlain on a sea-surface elevation (η) map from a stereo reconstruction and (b,d) the along-crest gradient in the breaking force ($\frac{\partial \mathrm{F}_{\mathrm{br},x_c}}{\partial y_c}$) overlain on a rectified image estimated for the identified breaking wave crests (orange regions). $\mathrm{F}_{\mathrm{br},x_c}$ and $\partial \mathrm{F}_{\mathrm{br},x_c} \partial y_c$ along the wave crest (color contour along breaker toe) were plotted as a function of the cross-shore (x) and alongshore (y) position and were estimated with wave geometric properties along cross-crest transects (black lines crossing crests and plotted at $\Delta y = 0.45$ m in (a,c)). These examples are from trial *G2d* at time, t (s after 10 min).

The average along-crest profiles of D, $\mathrm{F}_{\mathrm{br},x_c}$, and $\partial \mathrm{F}_{\mathrm{br},x_c}/\partial y_c$ for each trial were computed by normalizing each crest length ($\hat{y}_c$) and neglecting any values that were within 1.25 m of the side walls or extending outside of the defined surfzone region ($-12 < x < 12$ m). Average

along-crest profiles were similar when wave crests touching side walls or exiting the analysis region were completely omitted. Gaussian curves with form $y = \sum_{i=1}^{2} a_i e^{-((x-b_i)/c_i)^2}$ were fit to the dissipation and breaking force profiles from $y_c = -0.5$ to 0.5 along the normalized crest, where the coefficients, a_i, b_i, and c_i, were selected to minimize differences between the observed and fit profile. The modeled along-crest gradient in breaking force was computed from the Gaussian fit for the breaking force. Results did not vary significantly when sampled at 2 Hz, instead of 8 Hz.

Note that results were similar when the dissipation profile was estimated by equating dissipation across a borefront to the total dissipation across a hydraulic jump using the water depth at the crest and trough [*Svendsen*, 1984a]. Average along-crest profiles estimated with the hydraulic jump approach had a similar shape with 30% lower dissipation values than estimated with the roller model, on average, consistent with previous studies [*Carini*, 2014]. As the roller length in Eqn. 3.9 was based on the presence of bright features (bubbles) indicative of a breaker, a tapering crest end may have been better characterized with the Duncan model.

The Duncan model and hydraulic jump approximations were both established for a well-developed bore within the surf zone. Thus, there may be limitations in applying this formulation near the onset of wave breaking. Intense dissipation during breaking as a plunging wave [*Lamarre and Melville*, 1991; *Blenkinsopp and Chaplin*, 2007; *Iafrati*, 2011] or dissipation estimates per unit length [*Phillips*, 1985] were not accounted for in the wave-average Duncan model dissipation estimates used here. Additionally, these estimates relied heavily on the stereo reconstructions which had higher sea-surface elevation variance than in situ sensors at all frequencies in the outer surf zone particularly for smaller directional spreads [*Baker et al.*, in review]. The discrepancies between in situ sensors and stereo reconstructions are attributed to higher water surface estimates during plunging breakers with a discontinuous water column and lower estimates in troughs when less surface foam was present. The higher water surface estimates may slightly alter the roller length and angle (L_r, θ_r), occasionally leading to higher dissipation rates in the outer surf zone.

3.3.5 In situ and remotely sensed low frequency spectral and spatial analysis

Low-frequencies were defined as $f < 0.2$ Hz, while very low-frequencies were defined as $f < 0.02$ Hz, defined based on previous literature defining these ranges in field conditions [*Lippmann et al.*, 1999; *MacMahan et al.*, 2010b] and scaling the 2-s wave in the laboratory to typical wave conditions in the field (*i.e.,* waves with a peak frequency of 10 s). Auto-spectra from the pressure sensors ($S_{\eta\eta}$, corrected for depth attenuation) and cross- and alongshore velocities ($S_{uu}(f), S_{vv}(f)$) were analyzed to detect very low-frequency variance and tank seiching modes. The spectra were computed using a Hanning window period of 256 s with an overlap period of 128 s over a 35-min time series (5–40 min, DOF = 45). The very low-frequency (VLF) velocity power (σ^2_{vlf}) was estimated as the integral of $S_{uu}(f) + S_{vv}(f)$ over very low-frequencies (DOF = 270), where rotational motion were dominant [Figure 3.21, *Lippmann et al.*, 1999; *MacMahan et al.*, 2010a; *Feddersen et al.*, 2011; *Elgar et al.*, 2019]. There was no cross-shore seiching patterns at VLFs observed for any wave conditions (Appendix 3.8).

The second-order alongshore velocity structure functions (Eqn. 3.4, $S(\Delta f)$) from all possible alongshore lags (Δy) were computed from 8-s median filtered in situ sensors and PIV velocities over a 10-min time series with the mean removed. Alongshore velocity structure functions were computed with the outer and inner surfzone array of ADVs ($x = 28.5, 30.7$ m, Figure 3.3a, blue and pink). Additionally, structure functions from optically-derived alongshore velocities were computed from locations between $y = -8$ to 8 m at each cross-shore position from $x = 28$ to 31.5 m. The surfzone averaged structure function was computed as the cross-shore average from $x = 28$ to 31.5 m with estimates every 8 cm in the cross-shore. In strictly two-dimensional turbulence, the direct enstrophy cascade scales with $S \sim \Delta y^2$, and the inverse energy cascade scales with $S \sim \Delta y^{2/3}$. To test how well the structure function curves fit theory, the least squares fit to $C\Delta y^a$ was performed for the direct enstrophy cascade from $\Delta y = 0.08$ to 0.3 m and inverse energy cascade from $\Delta y = 0.3$ to 6 m, where the exponent (a) and constant (C) vary per trial and between inertial ranges. The exponent

for the inverse energy cascade was not sensitive to small changes in the lower and upper bounds of the inverse energy cascade region (*e.g.,* estimates from $\Delta y = 0.5$ to 5 m yielded similar results).

Constraining the structure function analysis region to the center of the tank reduced any signals due to the concrete side walls, such as near-wall pressure gradients that led to weak mean circulation patterns from $y < -10$ m and $y > 10$ m (Figure 3.3) that could alter eddy processes. Computing structure functions with low-frequency alongshore velocities, as opposed to low-frequency cross-shore velocities, conservatively reduces any effects on the velocity signal due to cross-shore seiching patterns as opposed to surfzone eddy processes and also allows estimates at longer lags, consistent with [*Spydell and Feddersen*, 2009; *Elgar and Raubenheimer*, 2020] Regardless, cross-shore seiching patterns at low-frequencies were small for directionally spread waves, and there was no evidence of alongshore seiching patterns (Appendix 3.8). Moreover, computing structure functions with alongshore velocities was critical to resolve the necessary lags, because PIV-derived velocities were limited near the surfzone edge due to a lack of sufficient surface foam, and the alongshore PIV velocities generally have better agreement with in situ measurements (Appendix 3.7).

3.4 Results

3.4.1 The along-crest gradient in the breaking force

The along-crest profile of the wave energy dissipation (D), breaking force ($\mathrm{F}_{\mathrm{br},x_c}$), and along-crest gradient in the breaking force ($\partial \mathrm{F}_{\mathrm{br}}/\partial y_c$) were computed for each RBIS-identified wave crest over 10-min time series for all trials (Table 3.1) with Eqn. 3.5 (see Section 3.3.4). Dissipation is found to be highly irregular along individual wave crests and to vary substantially from crest to crest (Figure 3.5). To demonstrate this, three example waves from trial *G2d* ($\sigma_\theta = 24°$) are selected both onshore and offshore of the deepest region of the trough at $x \approx 29.5$ m (*i.e.,* termed the 'inner' and 'outer' surf zone hereafter).

Dissipation estimated with the Duncan roller model (Eqn. 3.9) is a function of the roller

length (L_r) and roller angle (θ_r). For trial *G2d*, the average roller length for all wave crests at all along-crest positions in the outer (inner) surf zone is 0.49 m (0.34 m) with a standard deviation (σ_{L_r}) of 0.20 m (0.14 m). The average roller angle is 12.7° with 10° standard deviation in both the outer and inner surf zone. The average wave energy dissipation is 15.9 J/s (8.3 J/s) with a standard deviation of 15.1 J/s (7.2 J/s) in the outer (inner) surf zone (Figure 3.5c,j). The cross-shore integrated dissipation estimates are typically less than bulk energy estimates based on linear wave theory and higher for unidirectional wave conditions than wave conditions with large directional spreads (not shown). There is typically a clear demarcation between the dissipation values within the RBIS-identified crest and regions just outside of it that are set to zero dissipation. From dissipation, the breaking force (Eqn. 3.7) is computed with the bore celerity (c_b) and mean water depth at the crest (h_c). Bore celerity was on average 1.6 m/s across the surf zone with a standard deviation of 0.6 m/s (Appendix 3.7). Water depths vary along-crest due to the oblique angle of crescent shaped waves. Breaking force estimates are larger in the outer surf zone (average: -0.07 m/s^2) than in the inner surf zone (average: -0.03 m/s^2) and have similar along-crest patterns to dissipation estimates (*e.g.,* Figure 3.5 compare c and f).

The along-crest gradient in the breaking force varies significantly from crest to crest ($\partial \mathrm{F}_{\mathrm{br},x_c}/\partial y_c$: outer surf zone $\sigma_D = 0.27$ s^{-2}, inner surf zone $\sigma_D = 0.11$ s^{-2}) as well as along individual crests. Due to the highly irregular breaking force profile, the along-crest gradient in the breaking force changes signs along the wave crest. There are many mechanisms that could lead to along-crest variations in the breaking force. Short-crested waves may dissipate rapidly as a plunger near the center [*Iafrati*, 2011], but may have alongshore-varying breaker characteristics (*e.g.,* not plunging near the sides or varying in void size), resulting in complex along-crest breaking force (*e.g.,* Figures 3.4a and 3.5a, dark blue). Oblique sections of crests may simultaneously occupy cross-shore positions with differing water depths, altering breaking patterns and bore celerity (*e.g.,* Figure 3.5e,l). Breaking waves occasionally intersect or interact with reflected waves, resulting in highly along-crest variable breaking characteristics. Despite the wave-by-wave differences, some trends emerge.

Typically, the values are negative and positive at left and right crest ends. On average, dissipation and breaking force estimates are larger in the outer surf zone than the inner surf zone, but vary along each crest (Figures 3.4 and 3.5e,f vs. l,m). Due to the significant along-crest variability, the external vorticity forcing per crest, estimated as the sum of the absolute value of the breaking force gradient for each crest ($N_c^{-1} \sum |\partial \mathrm{F}_{\mathrm{br},x_c}/\partial y_c|$), may be larger for longer wave crests, particularly near the onset of breaking (*e.g.,* compare blue vs. yellow lines in Figure 3.5g).

The total external vorticity forcing per surf zone ($\sum |\partial \mathrm{F}_{\mathrm{br},x_c}/\partial y_c|$ for all waves per snapshot in time) is estimated for each wave condition (Trials 3.1) to assess the relationship between the breaking force gradient and the crest length and number of ends. The peak of the probability density function for the per-surfzone total external vorticity forcing increases with increasing directional spread (Figure 3.6b). Unidirectional wave conditions occasionally have the largest observed total external vorticity forcing, due to along-crest variability near the onset of breaking along long crests spanning the tank. At most times, however, there is little or no total external vorticity forcing within the surf zone for unidirectional waves. In contrast, wave conditions with larger directional spreads nearly always have non-zero total external vorticity forcing. Although the magnitude range of the total external vorticity forcing is much greater than the number of crest ends, both the total external vorticity forcing and number of crest ends per surf zone sort by directional spread (Figure 3.6).

3.4.2 Low-frequency, large scale rotational motion in the surf zone

Surfzone mean circulation patterns, the time-averaged median filtered velocities from PIV and in situ sensors, are typically small away from side walls ($\mathbf{u} < 0.05$ m/s). Just onshore of the bar crest ($x = 28.4$ m), there is a near-bottom return current measured with in situ sensors (u varies from -0.1 m/s to -0.04 m/s) and near zero surface flow estimated from PIV velocities, suggesting that the water column is strongly sheared. There is no evidence of a strongly sheared water column in the inner surf zone ($x = 30.7$ m). A weak mean circulation pattern is evident near side walls in PIV estimates (*i.e.,* onshore directed flows

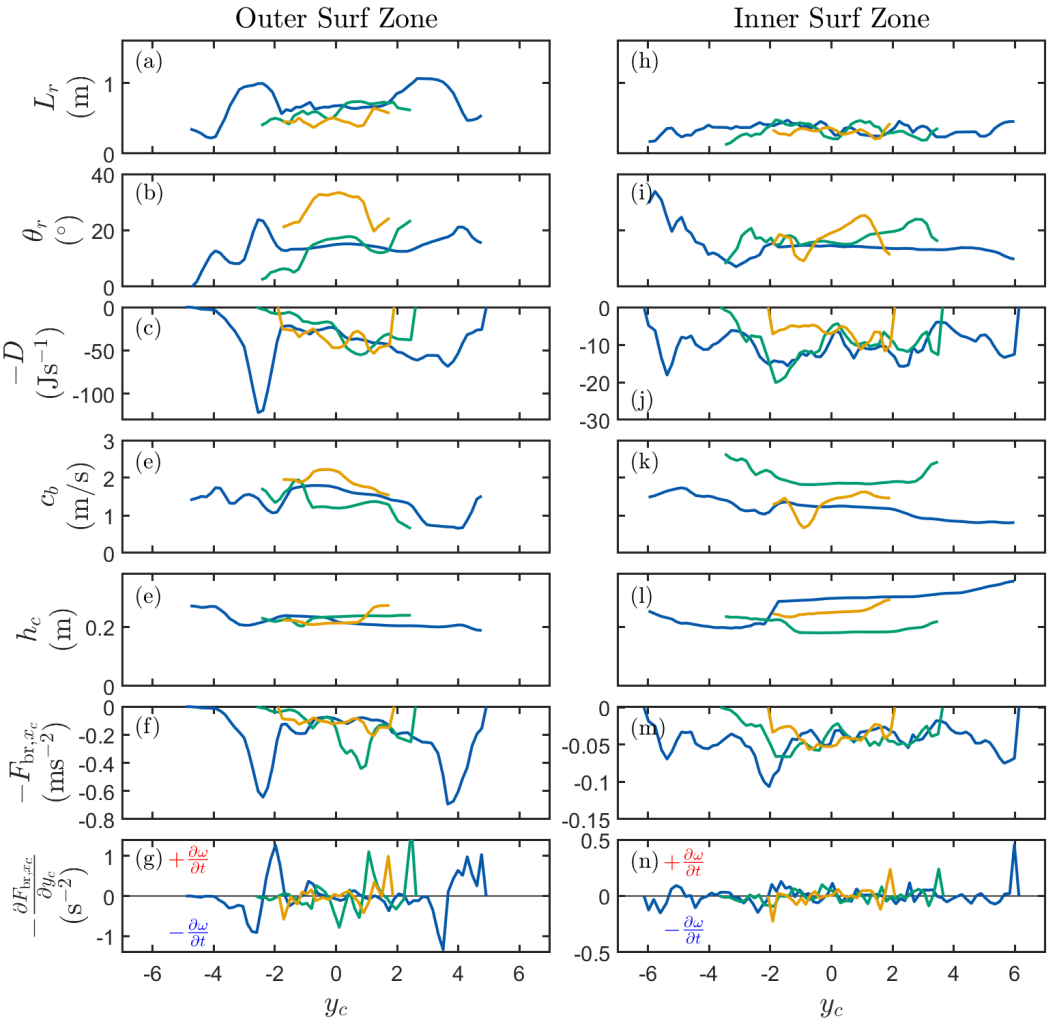

Figure 3.5: Six example along-crest (y_c) profiles, three from the outer surf zone (colors in the left column) and inner surf zone (colors in the right column), of the roller length (a,h, L_r), roller angle (b,i, θ_r), dissipation (c,j, D), bore celerity (e,k, c_b), crest water depth (e,l, h_c), breaking force (f,m, $\mathrm{F}_{\mathrm{br},x_c}$), and breaking force gradient (g,n, $\partial \mathrm{F}_{\mathrm{br},x_c}/\partial y_c$) from trial *G2d*. (g,n) Negative and positive values of the breaking force gradient indicate negative and positive injected vorticity (ω). Examples are from the time (t, s after 10 min) and average cross-shore position ($\langle x \rangle$) in the outer surf zone: $t = 115.9$ s and $\langle x \rangle = 29.3$ m (blue, also in Figure 3.4a,b), $t = 60.6$ s and $\langle x \rangle = 29.1$ m (green), and $t = 281.3$ s and $\langle x \rangle = 28.3$ m (yellow). Examples in the inner surf zone: $t = 9$ s and $\langle x \rangle = 30.8$ m (blue), $t = 195.1$ s and $\langle x \rangle = 31.3$ m (green, also in Figure 3.4c,d), and $t = 402.4$ s and $\langle x \rangle = 30.8$ m (yellow). Note the differing y-axis ranges in (j,m,n).

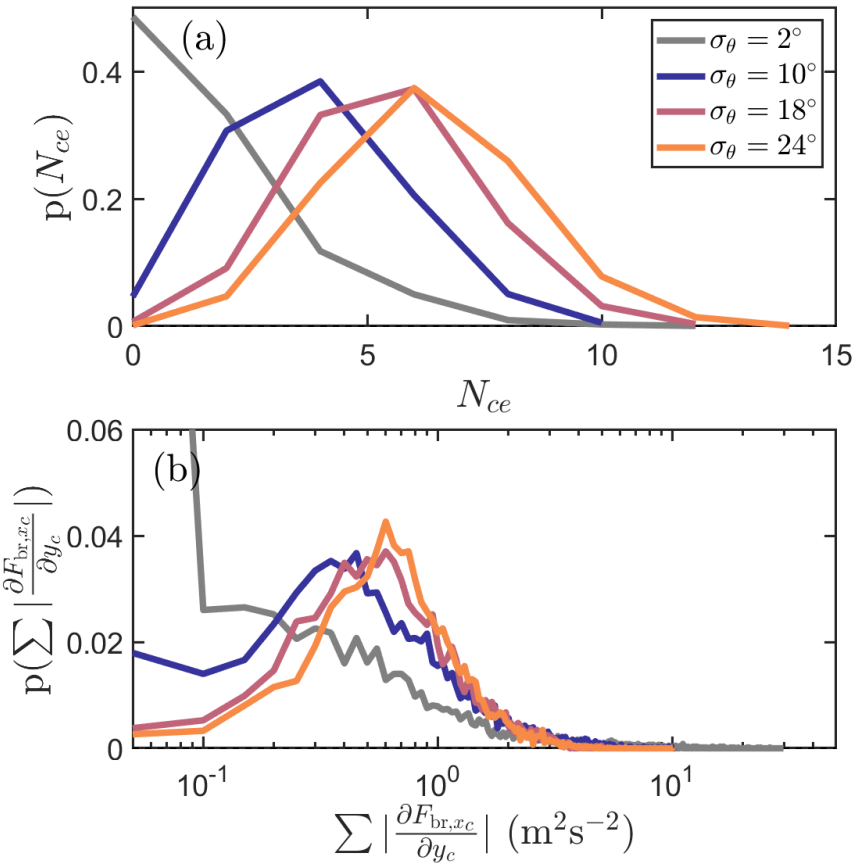

Figure 3.6: Probability Density Functions of the number of crest ends (a, N_{ce}, bin width = 2 crest ends) and total external vorticity forcing per surf zone (b, $\sum |\partial \mathrm{F}_{\mathrm{br},x_c}/\partial y_c|$, bin width = 0.05 m^{2}s^{-2}) for varying directional spreads (σ_θ, colors). (b) In the probability of near zero total external vorticity forcing (bin = 0.05 m^{2}s$^-$2) is 0.24 for $\sigma_\theta = 2°$.

near side walls with little mean current near the center of the tank). Stronger mean currents near the swash zone ($x > 32$ m, $\mathbf{u} \leq 0.1$ m/s) and offshore edge of the bar crest ($x < 27$ m, $\mathbf{u} \leq 0.1$ m/s) may be biased due to the crest removal workflow that was not developed for the swash zone and occasionally misses breakers in regions near the surfzone edge, where stereo reconstructions were poorly resolved. Importantly, the mean currents are much weaker than

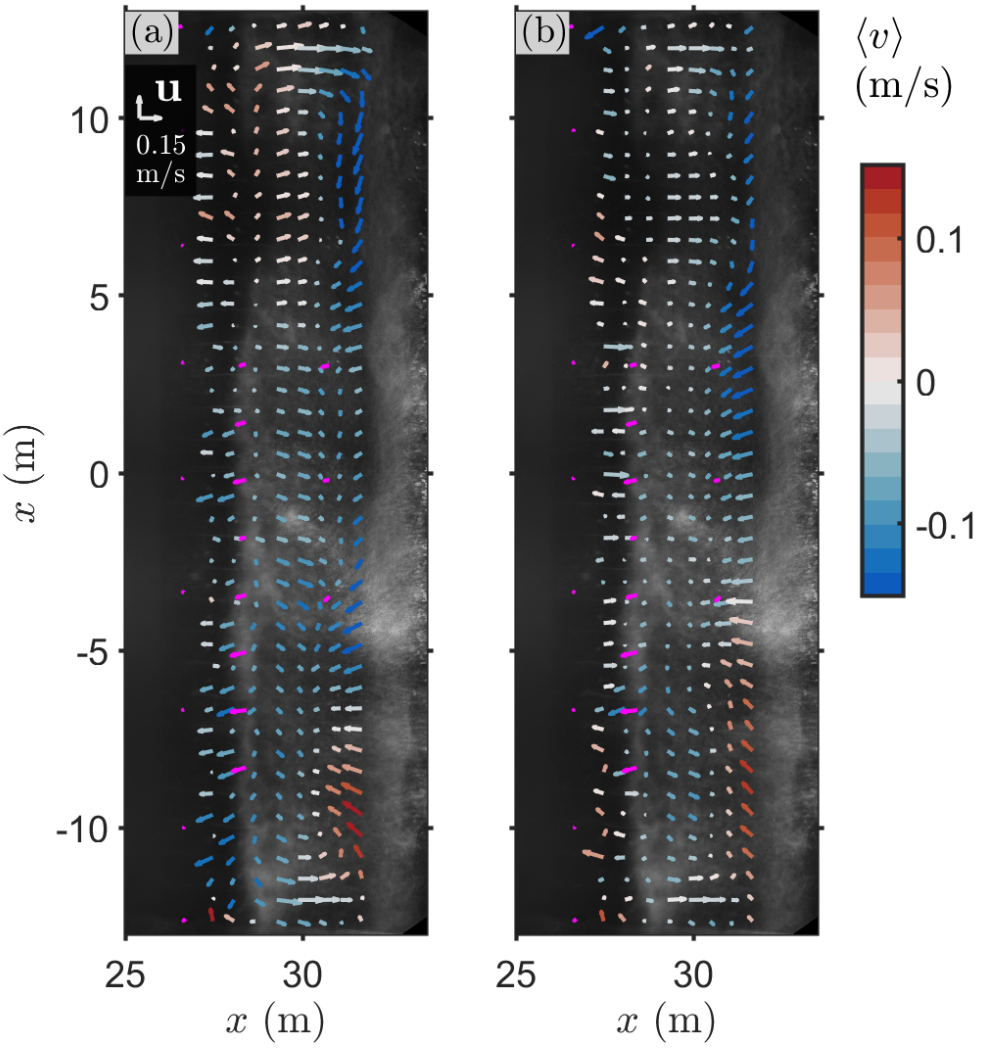

Figure 3.7: The mean velocities (**u**) from surface PIV (red to blue arrows, colored by the mean alongshore velocity, $\langle v \rangle$, plotted at $\Delta x = \Delta y = 0.6$ m) and near-bed in situ sensors (magenta) over a 10-min time series for *G2b* (a) and *G2d* (b) overlain on a wave averaged image as a function of the cross- (x) and alongshore (y) coordinate. The in situ arrays in the surf zone and inner shelf are from two trials with the same wave conditions. Turbulent processes may vary for repeated trials, but mean circulation patterns are similar based on inspection of repeated trials with the same surfzone array.

low-frequency velocities within the tank (compare Figure 3.7 and 3.8).

The low-frequency PIV velocity field (8-s median filtered, Section 3.3.3) includes rotational, coherent structures with varying spatial scales and temporal persistence (Figure 3.8b-c). Visually identified spatial scales of coherent, rotational structures, occasionally including pairs of counter-rotating vortices, vary from less than 1 m in diameter to the surf zone width in the cross-shore and occasionally exhibit longer alongshore scales. Structure functions computed from low-frequency PIV and in situ alongshore velocities vary with wave directional spread (Figure 3.9). For unidirectional waves (*G2a*, Figure 3.9a), the scales and magnitudes of the structure functions are similar across the surf zone ($x = 28 - 31.5$ m). The scales and magnitudes of the structure functions for directionally spread wave conditions (*i.e., G2b,d*, Figure 3.9b,c) are cross-shore dependent for lags greater than 0.5 m.

The consistency of the surfzone cross-shore averaged structure functions with a two-dimensional turbulence inverse energy cascade varies with wave directional spread (Figure 3.9, compare black lines with dashed red). Strictly two-dimensional turbulence exhibits a scale of $\sim \Delta y^{2/3}$ between the injection length scale and maximum length scale of the system (see Section 3.2). The scale of the surfzone-average structure function at $\Delta y > 0.5$ m is nearly zero for unidirectional waves (*G2a*), suggesting that alongshore velocities are uncorrelated at these lags (Figure 3.9a). The inverse cascade region scale of the surfzone-average structure functions over lags of $\Delta y = 0.5 - 6$ m is more consistent with a two-dimensional turbulence cascade for wave conditions with larger directional spread. For example, the spectral scaling is $\sim (\Delta y)^{7/8}$ for *G2b* with $\sigma_\theta = 10^\circ$ and the scale is $\sim (\Delta y)^{3/4}$ for *G2d* with $\sigma_\theta = 24^\circ$ (Figure 3.9b,c compare red dashed lines over $\Delta y = 0.5 - 6$ m). Additionally, the maximum lags at which alongshore velocities are correlated (scale of surfzone-average $S(\Delta y)$ is non-zero) decrease with directional spread (*i.e.,* inflection point for *G2b* is $\Delta y \sim 11.5$ m and for *G2b* is $\Delta y \sim 5.5$ m). In the enstrophy-cascade inertial regions ($\Delta y < 0.3$ m), the scales for the structure functions are $\sim (\Delta y)^{3/2}$, less steep than expected for an enstrophy cascade ($(\Delta y)^2$). The 24-cm median filter likely influences correlation between velocities over these lags.

The structure function estimates from in situ sensors in the inner surf zone are on average

3 times larger than estimates from in situ sensors in the outer surf zone ($x = 28.54$ m). PIV estimates are larger than the in situ estimates at the concurrent lags, especially in the outer surf zone (Figure 3.9, compare triangles and circles). In situ observations in the inner surf zone reveal more similar structure-function spectral scalings to those identified with PIV alongshore velocities. In contrast, the velocity variance measured by the near-bottom in situ sensors in the outer surf zone is less correlated along the beach (nearly flat structure function). This may be due to depth dependent low-frequency variability, especially in the outer surf zone where the water column is sheared (Figure 3.7) or biases in PIV estimates leading to higher variance. The depth-variable low-frequency fluctuations are consistent with observations and numerical simulations suggesting that vertical variability in very low-frequency currents are more significant near prominent bar-trough features in the outer surfzone [*Lippmann and Bowen*, 2016; *Henderson et al.*, 2017; *Baker et al.*, 2021].

For directionally spread wave conditions, rotational motion was dominant over irrotational motions at very low-frequencies (VLF, $f < 0.02$ Hz) in the wave basin surf zone (Appendix 3.8). The average power of VLF motions (σ^2_{vlf}, integral of the surfzone velocity variance over very low-frequencies) computed from in situ sensors at each cross-shore position is surfzone-region dependent and varies with wave directional spread and height (Figure 3.10). Here, VLF motions are analyzed with only in situ sensors over 35 min as the length of the PIV time series was insufficient to assess VLF velocities (10 min). The average VLF power is smallest for the stack of sensors at the toe of the beach slope ($x = 24.5$ m) and 3–4 times larger just offshore of the surf zone (Figure 3.10, compare red and black). Just offshore of the surf zone, total VLF power is on average 1.5 times larger for trials with larger waves, where the surfzone edge is farther offshore (Table 3.1, Figure 3.10, compare red triangles and circles). VLF velocity power is typically 3–4 times larger within the surf zone than just offshore of the surf zone (Figure 3.10, compare blue/pink with red) for directionally spread wave conditions ($\sigma_\theta \geq 9^\circ$) and 2–3 times larger for unidirectional conditions.

In the outer surf zone ($x = 28.4$ m), the VLF velocity power increases with directional spread from $\sigma_\theta = 2 - 18^\circ$ and plateaus or decreases for $\sigma_\theta > 18^\circ$ (Figure 3.10, blue) for all

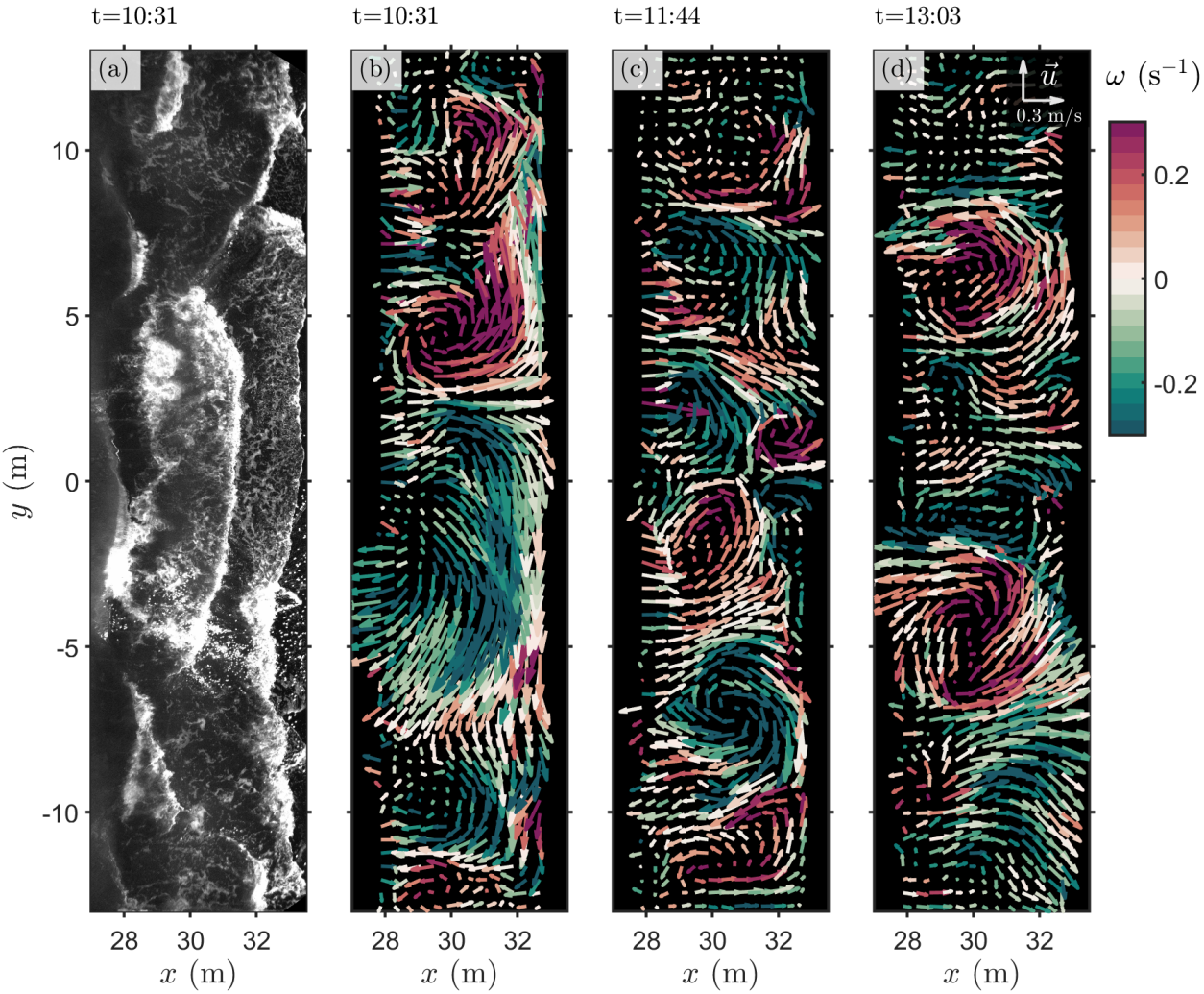

Figure 3.8: A rectified image and snapshots of low-frequency surface particle image velocimetry (PIV) velocities within the surf zone (mean removed) for directionally spread waves in trial *G1c*. (a) Waves break near the surf zone edge at the cross-shore position (x) around 27.3 m, generating bright surface foam used to track surface currents along (y) the tank. (b-d) The optically-derived velocities vary over time (t) and are depicted by the vector field (legend in d) and colored by the vorticity (ω). The red and green regions represent positive and negative vortex structures.

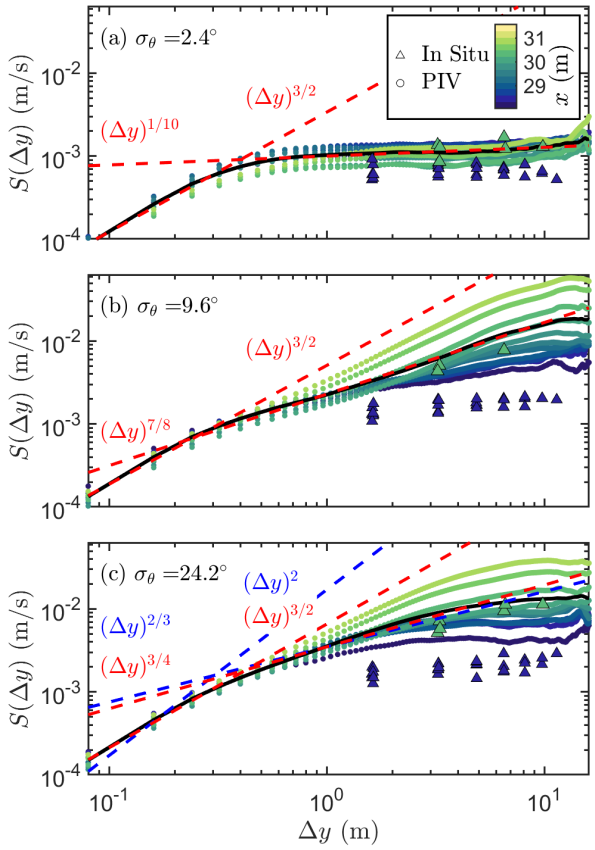

Figure 3.9: Structure functions computed from alongshore velocities ($S(\Delta y)$) as a function of the alongshore lag (Δy) computed with PIV (circles) and in situ sensors (triangles) for trials (a) *G2a*, (b) *G2b*, and (c) *G2d* (wave directional spreads, σ_θ in figure). PIV estimates are plotted every 32 cm in the cross-shore (x, colored by cross-shore position) and for the surfzone average (black, average of $x = 28 - 31.5$ m). In situ sensor estimates are shown for the outer ($x = 28.5$ m) and inner surf zone ($x = 30.7$ m). The lines of least squares fits with form $C\Delta y^a$ are shown (red dashed and red text labels) for the direct enstrophy ($\Delta y = 0.08 - 0.3$ m) and inverse energy cascade ($\Delta y = 0.3 - 6$ m) inertial ranges. (c) The line of least squares fit to $C\Delta y^{2/3}$ and $C\Delta y^2$ are shown (blue dashed and blue text), where 2/3 and 2 are the expected exponent for the inverse energy cascade and direct enstrophy cascade in strictly two-dimensional turbulence.

wave heights. Trends are similar in the inner surf zone (Figure 3.10, pink), but the shift from positive to zero or negative slope in directional spread vs. VLF velocity power occurs at smaller directional spreads ($\sigma_\theta = 2-9°$) for 24-cm waves (*G2a-d*) and is not well resolved for larger waves due to the absence of wave conditions with $\sigma_\theta = 10°$. Within the surf zone, there are no significant differences in total VLF power between the two wave height groups (Figure 3.10, error bars represent alongshore standard deviation of total VLF power). The exception to this is in the inner surf zone for the largest directional spreads (x = 30.7 m, $\sigma_\theta \approx 25°$), where there is more total VLF power for trials with larger wave heights.

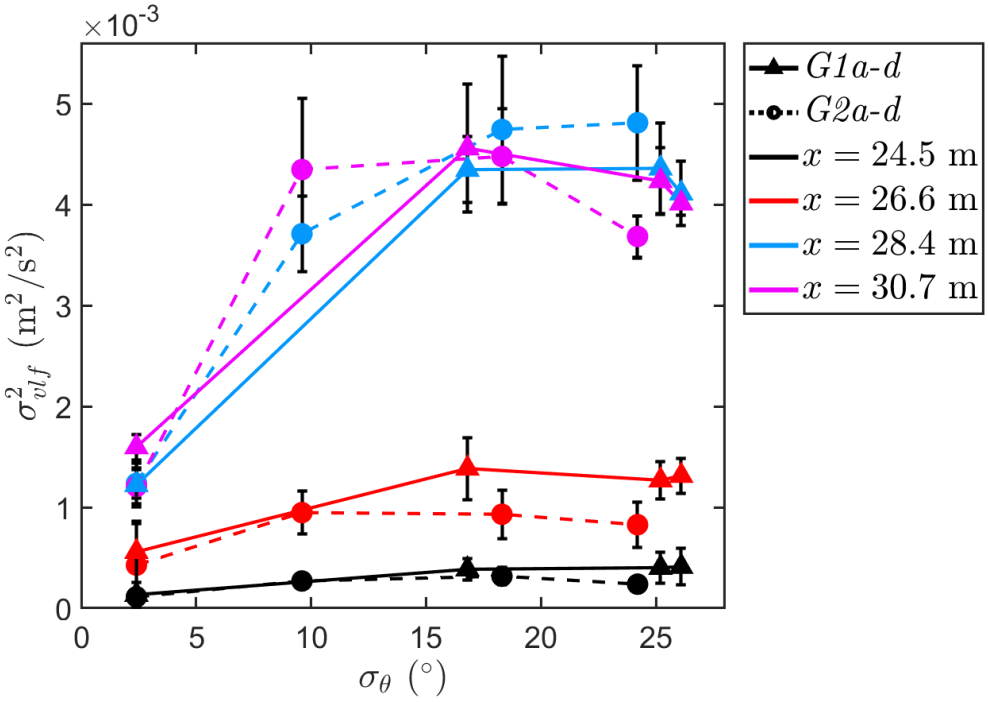

Figure 3.10: The alongshore-average (shape) and standard deviation (error bar) of the total velocity power (σ^2_{vlf}, integrals under curves at very low-frequencies, Figure 3.21a) per surf zone region (colors) as a function of directional spread (σ_θ) for *G1a-d* (solid line, triangles) and *G2a-d* (dashed line, circles).

3.5 Discussion

3.5.1 Vortex length scales and wave-field dependencies

Along-crest gradients in wave height during short-crested wave breaking are hypothesized to generate vertical vorticity within the surf zone [*Peregrine*, 1998; *Bühler*, 2000; *Johnson and Pattiaratchi*, 2006; *Wei et al.*, 2017]. The time-rate of change in vertical vorticity may be approximated by the curl in the breaking force [Eqn. 3.5, *Spydell and Feddersen*, 2009; *Feddersen*, 2014; *Kirby and Derakhti*, 2019]. Thus, the length-scales over which there is an along-crest gradient in dissipation may play a role in the vorticity injection length scales. Previous field observations have assumed a pre-defined length scale (L_ω, a distance with an along-crest gradient in the breaking force) that resulted in wave-breaking-injected vorticity without prior knowledge of how the injection length scales varied across the surf zone on a wave-by-wave basis [*Clark et al.*, 2012].

Here, we find that along-crest variability in the breaking force is highly irregular on a wave-by-wave basis with some dependencies on surfzone region (Figures 3.4 and 3.5). This gradient in the breaking force is sensitive to variations in breaking force estimates that are ubiquitous along wave crests. However, some trends emerged. Generally, there are significant peaks in the injection magnitude near crest ends at the demarcation between breaking and an unbroken water surface, with smaller-scale fluctuations along the wave crest. Also, the breaking force gradient is more often negative on the right-hand-side and positive on the left-hand-side of the wave crest from the perspective of an observer at the breaking wave crest looking onshore. The time-rate of change in vorticity due to a breaking wave can be approximated by the negative along-crest gradient in the breaking force ($-\partial \mathrm{F}_{\mathrm{br},x_c}/\partial y_c$, Eqn. 3.5). Thus, to explore these trends in the wave-forced vorticity injection, the average along-crest profiles of the breaking wave force and gradient in the wave force were computed by averaging over all crests in each wave condition, normalizing each crest by length prior to averaging.

In the outer surf zone of trial *G2d* (Figure 3.11a, $\sigma_\theta = 24°$, $28 < x \leq 29.5$ m), the average

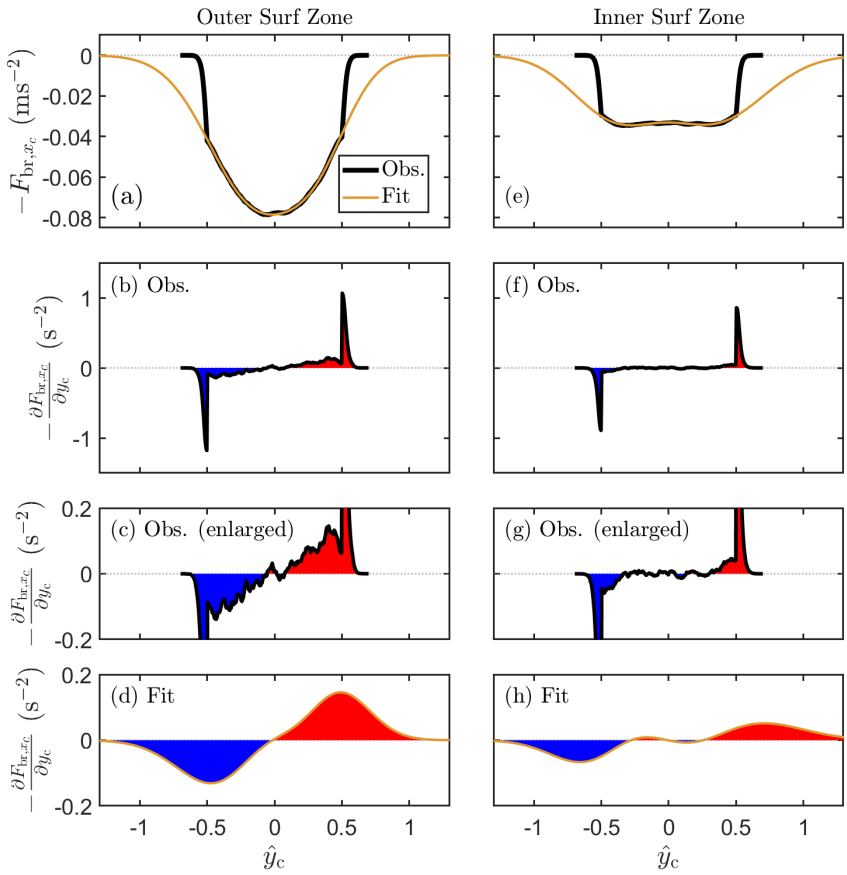

Figure 3.11: The observed (a-c,e-g, black) and fit (a,d,e,h, gold) average wave breaking force (a,e, F_{br,x_c}) and along-crest gradient in the breaking force (c-e,f-h, $dF_{br,x_c}/d\hat{y}_c$) along the normalized along-crest profile ($\hat{y}_c$). The average profiles for the outer surf zone (a-d, $28 < x \leq 29.5$, 6964 wave crests) and inner surf zone (e-h, $27 < x \leq 29.5$, 11078 wave crests) from trial *G2d* ($\sigma_\theta = 24°$) with an average crest length of 4.5 m over a 10-min time series. (a,b) Gaussian curves are fit to the average profile (gold). The along-crest gradient of the Gaussian fitted-curve for breaking force ($dF_{br,x_c}/d\hat{y}_c$) is shown in (d,h). (c,g) The y-axis near zero is enlarged to show the observed along-crest profile. (c-d,f-h) The positive and negative regions of $dF_{br,x_c}/d\hat{y}_c$ are colored red and blue and are an approximation for the time-rate of change in vorticity by Eqn. 3.5. Note that the width of the observed breaking gradient at crest ends is due to the normalization of varying crest lengths and altering the normalized distances to the neighboring grid with no dissipation ($dy = 0.15$ m in observations).

along-crest profile of the breaking force is arced, displaying a maximum breaking force near the center of the wave crest. Then, the breaking force drops to zero at crest ends if the transition between breaking and non-breaking is abrupt at the edge of the visibly identifiable wave crest (*i.e.,* edge of the bright foam passing the RBIS-threshold, orange region in Figure 3.4). This gradually-varying along-crest profile results in a non-zero breaking force gradient along the wave crest over a length-scale (L_ω) that is approximately half of the crest length (L_c), while also spiking near the crest end, where the largest gradient in the breaking force occurs (Figure 3.11b,c). Thus, near the onset of breaking, the average injected vorticity (*i.e.,* $d\omega/dt$, the time-rate of change in vorticity from Eqn. 3.5) is negative and positive along the left and right side of the wave crest, respectively. Additionally, injected vorticity may have length scales $L_\omega \sim \frac{1}{2}L_c$ with the largest values near crest ends on average (Figure 3.12a).

In contrast to the outer surf zone, there is little along-crest variability in the average breaking force in the inner surf zone, where bores are typically well developed (Figure 3.11e). This results in a near-zero breaking force gradient in the center of the crest, spanning over half the crest length ($L_\omega \lesssim \frac{1}{4}L_c$). Thus, the distance over which vorticity injection occurs (L_ω) may be much smaller in the inner surf zone than in the outer surf zone (Figure 3.12b). For example, based on the average crest length for trial *G2d* (L_c = 4.5 m) and average breaking force gradient profiles, the average outer surf zone injection scales would be 2.3 m, while the inner surf zone would be less than half that length. If L_ω decreases to length scales at which injected vortices cannot be considered two-dimensional (*e.g.,* possible when $L_\omega \approx h_c$, water depth), turbulence fluctuations may dissipate due to bottom friction or other dissipative processes rather than contributing to an inverse energy cascade.

An abrupt demarcation between an aerated, dissipating crest and an unbroken water surface results from computing dissipation with a model for a well-developed bore over a brightness-identified region [*Duncan*, 1981]. However, some dissipation may be occurring outside of the bright region, *i.e.,* dissipation that does not entrain sufficient air to be visualized [*Zappa et al.*, 2001]. To represent a more gradual transition between the breaking and

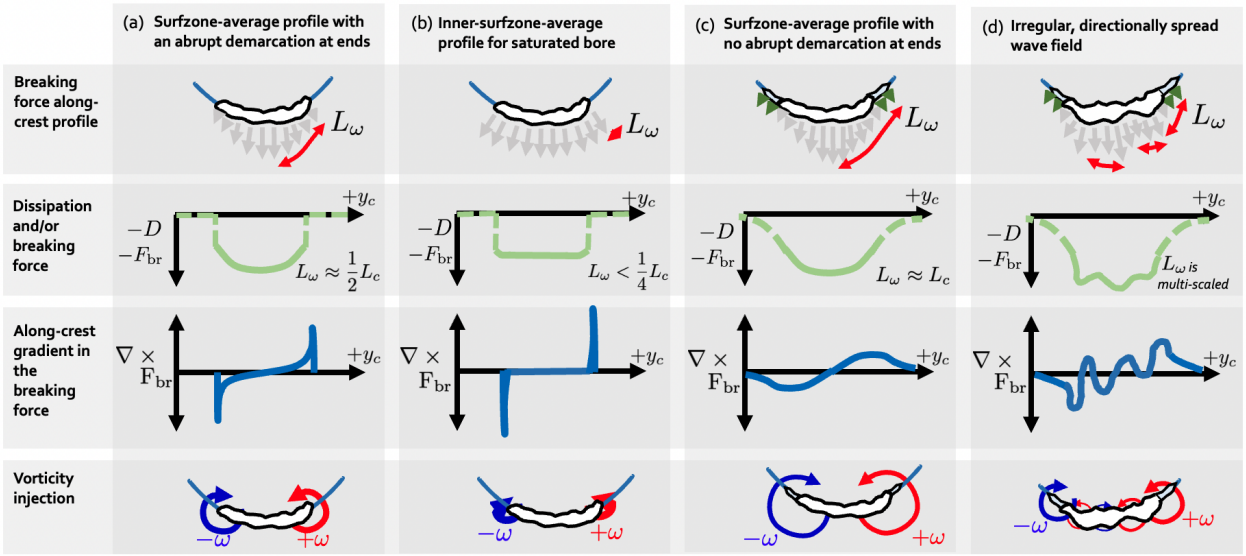

Figure 3.12: Example models of the relationship between the along-crest profiles (y_c) of the dissipation (D) or the breaking force (F_{br}, grey arrows in the schematic top row, example profile second row) and the gradient in breaking force ($\partial F_{br,x_c}/\partial y_c$, third row) and potential vorticity injection (ω, forth row). Four options of potential breaking force profile are (a) along-crest gradually varying or (b) nearly constant breaking force with zero breaking force outside the identified crest as well as (c) Gaussian profile and (d) along-crest variable breaking force with a gradual decrease to zero near crest ends. Depending on the along-crest profile and crest end assumptions, the length over which there is a breaking force gradient (L_ω) may vary with crest length (L_c), which alters the vorticity injection length scales.

non-breaking, a Gaussian is fit to the average breaking force, resulting in dissipation slowly tapering crest ends (Figure 3.11a,e, gold). Although the total external vorticity forcing per wave crest ($N_c^{-1} \sum |\partial F_{br,x_c}/\partial y_c|$ for the average wave profile) is independent of the crest-end assumption, the implications for vorticity injection length scales may vary significantly (Figure 3.12, compare a vs. c). L_ω for the Gaussian fit is nearly twice the length of the abrupt crest-end in observations (Figure 3.11, compare c vs. d, g vs. h). For example, for a wave with a crest length of 4.5 m (*i.e.,* the average crest length for *G2d*), the length over which

there is a breaking force gradient would vary from 2.3 to 4.5 m. The abrupt demarcation at crest ends in direct observations and the Gaussian fit provide bounds on the relevant vorticity injection length scales, L_ω.

Similar to waves with $\sigma_\theta = 24°$ (trial *G2d*), the average along-crest profile of the breaking force and breaking force gradient along the normalized crest length for smaller spread (*i.e.,* $\sigma_\theta = 10°$, trial *G2b*) is along-crest varying in the outer surf zone and nearly independent of along-crest position in the inner surf zone (Figure 3.13a-d). The similar shapes of the breaking force gradient suggest that L_ω would increase with increasing L_c (*i.e.,* L_c increases from about 5 to 7 m from *G2d* to *G2b*). For waves in the outer surf zone, the breaking force for the trial with $\sigma_\theta = 10°$ and a longer average crest length ($L_c = 7.7$ m) is 25% higher than for the trial with $\sigma_\theta = 24°$, resulting in a larger breaking force gradient. Conversely, there is little difference in the profiles within the inner surf zone for differing directional spreads. Average trends for different directional spreads are similar across all trials (not shown). The average along-crest breaking force estimated for trials with larger wave heights (*i.e.,* $H_s \approx 0.27$ m, *G1a-d*) is 30% larger for waves in the outer surf zone, and similar to trials with smaller wave heights in the inner surf zone. The along-crest profile of the dissipation and breaking force for unidirectional wave conditions does not exhibit the same arced shape as seen in directionally spread wave conditions (not shown). For unidirectional waves (*G1a, G2a*), the average along-crest profile is highly irregular, partially due to averaging over a small number of crests (n = 6051 and 6500, 30% of waves relative to directionally spread cases).

On average, wave conditions with lower directional spread and longer crest lengths have larger external vorticity forcing per wave crest in the outer surf zone (*e.g.,* Figure 3.13, a similar profile for longer crest length indicates greater external vorticity forcing per crest, $N_c^{-1} \sum |\partial \mathrm{F}_{\mathrm{br},x_c} / \partial y_c|$). Small-scale along-crest variability in the breaking force for long waves may amount to larger external vorticity forcing per wave crest (*e.g.,* Figure 3.5, black curves), occasionally leading to much larger total external vorticity forcing per surf zone (*e.g.,* see Figure 3.6b, grey curve). However, it is unclear if the small-scale, cross-shore evolving variability

in the crest-by-crest breaking force amounts to injected vorticity that can cascade to larger scales (Figure 3.12d, *e.g.,* small scale features along wave crests vary as the wave propagates shoreward). Turbulence fluctuations with scales similar to the water depth (*i.e.,* not considered two-dimensional) may instead dissipate through the direct energy cascade (if considered three-dimensional) or enstrophy cascade (if still considered two-dimensional) [*Boffetta and Ecke*, 2012].

These crest-by-crest attributes do not account for the increase in the number of crests with increasing directional spread (Figure 3.6a). At any given time, trials with larger directional spreads often have more individual waves that each contribute external vorticity forcing. For example, trials with lower directional spread and longer waves are characterized by intermittent large external vorticity forcing across the surf zone between times with near-zero external vorticity forcing (Figure 3.6, $\sigma_\theta = 2^\circ$, grey). In contrast, trials with larger directional spread nearly always have significant external vorticity forcing within the surf zone (Figure 3.6, compare $\sigma_\theta = 10^\circ$ and 24°). Due to the intermittency and non-Gaussian distribution of forcing, it is unclear if the average magnitude of the breaking force gradient along a normalized crest is indicative of forcing that contributes to low-frequency eddy activity within the surf zone.

Lab observations of the along-crest gradient in the breaking force suggest that L_ω varies widely between individual waves and surfzone regions and depends on the assumed dissipation profile near crest ends. Previous observations with a 10-m diameter ring of ADVs employed Kelvin's circulation theorem [*Peregrine*, 1998] to measure the vorticity injection at crest ends on a wave-by-wave basis [*Clark et al.*, 2012]. The predicted vertical vorticity based on wave height, water depth, and an alongshore length scale was consistent with observations of vorticity near crest ends for regions with intense dissipation, but over-predicted when the array was positioned at other regions of the surf zone [*e.g.,* a bar trough *Clark et al.*, 2012]. The lab-observed cross-shore dependence of the along-crest profile and ramifications for vorticity injection may provide context for past observations, elicit the need to assess vorticity at multiple length scales, and prompt further consideration of the along-crest

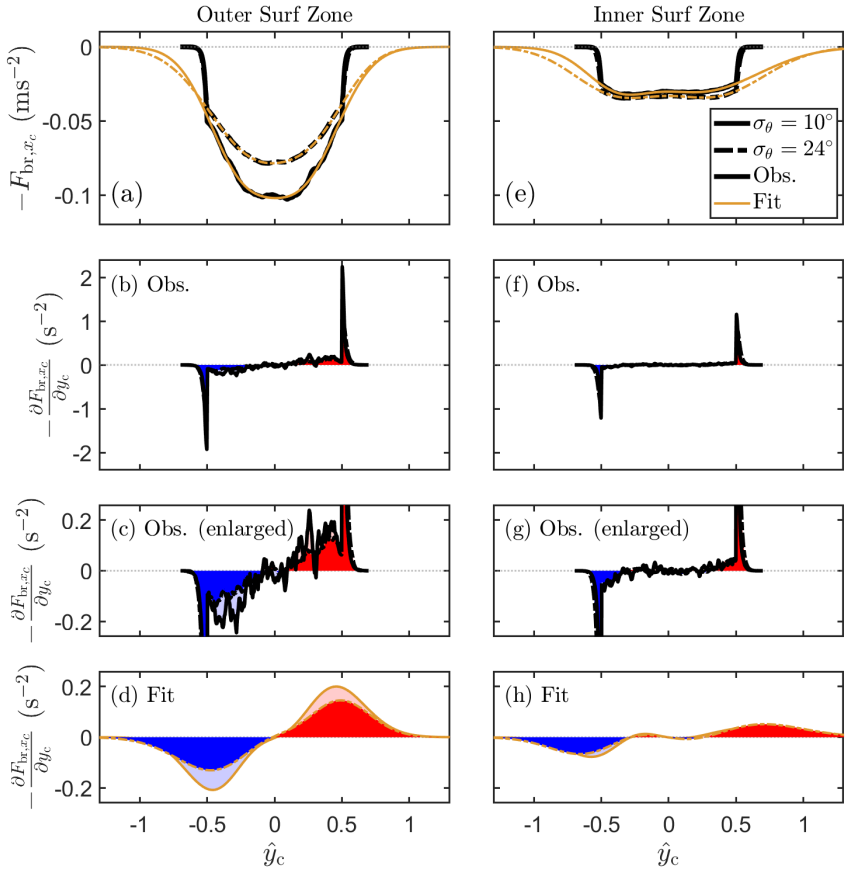

Figure 3.13: The observed (a-c,e-g, black) and fit (a,d,e,h, gold) average wave breaking force (a,e, $\mathrm{F}_{\mathrm{br},x_c}$) and along-crest gradient in the breaking force (c-e,f-h, $d\mathrm{F}_{\mathrm{br},x_c}/d\hat{y}_c$) along the normalized along-crest profile ($\hat{y}_c$) for trial *G2b* ($\sigma_\theta = 10°$, solid curves) and *G2d* ($\sigma_\theta = 24°$, dashed curves). The average profiles for the outer surf zone (a-d, $28 < x \leq 29.5$, *G2b*: 4746 wave crests, *G2d*: 6964 wave crests) and inner surf zone (e-h, $27 < x \leq 29.5$, *G2b*: 7172 wave crests, *G2d*: 11078 wave crests) with an average crest length of 7.7 m for *G2b* and 4.5 for *G2d* over a 10-min time series. (a,b) Gaussian curves are fit to the average profile (gold). The along-crest gradient of the Gaussian fitted-curve for breaking force ($d\mathrm{F}_{\mathrm{br},x_c}/d\hat{y}_c$) is shown in (d,h). (c,g) The y-axis near zero is enlarged to show the observed along-crest profile. (c-d,f-h) The positive and negative regions of $d\mathrm{F}_{\mathrm{br},x_c}/d\hat{y}_c$ are colored red and blue and are an approximation for the time-rate of change in vorticity by Eqn. 3.5.

dissipation profile near crest ends.

Similar to the average along-crest profile of the gradient in the breaking force here, results from numerical simulations of directionally spread wave fields over alongshore-uniform bathymetry found that the injection length scale decreased with increasing directional spread [lengths scales ranged from 4-20 m, *Spydell and Feddersen*, 2009; *Feddersen*, 2014] scaling with the breaking crest length [*Kirby and Derakhti*, 2019]. Furthermore, a set of field observations found evidence that the inverse energy cascade may span to length scales down to 10 m for some surfzone regions [*Elgar and Raubenheimer*, 2020]. Based on the *Longuet-Higgins* [1956] formulations for non-breaking along-crest wavelengths that were adapted for breaking wave crests [*Baker et al.*, in review], the average L_c for wave conditions simulated in *Feddersen* [2014] (*e.g.,* about $T_p = 8$ s, $\sigma_\theta = 10 - 30°$) with a depth of 1 m would range from 18–70 m. Thus, numerically simulated vorticity injection length scales are likely significantly less than the average L_c [*Feddersen*, 2014]. Based on visual inspection of three-dimensional numerical simulations of regular waves and two intersecting wave trains, length scales of the vertical vorticity at crest ends were about 1/4–1/2 of L_c [*Wei et al.*, 2017; *Kirby and Derakhti*, 2019]. However, it is unclear how mutual advection in the small gap between wave crests altered vortex length scales relative to irregular, directionally spread wave conditions.

The contrast between the dissipation and breaking force profiles in the outer surf zone and the inner surf zone, suggest that the wave-injected vorticity may substantially vary across the surfzone. The along-crest variability near the onset of breaking may be due to an along-crest dependence in the void size of plunging waves [*Ting and Kirby*, 1995; *Iafrati*, 2011], non-linearities in the wave field [*Wei et al.*, 2017; *Kirby and Derakhti*, 2019], or along-crest varying breaking onset location and type (*e.g.,* plunging initially, then surging or collapsing near crest ends as waves propagate into shallower waters). Within the inner surf zone, steady state bores have less along-crest variability, possibly because wave heights may be depth-limited and primarily a function of water depth [*Thornton and Guza*, 1982], in contrast to the offshore along-crest varying wave amplitude.

For the irregular, directionally spread wave field in the laboratory, breaking characteristics

and onset location vary from crest to crest. However, for simplicity, we employ only the Duncan dissipation model for a steady-state bore [*Duncan*, 1981]. Based on scaling of wave conditions in the laboratory, estimated roller length, angle, and dissipation are typically within the range observed in the field at a single cross-shore transect [*Martins et al.*, 2018]. Despite this, the Duncan roller model may not appropriately represent some of the energetics near the onset of breaking, especially for plunging breakers [*Iafrati*, 2011]. Neither approaches were developed to assess along-crest variability.

Additional uncertainty in the breaking force estimates may be attributed to biases imparted by stereo reconstructions or limitations of the laboratory setting. Along-crest dependence in stereo reconstruction biases could be due to brighter foam near the center of crests leading to over-exposed imagery, noise or post-processing spatial filters in the stereo estimates, or differences between remote-sensing observations and those ascribed by in situ sensors [*e.g.,* during plunging, *Baker et al.*, in review]. Although the surf similarity number [*Battjes*, 1974] was similar to some field environments, the bathymetry was steeper than found on natural beaches and included a steep bar-trough feature that was dissimilar to previous studies of wave-breaking injected vorticity dynamics on a planar beach [*e.g., Spydell and Feddersen*, 2009; *Suanda and Feddersen*, 2015]. Thus, waves occasionally break as a plunger near the bar crest, reform over the trough, and break as a well-developed bore on the beach face. Similar to many field environments, this leads to two distinct regions of dissipation where wave-breaking injected vorticity may be more ubiquitous, as well as a relatively deep trough that may enhance eddy interaction and nonlinear transfers of energy [*Bühler and Jacobson*, 2001]. Due to the removal of observations near side walls, it is unlikely that the side-wall-constraints altered the primary findings related to the breaking force gradient for directionally spread wave conditions.

The vorticity injection in the water column was not directly measured to relate with the breaking force estimates. Future work should compare the breaking force estimates to measurements of vorticity to assess the contribution of breaking force gradients along varying spatial scales to the inverse energy cascade. More observations of the along-crest

variability in dissipation for more idealized conditions as well as in field settings would help better characterize the expected vorticity injection on a wave-by-wave basis and inform model parameterizations of the breaking force. Further examination of along-crest dissipation characteristics could improve dissipation and breaking force parameterizations in numerical models, most of which have not been tested for along-crest variability [*e.g., Chen et al.*, 2003] and often rely on a free tuning parameter to represent the physics [*Kennedy et al.*, 2000].

Here, we focused on the along-crest gradient in the breaking force to approximate the expected instantaneous vorticity injection length scales, (L_ω) and showed that it varies with the breaking crest length (L_c). However, other physical processes may define the injection length scales (l_i) that result in a non-linear transfer of energy to longer length scales through an inverse cascade (Figure 3.1b,d). As injected vorticity must have characteristic injection length scales with dimensions that are longer than the vertical dimension of the flow to be considered two-dimensional, the water depth at breaking (h_c) may be a minimum injection length scale that results in an inverse cascade. As waves propagate shoreward with length scales modulated by the water depth, they may inject same-signed vorticity near crest ends, resulting in a vortex sheet that can roll up with increasing circulation and differing length scales constrained by the vortex sheet [L_s, *Peregrine and Bokhove*, 1999; *Peregrine*, 1999; *Bonneton et al.*, 2010]. Theoretically, vortices could remain attached to the crest end until they are shed from the wave when breaking subsides, either at the shoreline or in a deeper trough region [*Peregrine*, 1999]. At this point, vortices may self- or multi-advect within the surf zone, continuing to interact with the ambient vorticity field and proceeding or neighboring waves. Other relevant length scales are the gaps between breaking crests (L_g), that could constrain whether vortices mutually advect or interact with neighboring wave-breaking injected vortices rather than the opposite signed vortex from the other end of the consecutive wave. Additionally, the wave period defines the timescale that vortices evolve before interacting with a subsequent wave and wave-injected vortices. For a directionally spread irregular wave field, these processes may result in forcing at a variety of length scales

that contribute to the presence of large-scale, low-frequency rotational flows. Future work could examine the relative contributions of these processes to surfzone vorticity variability as well as their implications for mixing and dispersion within the surf zone and cross-shore exchange via the formation of transient rip currents.

3.5.2 Surfzone eddy evolution consistency with two-dimensional turbulence

Once vortices are injected by a breaking wave, they interact with other waves, vortical motions, and mean currents within the surfzone. Vortices with some range of length scales (L_ω, explored in Section 3.5.1) are hypothesized to non-linearly transfer energy to larger scale low-frequency motions within the surf zone [*Peregrine*, 1999; *Bonneton et al.*, 2010; *Spydell and Feddersen*, 2009; *Feddersen*, 2014; *Elgar and Raubenheimer*, 2020]. Here, we contextualize the in situ and optically-derived measurements of surfzone eddies in the wave basin to determine their consistency with a two-dimensional turbulence system and the variability with wave field characteristics (Figure 3.1c,d).

At very low-frequencies (scaled to the basin wave field), vortical motion is dominant in the surf zone for directionally spread wave conditions, consistent with field observations [*e.g., Lippmann et al.*, 1999; *Elgar et al.*, 2019]. Similar to previous results from field observations and numerical modeling [*Kennedy*, 2005; *Spydell et al.*, 2007; *Spydell and Feddersen*, 2009; *Feddersen*, 2014], very low-frequency rotational motions are more energetic within the surf zone than just offshore of the surf zone (Figure 3.10). This supports the hypothesis that energy is transferred from short-crested wave-breaking injected vorticity to lower-frequency currents. However, unlike previous studies that suggested that low-frequency velocity variance increases monotonically with directional spread [*Elgar and Raubenheimer*, 2020; *Suanda and Feddersen*, 2015], we find that large-scale eddy variability increases with directional spread initially, but then reaches a limit of maximum variance and even slightly decreases with directional spread. If there is too much random forcing in a two-dimensional turbulence system, the formation of large-scale coherent eddies may be disrupted, limiting the likelihood of an inverse energy cascade [*Kellay and Goldburg*, 2002]. Additionally, veloc-

ity variance associated with very low-frequency rotational motions is generally homogeneous across the surf zone, with slightly larger velocity variance in the outer surf zone for 24-cm waves (Trial *G2d*).

The lack of dependence of large-scale rotational motions on the wave height may be due to energy dissipation and resulting vorticity injection for the largest waves on the offshore side of the bar crest ($x < 27.7$ m), resulting in similar wave-breaking injected vorticity onshore of the bar crest and possible saturated wave conditions within the surf zone [*Sallenger and Holman*, 1985; *Raubenheimer et al.*, 1996]. Breaking may cease while waves propagate over the deep trough onshore of the wave crest, potentially resulting in the trailing vorticity to roll up and self- or mutually advect into deeper waters, rather than advecting onshore with the wave crest [*Peregrine*, 1999]. This may explain the higher variance measured just outside of the surf zone for increasing wave heights (Figure 3.10, compare red dashed and solid). Alternatively, the higher VLF velocity power just offshore of the bar crest for trials with $H_s \approx 0.27$ m may be due to enhanced cross-shore exchange for larger waves [*Suanda and Feddersen*, 2015]. Undoubtedly, the steep bar-trough profile in the laboratory may alter vorticity dynamics relative to other beach profiles [*Bühler and Jacobson*, 2001].

The surfzone-average alongshore velocity structure functions estimated from optically-derived velocities are nearly indistinguishable from each other at $\Delta y = 0.6 - 3$ m and satisfy the $S \sim (\Delta y)^{2/3}$ scaling for trials with large directional spread (Figures 3.9 and 3.14), including *G1c-d* ($H_s \approx 0.27$ m, $\sigma_\theta = 25 - 26°$) and *G2c-d* ($H_s \approx 0.24$ m, $\sigma_\theta = 18 - 26°$). The structure function scalings are less consistent with an inverse energy cascade for lower directional spreads, where the least squares fit is $S \sim (\Delta y)^{7/8}$ for trials *G1b* ($H_s \approx 0.27$ m, $\sigma_\theta = 18°$) and *G2b* ($H_s \approx 0.27$ m, $\sigma_\theta = 10°$). The structure function for both unidirectional trials (*G1a, G2a*) are uncorrelated for $\Delta y > 0.5$ m.

Field observations from alongshore arrays of ADVs also found that the structure function satisfied the scaling for an inverse cascade [*Elgar and Raubenheimer*, 2020], but did not reveal how the scaling of $S \sim (\Delta y)^{2/3}$ varied with the wave conditions. Alongshore velocity structure functions computed from phase-resolved, depth-averaged numerical simulations

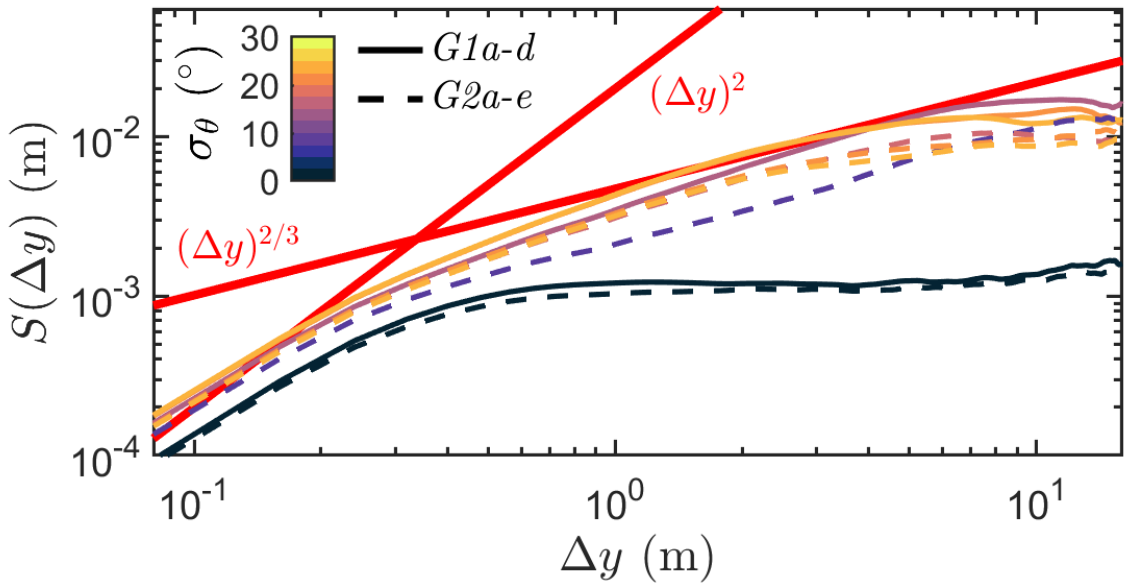

Figure 3.14: The surfzone-average structure function computed from 8-s median filtered PIV alongshore velocities ($S(\Delta y)$ from $28 < x < 31.5$ m) as a function of the alongshore lag (Δy) for trials *G1a-d* (27-cm waves, solid curves) and *G2a-d* (24-cm waves, solid curves) with directional spreads (σ_θ, curve colors) from 2-26°. The theoretical scalings for the second-order velocity structure function in strictly two-dimensional turbulence are shown (red lines), including a direct enstrophy cascade ($S \sim \Delta y^2$) and inverse energy cascade ($\sim \Delta y^{2/3}$, blue dashed lines).

over alongshore-uniform bathymetry [*Spydell and Feddersen*, 2009] were more consistent with an inverse cascade for larger directional spreads for $\Delta y = 5 - 100$ m ($\sigma_\theta = 14,\ 20°$). Additionally, they found that structure functions exhibited scalings less consistent with an inverse energy cascade for smaller directional spreads ($\sigma_\theta \leq 7°$), similar to lab observations. The better consistency with an inverse energy cascade for large directional spreads relative to smaller directional spreads suggests there may be an optimal forcing length scale or spatial distribution of injected vorticity that enhances the nonlinear transfer of energy to larger

scale rotational motion [*Peregrine*, 1999]. The steeper scalings for small directional spreads (*i.e.,* $\sim \Delta y^{7/8}$ in Figures 3.9 and 3.14) may be due to the presence of additional dynamics enhancing nonlinear interactions between eddies and vortices or the presence of anisotropy in the flow. This could be due to fluctuations of mean circulation patterns extending towards the center of the tank or infragravity wave modulations due to interactions with side walls during low directional spreads (Figures 3.10 and 3.7). Similar to numerical modeling and field observations [*Spydell and Feddersen*, 2009; *Elgar and Raubenheimer*, 2020], the magnitude of the structure function is larger within the inner surf zone, where significant wave dissipation occurs. Note that the other intense dissipation region is the offshore edge of the bar crest, offshore of the outer-most structure function estimate. These results are more consistent with an inverse energy cascade than previous numerical simulations with an alongshore current [*Feddersen*, 2014], where the scalings of an alongshore-wavenumber spectra of vorticity were only occasionally consistent with expected scalings for two-dimensional turbulence.

These optically-derived estimates are the first set of observations to characterize the longest length scale of eddies in the surf zone (l_0), the maximum length scale at which velocities are correlated. Here, l_0 decreases with directional spread, consistent with numerical simulations [*Spydell and Feddersen*, 2009], and weakly increases with wave height (Figure 3.14). l_0 decreases from 7 to 4 m from $\sigma_\theta = 17 - 26^\circ$ for $H_s \approx 0.27$ m (trials *G1b-G1d*) and 12.3 to 3.5 m from $\sigma_\theta = 10 - 16^\circ$ for $H_s \approx 0.24$ m (*G2b-G2d*). Similar to numerical simulations [*Spydell and Feddersen*, 2009], the largest alongshore length scales of the flow are on the order of the surfzone width ($W_{\text{sz}} \approx 4.4 - 4.9$ m, Figure 3.1b) for wave conditions with large directional spread. Thus, it is possible that the surfzone width sets the longest length-scales of the flow (*e.g.,* Figure 3.8d). This is further supported by the larger l_0 for larger waves with a wider surf zone (Table 3.1).

In contrast to cases with large directional spreads, l_0 for small directional spreads is 2-3 times the width of the surf zone. Assuming that the eddy cross-shore length is determined by the surfzone width (*i.e.,* eddies are not extending outside of the surf zone), this suggests that eddies may be anisotropic with longer alongshore length scales than cross-shore length

scales (*e.g.,* the negatively-signed vortex structure in Figure 3.8b). An alternative hypothesis is that the crest length (L_c) or gaps between waves (L_g) controls the longest length scales (Figure 3.1b). For directionally spread waves, l_0 from structure functions are approximately L_c. Hypothetically, this length-scale-dependence could be explained by the average along-crest varying breaking force profile with Gaussian fit for crest ends (*i.e.,* where $L_\omega \approx L_c$, Figure 3.2c). However, this does not account for injection length scales varying across the surf zone (*i.e.,* Figure 3.2 a vs. b). As vortex scales may be limited by neighboring vortices of opposing signs, it is also possible that L_g is a limiting factor on the largest scale of generated vortices ($L_g = L_y - L_c$, where L_y is the alongshore wavenumber). Despite the relevant scales associated with L_c and L_g, this would suggest that the turbulent fluctuations could be injected at the maximum length scales of the system, thus limiting the relevance of an inverse cascade.

Previous studies have hypothesized that the scales of injected vorticity (l_i) can be estimated as the intersection of the enstrophy cascade ($S \sim (\Delta y)^2$) and inverse energy cascade ($S \sim (\Delta y)^{2/3}$) [*Spydell and Feddersen*, 2009; *Elgar and Raubenheimer*, 2020]. Previous numerical modeling results suggest that the intersection between the two inertial ranges decreases with directional spread [*Spydell and Feddersen*, 2009]. The intersection of the two inertial ranges with the least squares regression curves does not decrease with increasing directional spread from $\sigma_\theta = 10^\circ$ to $\sigma_\theta = 24^\circ$ for 24-cm waves (Figure 3.9b,c), and may be due to limitations of PIV estimates at small lags given that a 24x24-cm spatial median filter is applied to PIV estimates. Alternatively, if scalings expected for the enstrophy and inverse cascade were enforced when fitting the structure function curves as done in *Spydell and Feddersen* [2009] (*e.g.,* blue dashed lines in Figure 3.9c), l_i from laboratory observations would decrease with directional spread from 0.6 m to 0.3 m (not shown). Due to large variation in injection length scales on a crest-by-crest basis (Section 3.5.1), it is doubtful that vorticity injection is limited to the length scales indicated by intersection between scale for the enstrophy and inverse energy cascade (*i.e.,* broad yellow range in Figure 3.1d).

3.5.3 *Progress towards a conceptual model connecting directionally spread waves to cross-shore exchange*

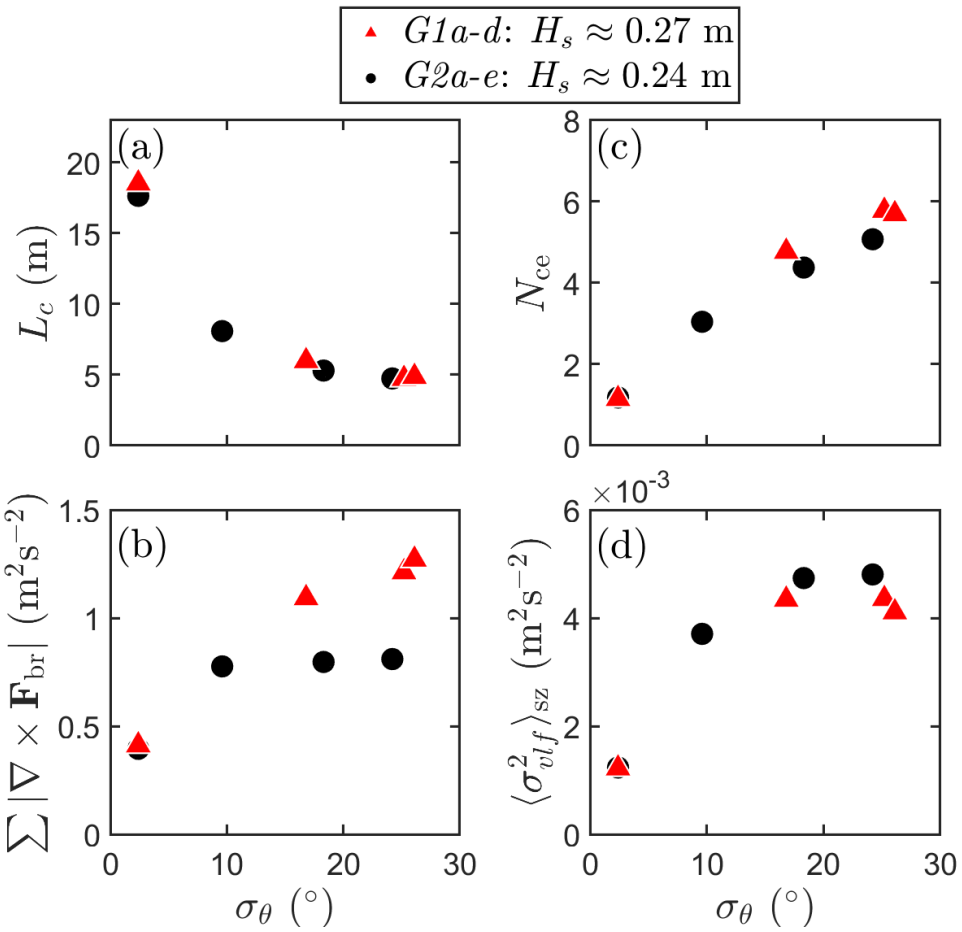

Figure 3.15: The relationship between directional spread (σ_θ) and (a) the average breaking crest length (L_c), (b) average number of crest ends (N_{ce}), (c) median total external vorticity forcing ($\sum |\nabla \times \mathbf{F}_{\mathrm{br}}|$) across the surf zone for a given instance in time. (d) These characteristics related to vorticity forcing are compared with the average total very low-frequency velocity power across the surf zone ($\langle \sigma^2_{vlf} \rangle_{\mathrm{sz}}$). Estimates are shown for trials *G1a-d* with $H_s \approx 0.27$ m (black circles) and *G2a-d* with $H_s \approx 0.24$ m (red triangles).

Progress towards a conceptual model is proposed based on laboratory observations for a

barred beach. As the directional spread of the wave field increases, the breaking crest length decreases and number of crest ends increases within the surf zone [Figure 3.15, *Baker et al.*, in review]. When short-crested breaking occurs, vorticity injection is driven by the curl of the breaking force (estimated here as the along-crest gradient of the cross-crest component of the breaking force, $\partial \mathrm{F}_{\mathrm{br},x_c}/\partial y_c$). The largest stereo-derived breaking force gradient is typically near crest ends, and gradients along the crest are ubiquitous for irregular directionally spread wave fields, altering vorticity injection length scales (Figure 3.5). The vorticity injection length scales differ by surfzone region and depend on the assumptions about breaking dissipation near crest ends, but may range from scales of the wave crest (*i.e.,* Figure 3.2c) to much smaller scales (*i.e.,* Figure 3.2b,d), especially for steady-state bores in the inner surf zone. On average, longer waves in the outer surf zone contribute more external forcing (gradient in the breaking force) than short waves in the inner surf zone (Figure 3.13). However, directionally spread waves consistently drive significant vorticity forcing (Figures 3.6 and 3.15,b), resulting in an increase in the median total external vorticity forcing with directional spread as well as wave height.

An increase in the number of crest ends and the total external vorticity forcing may be imperative to provide an input that is acted on by an inverse energy cascade, as indicated by the increase in surfzone-average very low-frequency velocity power with directional spread. Interestingly, larger total external vorticity forcing across the surf zone for larger wave heights does not result in an increase in large-scale low-frequency rotational motion. This could suggest that the number of crest ends, which exhibit little dependence on wave height, may play a more significant role in defining very low-frequency eddy activity. Alternatively, the steep barred bathymetry may alter the dependence of very low-frequency eddy activity on wave height. Further experiments with more wave heights and differing beach profiles should explore this relationship.

These findings have strong implications for dispersion within the surf zone and cross-shore exchange between the surf zone and the inner shelf. Visual examination of PIV velocities and imagery of wiffle ball ejections (Figure 3.16) suggest that the frequency of transient rip

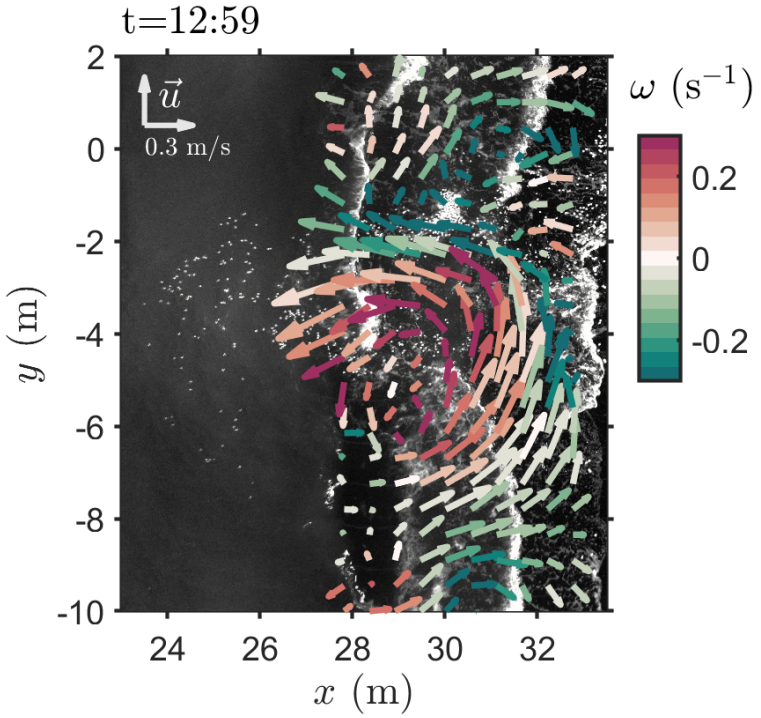

Figure 3.16: Example transient rip-current-ejection of wiffle balls from the surf zone onto the inner shelf. Low-frequency velocities ($\vec{u}$) estimated with particle image velocimetry (arrows, plotted every 0.55 m) are colored by the vertical vorticity (ω) and overlain on an image as a function of the cross- (x) and alongshore (y) position at time, t.

current ejections may increase from moderate to large directional spreads. For example, the frequency of visually identified ejections over a 10 min time series increased from 4 to 7 for 24-cm waves with $\sigma_\theta = 10°$ to 24° (trials *G2b* and *G2d*). Notably, preferential eddy ejection sites may have been altered by the mean circulation pattern near the side walls (Figure 3.7). For example, the cross-shore velocity estimates from PIV show offshore directed cross-shore velocities that persist within the middle 2/3 of the wave basin from $y \approx$-10 m to 10 m (not shown). Future work should explore the relationship between the wave conditions and ejection frequency and speed without limitations due to side walls.

In addition to the wave-averaged vorticity injection, other length scales and processes may

be relevant for surfzone eddy evolution and transient rip current ejections, such as the sheet of vortices injected by a wave across the surf zone (*e.g.,* relevance of a vortex strip roll up), the spacing between waves, and wave-current interaction (Figure 3.1b). Furthermore, this paper focused primarily on vertical vorticity and the relevance of two-dimensional turbulence within the surf zone. However, there are a numerous reasons why the surf zone may not be consistent with a strictly two-dimensional turbulence system. The surf zone has a sloping bottom, a short cross-shore extent relative to the alongshore domain, an open offshore boundary, unsteady forcing (*i.e.,* short-crested wave breaking vorticity injection may vary in space and time), and mean circulation features that may alter the flow-field. The impact of these differences on the circulation of eddies are not known, but likely result in more complex dynamics and energy-transfers than can be explained by two-dimensional turbulence. A few recent studies suggest that wave-forced vorticity may be more similar to an applied surface stress [*Kirby and Derakhti*, 2019] and that vertical variability of wave-forced vorticity may be relevant to the efficiency of an inverse energy cascade [*Uchiyama et al.*, 2017; *McWilliams et al.*, 2018; *Marchesiello et al.*, 2021b]. Thus, the three-dimensionality of these processes may play a role in surfzone dispersion and exchange processes.

Although results from the laboratory observations support many findings consistent with field-scale numerical model simulations and one set of field observations, the finite width of the laboratory and steep bathymetry may differ from the field environment, discussed in detail in [*Baker et al.*, in review]. Future work should explore the sensitivity of the inverse cascade, maximum length scales, and ejection sites to varying bathymetry and wave conditions in the field.

3.6 Summary and conclusions

Energy associated with wave-breaking-injected vorticity, ubiquitous for short-crested wave fields, may be non-linearly transferred to large scale eddies that enhance transient rip-current-driven exchange. Laboratory experiments in a directional wave basin with a combination of in situ and remotely-sensed observations permitted quantification of surfzone vorticity

dynamics.

A theoretical framework using along-crest coordinates to assess the curl of the breaking force is proposed and applied to laboratory observations. Using stereo reconstructions of the laboratory water surface, the along-crest dissipation and breaking force were estimated with a roller model. The breaking force and its curl, which drives a time-rate of change in surfzone vorticity, are highly irregular along individual waves and vary from crest to crest. The curl of the breaking force is positively and negatively signed near opposite crest ends. Averaging over many crests, the shape of the crest-averaged curl of the breaking force varies by surfzone region and crest length, indicative of the vorticity injection length scales. Also, the assumptions about the decay of dissipation outside of an identified crest region may significantly alter the along-crest breaking force profile. The total external vorticity forcing (sum of the absolute value of the curl of the breaking force across the surf zone) is consistently large for more directionally spread waves. In contrast, waves with small spreads typically have small external vorticity forcing, with the exception of sporadic estimates of large vorticity input due to the highly along-crest variable breaking force for long waves near the onset of breaking.

The spatial characteristics of low-frequency currents, estimated from in situ sensors and remote particle image velocimetry (PIV), vary with wave directional spread and are similar to expected relationships for a two-dimensional turbulence inverse energy cascade. Very low frequency power increased from small to moderate directional spreads, but the relationship may be nonmonotonic, possibly due to a maximum forcing that leads to an enhancement of large-scale eddies. Alongshore velocity structure functions varied by surfzone region and between measurement types, which could be due to depth-variable low-frequency currents. Structure function scalings were more consistent with an inverse energy cascade for larger directional spreads, and the enstrophy cascade regions were not well resolved with PIV estimates. The maximum length scale of the inverse energy cascade increases with decreasing directional spread, varying from length scales of the surfzone width (large directional spreads) to several multiples of the surfzone width (moderate directional spreads), suggesting that

the eddies may be anisotropic.

Progress towards a conceptual model linking wave conditions to transient rip current formation is proposed. As directional spread increases, crest length decreases and number of ends increases [*Baker et al.*, in review], leading to continuously large total external vorticity forcing. The forcing leads to heightened low-frequency eddy activity, which is typically linked to a greater cross-shore exchange driven by transient rip currents. This effect is most pronounced when the directional spread is small to moderate, and it levels off or diminishes when the directional spread is large. These findings harbor strong implications for material dispersion mechanisms and transport pathways within the nearshore. Despite this progress, there are many additional questions regarding wave-injected vorticity and surfzone eddy evolution that require further attention.

3.7 Appendix A: Comparison between in situ and PIV velocities

The optically-derived surface velocities excluding crest regions with an 8-s median filter (Section 3.3.3) compared with bottom mounted ADV velocities at the nearest velocity estimate on the PIV grid. For directionally spread 0.24-m waves (trial *G2d*), the PIV estimates generally capture the velocity fluctuations (sign and temporal variability) observed with in situ sensors for both the cross- and alongshore velocities in the outer (Figure 3.17c,d) and inner surf zone (Figure 3.18c,d). The in situ and PIV velocities are correlated in the outer and inner surf zone (see correlations in Figures 3.17b, 3.18b) with a root-mean-squared deviation (RMSD) of 0.03-0.04 m/s and no bias. Results for cross-shore velocities are slightly less correlated with positive bias and a RMSD around 0.1 m/s (Figures 3.17a, 3.18a). Surface velocities are more coherent with in situ sensors at low-frequencies ($f < 0.2$ Hz), particularly for the alongshore velocity component in the inner surf zone (Figure 3.19b). Sheared cross-shore flows, for example due to onshore mass flux the near surface and return flow at the bottom, may limit the coherence of low-frequency velocity signals at different positions in the water column. Cross-shore velocities are more coherent at surface-gravity wave frequencies ($f \approx 0.5$ Hz).

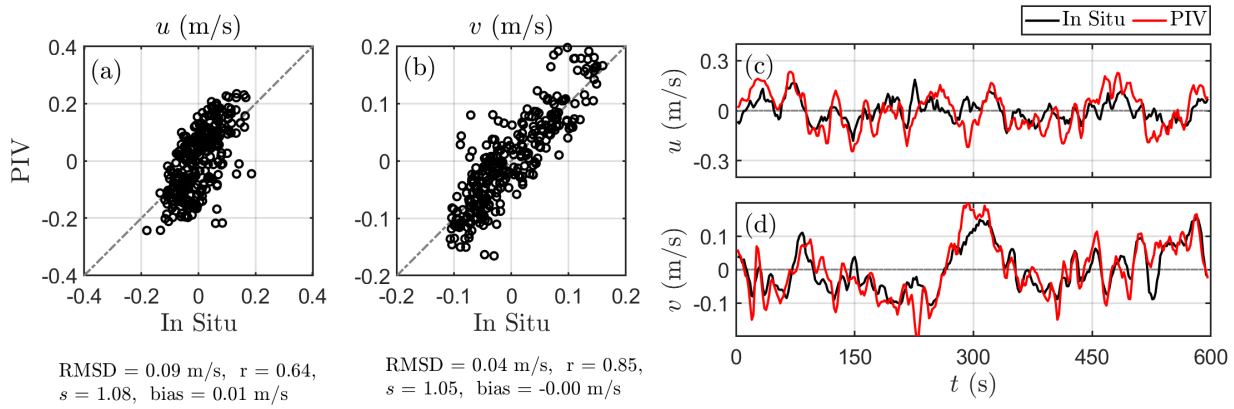

Figure 3.17: Example 8-s median filtered in situ and PIV velocities over a 10-min time series (subsampled at 0.5 Hz) with the mean removed for a location in the outer surf zone (p7, $x, y = 28.4, 1.6$ m) for trial *G2d* ($H_s = 0.24$ m, $\sigma_\theta = 24°$). (a,b) The in situ (x-axis) vs. PIV (y-axis) velocities for the (a) cross-shore (u) and (b) alongshore (v) velocities with a 1:1 line (dashed). (c,d) Time series (t) for the in situ (black) and PIV (red) (c) cross-shore and (d) alongshore velocities. The root-mean-squared deviation (RMSD), correlation (r), slope (s), and bias (positive indicates larger PIV estimates) are reported for the cross- and alongshore velocity time series.

These trends are consistent for other in situ sensors at the same cross-shore position and generally similar for different wave conditions. For a subset of trials (*G1a, G1c, G1d, G2d*) with varying wave height and directional spread, the RMSDs between PIV and in situ velocities are typically lower for alongshore velocities than for cross-shore velocities (Table 3.2). RMSDs are similar in the outer and inner surf zone for cross-shore velocities, while they are smaller in the outer surf zone for alongshore velocities. PIV cross- and alongshore velocities during smaller waves are better correlated with in situ estimates, while correlations are better in the outer surf zone for larger waves, where breaking (and thus, foam generation) starts farther offshore. Due to lack of persistent foam (inhibiting tracking), correlations between in situ and PIV estimates are lower for unidirectional waves. Additionally, alongshore velocity

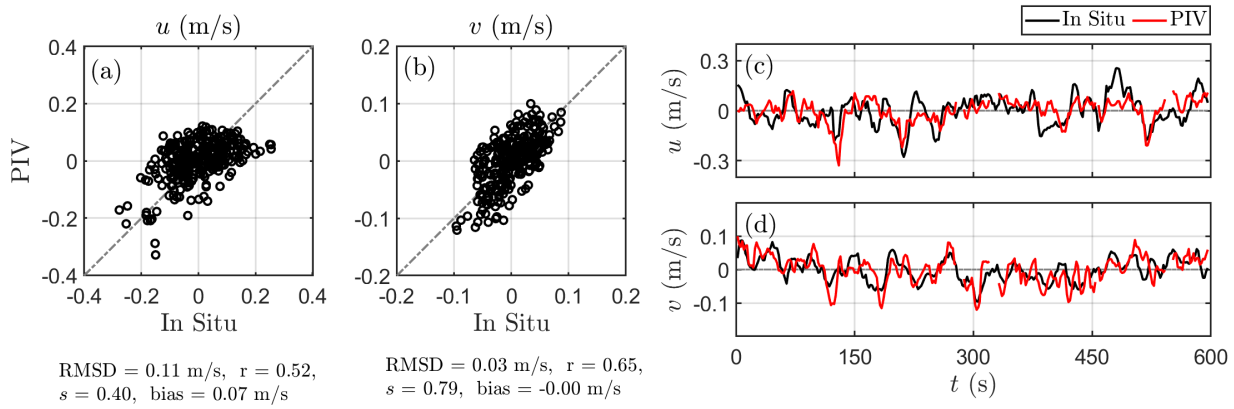

Figure 3.18: Same as in Figure 3.17, except for a sensor in the inner surf zone (p11, $x, y = 30.7, -0.1$ m).

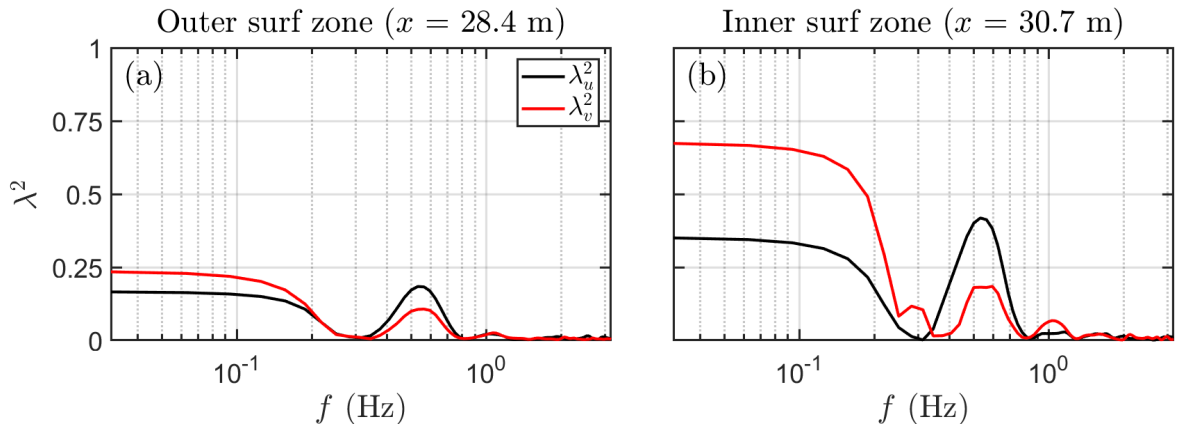

Figure 3.19: The average squared coherence (λ^2) as a function of frequency (f) between the 8-Hz in situ observations and PIV estimates for the cross-shore (u, black) and alongshore (v, red) velocities in the (a) outer surf zone ($x = 28.4$ m) and (b) inner surf zone ($x = 30.7$ m).

fluctuations during unidirectional waves are small ($v = \pm 0.05$ m/s) and on the order of PIV-estimate uncertainties.

Median filtered PIV velocities are less consistent when crests are not removed. PIV estimates in the outer surf zone are slightly improved when the distance around each removed

wave crest was expanded from 20 to 30 cm (*i.e.,* expanding RBIS-identified crest region only changes comparisons by $< 5\%$). Removing a larger region around breaking crests did not significantly change median filtered PIV estimates in the inner surf zone. Lowering the threshold values for the RBIS-identified crests (*i.e.,* selecting more crest features or larger regions) did not improve PIV estimates. The processing workflow was optimized for reducing differences between in situ and PIV estimates and maximizing the number of points retained. PIV vs. in situ comparisons were similar for longer median filters (*e.g.,* 6 or 8 s). Shorter median filters resulted in larger RMSD between the PIV and in situ velocities.

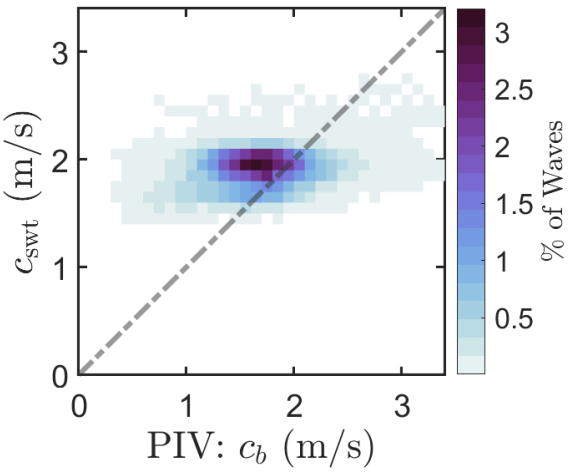

Figure 3.20: Two-dimensional histogram comparing the average bore celerity (c_b, bin width = 0.1 m/s) per wave crest measured with PIV vs. bore celerity estimated with solitary wave theory (c_{swt}, Eqn. 3.10) estimated with the along-crest mean water depth and height per wave crest. The plot is colored by the percent of waves for a 10-min timeseries from Trial *G2d*.

Bore celerity from PIV are used to estimate the wave breaking force (Section 3.3.4, Eqn. 3.5). Here, we compare the bore speeds identified directly with PIV with estimates based on solitary wave theory. For Trial *G2d*, the average PIV-derived bore celerity ($\overline{c_b(y_c)}$) along each crest of RBIS-identified crest are of a similar average magnitude to average celerity

Table 3.2: The root-mean-squared deviation (RMSD), correlation (r), slope (s), and bias (positive indicates larger PIV estimates) of the PIV velocity estimates relative to the in situ measurements. Statistics for the cross- (u) and alongshore (v) velocities are the average of sensors in the outer ($x = 28.5$ m) and inner ($x = 30.7$ m) surf zone for all trials (Table 3.1).

Measurement	Statistic	*G1a*	*G1c*	*G1d*	*G2d*
Offshore u	RMSD (m)	0.10	0.09	0.10	0.11
	r (m)	0.32	0.51	0.43	0.41
	s	0.34	0.49	0.37	0.29
	bias (m)	0.06	0.01	0.04	0.07
Offshore v	RMSD (m)	0.03	0.05	0.05	0.04
	r (m)	0.20	0.54	0.56	0.53
	s	0.24	0.87	0.97	0.62
	bias (m)	0.00	0.04	0.00	0.00
Onshore u	RMSD (m)	0.10	0.10	0.10	0.08
	r (m)	0.63	0.44	0.55	0.56
	s	0.59	0.71	0.96	0.93
	bias (m)	0.08	0.00	0.03	0.02
Onshore v	RMSD (m)	0.03	0.08	0.08	0.05
	r (m)	-0.07	0.62	0.62	0.82
	s	-0.04	0.96	0.99	0.99
	bias (m)	0.00	0.02	0.00	0.00

along each crest calculated with solitary wave theory (c_{swt}, Figure 3.20):

$$c_{\mathrm{swt}} = \sqrt{g\overline{h}\left(1 + \frac{H}{\overline{h}}\right)} \tag{3.10}$$

where $\overline{h}$ is the mean water depth at the bore crest [*Stringari et al.*, 2019] and H is the wave height estimated from stereo reconstructions. Solitary wave theory may be a better approximator of surfzone wave celerity than linear wave theory [*Postacchini and Brocchini*, 2014]. The PIV bore celerity estimates have a larger spread than the solitary wave theory (Figure 3.20), which may be expected due to wave-current interaction and other processes. Here, we choose to use the PIV estimate to represent a realistic range in celerity, acknowledging that the PIV speeds rely on surface foam and are sensitive to the method developed to select velocities of gridded estimates along the wave crest.

3.8 Appendix B: In situ velocity and pressure spectral analysis

The relative contribution of rotational and irrotational motions as well as the seiching patterns were analyzed with in situ velocity and pressure sensors. These relationships were found to be qualitatively consistent across sensor locations in the inner and outer surf zone. Here, a representative example is described from a 35-min time series (5-40 min) from a sensor in the outer surf zone ($x, y = 28.4, -6.2$) for unidirectional and directionally spread wave conditions (trials *G2a,d*: $\sigma_\theta = 2^\circ$ and 24°).

At very low-frequencies ($f < 0.02$ Hz), the velocity spectral levels ($S_{uu} + S_{vv}$) are 5 times larger than sea-surface elevation spectral levels converted to equivalent velocity using the linear finite-depth dispersion relationship ($S_{\eta\eta} * g/h$, where h is the mean water depth and g is gravitational acceleration, Figure 3.21a). This suggests that currents are primarily rotational at very low-frequencies [$f < 0.02$ Hz *Lippmann et al.*, 1999; *MacMahan et al.*, 2010a; *Feddersen et al.*, 2011; *Elgar et al.*, 2019].

Cross-shore seiching modes at low-frequencies decrease with increasing directional spread ($f < 0.2$ Hz, Figure 3.21b, gold region) and decreasing wave period (*e.g.,* from $T_p = 4$ to 2 s, not shown). The 2-s directionally spread wave conditions do not exhibit significant

cross-shore seiching patterns (Figure 3.10b, black curves). For example, the most significant cross-shore seiching mode at $f = 0.8$ Hz, apparent in the unidirectional case, is nearly absent for directionally spread waves. Despite this, analysis over low-frequencies conservatively used solely alongshore velocities (*i.e.,* structure function analysis), where there is little evidence of significant seiching modes in the alongshore velocities (Figure 3.21b, solid curves).

Cross-shore seiche modes at 23.4, 13.7, 8.6, and 6.8 s are slightly longer than periods computed with the Merian's formula for a rectangular basin with uniform depth [*i.e.,* 21.0, 10.5, 7.0, and 5.2 s for $n = 1 - 4$ *Rabinovich*, 2009]. As there is a slope starting at x =22 m from the wavemaker, Merian's formula may not produce the exact seiching periods [*e.g.,* estimates for a triangular basin with akin geometry have slightly longer seiching periods, *Rabinovich*, 2009]. Notably, there is a cross-shore seiche node for $f < 0.04$ Hz along the in situ array near $x = 28.4$ m (Figure 3.21a) and possibly an anti-node near $x = 30.7$ m that may alter breaking patterns and currents. When shorter time series over the 45 min trial were analyzed, there was no evidence that seiching patterns grew throughout the trial run. For example, Empirical Orthogonal Function (EOF) analyses of in situ sensors from the pressure gauges, ADVs and wire resistance gauges show no evidence of modes growing over time (not shown).

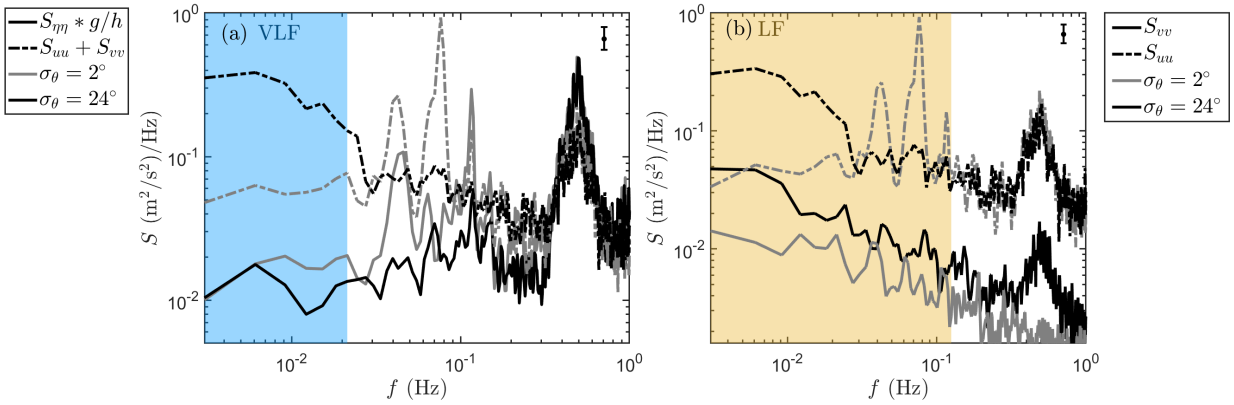

Figure 3.21: (a) The velocity spectra (dashed curves, sum of cross- and alongshore-auto spectra, $S_{uu} + S_{vv}$) and sea-surface elevation spectra converted to equivalent velocity using the linear finite-depth dispersion relationship (solid curves, $S_{\eta\eta} * g/h$, where h is the mean water depth and g is gravitational acceleration) as a function of frequency (f) are compared at very low-frequencies (VLF, blue shaded region, $f < 0.02$ Hz). (b) The cross- (S_{uu}, dashed curves) and alongshore velocities (S_{vv}, solid curves) are compared at low-frequencies (LF, brown shaded region, $f < 0.2$ Hz). (a,b) This example is from in situ sensors in the outer surf zone ($x, y = 28.4, -6.2$ m) for trials *G2a* (grey curves, $\sigma_\theta = 2°$) and *G2d* (black curves, $\sigma_\theta = 24°$) over a 35 min time series. The 95% confidence intervals (error bar) are shown.

Chapter 4

IMPLICATIONS AND FUTURE DIRECTIONS

4.1 Short-crested wave breaking and vorticity injection

Short-crested wave breaking alters dissipation patterns [*Kirby and Derakhti*, 2019] and injects vorticity into the water column [*Clark et al.*, 2012], enhancing dispersion [*Spydell and Feddersen*, 2009; *Clark et al.*, 2012]. The results from laboratory experiments established that as directional spread increases, the number of crest ends and total wave forcing increases, while breaking crest length decreases (Chapter 2). These insights are an initial step in connecting the wave field characteristics to vorticity injection, but many question remain.

4.1.1 How does dissipation and the breaking force vary with breaker characteristics across the surf zone?

Other than the findings in this thesis, there have not been observations of the along-crest variability of dissipation and the breaking force for short-crested waves. These processes are highly irregular on a wave-by-wave basis (Chapter 3) and the treatment of dissipation near crest ends is unclear. Most parameterizations for wave-by-wave energy dissipation during the onset of breaking [*Ting and Kirby*, 1995; *Iafrati*, 2011] or in a well developed bore [*Svendsen*, 1984a; *Duncan*, 1981] are derived and tested without regard to variability along a wave crest [*Martins et al.*, 2018; *Carini et al.*, 2015]. However, the along-crest variability in dissipation and breaking force patterns have strong implications for vorticity injection during breaking. Further research is necessary to develop a framework for quantifying and exploring the along-crest variability in wave energy dissipation and the breaking force. Currently, we still lack understanding of dissipation and the breaking force for short-crested wave fields in the following contexts: profiles near crest ends, variability between long- and short-crested

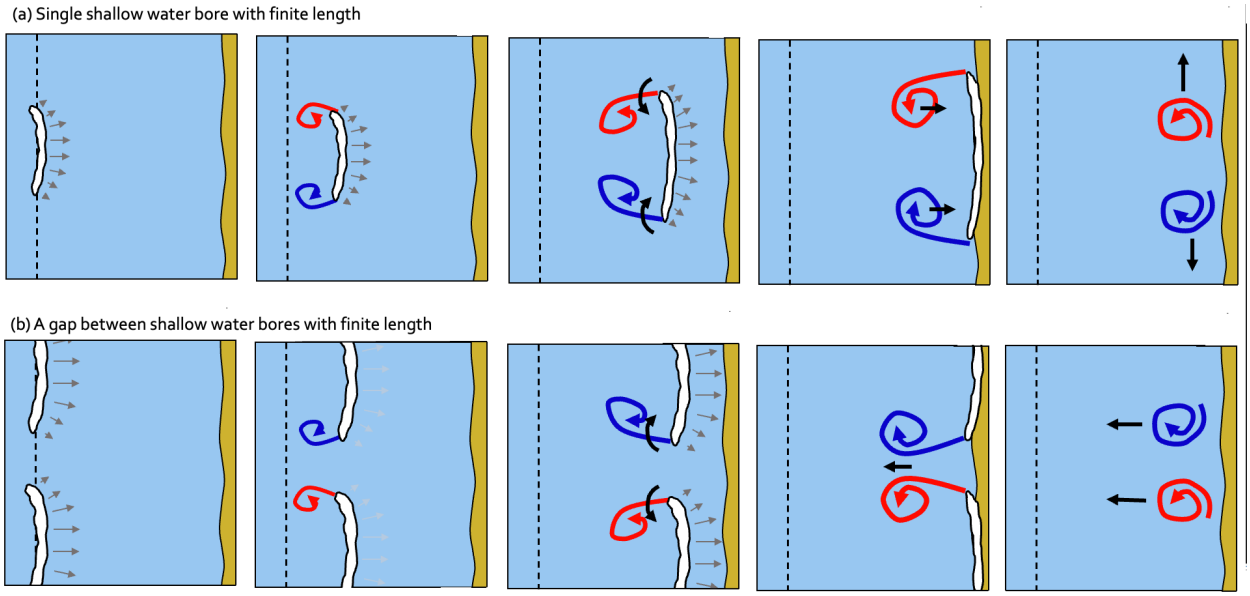

Figure 4.1: Schematic modified from *Peregrine* [1999] of theoretical vortices injected near crest ends for an (a) single wave crest and (b) gap between two wave crests. Waves inject vorticity across the surfzone as they propagate shoreward, resulting in a vortex strip that rolls up and can detach when breaking ceases at the shoreline or over deeper waters (*e.g.,* a trough). In the absence of other currents, (a) vortices on either side of a crest may advect shoreward with the wave until they reach the shoreline and propagate parallel the beach with their image. (b) Vortices interact in the gap between breaking crest ends, causing mutual advection in the direction opposite of the wave crest propagation.

waves, sensitivity to the beach profile and bathymetric variability, implications for sediment transport and runup, and accuracy of current numerical model parameterizations. Some of these topics are currently being investigated with a phase-resolved numerical modeling [*Nuss et al.*, in prep].

4.1.2 How does the curl in the breaking force relate to low-frequency vertical vorticity generation?

It is assumed that the time-rate of change in vertical vorticity is equal to the curl of the breaking force [*Spydell and Feddersen*, 2009; *Feddersen*, 2014]. The only set of field experiments that tested this found discrepancies between observed vortical vorticity and a highly-simplified parameterization of the alongshore gradient in the breaking force [*Clark et al.*, 2012]. Furthermore, two recent numerical modeling studies suggest that vertical vorticity injected at crest ends may be better represented as an applied surface stress than a depth-uniform process [*Kirby and Derakhti*, 2019], which has important implications for vorticity evolution in the surf zone [*Marchesiello et al.*, 2021a]. The laboratory observations here could not test this relationship between the curl of the breaking force and the time-rate of change in vorticity nor with the depth variability due to a lack of observations of vorticity at the timescales of individual wave crests. However, these observations surfaced pressing questions about how these process are conceptualized. For an irregular directionally spread wave field, the curl of the breaking force is highly irregular on a wave-by-wave basis (Chapter 3). We still do not know how this translates to vertical vorticity that can cascade to larger scales or the implications of the vertical variability in injected vortices. What characteristics length scales are necessary to quantify wave-generated circulation in the field setting? What are there limitations of measuring vorticity injection with Kelvin's circulation theorem at a pre-defined length scale [*Peregrine and Bokhove*, 1998; *Clark et al.*, 2012]?

4.1.3 How do individual wave-forced vortices evolve within the surf zone?

The vorticity injected at a crest end at one instance in time may not fully capture the nature of wave-forced vorticity across the surf zone. As proposed by *Peregrine* [1999], as waves propagate shoreward, they may inject same-signed vorticity into the surf zone, resulting in a vortex strip that can roll up with different length scales and circulation than the individual vortices (Figure 4.1). These vortices may self- or mutually advect within the surf zone

depending on the length scales on individual breakers or spacing between breakers (Figure 4.1). Furthermore, in the field, the vortices are injected into a surf zone with a pre-existing complex vorticity field. A few theoretical and numerical modeling studies have explored the evolution of individual vortices [*Bonneton et al.*, 2010; *Bühler*, 2000; *Bühler and Jacobson*, 2001]. The length scale dependencies of injected vortices, interaction with other vortices or changing bathymetry, and implications for an inverse energy cascade remain unknown (see more discussion in Section 3.5).

4.2 Eddy evolution and ejection

Vortices injected by individual breaking waves may cascade to larger scales that eject offshore as a transient rip current [*Johnson and Pattiaratchi*, 2006; *Hally-Rosendahl et al.*, 2014; *Hally-Rosendahl and Feddersen*, 2016; *Hally-Rosendahl et al.*, 2015], resulting in cross-shore exchange between the surf zone and inner shelf [*Suanda and Feddersen*, 2015; *Kumar and Feddersen*, 2017c, a]. In laboratory experiments (Section 3.5), the spatial characteristics of low-frequency currents suggest that a nonlinear transfer of energy from injected vorticity to low-frequency large-scale rotational motions occurs within the surf zone for wave conditions with large directional spreads. However, there are still many unknowns pertaining to the physical mechanisms enhancing or disrupting the likelihood of a nonlinear transfer of energy to larger scales and many questions relating to transient rip-current-driven surf-shelf exchange.

4.2.1 How well does an inverse energy cascade describe surfzone eddy evolution within the surf zone?

Despite recent studies [*Spydell and Feddersen*, 2009; *Elgar and Raubenheimer*, 2020] and laboratory observations herein identifying some spatial and temporal tendencies consistent with two-dimensional turbulence, the extent to which the surf zone exhibits properties consistent with a forced two-dimensional turbulence environment are not well established. Discrepancies between surfzone vorticity variability and two-dimensional turbulence have been

found in some numerical simulations [*Feddersen*, 2014]. Additionally, depth variability in low-frequency eddies may alter the efficiency of an inverse energy cascade [*Uchiyama et al.*, 2017; *McWilliams et al.*, 2018; *Marchesiello et al.*, 2021a]. In contrast to a strictly two-dimensional turbulence system (*e.g.,* Figure 3.1), the surf zone has a sloping profile, a short cross-shore extent relative to the alongshore domain, an open offshore boundary, unsteady forcing (*i.e.,* short-crested wave breaking vorticity injection may vary in space and time), variable bathymetry (*e.g.,* a steep bar crest in the laboratory experiments, Figure 4.2), and mean circulation features that may alter the flow-field. The impact of these differences on the magnitude and structure of surfzone eddies and the efficiency of the inverse cascade is still not well understood. These processes vary with directional spread, wave height, and mean wave angle [*e.g.,* Chapter 3 and in *Spydell et al.*, 2007; *Spydell and Feddersen*, 2009; *Suanda and Feddersen*, 2015], but a complete understanding of the mechanisms leading to these tendencies is unknown. Several characteristics of the wave field may alter the likelihood of an inverse cascade, including the strength and relative distribution of the forcing. For example, if there is too much random forcing (*e.g.,* possibly high directional spreads), the formation of large-scale coherent eddies may be disrupted [*Kellay and Goldburg*, 2002]. Moreover, in the absence of bathymetric variability, the maximum length scale of eddies within the surf zone are not well understood and may be related to the surfzone width [*e.g.,* Fig. 3.14, *Spydell and Feddersen*, 2009] or other processes if eddies are anisotropic. The length scale distribution may have implications for mixing along the surf zone and the likelihood of offshore ejections.

4.2.2 When do eddies eject from the surf zone, and how do they evolve once they exit the surf zone onto the inner shelf?

Numerical model results suggest that transient rip-current-driven exchange may increase with directional spread [*Suanda and Feddersen*, 2015], but strikingly, suggest that the distance cross-shore decay scale is inversely proportional to the directional spread. Based on this, it could be hypothesized that more ejections occur for higher directionally spreads. However, this may not mean that there is more net exchange of material when waves are more spread.

Although it is hypothesized that pairs of counter-rotating eddies mutually advect offshore as a transient rip current [*Johnson and Pattiaratchi*, 2004b, 2006], the dynamics leading up to an ejection remain unclear. Do counter-rotating dipoles appear near each other randomly, or is there proximity due to other processes related to wave forcing or wave-current interaction? Once ejected offshore, eddies become quasi-two-dimensional [*Uchiyama et al.*, 2017], where vortex stretching and tilting may transform the eddies into three-dimensional processes that can readily collapse to smaller eddies through a forward energy cascade (*e.g.,* Figure 4.2). These processes may induce vertical mixing on a stratified inner shelf [*Kumar and Feddersen*, 2017b; *Grimes et al.*, 2020a] and drive mean inner shelf circulation [*e.g.,* Figure 4.2, *Grimes and Feddersen*, 2021]. Due to challenges of studying this process in the field, most of the foundational work on transient rip-current-driven exchange was addressed with numerical modeling that relied on parameterizations to simulate vertical mixing and did not include two-way coupling between transient rip currents and onshore propagating wave fields. Although significant progress has been made to understand transient rip current driven exchange processes, there are still many questions regarding the decay of eddies in the inner shelf and implications of vertical variability on exchange pathways.

4.3 Field implications for water quality, ecosystems, and human safety

It is well established that surfzone eddies and transient rip currents play an important role in driving mixing and exchange on fairly alongshore-uniform beaches [*Spydell et al.*, 2007; *Clark et al.*, 2010; *Hally-Rosendahl et al.*, 2014; *Spydell and Feddersen*, 2009; *Spydell et al.*, 2019]. The role of these processes in differing field environments as well as the implications for material transport and rip current hazards should be further explored.

4.3.1 How relevant are these processes to dispersion and exchange in varying field environments?

Low-frequency surfzone eddies are ubiquitous on many coastlines, enhancing surfzone dispersion [*Clark et al.*, 2010; *Hally-Rosendahl et al.*, 2014] and surf-shelf exchange [*Suanda and*

Feddersen, 2015]. However, many open questions remain regarding the relative dominance of these processes for driving exchange and mixing in field environments with alongshore-variable bathymetry, differing dominant wave conditions (*e.g.,* oblique wave conditions), and other relevant physical processes (*e.g.,* freshwater input, strong winds, tides). Unlike the fairly uniform beaches of Southern California, the bathymetry in other regions can be highly alongshore variable, driving mean circulation patterns, such as bathymetric rip currents. Recent numerical modeling studies have found that alongshore bathymetric variability enhances the alongshore length scales of large surfzone eddies, while small length-scale eddies are intensified by wave directional spread [*O'Dea et al.*, 2021b; *Baker et al.*, 2021]. The implications of these dependencies for exchange and surfzone dispersion remain unknown. A better understanding of the primary exchange processes for the continuum between alongshore-uniform morphology with transient eddies to channeled morphology with bathymetrically driven rip currents would help fill this gap [*McCarroll et al.*, 2018]. Similarly, surfzone eddy-enhanced dispersion and transient rip current driven exchange on eminently barred beaches, rocky shorelines, or regions with reef systems have not yet been examined. The relative role of transient surfzone eddies in differing environments could better inform predictions of material transport.

4.3.2 How do surfzone eddy processes and transient rip-current-driven exchange alter the transport of pollutants, larvae, and sediment?

Material exchange and dispersion driven by surfzone eddy processes has largely been explored through dye or drifter studies [*Spydell et al.*, 2007; *Clark et al.*, 2010; *Hally-Rosendahl et al.*, 2014] or numerical modeling [*Spydell and Feddersen*, 2009; *Kumar and Feddersen*, 2017c; *Spydell et al.*, 2009]. These studies use Lagrangian and Eulerian statistics to study nearshore hydrodynamics, but do not account for the characteristics of the particles, such as their buoyancy and behavior [*e.g.,* ability to sink or swim, *Moulton et al.*, 2023]. In addition to wave-driven shoreward mass fluxes and bed return flow [*Garcez-Faria et al.*, 2000], the uncharacterized ability for low-frequency eddies to rapidly disperse particles within and

offshore of the surf zone may depend on particle characteristics, with strong implications for intertidal subsidies and larval recruitment [*Morgan et al.*, 2017; *Shanks et al.*, 2010]. Also, few studies have explored the influence of surfzone eddies on sediment suspension and fluxes [*Miles et al.*, 2002]. The role of surfzone eddies in the fate of phytoplankton blooms, neutrally or positively buoyant particles, and contaminated nearshore waters requires further examination.

4.3.3 Do transient rip currents heighten hazards for recreational swimmers?

Each year, rip currents cause hundreds of deaths at beaches worldwide and thousands of rescues [*da F. Klein et al.*, 2003; *Hartmann*, 2006]. Present US predictive models of rip current hazards (*e.g.,* National Weather Service (NWS) rip current forecasts) were trained in North Carolina [*Dusek and Seim*, 2013; *Moulton et al.*, 2017a], where bathymetric rip currents may be dominant, Therefore, the model may miss hazardous transient rip currents more common in other areas, such as Southern California. The swimmer hazards associated with transient rip currents are still unknown due to their less predictable nature and challenges of operationally delineating rip current types. Furthermore, research has mainly focused on constraining bulk exchange driven by transient rip currents [*e.g., Suanda and Feddersen*, 2015], rather than individual ejection frequency (spatial and temporal), speeds, and trajectories that may be better indicators of human hazard. Ongoing work is applying bathymetric and transient rip current parameterizations [*Moulton et al.*, 2017b; *Suanda and Feddersen*, 2015] to test the NWS rip current forecasts [*Casper et al.*, in prep]. Future research could explore the characteristics of hazardous ejection events and their likelihood for a variety of beaches.

4.4 The role of laboratory experiments in exploring eddy dynamics

Most of our knowledge pertaining to vorticity injection, evolution, and ejection is from numerical models that parameterize breaking dissipation [*Kennedy et al.*, 2000], and vertical mixing [*Warner et al.*, 2005; *Kumar et al.*, 2012], and often cannot simulate two-way

interaction between breaking waves and surfzone currents [*Kumar and Feddersen*, 2017a; *Grimes et al.*, 2020b]. The lack of observations is largely due to the challenges of obtaining adequate spatial and temporal measurements that constrain these processes. Physical experiments are advantageous for exploring a phenomenon without simplifying assumptions or unknowns required in analytical or numerical modeling, while avoiding complexities of the field. Thus, this body of work was performed in the laboratory setting with alongshore uniform bathymetry, the absence of strong mean circulation patterns, repeatable and wave conditions spanning a wide parameter space with a range of expected vorticity injection, and an optimal setup for remote sensing observations. However, the laboratory environment is not without limitations that may alter the dynamics of interest.

Some may view a clear delineation between the idealized, controlled lab environment and the unpredictable, multi-faceted field setting, but perhaps there is a space between. Here, we studied stochastic processes imparted by a random directionally spread wave field generated by a mechanical wave maker in a basin constrained by side walls with a steep slope. Waves collided with and reflected off walls as they propagated shoreward. There was a weak mean current that may have caused preferential ejections away from side walls and seiching patterns that interacted with the wave and current field (see more in Section 2.4.3). Yet, we were able to address questions that may not otherwise be feasible in more idealized lab experiments nor the field. The previous three sections outlined current gaps in our knowledge pertaining to surfzone eddy processes that may be best addressed with differing and, ideally, multiple tools. Here, I provide several examples of questions prime for experimentation in the laboratory that are ordered by more idealized[1] and complex physical experiments.

Idealized laboratory experiments are primed for addressing questions about short-crested wave dissipation, vorticity injection, and evolution of individual vortices across the surf zone. Most of of our current parameterizations for wave dissipation were vetted in the laboratory

[1]Here, I refer to idealized laboratory experiments as those omitting forcing from an irregular, directionally spread wave field and that may be possible in smaller facilities.

setting [*e.g., Svendsen*, 1984a; *Duncan*, 1981; *Lamarre and Melville*, 1991]. Experiments of individual finite breaking crests could elucidate the along-crest variability in dissipation and the breaking force as well as the depth-dependence and evolution of coherent vortex structures injected during breaking (Figure 4.1a). Two intersecting [*Garnier et al.*, 2014] or pseudo-intersecting [*Choi and Roh*, 2021] wave trains could be employed to study the interaction between vortices, acceleration and decay of hydrodynamically-forced rip currents, and other wave-(rotational) current interaction processes (Figure 4.1b). Similar experiments could explore particle trajectories and mixing due to horizontal eddies and rip current-like flows. Potentially, vertical and horizontal mixing driven by ejected surfzone eddies on a stratified shelf could inform parameterizations or test numerical model predictions (Figure 4.2). Simplified experiments with vortices generated by mechanisms other than surface gravity waves could inform our knowledge of eddy evolution in the surf zone.

In addition to examples provided above, large scale experiments could be used to explore the evolution of randomly forced eddies by irregular directionally spread waves. Informed by laboratory observations herein, future experiments could improve our understanding vorticity field characteristics (*e.g.,* velocity variance and length scale distribution) and their sensitivity to differing beach profiles or a broader set of wave conditions. The contribution of eddy processes to surfzone mixing in the presence of variable bathymetry or an alongshore current (feasible in some facilities) could be explored. Sediment suspension via short-crested breakers or the possible feedback between morphology and low-frequency currents may be feasible in a large scale facility.

While the uncertainties that proliferate this field of study have partially been resolved herein, building on a strong foundation of prior work, the progress here has only begun to set the stage for future curious minds to solve the crucial yet elusive questions that define surfzone processes.

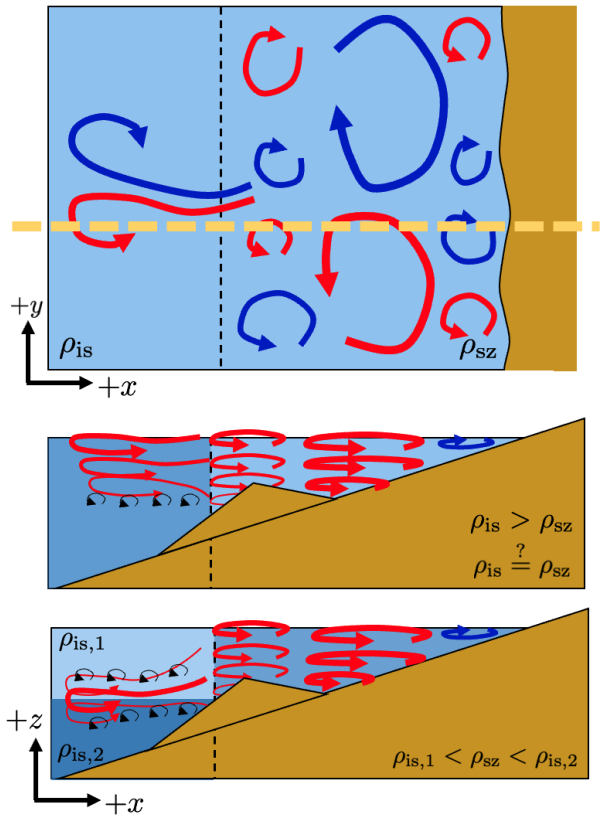

Figure 4.2: A schematic of two counter-rotating vortices ejecting onto the inner shelf. (a) The plan view as a function of the cross- (x) and alongshore (y) position shows positive (red) and negative (blue) vortices with a variety of length scales within the surf zone (dashed black line) to the shoreline (brown feature). Two counter-rotating vortices are ejecting from the surf zone with density, ρ_{sz}, onto the inner shelf (offshore of dashed black line) with density, $\rho_{sz,1}$. (a) A cross-shore transect (yellow line) extending from the shoreline to offshore is shown for (b) a surf zone with less dense or equivalently dense water than the inner shelf and (c) a two-layer stratified surf zone with less dense water near surface ($\rho_{is,1}$) than near bottom ($\rho_{is,2}$). The difference in water densities could be due to temperature or a possible freshwater input. The transient rip current drives vertical mixing (black arrows representing horizontal vorticity) in the inner shelf.

Chapter 5

SUMMARY

Chapter 2: Breaking characteristics of short-crested wave fields quantified with remote sensing techniques vary with directional spread.

- Wave transformation observed with stereo reconstructions and LiDAR measurements are similar to in situ observations.
- Average breaker along-crest length decreases and the number of crest ends increases with increasing directional spread.
- Parameterized crest length and number of ends trend similarly to observations.

Chapter 3: Progress towards a conceptual model of transient rip current formation is proposed by linking wave field directional spread, breaking crest characteristics, vorticity forcing, and low-frequency eddy activity.

- The breaking force and its curl, which drives a time-rate of change in surfzone vorticity, is highly irregular along individual waves and varies from crest to crest.
- The crest-averaged curl of the breaking force varies by surfzone region and strongly depends on assumptions about the decay of dissipation near the crest ends.
- The spatial characteristics of low-frequency currents vary with wave directional spread and are similar to the expected relationships for a two-dimensional turbulence inverse energy cascade.

Chapter 4: Further investigation of vorticity injection by short-crested wave breaking, surfzone vorticity evolution, and transient rip current ejections is required.

BIBLIOGRAPHY

Abcha, N., T. Zhang, A. Ezersky, E. Pelinovsky, and I. Didenkulova, Subharmonic resonant excitation of edge waves by breaking surface waves, *Nonlinear Processes in Geophysics*, *24*(2), 157–165, doi:10.5194/npg-24-157-2017, 2017.

Adeyemo, M. D., Velocity Fields in the Wave Breaker Zone, in *Coastal Engineering 1970*, pp. 435–460, American Society of Civil Engineers, Washington, D.C., United States, doi:10.1061/9780872620285.027, 1970.

Adrian, R. J., Twenty years of particle image velocimetry, *Experiments in Fluids*, *39*(2), 159–169, doi:10.1007/s00348-005-0991-7, 2005.

Allen, J. S., P. A. Newberger, and R. A. Holman, Nonlinear shear instabilities of alongshore currents on plane beaches, *Journal of Fluid Mechanics*, *310*, 181–213, doi:10.1017/S0022112096001772, 1996.

Almar, R., S. Larnier, B. Castelle, T. Scott, and F. Floc'h, On the use of the Radon transform to estimate longshore currents from video imagery, *Coastal Engineering*, *114*, 301–308, doi:10.1016/j.coastaleng.2016.04.016, 2016.

Almeida, L. P., et al., Lidar Observations of the Swash Zone of a Low-Tide Terraced Tropical Beach under Variable Wave Conditions: The Nha Trang (Vietnam) COASTVAR Experiment, *Journal of Marine Science and Engineering*, *8*(5), 302, doi:10.3390/jmse8050302, number: 5 Publisher: Multidisciplinary Digital Publishing Institute, 2020.

Anderson, D., A. S. Bak, K. L. Brodie, N. Cohn, R. A. Holman, and J. Stanley, Quantifying Optically Derived Two-Dimensional Wave-Averaged Currents in the Surf Zone, *Remote*

Sensing, *13*(4), 690, doi:10.3390/rs13040690, number: 4 Publisher: Multidisciplinary Digital Publishing Institute, 2021.

Anderson, D. M., Approaches to monitoring, control and management of harmful algal blooms (HABs), *Ocean & Coastal Management*, *52*(7), 342–347, doi:10.1016/j.ocecoaman.2009.04.006, 2009.

Apotsos, A., B. Raubenheimer, S. Elgar, and R. T. Guza, Wave-driven setup and alongshore flows observed onshore of a submarine canyon, *Journal of Geophysical Research: Oceans*, *113*(C7), doi:10.1029/2007JC004514, _eprint: https://agupubs.onlinelibrary.wiley.com/doi/pdf/10.1029/2007JC004514, 2008.

Baker, C. M., M. Moulton, B. Raubenheimer, S. Elgar, and N. Kumar, Modeled Three-Dimensional Currents and Eddies on an Alongshore-Variable Barred Beach, *Journal of Geophysical Research: Oceans*, *126*(7), doi:10.1029/2020JC016899, 2021.

Baker, C. M., M. Moulton, M. Palmsten, K. Brodie, E. Nuss, and C. C. Chickadel, Remotely sensed short-crested waves in a laboratory directional wave basin, in review.

Baldock, T., P. Holmes, S. Bunker, and P. Van Weert, Cross-shore hydrodynamics within an unsaturated surf zone, *Coastal Engineering*, *34*(3-4), 173–196, doi:10.1016/S0378-3839(98)00017-9, 1998.

Banner, M. L., A. V. Babanin, and I. R. Young, Breaking Probability for Dominant Waves on the Sea Surface, *Journal of Physical Oceanography*, *30*(12), 3145–3160, doi:10.1175/1520-0485(2000)030⟨3145:BPFDWO⟩2.0.CO;2, publisher: American Meteorological Society Section: Journal of Physical Oceanography, 2000.

Basco, D., *Design of Coastal Hazard Mitigation Alternatives for Rising Seas*, vol. 49, World Scientific, 2020.

Basco, D. R., A Qualitative Description of Wave Breaking, *Journal of Waterway, Port, Coastal, and Ocean Engineering*, *111*(2), 171–188, doi:10.1061/(ASCE)0733-950X(1985)111:2(171), publisher: American Society of Civil Engineers, 1985.

Battjes, J. A., SURF SIMILARITY, *Coastal Engineering Proceedings*, (14), 26–26, doi:10.9753/icce.v14.26, number: 14, 1974.

Battjes, J. A., Surf similarity, in *Coastal Engineering 1974*, pp. 466–480, 1975.

Battjes, J. A., Surf-Zone Dynamics, *Annual Review of Fluid Mechanics*, *20*(1), 257–291, doi:10.1146/annurev.fl.20.010188.001353, _eprint: https://doi.org/10.1146/annurev.fl.20.010188.001353, 1988.

Battjes, J. A., and M. J. F. Stive, Calibration and verification of a dissipation model for random breaking waves, *Journal of Geophysical Research: Oceans*, *90*(C5), 9159–9167, doi:10.1029/JC090iC05p09159, _eprint: https://agupubs.onlinelibrary.wiley.com/doi/pdf/10.1029/JC090iC05p09159, 1985.

Bechle, A. J., and C. H. Wu, Virtual wave gauges based upon stereo imaging for measuring surface wave characteristics, *Coastal Engineering*, *58*(4), 305–316, doi:10.1016/j.coastaleng.2010.11.003, 2011.

Benetazzo, A., Measurements of short water waves using stereo matched image sequences, *Coastal Engineering*, *53*(12), 1013–1032, doi:10.1016/j.coastaleng.2006.06.012, 2006.

Benetazzo, A., F. Fedele, G. Gallego, P. C. Shih, and A. Yezzi, Offshore stereo measurements of gravity waves, *Coastal Engineering*, *64*, 127–138, doi:10.1016/j.coastaleng.2012.01.007, 2012.

Benetazzo, A., F. Barbariol, F. Bergamasco, A. Torsello, S. Carniel, and M. Sclavo, Observation of Extreme Sea Waves in a Space–Time Ensemble, *Journal of Physical Oceanography*, *45*(9), 2261–2275, doi:10.1175/JPO-D-15-0017.1, publisher: American Meteorological Society Section: Journal of Physical Oceanography, 2015.

Berkhoff, J. C. W., Computation of Combined Refraction — Diffraction, pp. 471–490, doi: 10.1061/9780872620490.027, publisher: American Society of Civil Engineers, 1972.

Bishop, C. T., and M. A. Donelan, Measuring waves with pressure transducers, *Coastal Engineering*, *11*(4), 309–328, doi:10.1016/0378-3839(87)90031-7, 1987.

Blenkinsopp, C., and J. Chaplin, Void fraction measurements in breaking waves, *Proceedings of the Royal Society A: Mathematical, Physical and Engineering Sciences*, *463*(2088), 3151–3170, doi:10.1098/rspa.2007.1901, 2007.

Blenkinsopp, C. E., et al., High-resolution, large-scale laboratory measurements of a sandy beach and dynamic cobble berm revetment, *Scientific Data*, *8*(1), 22, doi:10.1038/s41597-021-00805-1, number: 1 Publisher: Nature Publishing Group, 2021.

Boehm, A. B., and J. A. Soller, Recreational Water Risk: Pathogens and Fecal Indicators, in *Environmental Toxicology: Selected Entries from the Encyclopedia of Sustainability Science and Technology*, edited by E. A. Laws, pp. 441–459, Springer, New York, NY, doi:10.1007/978-1-4614-5764-0_16, 2013.

Boehm, A. B., S. B. Grant, J. H. Kim, S. L. Mowbray, C. D. McGee, C. D. Clark, D. M. Foley, and D. E. Wellman, Decadal and Shorter Period Variability of Surf Zone Water Quality at Huntington Beach, California, *Environmental Science & Technology*, *36*(18), 3885–3892, doi:10.1021/es020524u, 2002.

Boehm, A. B., N. S. Ismail, L. M. Sassoubre, and E. A. Andruszkiewicz, Oceans in Peril: Grand Challenges in Applied Water Quality Research for the 21st Century, *Environmental Engineering Science*, *34*(1), 3–15, doi:10.1089/ees.2015.0252, 2017.

Boffetta, G., and R. E. Ecke, Two-Dimensional Turbulence, *Annual Review of Fluid Mechanics*, *44*(1), 427–451, doi:10.1146/annurev-fluid-120710-101240, 2012.

Boffetta, G., A. Celani, and M. Vergassola, Inverse energy cascade in two-dimensional turbulence: Deviations from Gaussian behavior, *Physical Review E*, *61*(1), R29–R32, doi:10.1103/PhysRevE.61.R29, 2000.

Bonneton, P., N. Bruneau, B. Castelle, and F. Marche, Large-scale vorticity generation due to dissipating waves in the surf zone, *Discrete and Continuous Dynamical Systems - Series B*, *13*(4), 729–738, doi:10.3934/dcdsb.2010.13.729, 2010.

Bowen, A., The generation of longshore currents on a plane beach, *J. Mar. Res.*, *27*(2), 206–215, 1969.

Bowen, A. J., and R. A. Holman, Shear instabilities of the mean longshore current: 1. Theory, *Journal of Geophysical Research: Oceans*, *94*(C12), 18,023–18,030, doi:10.1029/JC094iC12p18023, 1989.

Bowen, A. J., and D. L. Inman, Rip currents: 2. Laboratory and field observations, *Journal of Geophysical Research (1896-1977)*, *74*(23), 5479–5490, doi:10.1029/JC074i023p05479, _eprint: https://onlinelibrary.wiley.com/doi/pdf/10.1029/JC074i023p05479, 1969.

Bowen, A. J., and D. L. Inman, Edge waves and crescentic bars, *Journal of Geophysical Research (1896-1977)*, *76*(36), 8662–8671, doi:10.1029/JC076i036p08662, _eprint: https://onlinelibrary.wiley.com/doi/pdf/10.1029/JC076i036p08662, 1971.

Bowen, A. J., D. L. Inman, and V. P. Simmons, Wave 'set-down' and set-Up, *Journal of Geophysical Research (1896-1977)*, *73*(8), 2569–2577, doi:10.1029/JB073i008p02569, _eprint: https://onlinelibrary.wiley.com/doi/pdf/10.1029/JB073i008p02569, 1968.

Brewster, B. C., R. E. Gould, and R. W. Brander, Estimations of rip current rescues and drowning in the United States, *Natural Hazards and Earth System Sciences*, *19*(2), 389–397, doi:10.5194/nhess-19-389-2019, publisher: Copernicus GmbH, 2019.

Brodie, K. L., B. Raubenheimer, S. Elgar, R. K. Slocum, and J. E. McNinch, Lidar and Pressure Measurements of Inner-Surfzone Waves and Setup, *Journal of Atmospheric*

and Oceanic Technology, *32*(10), 1945–1959, doi:10.1175/JTECH-D-14-00222.1, publisher: American Meteorological Society, 2015.

Brodtkorb, P. A., P. Johannesson, G. Lindgren, I. Rychlik, J. Rydén, and E. Sjö, WAFO - A Matlab Toolbox For Analysis of Random Waves And Loads, OnePetro, 2000.

Brown, J. A., J. H. MacMahan, A. J. H. M. Reniers, and E. B. Thornton, Field Observations of Surf Zone–Inner Shelf Exchange on a Rip-Channeled Beach, *Journal of Physical Oceanography*, *45*(9), 2339–2355, doi:10.1175/JPO-D-14-0118.1, 2015.

Bruder, B. L., and K. L. Brodie, CIRN Quantitative Coastal Imaging Toolbox, *SoftwareX*, *12*, 100,582, doi:10.1016/j.softx.2020.100582, 2020.

Bruneau, N., P. Bonneton, B. Castelle, and R. Pedreros, Modeling rip current circulations and vorticity in a high-energy mesotidal-macrotidal environment, *Journal of Geophysical Research: Oceans*, *116*(C7), doi:10.1029/2010JC006693, _eprint: https://agupubs.onlinelibrary.wiley.com/doi/pdf/10.1029/2010JC006693, 2011.

Bryan, O., P. M. Bayle, C. E. Blenkinsopp, and A. J. Hunter, Breaking Wave Imaging Using Lidar and Sonar, *IEEE Journal of Oceanic Engineering*, pp. 1–11, doi:10.1109/JOE.2019.2900967, 2019.

Bühler, O., On the vorticity transport due to dissipating or breaking waves in shallow-water flow, *Journal of Fluid Mechanics*, *407*, 235–263, doi:10.1017/S0022112099007508, 2000.

Bühler, O., and T. E. Jacobson, Wave-driven currents and vortex dynamics on barred beaches, *Journal of Fluid Mechanics*, *449*, 313–339, doi:10.1017/S0022112001006322, 2001.

Callaghan, A. H., G. B. Deane, and M. D. Stokes, Two Regimes of Laboratory Whitecap Foam Decay: Bubble-Plume Controlled and Surfactant Stabilized, *Journal of Physical Oceanography*, *43*(6), 1114–1126, doi:10.1175/JPO-D-12-0148.1, 2013.

Campbell, A. J., A. J. Bechle, and C. H. Wu, Observations of surface waves interacting with ice using stereo imaging, *Journal of Geophysical Research: Oceans*, *119*(6), 3266–3284, doi:10.1002/2014JC009894, _eprint: https://agupubs.onlinelibrary.wiley.com/doi/pdf/10.1002/2014JC009894, 2014.

Carini, R. J., Estimating energy dissipation due to wave breaking in the surf zone using infrared imagery, *Masters Thesis, University of Washington*, 2014.

Carini, R. J., C. C. Chickadel, A. T. Jessup, and J. Thomson, Estimating wave energy dissipation in the surf zone using thermal infrared imagery, *Journal of Geophysical Research: Oceans*, *120*(6), 3937–3957, doi:10.1002/2014JC010561, _eprint: https://agupubs.onlinelibrary.wiley.com/doi/pdf/10.1002/2014JC010561, 2015.

Carini, R. J., C. C. Chickadel, and A. T. Jessup, Surf Zone Waves at the Onset of Breaking: 1. LIDAR and IR Data Fusion Methods, *Journal of Geophysical Research: Oceans*, *126*(4), e2020JC016,934, doi:https://doi.org/10.1029/2020JC016934, _eprint: https://onlinelibrary.wiley.com/doi/pdf/10.1029/2020JC016934, 2021.

Casper, A., E. Nuss, C. Baker, G. Dusek, and M. Moulton, Assessing noaa rip-current hazard likelihood predictions: Comparison of an operational model with lifeguard observations in the context of rip-current types, in prep.

Castelle, B., and G. Coco, Surf zone flushing on embayed beaches, *Geophysical Research Letters*, *40*(10), 2206–2210, doi:10.1002/grl.50485, _eprint: https://agupubs.onlinelibrary.wiley.com/doi/pdf/10.1002/grl.50485, 2013.

Castelle, B., R. Almar, M. Dorel, J.-P. Lefebvre, N. Senechal, E. J. Anthony, R. Laibi, R. Chuchla, and Y. d. Penhoat, Rip currents and circulation on a high-energy low-tide-terraced beach (Grand Popo, Benin, West Africa), *Journal of Coastal Research*, *70*(sp1), 633–638, doi:10.2112/SI70-107.1, publisher: Coastal Education and Research Foundation, 2014.

Castelle, B., T. Scott, R. W. Brander, and R. J. McCarroll, Rip current types, circulation and hazard, *Earth-Science Reviews*, *163*, 1–21, doi:10.1016/j.earscirev.2016.09.008, 2016.

Chen, Q., J. T. Kirby, R. A. Dalrymple, F. Shi, and E. B. Thornton, Boussinesq modeling of longshore currents, *Journal of Geophysical Research: Oceans*, *108*(C11), doi:10.1029/2002JC001308, _eprint: https://onlinelibrary.wiley.com/doi/pdf/10.1029/2002JC001308, 2003.

Chickadel, C. C., Remote measurements of waves and currents over complex bathymetry, Ph.D., Oregon State University, United States – Oregon, iSBN: 9780549284512, 2007.

Chickadel, C. C., R. A. Holman, and M. H. Freilich, An optical technique for the measurement of longshore currents, *Journal of Geophysical Research*, *108*(C11), 3364, doi:10.1029/2003JC001774, 2003.

Chickadel, C. C., S. A. Talke, A. R. Horner-Devine, and A. T. Jessup, Infrared-Based Measurements of Velocity, Turbulent Kinetic Energy, and Dissipation at the Water Surface in a Tidal River, *IEEE Geoscience and Remote Sensing Letters*, *8*(5), 849–853, doi:10.1109/LGRS.2011.2125942, 2011.

Choi, J., and M. Roh, A laboratory experiment of rip currents between the ends of breaking wave crests, *Coastal Engineering*, *164*, 103,812, doi:10.1016/j.coastaleng.2020.103812, 2021.

Clark, D. B., F. Feddersen, and R. T. Guza, Cross-shore surfzone tracer dispersion in an alongshore current, *Journal of Geophysical Research: Oceans*, *115*(C10), doi:10.1029/2009JC005683, 2010.

Clark, D. B., F. Feddersen, and R. T. Guza, Modeling surf zone tracer plumes: 2. Transport and dispersion, *Journal of Geophysical Research: Oceans*, *116*(C11), doi:10.1029/2011JC007211, 2011.

Clark, D. B., S. Elgar, and B. Raubenheimer, Vorticity generation by short-crested wave breaking, *Geophysical Research Letters*, *39*(24), doi:10.1029/2012GL054034, 2012.

Colford, J. M., et al., Using rapid indicators for Enterococcus to assess the risk of illness after exposure to urban runoff contaminated marine water, *Water Research*, *46*(7), 2176–2186, doi:10.1016/j.watres.2012.01.033, 2012.

Cowen, R. K., and S. Sponaugle, Larval Dispersal and Marine Population Connectivity, *Annual Review of Marine Science*, *1*(1), 443–466, doi:10.1146/annurev.marine.010908.163757, 2009.

Cox, D. T., and S. Shin, Laboratory Measurements of Void Fraction and Turbulence in the Bore Region of Surf Zone Waves, *Journal of Engineering Mechanics*, *129*(10), 1197–1205, doi:10.1061/(ASCE)0733-9399(2003)129:10(1197), 2003.

da F. Klein, A. H., G. G. Santana, F. L. Diehl, and J. T. de Menezes, Analysis of Hazards Associated with Sea Bathing: Results of Five Years Work in Oceanic Beaches of Santa Catarina State, Southern Brazil, *Journal of Coastal Research*, pp. 107–116, publisher: Coastal Education & Research Foundation, Inc., 2003.

Dally, W. R., and C. A. Brown, A modeling investigation of the breaking wave roller with application to cross-shore currents, *Journal of Geophysical Research: Oceans*, *100*(C12), 24,873–24,883, doi:10.1029/95JC02868, _eprint: https://agupubs.onlinelibrary.wiley.com/doi/pdf/10.1029/95JC02868, 1995.

Dalrymple, R. A., A mechanism for rip current generation on an open coast, *Journal of Geophysical Research (1896-1977)*, *80*(24), 3485–3487, doi:https://doi.org/10.1029/JC080i024p03485, _eprint: https://agupubs.onlinelibrary.wiley.com/doi/pdf/10.1029/JC080i024p03485, 1975.

Dalrymple, R. A., Directional wavemaker theory with sidewall reflection, *Journal of Hy-*

draulic Research, *27*(1), 23–34, doi:10.1080/00221688909499241, publisher: Taylor & Francis _eprint: https://doi.org/10.1080/00221688909499241, 1989.

Dalrymple, R. A., and G. A. Lanan, Beach cusps formed by intersecting waves, *GSA Bulletin*, *87*(1), 57–60, doi:10.1130/0016-7606(1976)87⟨57:BCFBIW⟩2.0.CO;2, publisher: GeoScienceWorld, 1976.

Dalrymple, R. A., J. H. MacMahan, A. J. Reniers, and V. Nelko, Rip Currents, *Annual Review of Fluid Mechanics*, *43*(1), 551–581, doi:10.1146/annurev-fluid-122109-160733, 2011.

de Reilhac, P. R., F. Bonnefoy, and P. Ferrant, Generation of Large Angle Bimodal Sea States Using One-Side Segmented Wavemaker, *Journal of Offshore Mechanics and Arctic Engineering*, *130*(3), doi:10.1115/1.2904953, 2008.

de Vries, S., D. F. Hill, M. A. de Schipper, and M. J. F. Stive, Remote sensing of surf zone waves using stereo imaging, *Coastal Engineering*, *58*(3), 239–250, doi:10.1016/j.coastaleng.2010.10.004, 2011.

Dean, R. G., and R. A. Dalrymple, *Water Wave Mechanics For Engineers And Scientists*, World Scientific Publishing Company, google-Books-ID: 1SM8DQAAQBAJ, 1991.

Derakhti, M., J. T. Kirby, M. L. Banner, S. T. Grilli, and J. Thomson, A Unified Breaking Onset Criterion for Surface Gravity Water Waves in Arbitrary Depth, *Journal of Geophysical Research: Oceans*, *125*(7), e2019JC015,886, doi:10.1029/2019JC015886, _eprint: https://agupubs.onlinelibrary.wiley.com/doi/pdf/10.1029/2019JC015886, 2020.

Dingemans, M., A. Radder, and H. De Vriend, Computation of the driving forces of wave-induced currents, *Coastal Engineering*, *11*(5-6), 539–563, doi:10.1016/0378-3839(87)90026-3, 1987.

Dodd, N., J. Oltman-Shay, and E. B. Thornton, Shear Instabilities in the Longshore Current: A Comparison of Observation and Theory, *Journal of Physical Oceanography*, *22*(1), 62–82, doi:10.1175/1520-0485(1992)022⟨0062:SIITLC⟩2.0.CO;2, 1992.

Dugan, J. P., C. C. Piotrowski, and J. Z. Williams, Water depth and surface current retrievals from airborne optical measurements of surface gravity wave dispersion, *Journal of Geophysical Research: Oceans*, *106*(C8), 16,903–16,915, doi:https://doi.org/10.1029/2000JC000369, _eprint: https://agupubs.onlinelibrary.wiley.com/doi/pdf/10.1029/2000JC000369, 2001.

Duncan, J., An experimental investigation of breaking waves produced by a towed hydrofoil, *Proceedings of the Royal Society of London. A. Mathematical and Physical Sciences*, *377*(1770), 331–348, doi:10.1098/rspa.1981.0127, 1981.

Dusek, G., and H. Seim, A Probabilistic Rip Current Forecast Model, *Journal of Coastal Research*, *289*, 909–925, doi:10.2112/JCOASTRES-D-12-00118.1, 2013.

Díaz, H., P. A. Catalán, and G. W. Wilson, Quantification of Two-Dimensional Wave Breaking Dissipation in the Surf Zone from Remote Sensing Data, *Remote Sensing*, *10*(1), 38, doi:10.3390/rs10010038, number: 1 Publisher: Multidisciplinary Digital Publishing Institute, 2018.

Eckstein, A. C., J. Charonko, and P. Vlachos, Phase correlation processing for DPIV measurements, *Experiments in Fluids*, *45*(3), 485–500, doi:10.1007/s00348-008-0492-6, 2008.

Elgar, S., and B. Raubenheimer, Field Evidence of Inverse Energy Cascades in the Surfzone, *Journal of Physical Oceanography*, *50*(8), 2315–2321, doi:10.1175/JPO-D-19-0327.1, 2020.

Elgar, S., R. T. Guza, and M. H. Freilich, Eulerian measurements of horizontal accelerations in shoaling gravity waves, *Journal of Geophysical Research: Oceans*, *93*(C8), 9261–9269, doi:10.1029/JC093iC08p09261, _eprint: https://onlinelibrary.wiley.com/doi/pdf/10.1029/JC093iC08p09261, 1988.

Elgar, S., B. Raubenheimer, D. B. Clark, and M. Moulton, Extremely Low Frequency (0.1 to 1.0 mHz) Surf Zone Currents, *Geophysical Research Letters*, *46*(3), 1531–1536, doi:10.1029/2018GL081106, 2019.

Feddersen, F., Weakly nonlinear shear waves, *Journal of Fluid Mechanics*, *372*, 71–91, doi: 10.1017/S0022112098002158, publisher: Cambridge University Press, 1998.

Feddersen, F., Scaling surf zone turbulence, *Geophysical Research Letters*, *39*(18), doi:https://doi.org/10.1029/2012GL052970, _eprint: https://agupubs.onlinelibrary.wiley.com/doi/pdf/10.1029/2012GL052970, 2012.

Feddersen, F., The Generation of Surfzone Eddies in a Strong Alongshore Current, *Journal of Physical Oceanography*, *44*(2), 600–617, doi:10.1175/JPO-D-13-051.1, 2014.

Feddersen, F., R. T. Guza, S. Elgar, and T. H. C. Herbers, Alongshore momentum balances in the nearshore, *Journal of Geophysical Research: Oceans*, *103*(C8), 15,667–15,676, doi: 10.1029/98JC01270, 1998.

Feddersen, F., D. B. Clark, and R. T. Guza, Modeling surf zone tracer plumes: 1. Waves, mean currents, and low-frequency eddies, *Journal of Geophysical Research: Oceans*, *116*(C11), doi:10.1029/2011JC007210, 2011.

Fedele, F., A. Benetazzo, G. Gallego, P.-C. Shih, A. Yezzi, F. Barbariol, and F. Ardhuin, Space–time measurements of oceanic sea states, *Ocean Modelling*, *70*, 103–115, doi:10. 1016/j.ocemod.2013.01.001, 2013.

Filipot, J.-F., et al., La Jument lighthouse: a real-scale laboratory for the study of giant waves and their loading on marine structures, *Philosophical Transactions of the Royal Society A: Mathematical, Physical and Engineering Sciences*, *377*(2155), 20190,008, doi: 10.1098/rsta.2019.0008, publisher: Royal Society, 2019.

Flores, R. P., P. A. Catalán, and M. C. Haller, Estimating surfzone wave transformation and wave setup from remote sensing data, *Coastal Engineering*, *114*, 244–252, doi:10.1016/j. coastaleng.2016.04.008, 2016.

Fowler, R. E., and R. A. Dalrymple, Wave Group Forced Nearshore Circulation, in *Coastal Engineering 1990*, pp. 729–742, American Society of Civil Engineers, Delft, The Netherlands, doi:10.1061/9780872627765.058, 1991.

Gallego, G., A. Yezzi, F. Fedele, and A. Benetazzo, A Variational Stereo Method for the Three-Dimensional Reconstruction of Ocean Waves, *IEEE Transactions on Geoscience and Remote Sensing*, *49*(11), 4445–4457, doi:10.1109/TGRS.2011.2150230, conference Name: IEEE Transactions on Geoscience and Remote Sensing, 2011.

Garcez-Faria, A. F., E. B. Thornton, T. C. Lippmann, and T. P. Stanton, Undertow over a barred beach, *Journal of Geophysical Research: Oceans*, *105*(C7), 16,999–17,010, doi:10.1029/2000JC900084, 2000.

Garnier, R., D. Calvete, A. Falques, and M. Caballeria, Generation and nonlinear evolution of shore-oblique/transverse sand bars, *Journal of Fluid Mechanics*, *567*, 327, doi:10.1017/S0022112006002126, 2006.

Garnier, R., G. Coco, P. Lomonaco, R. A. Dalrymple, A. Alvarez, M. Gonzalez, and R. Medina, Laboratory Experiments of Rip Current Generation, *AGU Fall Meeting Abstracts*, *14*, OS14A–05, 2014.

Gilbert, G., and S. W. Huntington, A technique for the generation of short crested waves in wave basins, *Journal of Hydraulic Research*, *29*(6), 789–799, doi:10.1080/00221689109498959, 1991.

Goda, Y., Statistical Variability of Sea State Parameters as a Function of Wave Spectrum, *Coastal Engineering in Japan*, *31*(1), 39–52, doi:10.1080/05785634.1988.11924482, publisher: Taylor & Francis _eprint: https://doi.org/10.1080/05785634.1988.11924482, 1988.

Goda, Y., *Random seas and design of maritime structures*, vol. 33, World Scientific Publishing Company, 2010.

Gorman, R. M., Estimation of directional spectra from wave buoys for model validation, *Procedia IUTAM*, *26*, 81–91, doi:10.1016/j.piutam.2018.03.008, 2018.

Grimes, D. J., and F. Feddersen, The self-similar stratified inner-shelf response to transient rip-current-induced mixing, *Journal of Fluid Mechanics*, *915*, doi:10.1017/jfm.2021.140, publisher: Cambridge University Press, 2021.

Grimes, D. J., F. Feddersen, S. N. Giddings, and G. Pawlak, Cross-Shore Deformation of a Surfzone-Released Dye Plume by an Internal Tide on the Inner Shelf, *Journal of Physical Oceanography*, *50*(1), 35–54, doi:10.1175/JPO-D-19-0046.1, publisher: American Meteorological Society Section: Journal of Physical Oceanography, 2020a.

Grimes, D. J., F. Feddersen, and N. Kumar, Tracer Exchange Across the Stratified Inner-Shelf Driven by Transient Rip-Currents and Diurnal Surface Heat Fluxes, *Geophysical Research Letters*, *47*(10), e2019GL086,501, doi:10.1029/2019GL086501, _eprint: https://onlinelibrary.wiley.com/doi/pdf/10.1029/2019GL086501, 2020b.

Guza, R. T., and R. E. Davis, Excitation of edge waves by waves incident on a beach, *Journal of Geophysical Research (1896-1977)*, *79*(9), 1285–1291, doi:10.1029/JC079i009p01285, _eprint: https://onlinelibrary.wiley.com/doi/pdf/10.1029/JC079i009p01285, 1974.

Guza, R. T., and F. Feddersen, Effect of wave frequency and directional spread on shoreline runup, *Geophysical Research Letters*, *39*(11), doi:10.1029/2012GL051959, _eprint: https://onlinelibrary.wiley.com/doi/pdf/10.1029/2012GL051959, 2012.

Guza, R. T., and D. L. Inman, Edge waves and beach cusps, *Journal of Geophysical Research (1896-1977)*, *80*(21), 2997–3012, doi:10.1029/JC080i021p02997, _eprint: https://onlinelibrary.wiley.com/doi/pdf/10.1029/JC080i021p02997, 1975.

Guza, R. T., and E. B. Thornton, Local and shoaled comparisons of sea surface elevations, pressures, and velocities, *Journal of Geophysical Research: Oceans*, *85*(C3), 1524–1530, doi:10.1029/JC085iC03p01524, 1980.

Guza, R. T., and E. B. Thornton, Swash oscillations on a natural beach, *Journal of Geophysical Research: Oceans*, *87*(C1), 483–491, doi:10.1029/JC087iC01p00483, _eprint: https://agupubs.onlinelibrary.wiley.com/doi/pdf/10.1029/JC087iC01p00483, 1982.

Guza, R. T., A. Professor, and A. J. Bowen, Resonant Interactions for Waves Breaking on a Beach, *COASTAL ENGINEERING*, p. 20, 1976.

Haller, M. C., and P. A. Catalán, Remote sensing of wave roller lengths in the laboratory, *Journal of Geophysical Research: Oceans*, *114*(C7), doi:10.1029/2008JC005185, _eprint: https://onlinelibrary.wiley.com/doi/pdf/10.1029/2008JC005185, 2009.

Haller, M. C., U. Putrevu, J. Oltman-Shay, and R. A. Dalrymple, Wave Group Forcing of Low Frequency Surf Zone Motion, *Coastal Engineering Journal*, *41*(2), 121–136, doi: 10.1142/S0578563499000085, 1999.

Hally-Rosendahl, K., and F. Feddersen, Modeling surfzone to inner-shelf tracer exchange, *Journal of Geophysical Research: Oceans*, *121*(6), 4007–4025, doi:10.1002/2015JC011530, 2016.

Hally-Rosendahl, K., F. Feddersen, and R. T. Guza, Cross-shore tracer exchange between the surfzone and inner-shelf, *Journal of Geophysical Research: Oceans*, *119*(7), 4367–4388, doi:https://doi.org/10.1002/2013JC009722, _eprint: https://agupubs.onlinelibrary.wiley.com/doi/pdf/10.1002/2013JC009722, 2014.

Hally-Rosendahl, K., F. Feddersen, D. B. Clark, and R. T. Guza, Surfzone to inner-shelf exchange estimated from dye tracer balances, *Journal of Geophysical Research: Oceans*, *120*(9), 6289–6308, doi:10.1002/2015JC010844, 2015.

Halpern, B. S., K. L. McLeod, A. A. Rosenberg, and L. B. Crowder, Managing for cumulative impacts in ecosystem-based management through ocean zoning, *Ocean & Coastal Management*, *51*(3), 203–211, doi:10.1016/j.ocecoaman.2007.08.002, 2008.

Halpern, B. S., et al., An index to assess the health and benefits of the global ocean, *Nature*, *488*(7413), 615–620, doi:10.1038/nature11397, bandiera_abtest: a Cg_type: Nature Research Journals Number: 7413 Primary_atype: Research Publisher: Nature Publishing Group Subject_term: Ocean sciences;Policy Subject_term_id: ocean-sciences;policy, 2012.

Hammack, J., N. Scheffner, and H. Segur, Two-dimensional periodic waves in shallow water, *Journal of Fluid Mechanics*, *209*, 567–589, doi:10.1017/S0022112089003228, 1989.

Hansen, J. E., B. Raubenheimer, J. H. List, and S. Elgar, Modeled alongshore circulation and force balances onshore of a submarine canyon, *Journal of Geophysical Research: Oceans*, *120*(3), 1887–1903, doi:10.1002/2014JC010555, _eprint: https://agupubs.onlinelibrary.wiley.com/doi/pdf/10.1002/2014JC010555, 2015.

Hartmann, D., Drowning and Beach-Safety Management (BSM) along the Mediterranean Beaches of Israel—A Long-Term Perspective, *Journal of Coastal Research*, *2006*(226), 1505–1514, doi:10.2112/05-0497.1, publisher: Coastal Education and Research Foundation, 2006.

Hashimoto, N., K. Kobune, S. R. Engineer, and M. H. Division, Directional Spectrum Estimation from a Bayesian Approach, *COASTAL ENGINEERING*, 1988.

Hashimoto, N., T. Nagai, and T. Asai, Extension of the Maximum Entropy Principle Method for Directional Wave Spectrum Estimation, in *Coastal Engineering 1994*, pp. 232–246, American Society of Civil Engineers, Kobe, Japan, doi:10.1061/9780784400890.019, 1995.

Hasselmann, D. E., M. Dunckel, and J. A. Ewing, Directional Wave Spectra Observed during JONSWAP 1973, *Journal of Physical Oceanography*, *10*(8), 1264–1280, doi:10.1175/1520-0485(1980)010⟨1264:DWSODJ⟩2.0.CO;2, publisher: American Meteorological Society Section: Journal of Physical Oceanography, 1980.

Hasselmann, K., On the mass and momentum transfer between short gravity waves

and larger-scale motions, *Journal of Fluid Mechanics*, *50*(1), 189–205, doi:10.1017/S0022112071002520, publisher: Cambridge University Press, 1971.

Hasselmann, K. F., et al., Measurements of wind-wave growth and swell decay during the joint North Sea wave project (JONSWAP)., *Ergänzungsheft zur Deutschen Hydrographischen Zeitschrift, Reihe A*, *Nr. 12*, 1973.

Henderson, S. M., J. Arnold, H. T. Özkan-Haller, and S. A. Solovitz, Depth Dependence of Nearshore Currents and Eddies, *Journal of Geophysical Research: Oceans*, *122*(11), 9004–9031, doi:10.1002/2016JC012349, 2017.

Herbers, T. H. C., and S. J. Lentz, Observing Directional Properties of Ocean Swell with an Acoustic Doppler Current Profiler (ADCP), *Journal of Atmospheric and Oceanic Technology*, *27*(1), 210–225, doi:10.1175/2009JTECHO681.1, 2010.

Herbers, T. H. C., S. Elgar, and R. T. Guza, Directional spreading of waves in the nearshore, *Journal of Geophysical Research: Oceans*, *104*(C4), 7683–7693, doi:10.1029/1998JC900092, _eprint: https://onlinelibrary.wiley.com/doi/pdf/10.1029/1998JC900092, 1999.

Holman, R., and M. C. Haller, Remote Sensing of the Nearshore, *Annual Review of Marine Science*, *5*(1), 95–113, doi:10.1146/annurev-marine-121211-172408, _eprint: https://doi.org/10.1146/annurev-marine-121211-172408, 2013.

Holman, R. A., and A. J. Bowen, Longshore structure of infragravity wave motions, *Journal of Geophysical Research: Oceans*, *89*(C4), 6446–6452, doi:10.1029/JC089iC04p06446, _eprint: https://agupubs.onlinelibrary.wiley.com/doi/pdf/10.1029/JC089iC04p06446, 1984.

Huntley, D. A., and M. A. Davidson, Estimating the Directional Spectrum of Waves near a Reflector, *Journal of Waterway, Port, Coastal, and Ocean Engineering*, *124*(6), 312–319, doi:10.1061/(ASCE)0733-950X(1998)124:6(312), 1998.

Hwang, P. A., D. W. Wang, E. J. Walsh, W. B. Krabill, and R. N. Swift, Airborne Measurements of the Wavenumber Spectra of Ocean Surface Waves. Part II: Directional Distribution, *Journal of Physical Oceanography*, *30*(11), 2768–2787, doi:10.1175/1520-0485(2001)031⟨2768:AMOTWS⟩2.0.CO;2, publisher: American Meteorological Society Section: Journal of Physical Oceanography, 2000.

Iafrati, A., Energy dissipation mechanisms in wave breaking processes: Spilling and highly aerated plunging breaking events, *Journal of Geophysical Research: Oceans*, *116*(C7), doi:10.1029/2011JC007038, _eprint: https://agupubs.onlinelibrary.wiley.com/doi/pdf/10.1029/2011JC007038, 2011.

Inman, D. L., R. J. Tait, and C. E. Nordstrom, Mixing in the surf zone, *Journal of Geophysical Research (1896-1977)*, *76*(15), 3493–3514, doi:10.1029/JC076i015p03493, _eprint: https://onlinelibrary.wiley.com/doi/pdf/10.1029/JC076i015p03493, 1971.

Intergovernmental Panel on Climate Change (IPCC), *The Ocean and Cryosphere in a Changing Climate: Special Report of the Intergovernmental Panel on Climate Change*, 1 ed., Cambridge University Press, doi:10.1017/9781009157964, 2022.

Irish, J. L., J. M. Wozencraft, A. G. Cunningham, and C. Giroud, Nonintrusive Measurement of Ocean Waves: Lidar Wave Gauge, *Journal of Atmospheric and Oceanic Technology*, *23*(11), 1559–1572, doi:10.1175/JTECH1936.1, 2006.

Iversen, H. W., Waves and Breakers in Shoaling water, *Coastal Engineering Proceedings*, (3), 1–1, doi:10.9753/icce.v3.1, number: 3, 1952.

Jahanmard, V., S. Varbla, N. Delpeche-Ellmann, and A. Ellmann, Retrieval of directional power spectral density and wave parameters from airborne LiDAR point cloud, *Ocean Engineering*, *266*, 112,694, doi:10.1016/j.oceaneng.2022.112694, 2022.

Ji, X., S. Liu, J. Li, and W. Jia, Experimental investigation of the interaction of mul-

tidirectional irregular waves with a large cylinder, *Ocean Engineering*, *93*, 64–73, doi: 10.1016/j.oceaneng.2014.10.004, 2015.

Johannessen, T., and C. Swan, A laboratory study of the focusing of transient and directionally spread surface water waves, *Proceedings of the Royal Society of London. Series A: Mathematical, Physical and Engineering Sciences*, *457*(2008), 971–1006, doi: 10.1098/rspa.2000.0702, publisher: Royal Society, 2001.

Johnson, D., and C. Pattiaratchi, Application, modelling and validation of surfzone drifters, *Coastal Engineering*, *51*(5), 455–471, doi:10.1016/j.coastaleng.2004.05.005, 2004a.

Johnson, D., and C. Pattiaratchi, Transient rip currents and nearshore circulation on a swell-dominated beach, *Journal of Geophysical Research: Oceans*, *109*(C2), doi:10.1029/ 2003JC001798, 2004b.

Johnson, D., and C. Pattiaratchi, Boussinesq modelling of transient rip currents, *Coastal Engineering*, *53*(5), 419–439, doi:10.1016/j.coastaleng.2005.11.005, 2006.

Jähne, B., *Spatio-Temporal Image Processing: Theory and Scientific Applications*, Springer Science & Business Media, google-Books-ID: gO6V5gh4IXsC, 1993.

Jähne, B., J. Klinke, and S. Waas, Imaging of short ocean wind waves: a critical theoretical review, *JOSA A*, *11*(8), 2197–2209, doi:10.1364/JOSAA.11.002197, publisher: Optical Society of America, 1994.

Kaminsky, G. M., and N. C. Kraus, Evaluation of Depth-Limited Wave Breaking Criteria, pp. 180–193, ASCE, 1994.

Kamphuis, J. W., *Introduction to coastal engineering and management*, vol. 48, World Scientific, 2020.

Keeley, J. R., and A. J. Bowen, Longshore variations in longshore currents, *Canadian Journal of Earth Sciences*, *14*(8), 1897–1905, doi:10.1139/e77-160, 1977.

Kellay, H., and W. I. Goldburg, Two-dimensional turbulence: a review of some recent experiments, *Reports on Progress in Physics*, *65*(5), 845–894, doi:10.1088/0034-4885/65/5/204, publisher: IOP Publishing, 2002.

Kennedy, A. B., Fluctuating circulation forced by unsteady multidirectional breaking waves, *Journal of Fluid Mechanics*, *538*(-1), 189, doi:10.1017/S0022112005005549, 2005.

Kennedy, A. B., Q. Chen, J. T. Kirby, and R. A. Dalrymple, Boussinesq Modeling of Wave Transformation, Breaking, and Runup. I: 1D, *Journal of Waterway, Port, Coastal, and Ocean Engineering*, *126*(1), 39–47, doi:10.1061/(ASCE)0733-950X(2000)126:1(39), 2000.

Kim, J. H., S. B. Grant, C. D. McGee, B. F. Sanders, and J. L. Largier, Locating Sources of Surf Zone Pollution: A Mass Budget Analysis of Fecal Indicator Bacteria at Huntington Beach, California, *Environmental Science & Technology*, *38*(9), 2626–2636, doi:10.1021/es034831r, 2004.

Kim, M., S. Lee, and J.-W. Hong, Empirical estimation of the breaker index using a stereo camera system, *Ocean Engineering*, *265*, 112,522, doi:10.1016/j.oceaneng.2022.112522, 2022.

King, B. A., M. W. L. Blackley, A. P. Carr, and P. J. Hardcastle, Observations of wave-induced set-up on a natural beach, *Journal of Geophysical Research: Oceans*, *95*(C12), 22,289–22,297, doi:10.1029/JC095iC12p22289, _eprint: https://agupubs.onlinelibrary.wiley.com/doi/pdf/10.1029/JC095iC12p22289, 1990.

Kirby, J. T., and R. A. Dalrymple, Modeling Waves in Surfzones and Around Islands, *Journal of Waterway, Port, Coastal, and Ocean Engineering*, *112*(1), 78–93, doi:10.1061/(ASCE)0733-950X(1986)112:1(78), 1986.

Kirby, J. T., and M. Derakhti, Short-crested wave breaking, *European Journal of Mechanics - B/Fluids*, *73*, 100–111, doi:10.1016/j.euromechflu.2017.11.001, 2019.

Kleiss, J. M., and W. K. Melville, Observations of Wave Breaking Kinematics in Fetch-Limited Seas, *Journal of Physical Oceanography*, *40*(12), 2575–2604, doi:10.1175/2010JPO4383.1, publisher: American Meteorological Society Section: Journal of Physical Oceanography, 2010.

Komar, P. D., and M. K. Gaughan, Airy Wave Theory and Breaker Height Prediction, pp. 405–418, doi:10.1061/9780872620490.023, publisher: American Society of Civil Engineers, 1972.

Kraichnan, R. H., Inertial Ranges in Two-Dimensional Turbulence, *The Physics of Fluids*, *10*(7), 1417–1423, doi:10.1063/1.1762301, 1967.

Kuik, A. J., G. P. v. Vledder, and L. H. Holthuijsen, A Method for the Routine Analysis of Pitch-and-Roll Buoy Wave Data, *Journal of Physical Oceanography*, *18*(7), 1020–1034, doi:10.1175/1520-0485(1988)018⟨1020:AMFTRA⟩2.0.CO;2, publisher: American Meteorological Society Section: Journal of Physical Oceanography, 1988.

Kumar, N., and F. Feddersen, The Effect of Stokes Drift and Transient Rip Currents on the Inner Shelf. Part I: No Stratification, *Journal of Physical Oceanography*, *47*(1), 227–241, doi:10.1175/JPO-D-16-0076.1, 2017a.

Kumar, N., and F. Feddersen, The Effect of Stokes Drift and Transient Rip Currents on the Inner Shelf. Part II: With Stratification, *Journal of Physical Oceanography*, *47*(1), 243–260, doi:10.1175/JPO-D-16-0077.1, 2017b.

Kumar, N., and F. Feddersen, A new offshore transport mechanism for shoreline-released tracer induced by transient rip currents and stratification, *Geophysical Research Letters*, *44*(6), 2843–2851, doi:10.1002/2017GL072611, _eprint: https://agupubs.onlinelibrary.wiley.com/doi/pdf/10.1002/2017GL072611, 2017c.

Kumar, N., G. Voulgaris, J. C. Warner, and M. Olabarrieta, Implementation of the vortex force formalism in the coupled ocean-atmosphere-wave-sediment transport (COAWST)

modeling system for inner shelf and surf zone applications, *Ocean Modelling*, *47*, 65–95, doi:10.1016/j.ocemod.2012.01.003, 2012.

Lamarre, E., and W. K. Melville, Air entrainment and dissipation in breaking waves, *Nature*, *351*(6326), 469–472, doi:10.1038/351469a0, 1991.

Leckler, F., F. Ardhuin, C. Peureux, A. Benetazzo, F. Bergamasco, and V. Dulov, Analysis and Interpretation of Frequency–Wavenumber Spectra of Young Wind Waves, *Journal of Physical Oceanography*, *45*(10), 2484–2496, doi:10.1175/JPO-D-14-0237.1, publisher: American Meteorological Society Section: Journal of Physical Oceanography, 2015.

Lentz, S., and B. Raubenheimer, Field observations of wave setup, *Journal of Geophysical Research: Oceans*, *104*(C11), 25,867–25,875, doi:10.1029/1999JC900239, _eprint: https://agupubs.onlinelibrary.wiley.com/doi/pdf/10.1029/1999JC900239, 1999.

Lentz, S. J., and M. R. Fewings, The Wind- and Wave-Driven Inner-Shelf Circulation, *Annual Review of Marine Science*, *4*(1), 317–343, doi:10.1146/annurev-marine-120709-142745, _eprint: https://doi.org/10.1146/annurev-marine-120709-142745, 2012.

Lin, M.-C., C.-T. Wu, Y.-C. Lu, and N.-K. Liang, Effects of Short-Crested Waves on the Scouring Around the Breakwater, pp. 2050–2064, doi:10.1061/9780872626003.151, iSBN: 9780872626003 Publisher: American Society of Civil Engineers, 1986.

Lippmann, T. C., and A. J. Bowen, The Vertical Structure of Low-Frequency Motions in the Nearshore. Part II: Theory, *Journal of Physical Oceanography*, *46*(12), 3713–3727, doi:10.1175/JPO-D-16-0015.1, 2016.

Lippmann, T. C., A. H. Brookins, and E. B. Thornton, Wave energy transformation on natural profiles, *Coastal Engineering*, *27*(1), 1–20, doi:10.1016/0378-3839(95)00036-4, 1996.

Lippmann, T. C., T. H. C. Herbers, and E. B. Thornton, Gravity and Shear Wave Contributions to Nearshore Infragravity Motions, *Journal of Physical Oceanography*, *29*(2), 231–239, doi:10.1175/1520-0485(1999)029⟨0231:GASWCT⟩2.0.CO;2, 1999.

Long, J. W., and H. T. Özkan Haller, Low-frequency characteristics of wave group–forced vortices, *Journal of Geophysical Research*, *114*(C8), doi:10.1029/2008JC004894, 2009.

Longuet-Higgins, M., The statistical analysis of a random, moving surface, p. 67, 1957.

Longuet-Higgins, M. S., The refraction of sea waves in shallow water, *Journal of Fluid Mechanics*, *1*(2), 163–176, doi:10.1017/S0022112056000111, publisher: Cambridge University Press, 1956.

Longuet-Higgins, M. S., Longshore currents generated by obliquely incident sea waves: 2, *Journal of Geophysical Research (1896-1977)*, *75*(33), 6790–6801, doi:10.1029/JC075i033p06790, 1970.

Longuet-Higgins, M. S., and R. W. Stewart, The changes in amplitude of short gravity waves on steady non-uniform currents, *Journal of Fluid Mechanics*, *10*(4), 529–549, doi:10.1017/S0022112061000342, publisher: Cambridge University Press, 1961.

Longuet-Higgins, M. S., and R. w. Stewart, Radiation stresses in water waves; a physical discussion, with applications, *Deep Sea Research and Oceanographic Abstracts*, *11*(4), 529–562, doi:10.1016/0011-7471(64)90001-4, 1964.

Longuet-Higgins, M. S., D. E. Cartwright, and N. D. Smith, Observations of the directional spectrum of sea waves using the motions of a floating buoy, *Ocean Wave Spectra*, *12*(1), 111–132, doi:10.1016/0011-7471(65)91457-9, 1963.

MacCready, P., Calculating Estuarine Exchange Flow Using Isohaline Coordinates, *Journal of Physical Oceanography*, *41*(6), 1116–1124, doi:10.1175/2011JPO4517.1, publisher: American Meteorological Society Section: Journal of Physical Oceanography, 2011.

Maciñeira, E. G., and H. F. Burcharth, Stability of cube armoured roundheads exposed to long crested and short crested waves, *Coastal Engineering*, *112*, 99–112, doi:10.1016/j.coastaleng.2016.03.002, 2016.

MacMahan, J., et al., Mean Lagrangian flow behavior on an open coast rip-channeled beach: A new perspective, *Marine Geology*, *268*(1), 1–15, doi:10.1016/j.margeo.2009.09.011, 2010a.

MacMahan, J. H., E. B. Thornton, and A. J. H. M. Reniers, Rip current review, *Coastal Engineering*, *53*(2), 191–208, doi:10.1016/j.coastaleng.2005.10.009, 2006.

MacMahan, J. H., A. J. H. M. Reniers, and E. B. Thornton, Vortical surf zone velocity fluctuations with 0(10) min period, *Journal of Geophysical Research*, *115*(C6), C06,007, doi:10.1029/2009JC005383, 2010b.

Malila, M. P., F. Barbariol, A. Benetazzo, Breivik, A. K. Magnusson, J. Thomson, and B. Ward, Statistical and dynamical characteristics of extreme wave crests assessed with field measurements from the North Sea, *Journal of Physical Oceanography*, *-1*(aop), doi: 10.1175/JPO-D-22-0125.1, publisher: American Meteorological Society Section: Journal of Physical Oceanography, 2022a.

Malila, M. P., J. Thomson, Breivik, A. Benetazzo, B. Scanlon, and B. Ward, On the Groupiness and Intermittency of Oceanic Whitecaps, *Journal of Geophysical Research: Oceans*, *127*(1), e2021JC017,938, doi:10.1029/2021JC017938, _eprint: https://onlinelibrary.wiley.com/doi/pdf/10.1029/2021JC017938, 2022b.

Mansard, E., and M. Miles, Experimental Validation Of Directional Wave Maker Theory With Side Wall Reflections, *International Journal of Offshore and Polar Engineering*, *4*(04), 1994.

Marchesiello, P., F. Auclair, L. Debreu, J. McWilliams, R. Almar, R. Benshila, and F. Dumas, Tridimensional nonhydrostatic transient rip currents in a wave-resolving model, *Ocean Modelling*, *163*, 101,816, doi:10.1016/j.ocemod.2021.101816, 2021a.

Marchesiello, P., J. Chauchat, H. Shafiei, R. Almar, R. Benshila, and F. Dumas, 3D wave-resolving simulation of sandbar migration, 2021b.

Martins, K., C. E. Blenkinsopp, R. Almar, and J. Zang, The influence of swash-based reflection on surf zone hydrodynamics: a wave-by-wave approach, *Coastal Engineering*, *122*, 27–43, doi:10.1016/j.coastaleng.2017.01.006, 2017a.

Martins, K., P. Bonneton, F. Frappart, G. Detandt, N. Bonneton, and C. E. Blenkinsopp, High Frequency Field Measurements of an Undular Bore Using a 2D LiDAR Scanner, *Remote Sensing*, *9*(5), 462, doi:10.3390/rs9050462, number: 5 Publisher: Multidisciplinary Digital Publishing Institute, 2017b.

Martins, K., C. E. Blenkinsopp, R. Deigaard, and H. E. Power, Energy Dissipation in the Inner Surf Zone: New Insights From LiDAR-Based Roller Geometry Measurements, *Journal of Geophysical Research: Oceans*, *123*(5), 3386–3407, doi:10.1029/2017JC013369, _eprint: https://onlinelibrary.wiley.com/doi/pdf/10.1029/2017JC013369, 2018.

Martins, K., P. Bonneton, A. Mouragues, and B. Castelle, Non-hydrostatic, Non-linear Processes in the Surf Zone, *Journal of Geophysical Research: Oceans*, *125*(2), e2019JC015,521, doi:10.1029/2019JC015521, _eprint: https://onlinelibrary.wiley.com/doi/pdf/10.1029/2019JC015521, 2020.

Masnadi, N., C. C. Chickadel, and A. T. Jessup, On the Thermal Signature of the Residual Foam in Breaking Waves, *Journal of Geophysical Research: Oceans*, *126*(1), e2020JC016,511, doi:10.1029/2020JC016511, _eprint: https://agupubs.onlinelibrary.wiley.com/doi/pdf/10.1029/2020JC016511, 2021.

Massel, S. R., *Ocean surface waves: their physics and prediction*, vol. 11, World scientific, 1996.

McCarroll, R. J., R. W. Brander, T. Scott, and B. Castelle, Bathymetric Controls on Rotational Surfzone Currents, *Journal of Geophysical Research: Earth Surface*, *123*(6), 1295–1316, doi:https://doi.org/10.1029/2017JF004491, _eprint: https://onlinelibrary.wiley.com/doi/pdf/10.1029/2017JF004491, 2018.

McCowan, J., Xxxix. on the highest wave of permanent type, *The London, Edinburgh, and Dublin Philosophical Magazine and Journal of Science*, *38*(233), 351–358, 1894.

McWilliams, J. C., C. Akan, and Y. Uchiyama, Robustness of nearshore vortices, *Journal of Fluid Mechanics*, *850*, doi:10.1017/jfm.2018.510, publisher: Cambridge University Press, 2018.

Mei, C. C., M. A. Stiassnie, and D. K.-P. Yue, *Theory and applications of ocean surface waves: Part 1: linear aspects*, World Scientific, 2005.

Micha, M., The reflective power of maritime structures exposed ̀to the action of the swell, 1951.

Miles, J., P. Russell, B. Ruessink, and D. Huntley, Field observations of the effect of shear waves on sediment suspension and transport, *Continental Shelf Research*, *22*(4), 657–681, doi:10.1016/S0278-4343(01)00095-4, 2002.

Miles, J. W., On the generation of surface waves by shear flows, *Journal of Fluid Mechanics*, *3*(2), 185–204, doi:10.1017/S0022112057000567, publisher: Cambridge University Press, 1957.

Mitsuyasu, H., F. Tasai, T. Suhara, S. Mizuno, M. Ohkusu, T. Honda, and K. Rikiishi, Observations of the Directional Spectrum of Ocean WavesUsing a Cloverleaf Buoy, *Journal of Physical Oceanography*, *5*(4), 750–760, doi:10.1175/1520-0485(1975)005⟨0750:OOTDSO⟩2.0.CO;2, publisher: American Meteorological Society Section: Journal of Physical Oceanography, 1975.

Molfetta, M. G., M. F. Bruno, L. Pratola, A. Rinaldi, A. Morea, G. Preziosa, D. Pasquali, M. Di Risio, and M. Mossa, A Sterescopic System to Measure Water Waves in Laboratories, *Remote Sensing*, *12*(14), 2288, doi:10.3390/rs12142288, number: 14 Publisher: Multidisciplinary Digital Publishing Institute, 2020.

Monahan, E. C., and C. R. Zietlow, Laboratory comparisons of fresh-water and salt-water whitecaps, *Journal of Geophysical Research (1896-1977)*, *74*(28), 6961–6966, doi:10.1029/JC074i028p06961, _eprint: https://onlinelibrary.wiley.com/doi/pdf/10.1029/JC074i028p06961, 1969.

Morgan, S. G., A. L. Shanks, J. MacMahan, A. J. H. M. Reniers, C. D. Griesemer, M. Jarvis, and A. G. Fujimura, Surf zones regulate larval supply and zooplankton subsidies to nearshore communities, *Limnology and Oceanography*, *62*(6), 2811–2828, doi:10.1002/lno.10609, _eprint: https://onlinelibrary.wiley.com/doi/pdf/10.1002/lno.10609, 2017.

Morgan, S. G., A. L. Shanks, J. H. MacMahan, A. J. Reniers, and F. Feddersen, Planktonic Subsidies to Surf-Zone and Intertidal Communities, *Annual Review of Marine Science*, *10*(1), 345–369, doi:10.1146/annurev-marine-010816-060514, 2018.

Moulton, M., G. Dusek, S. Elgar, and B. Raubenheimer, Comparison of Rip Current Hazard Likelihood Forecasts with Observed Rip Current Speeds, *Weather and Forecasting*, *32*(4), 1659–1666, doi:10.1175/WAF-D-17-0076.1, publisher: American Meteorological Society Section: Weather and Forecasting, 2017a.

Moulton, M., S. Elgar, B. Raubenheimer, J. C. Warner, and N. Kumar, Rip currents and alongshore flows in single channels dredged in the surf zone, *Journal of Geophysical Research: Oceans*, *122*(5), 3799–3816, doi:10.1002/2016JC012222, 2017b.

Moulton, M., S. H. Suanda, J. C. Garwood, N. Kumar, M. R. Fewings, and J. M. Pringle, Exchange of Plankton, Pollutants, and Particles Across the Nearshore Region, *Annual Review of Marine Science*, *15*(1), null, doi:10.1146/annurev-marine-032122-115057, _eprint: https://doi.org/10.1146/annurev-marine-032122-115057, 2023.

Munk, W. H., G. R. Miller, F. E. Snodgrass, and N. F. Barber, Directional recording of swell from distant storms, *Royal Society*, *255*(1062), 505–584, doi:10.1098/rsta.1963.0011, 1963.

Noyes, T. J., R. T. Guza, S. Elgar, and T. H. C. Herbers, Field observations of shear waves in the surf zone, *Journal of Geophysical Research: Oceans*, *109*(C1), doi:https://doi.org/10.1029/2002JC001761, _eprint: https://agupubs.onlinelibrary.wiley.com/doi/pdf/10.1029/2002JC001761, 2004.

Noyes, T. J., R. T. Guza, F. Feddersen, S. Elgar, and T. H. C. Herbers, Model-data comparisons of shear waves in the nearshore, *Journal of Geophysical Research: Oceans*, *110*(C5), doi:10.1029/2004JC002541, 2005.

Nuss, E., M. Moulton, S. Suanda, C. M. Baker, M. Palmsten, and K. Brodie, Short-crested wave breaking and associated vorticity input under varying directional spread, in prep.

O'Dea, A., K. Brodie, and S. Elgar, Field Observations of the Evolution of Plunging-Wave Shapes, *Geophysical Research Letters*, *48*(16), e2021GL093,664, doi:10.1029/2021GL093664, _eprint: https://onlinelibrary.wiley.com/doi/pdf/10.1029/2021GL093664, 2021a.

O'Dea, A., N. Kumar, and M. C. Haller, Simulations of the Surf Zone Eddy Field and Cross-Shore Exchange on a Nonidealized Bathymetry, *Journal of Geophysical Research: Oceans*, *126*(5), e2020JC016,619, doi:https://doi.org/10.1029/2020JC016619, _eprint: https://onlinelibrary.wiley.com/doi/pdf/10.1029/2020JC016619, 2021b.

Oltman-Shay, J., P. A. Howd, and W. A. Birkemeier, Shear instabilities of the mean longshore current: 2. Field observations, *Journal of Geophysical Research: Oceans*, *94*(C12), 18,031–18,042, doi:10.1029/JC094iC12p18031, 1989.

Omand, M. M., J. J. Leichter, P. J. S. Franks, R. T. Guza, A. J. Lucas, and F. Feddersen, Physical and biological processes underlying the sudden surface appearance of a red tide in the nearshore, *Limnology and Oceanography*, *56*(3), 787–801, doi:10.4319/lo.2011.56.3.0787, _eprint: https://onlinelibrary.wiley.com/doi/pdf/10.4319/lo.2011.56.3.0787, 2011.

Over, J.-S. R., A. C. Ritchie, C. J. Kranenburg, J. A. Brown, D. D. Buscombe, T. Noble, C. R. Sherwood, J. A. Warrick, and P. A. Wernette, Processing coastal imagery with Agisoft Metashape Professional Edition, version 1.6—Structure from motion workflow documentation, *USGS Numbered Series 2021-1039*, U.S. Geological Survey, Reston, VA, 2021.

Palmsten, M. L., and R. A. Holman, Laboratory investigation of dune erosion using stereo video, *Coastal Engineering*, *60*, 123–135, doi:10.1016/j.coastaleng.2011.09.003, 2012.

Patankar, S. V., Numerical heat transfer and fluid flow, hemisphere publ, *Corp., New York*, *58*, 288, 1980.

Pawka, S. S., Island shadows in wave directional spectra, *Journal of Geophysical Research: Oceans*, *88*(C4), 2579–2591, doi:https://doi.org/10.1029/JC088iC04p02579, _eprint: https://agupubs.onlinelibrary.wiley.com/doi/pdf/10.1029/JC088iC04p02579, 1983.

Peregrine, D., Surf Zone Currents, *Theoretical and Computational Fluid Dynamics*, *10*(1), 295–309, doi:10.1007/s001620050065, 1998.

Peregrine, D. H., Water waves, nonlinear Schrödinger equations and their solutions, *The ANZIAM Journal*, *25*(1), 16–43, doi:10.1017/S0334270000003891, 1983.

Peregrine, D. H., Large-scale vorticity generation by breakers in shallow and deep water, *European Journal of Mechanics - B/Fluids*, *18*(3), 403–408, doi:10.1016/S0997-7546(99)80037-5, 1999.

Peregrine, D. H., and O. Bokhove, Vorticity and Surf Zone Currents, in *Coastal Engineering 1998*, pp. 745–758, American Society of Civil Engineers, Copenhagen, Denmark, doi:10.1061/9780784404119.055, 1998.

Peregrine, D. H., and O. Bokhove, Vorticity and Surf Zone Currents, in *Coastal Engineering 1998*, pp. 745–758, American Society of Civil Engineers, Copenhagen, Denmark, doi:10.1061/9780784404119.055, 1999.

Perkovic, D., T. C. Lippmann, and S. J. Frasier, Longshore Surface Currents Measured by Doppler Radar and Video PIV Techniques, *IEEE Transactions on Geoscience and Remote Sensing*, *47*(8), 2787–2800, doi:10.1109/TGRS.2009.2016556, conference Name: IEEE Transactions on Geoscience and Remote Sensing, 2009.

Peureux, C., A. Benetazzo, and F. Ardhuin, Note on the directional properties of meter-scale gravity waves, *Ocean Science*, *14*(1), 41–52, doi:10.5194/os-14-41-2018, publisher: Copernicus GmbH, 2018.

Phillips, O. M., On the generation of waves by turbulent wind, *Journal of Fluid Mechanics*, *2*(5), 417–445, doi:10.1017/S0022112057000233, publisher: Cambridge University Press, 1957.

Phillips, O. M., Spectral and statistical properties of the equilibrium range in wind-generated gravity waves, *Journal of Fluid Mechanics*, *156*(-1), 505, doi:10.1017/S0022112085002221, 1985.

Pizzo, N. E., and W. K. Melville, Vortex generation by deep-water breaking waves, *Journal of Fluid Mechanics*, *734*, 198–218, doi:10.1017/jfm.2013.453, 2013.

Plant, W. J., Whitecaps in deep water, *Geophysical Research Letters*, *39*(16), doi:10.1029/2012GL052732, _eprint: https://agupubs.onlinelibrary.wiley.com/doi/pdf/10.1029/2012GL052732, 2012.

Postacchini, M., and M. Brocchini, A wave-by-wave analysis for the evaluation of the breaking-wave celerity, *Applied Ocean Research*, *46*, 15–27, doi:10.1016/j.apor.2014.01.005, 2014.

Postacchini, M., M. Brocchini, and L. Soldini, Vorticity generation due to cross-sea, *Journal of Fluid Mechanics*, *744*, 286–309, doi:10.1017/jfm.2014.44, publisher: Cambridge University Press, 2014.

Power, H. E., M. G. Hughes, T. Aagaard, and T. E. Baldock, Nearshore wave height variation in unsaturated surf, *Journal of Geophysical Research: Oceans*, *115*(C8), doi:10.1029/2009JC005758, _eprint: https://onlinelibrary.wiley.com/doi/pdf/10.1029/2009JC005758, 2010.

Prosch, R. M., and A. McLachlan, The Regeneration of Surf-Zone Nutrients by the Sand Mussel, Donax Serra Roding, 1984.

Prüss, A., Review of epidemiological studies on health effects from exposure to recreational water, *International Journal of Epidemiology*, *27*(1), 1–9, doi:10.1093/ije/27.1.1, 1998.

Puleo, J. A., G. Farquharson, S. J. Frasier, and K. T. Holland, Comparison of optical and radar measurements of surf and swash zone velocity fields, *Journal of Geophysical Research: Oceans*, *108*(C3), doi:10.1029/2002JC001483, _eprint: https://agupubs.onlinelibrary.wiley.com/doi/pdf/10.1029/2002JC001483, 2003.

Putrevu, U., J. Oltman-Shay, and I. A. Svendsen, Effect of alongshore nonuniformities on longshore current predictions, *Journal of Geophysical Research: Oceans*, *100*(C8), 16,119–16,130, doi:10.1029/95JC01459, 1995.

Rabinovich, A. B., Seiches and Harbor Oscillations, in *Handbook of Coastal and Ocean Engineering*, pp. 193–236, WORLD SCIENTIFIC, 2009.

Raubenheimer, B., R. T. Guza, and S. Elgar, Wave transformation across the inner surf zone, *Journal of Geophysical Research: Oceans*, *101*(C11), 25,589–25,597, doi:10.1029/96JC02433, _eprint: https://onlinelibrary.wiley.com/doi/pdf/10.1029/96JC02433, 1996.

Raubenheimer, B., R. T. Guza, and S. Elgar, Field observations of wave-driven setdown and setup, *Journal of Geophysical Research: Oceans*, *106*(C3), 4629–4638, doi:10.1029/2000JC000572, 2001.

Reniers, A. J. H. M., J. A. Roelvink, and E. B. Thornton, Morphodynamic modeling of an embayed beach under wave group forcing, *Journal*

of Geophysical Research: Oceans, *109*(C1), doi:10.1029/2002JC001586, _eprint: https://onlinelibrary.wiley.com/doi/pdf/10.1029/2002JC001586, 2004.

Reniers, A. J. H. M., J. H. MacMahan, E. B. Thornton, T. P. Stanton, M. Henriquez, J. W. Brown, J. A. Brown, and E. Gallagher, Surf zone surface retention on a rip-channeled beach, *Journal of Geophysical Research: Oceans*, *114*(C10), doi:10.1029/2008JC005153, 2009.

Reniers, A. J. H. M., J. H. MacMahan, F. J. Beron-Vera, and M. J. Olascoaga, Rip-current pulses tied to Lagrangian coherent structures, *Geophysical Research Letters*, *37*(5), doi:10.1029/2009GL041443, _eprint: https://agupubs.onlinelibrary.wiley.com/doi/pdf/10.1029/2009GL041443, 2010.

Romero, L., and W. K. Melville, Spatial Statistics of the Sea Surface in Fetch-Limited Conditions, *Journal of Physical Oceanography*, *41*(10), 1821–1841, doi:10.1175/2011JPO4535.1, publisher: American Meteorological Society Section: Journal of Physical Oceanography, 2011.

Ruessink, B. G., J. R. Miles, F. Feddersen, R. T. Guza, and S. Elgar, Modeling the alongshore current on barred beaches, *Journal of Geophysical Research: Oceans*, *106*(C10), 22,451–22,463, doi:https://doi.org/10.1029/2000JC000766, _eprint: https://onlinelibrary.wiley.com/doi/pdf/10.1029/2000JC000766, 2001.

Sallenger, A. H., and R. A. Holman, Wave energy saturation on a natural beach of variable slope, *Journal of Geophysical Research: Oceans*, *90*(C6), 11,939–11,944, doi:10.1029/JC090iC06p11939, _eprint: https://agupubs.onlinelibrary.wiley.com/doi/pdf/10.1029/JC090iC06p11939, 1985.

Salmon, *Lectures on Geophysical Fluid Dynamics*, 1998.

Schwendeman, M. S., and J. Thomson, Sharp-Crested Breaking Surface Waves Observed

from a Ship-Based Stereo Video System, *Journal of Physical Oceanography*, *47*(4), 775–792, doi:10.1175/JPO-D-16-0187.1, publisher: American Meteorological Society, 2017.

Schäffer, H., and C. Steenberg, Second-order wavemaker theory for multidirectional waves, *Ocean Engineering*, *30*(10), 1203–1231, doi:10.1016/S0029-8018(02)00100-2, 2003.

Shanks, A. L., S. G. Morgan, J. MacMahan, and A. J. H. M. Reniers, Surf zone physical and morphological regime as determinants of temporal and spatial variation in larval recruitment, *Journal of Experimental Marine Biology and Ecology*, *392*(1), 140–150, doi:10.1016/j.jembe.2010.04.018, 2010.

Shanks, A. L., S. G. Morgan, J. MacMahan, A. J. Reniers, M. Jarvis, J. Brown, A. Fujimura, L. Ziccarelli, and C. Griesemer, Persistent Differences in Horizontal Gradients in Phytoplankton Concentration Maintained by Surf Zone Hydrodynamics, *Estuaries and Coasts*, *41*(1), 158–176, doi:10.1007/s12237-017-0278-2, 2018.

Slinn, D. N., J. S. Allen, and R. A. Holman, Alongshore currents over variable beach topography, *Journal of Geophysical Research: Oceans*, *105*(C7), 16,971–16,998, doi:10.1029/2000JC900051, _eprint: https://onlinelibrary.wiley.com/doi/pdf/10.1029/2000JC900051, 2000.

Smit, P. B., and T. T. Janssen, Swell Propagation through Submesoscale Turbulence, *Journal of Physical Oceanography*, *49*(10), 2615–2630, doi:10.1175/JPO-D-18-0250.1, 2019.

Smithr, L. M., and V. Yakhot, Finite-size effects in forced two-dimensional turbulence, *Journal of Fluid Mechanics*, *274*, 115–138, doi:10.1017/S0022112094002065, publisher: Cambridge University Press, 1994.

Song, H., and L. Tao, Short-crested wave interaction with a concentric porous cylindrical structure, *Applied Ocean Research*, *29*(4), 199–209, doi:10.1016/j.apor.2008.01.001, 2007.

Spydell, M., and F. Feddersen, Lagrangian Drifter Dispersion in the Surf Zone: Directionally Spread, Normally Incident Waves, *Journal of Physical Oceanography*, *39*(4), 809–830, doi: 10.1175/2008JPO3892.1, 2009.

Spydell, M., F. Feddersen, R. T. Guza, and W. E. Schmidt, Observing Surf-Zone Dispersion with Drifters, *Journal of Physical Oceanography*, *37*(12), 2920–2939, doi:10.1175/2007JPO3580.1, 2007.

Spydell, M. S., The suppression of surfzone cross-shore mixing by alongshore currents, *Geophysical Research Letters*, *43*(18), 9781–9790, doi:10.1002/2016GL070626, _eprint: https://agupubs.onlinelibrary.wiley.com/doi/pdf/10.1002/2016GL070626, 2016.

Spydell, M. S., and F. Feddersen, A Lagrangian stochastic model of surf zone drifter dispersion, *Journal of Geophysical Research: Oceans*, *117*(C3), doi:10.1029/2011JC007701, _eprint: https://onlinelibrary.wiley.com/doi/pdf/10.1029/2011JC007701, 2012.

Spydell, M. S., F. Feddersen, and R. T. Guza, Observations of drifter dispersion in the surfzone: The effect of sheared alongshore currents, *Journal of Geophysical Research: Oceans*, *114*(C7), doi:https://doi.org/10.1029/2009JC005328, _eprint: https://agupubs.onlinelibrary.wiley.com/doi/pdf/10.1029/2009JC005328, 2009.

Spydell, M. S., F. Feddersen, and S. Suanda, Inhomogeneous Turbulent Dispersion across the Nearshore Induced by Surfzone Eddies, *Journal of Physical Oceanography*, *49*(4), 1015–1034, doi:10.1175/JPO-D-18-0102.1, publisher: American Meteorological Society Section: Journal of Physical Oceanography, 2019.

Squire, V. A., and F. Montiel, Evolution of Directional Wave Spectra in the Marginal Ice Zone: A New Model Tested with Legacy Data, *Journal of Physical Oceanography*, *46*(10), 3121–3137, doi:10.1175/JPO-D-16-0118.1, publisher: American Meteorological Society Section: Journal of Physical Oceanography, 2016.

Stoner, N., and M. Dorfman, Testing the waters: a guide to water quality at vacation beaches, *8*(12), 2007.

Stringari, C., D. Harris, and H. Power, A novel machine learning algorithm for tracking remotely sensed waves in the surf zone, *Coastal Engineering*, *147*, 149–158, doi:10.1016/j.coastaleng.2019.02.002, 2019.

Suanda, S. H., and F. Feddersen, A self-similar scaling for cross-shelf exchange driven by transient rip currents, *Geophysical Research Letters*, *42*(13), 5427–5434, doi:10.1002/2015GL063944, 2015.

Sullivan, P. P., J. C. McWILLIAMS, and W. K. Melville, Surface gravity wave effects in the oceanic boundary layer: large-eddy simulation with vortex force and stochastic breakers, *Journal of Fluid Mechanics*, *593*, 405–452, doi:10.1017/S002211200700897X, 2007.

Sutherland, P., and W. K. Melville, Field measurements and scaling of ocean surface wave-breaking statistics, *Geophysical Research Letters*, *40*(12), 3074–3079, doi:10.1002/grl.50584, _eprint: https://onlinelibrary.wiley.com/doi/pdf/10.1002/grl.50584, 2013.

Svendsen, I., Wave heights and set-up in a surf zone, *Coastal Engineering*, *8*(4), 303–329, doi:10.1016/0378-3839(84)90028-0, 1984a.

Svendsen, I., Introduction to nearshore hydrodynamics, adv. ser, *Ocean Eng*, *24*, 744, 2006.

Svendsen, I. A., Mass flux and undertow in a surf zone, *Coastal Engineering*, *8*(4), 347–365, doi:10.1016/0378-3839(84)90030-9, 1984b.

Sáez, F. J., P. A. Catalán, and C. Valle, Wave-by-wave nearshore wave breaking identification using U-Net, *Coastal Engineering*, *170*, 104,021, doi:10.1016/j.coastaleng.2021.104021, 2021.

Thomson, R. E., and W. J. Emery, *Data analysis methods in physical oceanography*, Newnes, 2014.

Thornton, E. B., Variation of Longshore Current Across the Surf Zone, pp. 291–308, doi: 10.1061/9780872620285.018, publisher: American Society of Civil Engineers, 1970.

Thornton, E. B., and R. T. Guza, Energy saturation and phase speeds measured on a natural beach, *Journal of Geophysical Research: Oceans*, *87*(C12), 9499–9508, doi:10.1029/JC087iC12p09499, _eprint: https://agupubs.onlinelibrary.wiley.com/doi/pdf/10.1029/JC087iC12p09499, 1982.

Thornton, E. B., and R. T. Guza, Transformation of wave height distribution, *Journal of Geophysical Research: Oceans*, *88*(C10), 5925–5938, doi:10.1029/JC088iC10p05925, _eprint: https://agupubs.onlinelibrary.wiley.com/doi/pdf/10.1029/JC088iC10p05925, 1983.

Thornton, E. B., J. J. Galvin, F. L. Bub, and D. P. Richardson, Kinematics of Breaking Waves, *Coastal Engineering Proceedings*, *1*(15), 25, doi:https://doi.org/10.9753/icce.v15.25, 1976.

Ting, F. C., and J. T. Kirby, Dynamics of surf-zone turbulence in a strong plunging breaker, *Coastal Engineering*, *24*(3-4), 177–204, doi:10.1016/0378-3839(94)00036-W, 1995.

Tsinober, A., and R. M. Madylam (Eds.), *An Informal Conceptual Introduction to Turbulence*, *Fluid Mechanics and Its Applications*, vol. 92, Springer Netherlands, Dordrecht, doi:10.1007/978-90-481-3174-7, 2009.

Uchiyama, Y., J. C. McWilliams, and C. Akan, Three-dimensional transient rip currents: Bathymetric excitation of low-frequency intrinsic variability, *Journal of Geophysical Research: Oceans*, *122*(7), 5826–5849, doi:10.1002/2017JC013005, _eprint: https://onlinelibrary.wiley.com/doi/pdf/10.1002/2017JC013005, 2017.

Van Dorn, W. G., Breaking invariants in shoaling waves, *Journal of Geophysical Research: Oceans*, *83*(C6), 2981–2988, doi:10.1029/JC083iC06p02981, _eprint: https://onlinelibrary.wiley.com/doi/pdf/10.1029/JC083iC06p02981, 1978.

Vieira, M., P. V. Guimarães, N. Violante-Carvalho, A. Benetazzo, F. Bergamasco, and H. Pereira, A Low-Cost Stereo Video System for Measuring Directional Wind Waves, *Journal of Marine Science and Engineering*, *8*(11), 831, doi:10.3390/jmse8110831, 2020.

Vittori, G., P. Blondeaux, G. Coco, and R. T. Guza, Subharmonic edge wave excitation by narrow-band, random incident waves, *Journal of Fluid Mechanics*, *868*, R4, doi:10.1017/jfm.2019.214, 2019.

Vousdoukas, M., T. Kirupakaramoorthy, H. Oumeraci, M. de la Torre, F. Wübbold, B. Wagner, and S. Schimmels, The role of combined laser scanning and video techniques in monitoring wave-by-wave swash zone processes, *Coastal Engineering*, *83*, 150–165, doi:10.1016/j.coastaleng.2013.10.013, 2014.

Walsh, E. J., D. W. H. Iii, D. E. Hines, R. N. Swift, and J. F. Scott, Wave-Measurment Capabilities of the Surface Contour Radar and the Airborne Oceanographic Lidar, *Johns Hopkins APL Technica l Digest*, *8*, 8, 1987.

Walstra, D. J. R., G. P. Mocke, and F. Smit, Roller Contributions as Inferred from Inverse Modelling Techniques, in *Coastal Engineering 1996*, pp. 1205–1218, American Society of Civil Engineers, Orlando, Florida, United States, doi:10.1061/9780784402429.094, 1997.

Wanek, J. M., and C. H. Wu, Automated trinocular stereo imaging system for three-dimensional surface wave measurements, *Ocean Engineering*, *33*(5-6), 723–747, doi:10.1016/j.oceaneng.2005.05.006, 2006.

Warner, J. C., W. R. Geyer, and J. A. Lerczak, Numerical modeling of an estuary: A comprehensive skill assessment, *Journal of Geophysical Research: Oceans*, *110*(C5), doi:10.1029/2004JC002691, _eprint: https://agupubs.onlinelibrary.wiley.com/doi/pdf/10.1029/2004JC002691, 2005.

Warrick, J. A., A. C. Ritchie, G. Adelman, K. Adelman, and P. W. Limber, New Techniques to Measure Cliff Change from Historical Oblique Aerial Photographs and

Structure-from-Motion Photogrammetry, *Journal of Coastal Research*, *33*(1), 39–55, doi:10.2112/JCOASTRES-D-16-00095.1, publisher: Coastal Education and Research Foundation, 2017.

Wei, Z., R. A. Dalrymple, M. Xu, R. Garnier, and M. Derakhti, Short-crested waves in the surf zone, *Journal of Geophysical Research: Oceans*, *122*(5), 4143–4162, doi:10.1002/2016JC012485, 2017.

Wu, X., F. Feddersen, and S. N. Giddings, Diagnosing surfzone impacts on inner-shelf flow spatial variability using realistic model experiments with and without surface gravity waves, *Journal of Physical Oceanography*, *-1*(aop), doi:10.1175/JPO-D-20-0324.1, publisher: American Meteorological Society Section: Journal of Physical Oceanography, 2021.

Young, I. R., On the measurement of directional wave spectra, *Applied Ocean Research*, *16*(5), 283–294, doi:10.1016/0141-1187(94)90017-5, 1994.

Zappa, C. J., W. E. Asher, and A. T. Jessup, Microscale wave breaking and air-water gas transfer, *Journal of Geophysical Research: Oceans*, *106*(C5), 9385–9391, 2001.

Zavadsky, A., A. Benetazzo, and L. Shemer, On the two-dimensional structure of short gravity waves in a wind wave tank, *Physics of Fluids*, *29*(1), 016,601, doi:10.1063/1.4973319, 2017.

Özkan Haller, H. T., and J. T. Kirby, Nonlinear evolution of shear instabilities of the longshore current: A comparison of observations and computations, *Journal of Geophysical Research: Oceans*, *104*(C11), 25,953–25,984, doi:10.1029/1999JC900104, 1999.